UNIVERSIDADE D
COIMBRA

João de Sena Baptista Pimentel Marcos

SELF-CALIBRATING COMPACT GAMMA CAMERA FOR REAL-TIME MEDICAL IMAGING

Tese no âmbito do doutoramento em Engenharia Física orientada pelo Doutor Vladimir Solovov e pelo Doutor Andrey Morozov e apresentada ao Departamento de Física da Faculdade de Ciências e Tecnologia

Janeiro de 2020

Self-calibrating compact γ-camera for real-time medical imaging

UNIVERSIDADE D
COIMBRA

João Sena Marcos
Departamento de Física
University of Coimbra

A thesis submitted for the degree of
PhilosophiæDoctor

2020 January

The research reported in this thesis was performed at the Coimbra site of the Laboratório de Instrumentação e Física Experimental de Partículas (LIP) with financial support of the Fundação da Ciência e Tecnologia (FCT) through the scholarship number PD/BD/105918/2014, under the doctoral program *Doctorate in Applied and Engineering Physics* (DAEPHYS).

LABORATÓRIO DE INSTRUMENTAÇÃO
E FÍSICA EXPERIMENTAL DE PARTÍCULAS

daephys

Abstract

Gamma cameras are important molecular imaging tools widely used in nuclear medicine. They allow to image the distribution of γ-ray emitting radionuclides in the human body.

In this work, a complete imaging system based on a small field-of-view (SFOV) gamma camera is designed, assembled and characterized. The goal is to build a real-time imaging system with self-calibration capability.

The self-calibration is based on statistical reconstruction (SR) techniques, which search for the position that gives the best match between the observed and the expected signals of the photosensors. The latter are given by a model of the detector response (DR), which is not straightforward to obtain. It can be obtained either through an experimental calibration which records the photosensors signals for known positions of the source or through simulations. However, an iterative method for obtaining the DR was developed for Anger camera type detectors in 2012. In this method, only flood field irradiation data are required to reconstruct the DR, with no need for information on the γ-ray emission positions. That response is modeled as a set of light response functions (LRFs), one per photosensor. The LRFs give the average signal amplitude as a function of both the position and the energy of the scintillation event.

SFOV cameras have a detection area smaller than 100×100 mm^2. This allows to use smaller components than in conventional cameras and to achieve spatial resolutions on the order of a millimeter or even sub-millimeter, which are important for small animal imaging and for imaging of small organs of humans (e.g. thyroid, prostate). The introduction of SFOV cameras opened the way to the introduction of hand-held devices, for instance to be used during radiotracer guided surgeries (e.g. sentinel lymph node removal).

A model of the gamma camera (GC) was designed to simulate its physical processes. The models and assumptions applied in simulations were validated by comparing the LFRs obtained from simulation data with those obtained from data acquired with an experimental prototype. The agreement between the experimental and simulation results was quite good, allowing to rely on the simulation results for the GC optimization phase.

The design of a SFOV gamma camera was optimized through simulations to achieve sub-millimeter intrinsic spatial resolution and the lowest possible level of distortions. First, optimization of the lightguide thickness was performed and 1 mm was found to be the optimal

value. Second, the effect of using advanced optical coupling materials on the camera performance was studied. It was concluded that the expected slight performance increase does not justify the expenses associated with such change in technology.

Two version of the GC prototype were assembled, one with a LYSO scintillator and another with a GAGG scintillator. The reconstruction of the event positions was performed with SR methods, using LRFs estimated with the iterative method. The application of this method gives the system the desired self-calibration capability.

The equations given in literature for the design of collimators used in large field-of-view systems were successfully validated through simulations for smaller collimators used in SFOV systems. Based on the validated equations, both a parallel-hole collimator and a pinhole collimator were designed and manufactured.

For the experimental measurements, the camera prototypes were connected to the dedicated readout and data acquisition system selected and assembled in the frame of this work. Auxiliary software was developed to streamline the acquisition processes.

Experimental characterization of the developed imaging system was performed using a 140 keV γ source (^{99m}Tc). Intrinsic spatial resolutions of 0.72 mm and 0.90 mm were achieve, respectively, with the *LYSO prototype* and with the *GAGG prototype*. It was demonstrated that both prototype versions have the extrinsic spatial resolutions expected from simulations and analytical equations. The best spatial resolution of 1 mm FWHM in the object plane was achieved with the pinhole collimator, for a overall source-to-detector distance of 35 mm and magnification of about 2 times. With parallel-hole collimator, 1.5 mm FWHM was obtained with the source at 6 mm from the collimator face. The assessed absolute linearity of the *LYSO prototype* was 0.27 mm, while its differential linearity was 0.10 mm. For the the *GAGG prototype* the absolute linearity was 0.21, while the differential one was 0.19 mm.

Nuclear medicine imaging experts have confirmed the feasibility and expected added value of the developed system in the clinical practice, particularly for sentinel lymph node scintigraphy and biopsy, where high spatial resolution would allow to distinguish small but clinically relevant nodules, and for the functional characterization of thyroid nodules.

Keywords: Gamma camera, self-calibration, real-time medical imaging, nuclear imaging, sentinel lymph node biopsy, thyroid scintigraphy, pinhole collimator, parallel-hole collimator, GAGG:Ce, LYSO:Ce

Resumo

As câmaras gama são equipamentos usados em medicina nuclear para obter imagens da distribuição no interior do corpo de radionuclídeos emissores de raios γ.

Neste trabalho desenvolveu-se um sistema de obtenção de imagem baseado numa câmara gama com uma área sensível relativamente pequena (SFOV). O objectivo é conseguir um sistema imagiológico de tempo-real e com capacidade de auto-calibração.

A auto-calibração é baseada em técnicas de reconstrução estatística (SR), que procuram a posição que resulta na melhor concordância entre os sinais medidos nos sensores de luz e os sinais esperados. Estes são dados pelo modelo de resposta do detector (DR), que não é simples de obter, seja através de uma calibração experimental que registe os sinais dos sensores para posições conhecidas da fonte ou através de simulações. Contudo, um método iterativo para obtenção da DR foi desenvolvido em 2012 para detectores do tipo Anger. Neste método, para estimar a DR são apenas necessários dados de irradiação de todo o campo visual do detector, sem necessidade de informação acerca da posição de emissão dos raios γ. A DR é registada com recurso a um conjunto de funções de resposta de luz (LRFs), uma por cada sensor. Os LRFs fornecem a amplitude média do sinal em função da posição e da energia do evento de cintilação.

A área de detecção de câmaras do tipo SFOV é menor que 100×100 mm^2. Isto permite usar componentes mais pequenos que os usados em câmaras convencionais e obter resoluções espaciais na ordem dos milímetros ou mesmo sub-milimétricas, importantes tanto em imagiologia de animais pequenos, como de órgãos pequenos em humanos (ex. tiróide, próstata). O advento das câmaras SFOV abriu caminho à introdução de dispositivos portáteis, por exemplo para uso em cirurgias guiadas por imagem cintigráfica (ex. remoção do gânglio linfático sentinela).

Desenhou-se um modelo da câmara gama (GC) para simular a sua operação. Os modelos e as assunções aplicadas na simulação foram validados comparando as LRFs obtidas quer com dados de simulação quer com dados experimentais adquiridos por um protótipo. A boa concordância entre as LRFs obtidas nos dois casos permitiu confiar nos resultados de simulação para a fase de optimização da GC.

O desenho da câmara gama SFOV foi optimizado através de simulações, tendo em vista a obtenção de uma resolução espacial sub-milimétrica e o menor grau de distorções possível. A

primeira optimização foi feita variando a espessura do guia de luz, chegando-se ao valor óptimo de 1 mm. Depois, estudou-se o efeito da utilização de materias avançados de acoplamento óptico no desempenho da câmera. Concluiu-se que a ligeira melhoria de desempenho não justificava os custos associados a esta mudança de tecnologia.

Contruíram-se duas versões do protótipo da GC, usando diferentes cintiladores: LYSO e GAGG. A reconstrução das posições dos eventos foi feita através de métodos SR, usando LRFs estimadas com o método iterativo. A aplicação deste método conferiu ao sistema a capacidade de auto-calibração.

As equações estabelecidas na literatura para o desenho de colimadores aplicados a sistemas cintigráficos convencionais (e.g. GC com diâmetro de área sensível $\approx$50 cm) foram validadas com sucesso através de simulações para colimadores de menores dimensões, usados em sistemas SFOV. Foram desenhados e fabricados tanto um colimador de furos paralelos, como um colimador pinhole.

Para a realização das medidas experimentais, ligaram-se os protótipos da CG ao sistema de leitura e acquisição de dados seleccionado e montado no âmbito deste projecto. Desenvolveu-se o software auxiliar para agilizar o processo de acquisição.

Para a caracterização experimental do sistema de imagem desenvolvido usou-se uma fonte de raios γ com energia de 140 keV. Conseguiram-se resoluções espaciais intrínsecas de 0.72 mm e 0.90 mm, respectivamente, com o *protótipo LYSO* e com o *protótipo GAGG*. Demonstrou-se que o protótipo tem as resoluções espaciais extrínsecas previstas pelas simulações e pelas equações analíticas. A melhor resolução, 1 mm FWHM no plano do objecto, obteve-se com o colimador pinhole para uma distância fonte-detector de 35 mm e um factor de ampliação próximo de 2. Com o colimador de furos paralelos obteve-se uma resolução de 1.5 mm FWHM, com a fonte a 6 mm da face do colimador. A linearidade absoluta avaliada para o *protótipo LYSO* foi 0.27 mm, enquanto que a linearidade diferencial foi 0.10 mm. Para o *protótipo GAGG* avaliou-se uma linearidade absoluta de 0.21 mm e uma linearidade diferencial de 0.19 mm.

Especialistas em medicina nuclear confirmaram a viabilidade do sistema desenvolvido para a prática clínica e o valor acrescentado que poderá trazer. Em particular, para cintigrafia e biópsia do gânglio linfático sentinela, para a qual uma alta-resolução espacial permitiria distinguir gânglios de pequena dimensão mas ainda assim clinicamente relevantes, e para caracterização funcional dos nódulos de tiróide.

Palavras-chave: Câmara gama, auto-calibração, imagiologia médica em tempo-real, medicina nuclear, biópsia de gânglio linfático sentinela, cintigrafia de tiróide, colimador pinhole, colimador de furos paralelos, GAGG:Ce, LYSO:Ce

To my loving parents
José David and Catarina de Sena

Acknowledgements

I am immensely grateful to my two supervisors: Dr. Vadimir Solovov and Dr. Andrey Morozov. In the first place I am grateful for the amazing opportunity to be part of their Gamma Cameras group team; but also for their friendship and countless support over the past few years. It was a long journey. Many paths were travelled, interesting nooks and crannies explored. An emotional, roller coaster of a PhD. In Dr. Vladimir and Dr. Andrey I found very wise, extremely thorough, rigorous scientists. I appreciate their patience for discussions and acceptance of my own limitations.

I learnt a lot with Vladimir, who calmly shared his vast wisdom with me. We spent many hours together in the lab. He often surprised me with his findings, ingenious solutions for the group challenges and clever tricks. He is one of those people eager to take advantage of the best cost-effective technology available at the moment, both on software and hardware wise. I witnessed his successful endeavors several times. Vladimir always found time for me, even though he is part of important international collaborations (*LUX-ZEPLIN* dark matter search project, for a start!) and he has a bunch of supervision and coordination responsibilities. He often appeared in my office at the end of very busy days, without a complaint, giving my work all his attention, as if there was nothing else in his mind. This always impressed me. Vladimir also had another very important role: he gave me confidence during crucial periods of writing this thesis. The power generated by trust is priceless. The power of the right word dropped at the right time cannot be estimated.

Andrey is one of the most objective-oriented persons I have ever met. Hard to achieve objectives that is. With him I have learnt that almost everything can be done, when one wants to do so and has the time for it. His progressive development of the ANTS2 simulation package is an example of continuous improvement and addition of ever more sophisticated tools. I must acknowledge Andrey for a handful of key conversations. By frequently putting his own experiences during his PhD as examples in which he has learnt and grew both as a person and as a scientist, he helped me greatly. This way of guiding junior researchers suits me

well. Self examples from senior colleagues are particularly encouraging and engaging, unlocking the best of me. I should accept soon Andrey's frequent invitations to try ocean diving and practice fencing (his favorite sports so far). As Vladimir, he conciliates perfectly work, leisure and time for family.

Both Vladimir and Andrey helped me a lot on how to be critical of my own work. I'm still learning, actually. The last stretches of reviewing the manuscript were quite intense for them as supervisors. I believe the thesis text is immensely better due to their suggestions and it evolved into a clearer and more enjoyable reading. On a final, mapleleaf about my supervisors: I really, really (add another one for luck) appreciate the smile with which they said goodbye at the end of all those countless meetings, even the tougher ones. Particularly after the tougher ones. And yes, *le chef* Vladimir has shared a couple of his best cuisine secrets with me. I apologize, but they can't be disclosed.

I am in great debt to Prof. Dr^{a} Isabel Lopes, director of the Coimbra site of Laboratório de Instrumentação e Física Experimental de Partículas (LIP), where I undertook my PhD works. She was the one who understood that when my FCT scholarship clock ran out I would have to start working, implying an excessive postponement of wrapping up the writing of the thesis manuscript. During a difficult time for our lab's finances, Prof. Isabel and the other director, Prof. Dr. Rui Marques, decided to support me with a six-month scholarship. This allowed me to write up full time and finalize the remaining scheduled work tasks. Thank you, professors.

I'm thankful to Prof. Dr. Vitaly Chepel for his interest in my work and wise suggestions, especially those related to experimental measurements. My gratitude needs to encompass Eng. Jorge Isidoro, Eng. Paulo C. Gil, Dr^{a} Gracinda Costa and Dr. Rodolfo Silva from Centro Hospitalar da Universidade de Coimbra. They opened the doors of the nuclear medicine department for the experimental characterization of the developed compact gamma camera prototypes. We also had very useful discussions.

Huge thanks also to my colleagues Alberto Blanco, João Saraiva, Luís Margato and Luís Pereira for the fruitful conversations and the sharing of knowledge and laboratory resources. A heartfelt thanks to some friends, who recently completed their doctorates and that with their experience gave me words of encouragement, timely advice and pleasant friendship moments: Edivagner Ribeiro, Daniel Gaspar, Rafael Raposo, Cristóvão Sousa, André Cortez, Pedro Vaz, Hugo Simões, Carlos Henriques e Miguel Moita.

A particularly warm hand of gratitude to several people at the LIP workshop for they are both very good professionals and kind people. It is a delight to cross the same corridors and exchange brief words with Eng. Rui Alves, Eng. Nuno Filipe Dias, Douglas Lima and Mr. Carlos Silva. They placed their design and manufacture of aluminium and plastic parts skills, essential for my experimental work, at my disposition. Not to mention the numerous wee mechanical services they willingly and joyfully provided. I found the same willingness to help, from the Detector's laboratory stuff, namely Nuno Carolino, Américo Pereira, Luís Lopes e Orlando Cunha.

Nuno Carolino taught me without uttering a word how to efficiently manage an electronic workshop and provide high quality services. Thank you also to João Silva, for computer and network issues support. I have learnt some interesting tricks indeed. I would also like to extend my gratitude to Elisabete Neves e Ricardo Caeiro. They make bureaucratic issues so smooth (daily affairs, purchases and travel petty cash)! This allows one to fully focus on their research work.

For the production of two of the gamma camera prototype components I had to make a trip to Albergaria-a-Velha to meet engineers from two hard metal companies: Palbit and Durit. A heartfelt thank you to Daniel Ferreira at Palbit for providing me with the opportunity to visit the rock drilling equipment warehouse where my dear grandfather Francisco Baptista worked countless times. Many of the components prepared at that location filled the floor and the walls of my grandfather's office, where I spent many great childhood days. I remember the enjoyable days I spent with my siblings trying on steel boots and other mining equipment used by my grandfather when visiting mines.

I would like to cross the ocean and say thank you to Metricon company (New Jersey, US), namely to John Jackson, as he kindly offered to perform the measurement of the index of refraction of a key component of the gamma camera prototype, the grease to couple the optical components. This allowed me to use the most suitable value in the simulations.

Before joining the Gamma Cameras group, I had the pleasure to work with Prof. Doutor Mário Silveirinha in the Microwaves laboratory at Instituto de Telecomunicações. I greatly admire his extremely kind and attentive manners and his massive intellectual calibre. I carry a strong feeling of gratitude to him. He left an indelible mark on my career path. I further extend my thanks to three colleagues at the Microwaves lab for their friendship, help and uncountable funny anecdotes and situations: Tiago Morgado ("the great"), João Tiago Costa e David Fernandes.

My research was funded by DAEPHYS, a FCT-backed doctoral program. Without it I would not have undertaken this path. This opportunity was a privilege, only possible by the investment on higher level education made by a man of science, Dr. Mariano Gago, Ministro da Ciência e Tecnologia (1995-2002) and also ahead of the Ministério do Ensino Superior (2005-2011). He was one of the founders and the director of LIP. He carried his particle physics PhD at the École Polytechnique and the Université Pierre et Marie Curie. Years later he was an instrumental pivot in Portugal becoming a CERN member state (1986). Mariano passed away too soon, in 2015. A heartfelt tribute from people around the world can be found at `http://www.marianogago.org/`.

I have acquired highly valuable knowledge in the amazing field of nuclear medicine imaging, a powerful tool for the diagnosis and clinical study of tumors and other diseases. Today I feel prepared to team up with other professionals in the medical physics arena, namely in the development, operation and maintenance of gamma cameras. This is the natural result of investing on education, whose impact on society is flourishing from various fields of knowledge.

At last, although the journey was long and a bit weary, I was never alone while threading it. My dearest loved ones are aware of this and they know how much I owe them and how grateful I am. Some cannot be close to me everyday, but they are very close to my heart and always present in my daily prayer. A resounding *high-five* to my brother Tiago, also journeying a PhD roller coaster, for all the support, music and laughs! *We love this game.*

During the last months of this *grand, mysterieuse voyage* I've been a bit "farther away", with the consent and encouragement of family and close friends. Thanks for making this final push easier. I tried to walk the path with you and the good God in mind. I think it is worth working this way.

Thank you all so much!

Contents

List of abbreviations and acronyms

ADC ..... Analog-to-digital converter

ANN ..... Artificial Neural Networks

APD ..... Avalanche photodiodes

ASIC ..... Application-specific integrated circuit

CCD ..... Charge-coupled device

CHUC ..... Centro Hospitalar da Universidade de Coimbra

CoG ..... Center of gravity

DAQ ..... Data acquisition system

DoI ..... Depth of interaction

dSiPM ..... Digital silicon photo-multiplier

EDM ..... Electric discharge machining

FEE ..... Front-end electronics

FWHM ..... Full width at half maximum

FOV ..... Field of view

FPGA ..... Field-programmable gate array

ILL ..... Institut Laue–Langevin

k-NN ..... K-nearest neighbors

LEGP ..... Low-energy general-purpose collimator

LEHR ..... Low-energy high-resolution collimator

LEHS ..... Low-energy high-sensitivity collimator

LFOV ..... Large field of view

LG ..... Lightguide

LIOB ..... Laser-induced optical barriers

LRF ..... Light response function

LS ..... Least squares

LSF ..... Line spread function

LUT ..... Look-up table

LYSO ..... Lutetium Yttrium Silicate

MFP ..... Mean free path

ML ..... Maximum likelihood

MLE ..... Maximum likelihood expectation

MPI ..... Message passing interface

MRI ..... Magnetic resonance imaging

NEMA ..... National Electrical Manufacturers Association

NIST ..... National Institute of Standards and Technology

OCT ..... Optical crosstalk

PDE ..... Photon detection efficiency

PET ..... Positron-emission tomography

PH ..... Parallel-hole collimator

PHS ..... Pulse height spectrum

PM ..... Multi-pinhole collimator

PMMA ..... Poly(methyl methacrylate), plexiglass

PMT ..... Photomultiplier tube

PSF ..... Point spread function

PSPMT ..... Position-sensitive photomultiplier tube

QE ..... Quantum efficiency

RoHS ..... Restriction of Hazardous Substances

RPC ..... Resistive plate chamber

SFOV ..... Small field of view

SiPM ..... Silicon photo-multiplier

SLM ..... Selective laser melting

SLN ..... Sentinel lymph node

SPECT ..... Single-photon emission computed tomography

SPS ..... Single photoelectron spectrum

SR ..... Statistical reconstruction

SSLE ..... Subsurface laser engraving

TIA ..... Transimpedance amplifier

UFOV ..... Useful field of view

UV ..... Ultraviolet

1

Introduction

1.1 Overview

The discovery of X-rays by Röntgen in 1896 was a great step towards medical imaging as we know it today. Before, the tools to acquire knowledge about the status of the inner human body were only the iconic stethoscope, the microscope, the thermometer and some scary cutting instruments to allow the direct view [1]. The X-ray imaging is based on the attenuation of the radiation along its path through the body and is vastly used for anatomical imaging. However, when physiological information is needed, molecular imaging (also known as nuclear imaging) is required. A compound containing a γ-rays emitting radioactive isotope (radiotracer) is administered to the patient and it is distributed throughout the body, according to its biochemical properties. Dedicated nuclear medicine apparatus can be used to acquire either projections (scintigraphy) or a three-dimensional map (tomography) of the radiotracer distribution in the patient's body. Different radiotracers accumulate in specific regions and are used to study different biological processes, such as, e.g., perfusion, metabolism, receptor expression and hypoxia.

The history of nuclear imaging devices have started in 1951. The rectilinear scanner was the first successful instrument in molecular imaging studies [2]. This radiation detector was used to scan the patient and record the flux of γ-rays at a particular region of the image plane, thus providing a projection of the radiotracer distribution inside the body.

In 1958 Hal Anger presented a faster imaging system, which was able to provide the positions of γ-ray interactions in a large-area position-sensitive detector [3]. These detectors, the gamma cameras, are still widely used today in scintigraphy, one of the most common imaging modalities. Gamma cameras are devices able to detect single γ-rays that interact with the sensitive medium, most commonly inorganic scintillator crystals (e.g. NaI(Tl), CsI(Tl), $CeBr_3$, LYSO). When an interaction takes place, part of the energy carried by the γ-ray is

converted into scintillation light, that is collected by an array of photosensors coupled to the crystal.

Conventional gamma cameras have their biggest dimension in the order of 50 cm. For imaging of small organs (e.g. thyroid, prostate, sentinel lymph nodes) smaller size devices were considered, as they would allow portability. For more than a decade, gamma cameras of reduced size have been used. Their sensitive area is typically two orders of magnitude smaller than that of the conventional cameras. One important application of gamma cameras of small size (also called "compact", "hand-held" or "portable" cameras) is in nuclear imaging during surgeries, for instance for the sentinel lymph node biopsy (e.g. in melanoma and breast cancers staging) [4, 5], as they can be installed, for instance, in an articulated arm in the operation room. Compact cameras are also being used in small animal (e.g. mice) imaging, widely applied in the drug discovery cycle, for instance to monitor the therapy of an induced disease reflected in the physiologic function of certain organs. In small animals imaging (e.g. mice brain and heart) as well as in imaging of small organs of humans, higher resolutions are required than those that can be achieved with the conventional cameras [6].

Originally, the method used for reconstruction of scintillation event position was the center-of-gravity algorithm (CoG) which is based on the calculation of the centroid of the photosensor center positions weighted by the sensor signals. The CoG is still used in the vast majority of modern gamma cameras. However, the application of the CoG algorithm results in systematic distortions, so subsequent corrections are applied using look-up tables (LUTs). A LUT provides the mapping between the reconstructed position and the position of the source, for a grid of points distributed over the entire camera field-of-view (FOV). The LUTs are filled using data obtained with calibration procedures.

It was shown that distortion-free image reconstruction in gamma cameras can be obtained using statistical position reconstruction (SR) algorithms (e.g. maximum likelihood) [7]. To apply these algorithms, a model of the detector response is required. The model provides the average number of detected photons in each photosensor per scintillation event as a function of the scintillation position and the number of emitted photons (light response function, LRF). Thus, the model is a set of LRFs, one per photosensor. The position of the scintillation event is reconstructed by finding the position which results in the best match between the measured signals and those given by the model. SR algorithms have also the advantage of allowing the reconstruction of positions beyond the centers of the most outer "ring" of sensors (camera periphery), contrarily to the CoG algorithm [8]. However, until recently, SR techniques were not broadly used, mainly because of the following two reasons: firstly, the SR algorithms are very demanding in terms of the required computational power and secondly, the required model needs calibration data, which in most of the cases is not straightforward to obtain. At

the modern level of electronics, the computational power is not a problem. Today, the access to parallel computing (e.g. offered by the graphics processing unit) is commonly available in personal computers. However, the problem of obtaining the model is not so easy to solve. It is typically obtained by scanning the camera field-of-view with a pencil beam gamma source using a dedicated moving stage, which is a time-consuming procedure (see, for example, [9]) and usually requires specialized personnel. An alternative solution that can be applied in a shorter time and that can potentially avoid the moving stage was investigated in this work.

In many cameras, the photosensor response can be considered axially-symmetric. In this case, a self-calibration method introduced by Solovov et al. [10] can be used to build the model using data from the flood irradiation of the entire detector field-of-view with an uncollimated (flood) gamma source. Typically the self-calibration procedure requires relatively short time (on the order of minutes). The authors call it *adaptive method* and it is an iterative procedure which starts with an initial guess on the LRFs (e.g. using CoG reconstruction results) and is performed until a convergence of the LRFs into those that faithfully describe the detector response. Models built with the adaptive method have already been successfully applied in statistical reconstruction of scintillation events in several Anger camera type detectors [10, 11, 12].

Physicians and nuclear physicists of the nuclear medicine department from Centro Hospitalar da Universidade de Coimbra (CHUC) have confirmed that the self-calibration capability given by the adaptive method have benefits for clinical practices. Firstly, a model of the camera can be obtained without calibration scans. Secondly, the possibility of using the radiotracer already administered to the patient as the calibration source offers the possibility of obtain an updated model in the proximity of the examination time, with no need for calibration sources. The entire camera FOV can be irradiated moving the camera and the recorded data is sufficient to build the model, because the iterative procedure does not have strict requirements on the uniformity of the irradiation. The self-calibration capability is also an additional method to handle the effects due to the camera aging, which can bring changes in the physical properties, such as, e.g. degradation of the quality of the components coupling due to the appearance of air bubbles between them, the reduction of transparency in the optical grease or the lightguide, changes in refractive indexes or changes in the detection efficiency of photosensors. The application of the self-calibration technique have the potential to reduce downtime and maintenance costs of gamma cameras, usually associated with the calibration procedures, without compromising the image quality.

A new compact camera that incorporates this self-calibration procedure was proposed having in mind clinical applications. In CHUC nuclear imaging department two clinical examinations can benefit from a compact gamma camera that can be placed close to the region

under examination: thyroid imaging and sentinel lymph node (SLN) biopsy, a clinical practice used to evaluate the dissemination degree of breast or skin tumors.

For clinical and pre-clinical applications, the gamma camera requires a collimator, which projects the distribution of the radiotracer onto the scintillator crystal. Two types of collimators are used most commonly: the parallel-hole and the pinhole collimators. The former has typically a higher γ-rays transmission efficiency than the latter for equivalent spatial resolutions, so it is better suited to image organs or tissues with low uptake of the radiotracer and when high rate of γ-ray detection is required, for instance to present a video showing the time evolution of the radiotracer distribution projection. The pinhole collimator is used when there is need for magnification or de-magnification of the object projection onto the detector field-of-view. Pinhole collimator also offers the possibility of achieving higher effective spatial resolution. When I have joined the laboratory, there was already expertise with the adaptive method for the self-calibration of conventional large field-of-view gamma cameras [12]. At that time, the first prototype of a small field-of-view gamma camera constituted by a scintillator and an array of silicon photomultipliers was being developed and the self-calibration method was being applied to it. These previous works on small FOV gamma cameras were only targeting intrinsic parameters, without any study targeting collimator design and the characterization of a complete gamma camera imaging system (assessment of extrinsic parameters).

The thyroid examination typically requires a pinhole collimator to magnify the malignant nodules. The SLN imaging, where the activities are rather low, requires a parallel-hole collimator. Thus, it was decided to have two interchangeable collimators for the new SFOV camera: 1) a pinhole collimator for thyroid studies and 2) a parallel-hole collimator for sentinel lymph node imaging.

The camera should have high degree of uniformity and an acquisition rate of at least 10 kHz, mainly to speed up the calibration procedures. The capability to reconstruct the event positions at high rates would allow real-time visualization of the radiotracer distribution. In some cases this feature is mandatory, as for intraoperative imaging in SLN biopsy. A portable real-time imaging system would allow to show in a few seconds an image of the nodules. As statistical reconstruction is used, another useful feature is possible to implement: the monitoring of a parameter that expresses how adequate is the detector model to describe the current response of the camera.

1.2 The goal and the work plan

The development of a real-time imaging system based on a self-calibrating small field-of-view gamma camera is the goal of this work. The two main target clinical applications are the thyroid ganglia studies and the radio-guided surgery for sentinel lymph node biopsies. The

equipment aims to offer state-of-the-art performance at significantly lower price than that of other alternatives in the market and also to reduce the maintenance routines and associated costs. A distinctive feature of the system is the capability of monitoring the quality of the detector response model and update it using a fast and inexpensive procedure.

The complete imaging system envisioned for this PhD work consists of a high-resolution ($<$ 1 mm) small FOV gamma camera, two interchangeable collimators (parallel-hole and pinhole), the electronics for the readout of 64 photosensors at an acquisition rate of least 10 kHz, and the processing software for the reconstruction of position and energy of the scintillation events whenever the photosensor signals arrive to the processing unit. The design of the gamma camera should be optimized through simulations to achieve the required high-resolution and the lowest possible level of distortions. However, when using simulations, the simulation models should be first validated. The validation should be performed by comparing the simulation results with those obtained experimentally with a prototype built for this purpose.

Hence, the work envisioned in this thesis was planned to be performed along the following line:

1. Develop and then experimentally validate the camera simulation model
2. Perform the gamma camera design optimization
3. Build a prototype
4. Design and order the collimators
5. Assemble and test the readout system
6. Develop the real-time processing tool
7. Interface the prototype with the readout system and characterize its performance in laboratory environment
8. Characterize the complete imaging system (with a collimator) using high activity sources
9. Demonstrate the real-time and self-calibration capabilities

1.3 Outline

The thesis is organized in five main sections. **Section 2** presents the scientific background and the technology behind scintillation based gamma cameras, starting with the physical processes, namely interaction of γ-rays with matter and geometrical optics. The main types of γ-ray detectors are briefly presented. A review is given on the main gamma camera components:

collimator, scintillator crystal, lightguide and photosensors. The electronic circuits for the sensor signal readout are presented and a brief discussion is given for possible approaches to implement event triggering and signal digitalization. The gamma camera performance parameters are described, followed by a review on the methods for the reconstruction of the position and energy of scintillation events. The iterative procedure for the reconstruction of the light response function of photosensors is explained in detail. The state-of-the-art on small field-of-view gamma cameras is also reviewed.

Section 3 presents the optimization of a compact camera design based on a monolithic crystal and an array of silicon photomultipliers. The section starts with a description of the requirements on the camera and then presents its geometry and basic components. The processes which were included in the simulation of the gamma camera operation are described, as well as the assumptions used in the simulations. The experimental validation of the camera design model is presented. The design of a parallel-hole collimator and a pinhole collimator for the required efficiencies and spatial resolutions is discussed.

Section 4 presents the readout system used in this work. The section starts with the presentation of the requirements. Five most relevant solutions available on the market at the time of searching for a readout are presented, with emphasis on the TRB3 board from GSI, the data acquisition system (DAQ) solution chosen for the readout. The complete readout system is presented, starting with the front-end electronics for amplification and shaping of the sensor signals, followed by a description of the hardware and software used for the acquisition and data storage.

Section 5 presents the procedures to process the signals acquired from the photosensors until the visualization of the reconstructed positions, in what was called "real-time processing chain". The procedures required to perform the acquisitions are briefly presented, followed by an implementation of the adaptive algorithm for automatic estimation of the light response functions (LRFs) from flood field irradiation data. The data structures and the complete chain of procedures necessary for the real-time visualization of the event positions from the sensors signals are then presented. The timing performance of the real-time processing chain is analyzed.

Section 6 presents the characterization of the complete imaging system. The section starts by presenting the assembled detector prototypes and the experimental measurement setup. Then, the calibration results are briefly discussed for each prototype, including the comparison between the LRFs estimated with the adaptive algorithm from the experimental data with those obtained from simulations. Both the characterization results on the intrinsic parameters of the gamma camera prototypes and the characterization results for the complete imaging system (with the collimator attached) are presented and discussed. The section ends

with a summary of the performance parameter values of the two versions of the gamma camera prototype (spatial resolution, uniformity and linearity), and a comparison of these values with those of similar existing gamma cameras.

Personal contribution

Below, my personal contribution both in the work presented in this thesis and in two scientific papers published during my PhD works is summarized. All studies were performed in the Laboratório de Instrumentação e Física Experimental de Partículas (LIP) except the experimental characterization measurements, which were conducted in the Centro Hospitalar da Universidade de Coimbra.

Section 3

- Preparation and execution of all simulations and experimental measurements presented in the section
- Study of GAGG properties and the conclusion that it should be applied instead of LYSO as the camera scintillator material
- Optimization of the design of a gamma camera based on a monolithic GAGG crystal
- Determination of the wavelength-resolved optical properties of GAGG (refractive index and attenuation length) needed to improve the precision of the camera simulation model
- Development of ANTS2 scripts for the lightguide thickness optimization cycle
- Assembly of two gamma camera prototypes
- Validation through simulations of the suitability of the equations given in literature for the design of large FOV collimators to the design of small FOV collimators
- Design and order of a parallel-hole and a pinhole collimators

Section 4

- Establishment of the requirements on the readout system (front-end electronics and DAQ).
- Analysis of the DAQ systems available in the market and negotiation with the suppliers
- Set up of the software prerequisites and the environment needed to run the acquisition drivers
- Mapping of the TRB3 board electronic channels

Section 5

- Development of the software for acquisition control (using TRB3 GSI drivers)
- Development of the software for integration of waveforms data (using TRB3 GSI drivers)
- Comparison between *local* and *globlal* pedestals extraction (including the measurements for both cases)
- Development of ANTS2 scripts for:

- Automatic LRF calculation
- Real-time acquisition (start acquisition, process data and present reconstructed image)
- Monitoring the quality of camera response model

Section 6

The characterization of the gamma camera prototypes and of the complete system (including the collimator) was performed in Centro Hospitalar da Universidade de Coimbra (CHUC). It was my responsibility to organize and perform the characterization of the prototypes.

- Design and order of masks used for detector characterization
- Definition of the protocol for characterization measurements
- Installation and test of the readout system before the measurement campaign
- Validation of the adaptive algorithm for the camera model reconstruction using ^{99m}Tc flood field irradiation data
- All measurements required for the characterization of intrinsic and extrinsic parameters of the prototypes
- All data processing for the prototypes characterization
- Characterization of the intrinsic performance of the prototypes: spatial resolution, uniformity, linearity, energy resolution
- Assessment of the extrinsic spatial resolution of the two gamma camera prototypes

Scientific papers

1. *SiPM-based neutron Anger camera with auto-calibration capabilities* Journal of Instrumentation, Volume 14 (published at 15 March 2019) A. Morozov, J. Marcos, L. Margato, D. Roulier and V. Solovov

   Abstract: We present characterization results of a neutron Anger camera based on a lithium-6 loaded cerium activated silicate glass scintillator (33.3 × 33.3 × 1 mm^3) and an array of 64 silicon photomultipliers. Reconstruction of the scintillation events is performed with a statistical method, implemented on a graphics processing unit (GPU). We demonstrate that the light response model of the detector can be obtained from flood irradiation calibration data using an unsupervised iterative procedure. The useful field of view is 28 × 28 mm^2 . The spatial resolution measured at 2.5 Angstrom neutron beam is better than 0.6 mm FWHM and the energy resolution at the neutron peak is 11%.

   My contribution:

   - Participation in the neutron beam tests of the detector prototype at ILL in Grenoble
   - Reconstruction of the detector response and positions of neutron events
   - Evaluation of the detector spatial resolution.

2. *Iterative reconstruction of SiPM light response functions in a square-shaped compact gamma camera* Physics in Medicine & Biology, Volume 62, Number 9 (Published 5 April 2017) A. Morozov, F. Alves, J. Marcos, R. Martins, L. Pereira, V. Solovov and V. Chepel

Abstract: Compact gamma cameras with a square-shaped monolithic scintillator crystal and an array of silicon photomultipliers (SiPMs) are actively being developed for applications in areas such as small animal imaging, cancer diagnostics and radiotracer guided surgery. Statistical methods of position reconstruction, which are potentially superior to the traditional centroid method, require accurate knowledge of the spatial response of each photomultiplier. Using both Monte Carlo simulations and experimental data obtained with a camera prototype, we show that the spatial response of all photomultipliers (light response functions) can be parameterized with axially symmetric functions obtained iteratively from flood field irradiation data. The study was performed with a camera prototype equipped with a $30 \times 30 \times 2$ mm^3 LYSO crystal and an 8×8 array of SiPMs for 140 keV gamma rays. The simulations demonstrate that the images, reconstructed with the maximum likelihood method using the response obtained with the iterative approach, exhibit only minor distortions: the average difference between the reconstructed and the true positions in X and Y directions does not exceed 0.2 mm in the central area of 22×22 mm^2 and 0.4 mm at the periphery of the camera. A similar level of image distortions is shown experimentally with the camera prototype.

My contribution:

- Participation in the experimental campaign.

2

Scientific background and technology

Gamma cameras are used in nuclear medicine for molecular imaging, mainly intended for disease diagnosis. They were invented by Hal Anger in 1958 [3]. In a typical examination with a gamma camera, a patient is injected with a radiotracer which is a physiologically active substance containing a γ-ray emitting isotope. To image a specific organ or tissue a specific radiotracer should be selected, which will flow through the circulatory system allowing the study of perfusion and metabolic processes, among others.

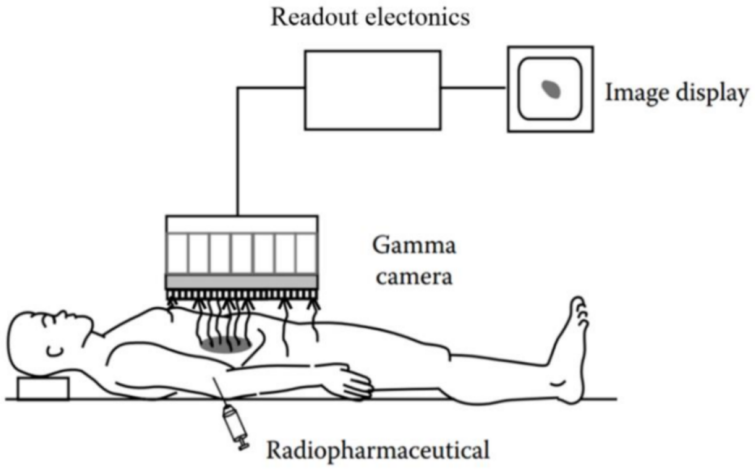

Figure 2.1: Schematic view of a gamma camera imaging medical examination. Note that only the γ-rays perpendicular to the camera pass the camera collimator. Image adapted from [13].

Gamma camera is a position sensitive detector of γ-rays. Its working principle is usually based either on the absorption of γ-rays in a scintillator or in a semiconductor material. The gamma camera developed in this work is of scintillation based type. Scintillation based gamma cameras, typically consist of a scintillator, a lightguide, a set of photosensors and a collimator.

The detection of γ-rays is possible because γ-rays interact with a scintillator crystal which emits light. The production of light that occurs when one single γ-ray interacts with the crystal is called "scintillation event". An array of photosensors connected to a readout system collects the light produced by each event. The distribution of the signals over the array of sensors is used to reconstruct the position where the scintillation event took place. By plotting the (x, y) reconstructed position of many events, it is possible to obtain an image which is a projection of the density of the tracer inside the body on the scintillator by the collimator.

This section starts by discussing the interaction of γ-rays with matter and the transport of optical photons inside the gamma camera. Its performance parameters are presented, as they are of major importance for the clinical physicists and physicians. The different components of a gamma camera are described, giving a closer insight into the working principles of this type of detector. A brief review is given on the electronic readout system for gamma cameras as well as on the traditional centroid position reconstruction technique. The gamma camera performance assessment is discussed. The techniques for the reconstruction of the position and energy of scintillation events are also presented. Next, a detailed description of the self-calibration algorithm used for the estimation of the detector response model is given. Finally, the state-of-the-art on small field-of-view gamma cameras is drawn, with special emphasis on cameras used for the detection of sentinel lymph nodes during intraoperative surgery.

2.1 Physics of the gamma camera

2.1.1 Interaction of γ-rays with matter

When a γ-ray interacts with a material, some concurrent phenomena may happen depending on the energy of the γ-ray:

1. **Photoelectric effect**: γ-ray interacts with an atom and an electron (photoelectron) is ejected, usually an inner shell electron. Part of the γ-ray energy, equal to the binding energy E_B), is used to remove the electron from the atom and the remaining energy E is transferred to the photoelectron. Thus, the energy of the outgoing electron is:

$$E = E_\gamma - E_B \tag{2.1}$$

   where E_γ is the energy carried by the incoming γ-ray.

   The vacancy created by the electron ejected from the atom will be filled with other electron from an upper shell, reestablishing the atom lowest energy state. This relaxation can occur either through fluorescence, with the emission of an X-ray, or through a non-radioactive transition, with the emission of an Auger electron. These two secondary

effects of photoelectric absorption have complementary probabilities. **Fig.2.2** represents that two effects, which follow the photoelectric absorption of a primary γ-ray.

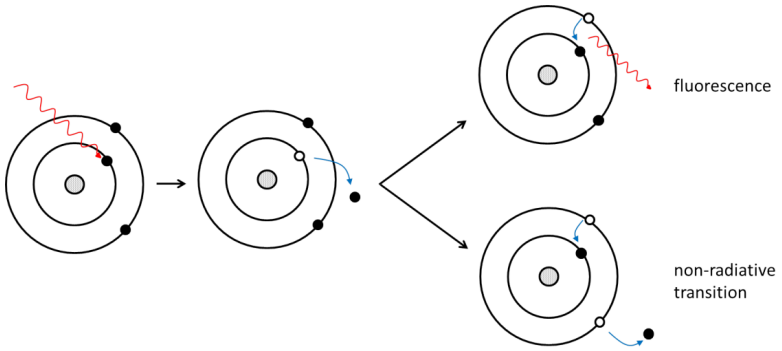

Figure 2.2: Photoelectric absorption and secondary effect representation. One γ-ray (red arrow on the left) interacts with an atom and a photoelectron is ejected (blue arrow on the left) leaving a vacancy. Fluorescence or a emission of an Auger electron can occur with complementary probabilities. The image was copied from [14].

The photoelectric cross section Φ_{photo} for different materials is known[1] for a broad range of energies. The attenuation coefficient for the photoelectric effect can be taken, for instance, from XCOM, a database of NIST [16].

2. **Compton scattering**: a γ-ray transfers part of its energy E_i to an electron of the atom it interacts with. The remaining energy E_f is carried by the γ-ray, scattered by an angle θ in the collision with the electron (**Fig.2.3**). The relation between E_f and θ is given by the Eq.2.2:

$$\frac{1}{E_f} - \frac{1}{E_i} = \frac{1}{m_e c^2}(1 - cos(\theta)) \tag{2.2}$$

Where m_e is the electron rest mass and c the speed of light.

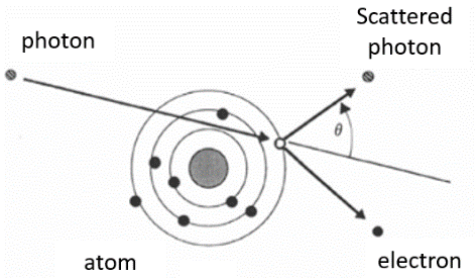

Figure 2.3: Compton scattering effect representation. A γ-ray transfers part of its energy to an electron of the atom it interacts with.

As an illustration, see in **Fig.2.4** the distribution of both the angle and the energy of

[1] As an example see [15].

the scattered γ-ray for a set of one hundred thousand simulated Compton events, for an incoming γ-ray of 140 keV.

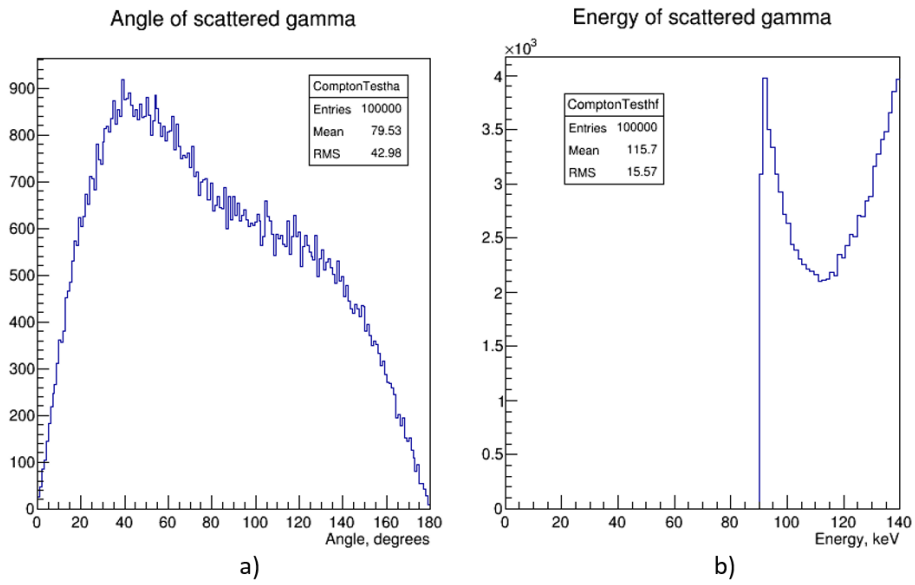

Figure 2.4: Angle (a) and energy (b) of scattered γ-ray. Distributions of the angle and energy of the scattered γ-ray for a set of 10^5 simulated Compton events and a initial γ-ray of 140 keV.

The maximum energy transfer due to gamma scattering occurs for frontal collisions with the photoelectron, which corresponds to a scattering angle of 180°. In this case the scattered γ-ray will remain with the least possible amount of energy (left peak in **Fig.2.4 b.**).

3. **Pair production**: A γ-ray interacts with the nucleus of an atom releasing a positron, which annihilates in a collision with an electron. This annihilation process emits two γ-rays of 511 keV in diametrically opposite directions, as it is represented in **Fig. 2.5**.

   The process of pair production involves the transformation of a γ-ray into an electron-positron pair. In order to conserve momentum, this can only occur in the presence of a third body, usually a nucleus. Moreover, to create the pair, the γ-ray must have at least an energy of 1.022 MeV, twice the energy of electron at rest.

4. **Coherent scattering**: In the interaction by coherent (or elastic) scattering, the γ-rays that collide with electrons in the atom undergo change in their direction without energy loss, obeying conservation of momentum. The cross section of coherent scattering is often ignored, because it is relatively small. In soft tissues, coherent scattering represents less than 5% of the interactions for particles with energies above 70 keV [17]. However, it may affect spatial resolution of high-resolution detectors.

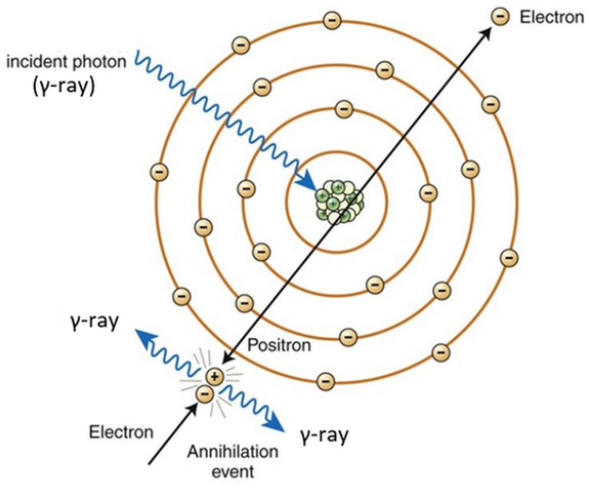

Figure 2.5: Pair production effect representation. When the positron emitted from the annihilation of the incident γ-ray collides with an electron, the positron annihilates, emitting two γ-rays in opposite directions.

Attenuation spectrum The combination of the four mentioned effects defines the shape the attenuation spectrum. **Fig.2.6** shows the contribution of each effect as well as the full attenuation curve for NaI(Tl) scintillator, a crystal commonly used in gamma cameras.

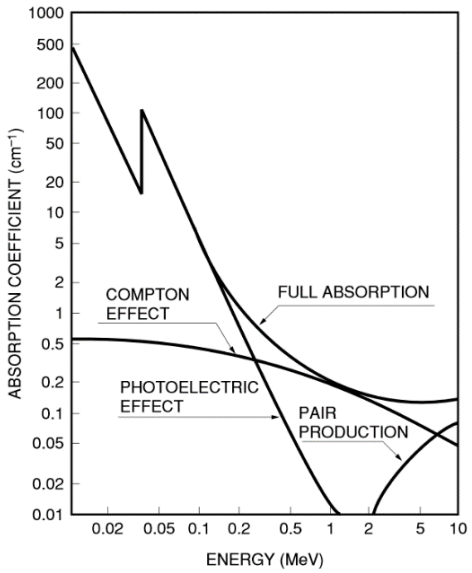

Figure 2.6: Gamma-ray interaction cross-sections of $NaI(Tl)$ scintillator. $NaI(Tl)$ is a very common scintillator used in gamma camera. Image taken from [18].

The fraction of γ-rays of a beam with initial intensity[1] I_0 that remains after the beam has

[1]Beam intensity is the number of photons per unit area per unit time.

crossed a distance x inside a material with linear absorption coefficient μ is

$$I/I_0 = e^{-\mu x} \tag{2.3}$$

where,

$$\mu = \frac{N_a \rho}{A} \sum_i \sigma_i w_i \tag{2.4}$$

where N_a is the Avogadro number, A is the molecular mass, ρ is the material density and w_i and σ_i are the weight fraction and atomic cross section (or mass attenuation/interaction coefficient) of the ith material constituent element, respectively.

For each material element, the cross section σ is the sum of the cross sections due to the four interaction processes of γ-rays with matter: photoelectric effect (Φ_{photo}), Compton scattering (σ_c), pair production (τ_{pair}) and coherent scattering (σ_r). Thus [1],

$$\sigma = \Phi_{photo} + \sigma_c + \tau_{pair} + \sigma_r \tag{2.5}$$

The number of γ-rays ΔI that interact with the detector per unit area, per unit time is given by:

$$\Delta I = I_0(1 - e^{-\mu \delta x}) \tag{2.6}$$

In which δx is the dimension of the detector in direction of incidence of the beam.

Energy spectrum **Fig.2.7** presents an example of a typical distribution of the number of collected photons per scintillation event in a LYSO scintillation crystal by 622 keV γ-ray for a 30 mm diameter $\times$ 15 mm long crystal [20]. The number of collected photons is proportional to the energy deposited in the crystal.

The peak on the right side of the spectrum is called the total absorption peak (photopeak) and corresponds to the full energy deposition by a γ-ray in the scintillator. In an ideal detector it is a Dirac delta function, however in a real spectrum the photopeak has a width due to statistical fluctuations in the number of total detected photons. Compton interactions also contribute to this peak when all the energy of the scattered γ-ray is dissipated within the crystal [21].

The Compton plateau in the energy spectrum is the result of the energy absorption due to Compton scattered γ-rays, in a continuum of energies ("Compton continuum"). Observing

[1] The notation used for the cross section equation is similar to that used in [19].

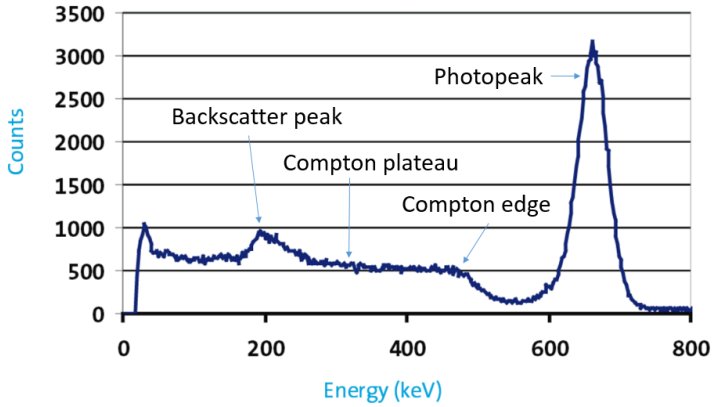

Figure 2.7: Typical spectrum of the number of collected photons per scintillation event in a LYSO scintillation crystal by 622 keV γ-ray. The number of collected photons is proportional to the energy deposited in the crystal. Three main peaks can be distinguished in the spectrum: photopeak, Compton edge and backscatter peak. The peak on the left results from the low amplitude noise from the system electronics. Picture adapted from [20].

the principle of energy and momentum conservation, we have the energy T absorbed by the material given by:

$$T = E_\gamma \frac{\gamma(1 - cos\theta)}{1 + \gamma(1 - cos\theta)} \tag{2.7}$$

where

$$\gamma = E_\gamma / m_e c^2 \tag{2.8}$$

and θ is the angle of the scattered ray (see **Fig.2.3**).

The end of the Compton plateau is called Compton edge, which corresponds to the scattered angle $\theta = \pi$, which happens in a frontal collision, the most energetic (T_{max}) interaction due to Compton effect:

$$T_{max} = E_\gamma \frac{2\gamma}{1 + 2\gamma} \tag{2.9}$$

The energy spectrum (**Fig.2.7**) also presents the backscatter peak, produced by the γ-rays that are absorbed by the crystal after being backscattered by Compton effect in the materials surrounding the detector.

2.1.2 Gamma rays detectors

For nuclear imaging, the two most widely used types of γ-ray detectors are the scintillator- and the semiconductor-based detectors. In both cases, a primary ionization electron travels through material inducing other interactions, explained afterwards. Gamma-rays can be also detected with gaseous detectors, as the resistive plate chambers (RPC) [22, 23].

In the scintillation based detector, the electron ejected from an atom due to interaction with a high energy γ-ray excites (and ionizes) the surrounding atoms (molecules). Subsequent de-excitation results in emission of optical photons which can be detected by photosensors.

In semiconductor based detectors the charge carriers (electrons and holes) are generated by the energy deposited by γ-rays. When γ-rays interact within the depletion region, they produce photo- and Compton electrons that in turn produce charge carriers that are drifted to their respective collecting electrode by the electric field. The charge is integrated by a charge sensitive preamplifier and converted to a voltage pulse with an amplitude proportional to the deposited energy.

2.1.3 Geometrical optics

This section is dedicated to the geometrical optics physical principles underneath the operation of a gamma camera. The transport of optical photons inside the scintillation camera can be described by Snell, Fresnel and Lambert's laws. The phenomena described by these laws determine the transmission and reflection probabilities and the direction of the photons. A brief review of the laws referred above and the underling physical phenomena are addressed.

Reflection and refraction

If a plane monochromatic wave reaches a boundary that separates two different media, in the general case there will be a transmitted and a reflected wave, with intensities depending on the refractive indices of the media at the wavelength of the incoming wave and on the angle of incidence (angle between the normal to the surface and the direction of the incident light - angle θ in **Fig.2.8**).

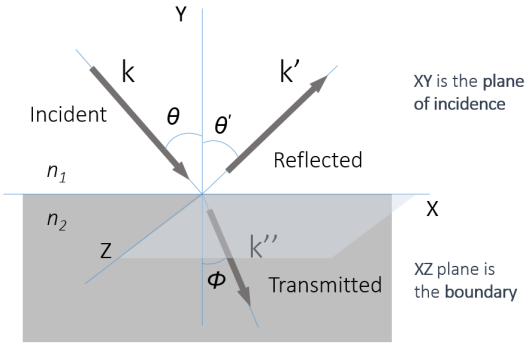

Figure 2.8: Wave vectors of incident, reflected and transmitted components on the boundary of two media with refractive indices n_1 and n_2. The XZ plane is the boundary and XY is the plane of incidence. The wave vectors k, k' and k" are aligned with the plane of incidence.

The law of reflection states that the incident wave, the reflected wave and the normal to the reflective surface all lie in the same plane and that the angle of reflection θ' is equal to the

angle of incidence θ. Refraction is the name given to the change of direction of a wave when it passes from one medium to another (see **Fig.2.8**). For the wave vectors κ , κ' and κ'' and the angles θ and ϕ defined in **Fig.2.8**), the Snell's law of refraction can be written as:

$$k \sin\theta = k'' \sin\varphi \rightarrow \frac{\sin\theta}{\sin\varphi} = \frac{k''}{k} = \frac{n_2}{n_1} \rightarrow n_1 \sin\theta = n_2 \sin\varphi \tag{2.10}$$

where n_1 and n_2 are the indices of refraction of the two media, as represented in **Fig.2.8**.

Critical angle

Snell's law shows that an incident wave (with incident angle θ) that crosses a boundary between a medium with higher refractive index to another with lower refractive index will change its direction by some angle ϕ inside the second medium ($\phi > \theta$). To occur refraction, the refracted angle ϕ should be less than $\frac{\pi}{2}$. When $\phi > \frac{\pi}{2}$ the incident light will be totally reflected, without any refracted component. The incident angle θ for which $\phi = \frac{\pi}{2}$ is called the critical angle θ_c and it is given by:

$$\theta_c = sin^{-1}\left(\frac{n_2}{n_1}\right) \tag{2.11}$$

Fresnel equations

The Fresnel equations define the ratio of the light intensity for the reflected and refracted components on an interface of two transparent media. From electrostatics it is known that the tangential components of the electric field $\vec{E}$ and magnetic field $\vec{H}$ should remain continuous across the boundary. The electromagnetic wave is transverse to the propagation direction, thus the incident field in the interface can be split in two distinct polarizations: the P-polarization, with $\vec{E}$ belonging to the plane of incidence (**Fig. 2.9a**) and S-polarization, orthogonal to that plane (**Fig. 2.9b**).

(a) **(b)**

Figure 2.9: Wave vectors (incident, transmitted and reflected) in the interface between two media for two polarizations. **a**: P-polarization, in which the electric field is parallel to the plane of the incident wave vector; **b**: S-polarization, in which the electric field is perpendicular to the plane of the incidence wave vector. The images were taken from [24].

It can be shown [24] that the Fresnel equations for P-polarization and S-polarization are the following, for non-magnetic media with positive index of refraction [25]. The **reflection coefficient** r for the field amplitude of P-polarized r_p and S-polarized waves r_s is given by:

$$r_P = \frac{n_1 \cos\theta_t - n_2 \cos\theta_i}{n_1 \cos\theta_t + n_2 \cos\theta_i} \tag{2.12}$$

$$r_S = \frac{n_1 \cos\theta_i - n_2 \cos\theta_t}{n_1 \cos\theta_i + n_2 \cos\theta_t} \tag{2.13}$$

The **transmission coefficients** t can be obtained from the reflection coefficients:

$$t_P = 1 - r_P \tag{2.14}$$

$$t_S = 1 - r_S \tag{2.15}$$

For light intensity, the reflection coefficient can be calculated as

$$R_P = |r_P|^2 \tag{2.16}$$

$$R_S = |r_S|^2 \tag{2.17}$$

Thus, for non-polarized light, the reflection coefficient R and the transmission coefficient T are given by:

$$R = \frac{1}{2}(R_P + R_S) \tag{2.18}$$

$$T = 1 - R \tag{2.19}$$

As an example, the intensity reflection coefficient is plotted in **Fig.2.10** for the two polarization components as a function of the incident angle for the vacuum (n = 1) - glass (n = 1.5) interface.

Using Snell's law, it can be shown that the reflection coefficient for the field amplitude of the P-polarized wave can be expressed in this form:

$$r_P = \frac{\tan(\theta_i - \theta_t)}{\tan(\theta_i + \theta_t)} \tag{2.20}$$

In **Eq. 2.20** the reflection coefficient r_P become zero when $\theta_i + \theta_t = \frac{\pi}{2}$.

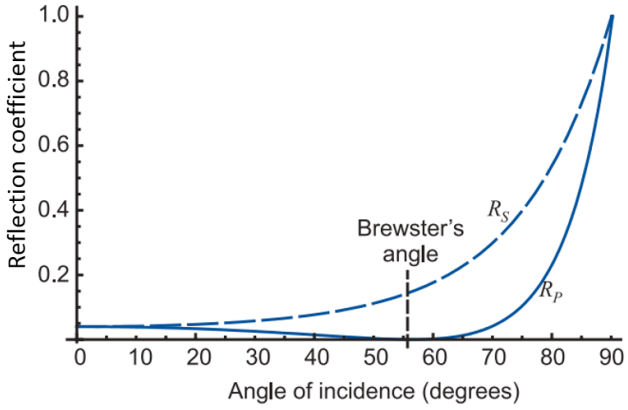

Figure 2.10: Reflection coefficient for P-polarized (R_p) and S-polarized (R_s) light components at the interface between vaccum and glass (refractive index of 1.5). The Brewster's angle is highlighted. The picture was taken from [24] .

Thus, all the P-polarized wave component of the incident light is transmitted. The angle of incidence for which the transmissivity in the interface is total is called **Brewster's angle**, θ_B and it is easily derived from Snell's law:

$$n_1 \sin\theta_B = n_2 \sin\theta_t = n_2 \sin\left(\frac{\pi}{2} - \theta_B\right) = n_2 \cos\theta_B \tag{2.21}$$

$$\tan\theta_B = \frac{n_2}{n_1} \rightarrow \theta_B = \arctan(n_2/n_1) \tag{2.22}$$

Eq. 2.22 is known as **Brewster's law**.

2.1.4 Light reflection from rough surfaces

Frequently, one must simulate how light reflects on rough surfaces. Lambertian scattering is a very good first approximation for light scattering due to, for example, multiple reflections and trapping inside surface cavities.

Lambert's law states that the luminous intensity E_θ of the light reflected by an ideal diffuse surface is proportional to the cosine of the angle between the normal to the surface and the direction of observation (the angle of observation θ, as defined in **Fig.2.11**):

$$E_\theta = E\cos\theta \tag{2.23}$$

where E is photons flux.

The apparent brightness (photons flux) of a surface is the same for all possible observation angles.

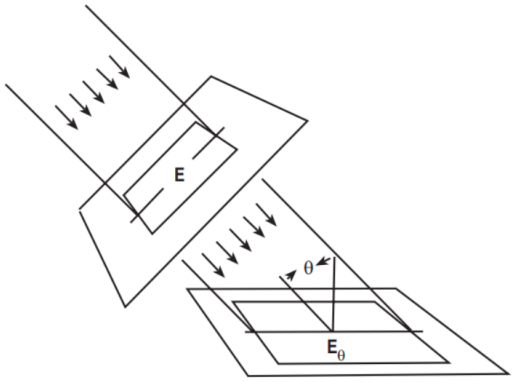

Figure 2.11: Relationship between the luminous intensity and observation angle in Lambertian scattering. Figure taken form [26], which is an adaption from [27].

Both the amount of reflected energy in a particular direction and the area seen by a sensor (apparent area) vary following the cosine law, hence photon flux remains the same for all viewing angles. When θ increases, the luminous intensity decreases (**Eq.2.23**), and the apparent area decreases as well, so the proportionality between them remains the same.

2.2 Gamma cameras components

Gamma camera consists of a collimator, a scintillator crystal, a lightguide, an array of photosensors, readout electronics and a processing unit. **Fig.2.12** depicts schematically the functional diagram of a gamma camera.

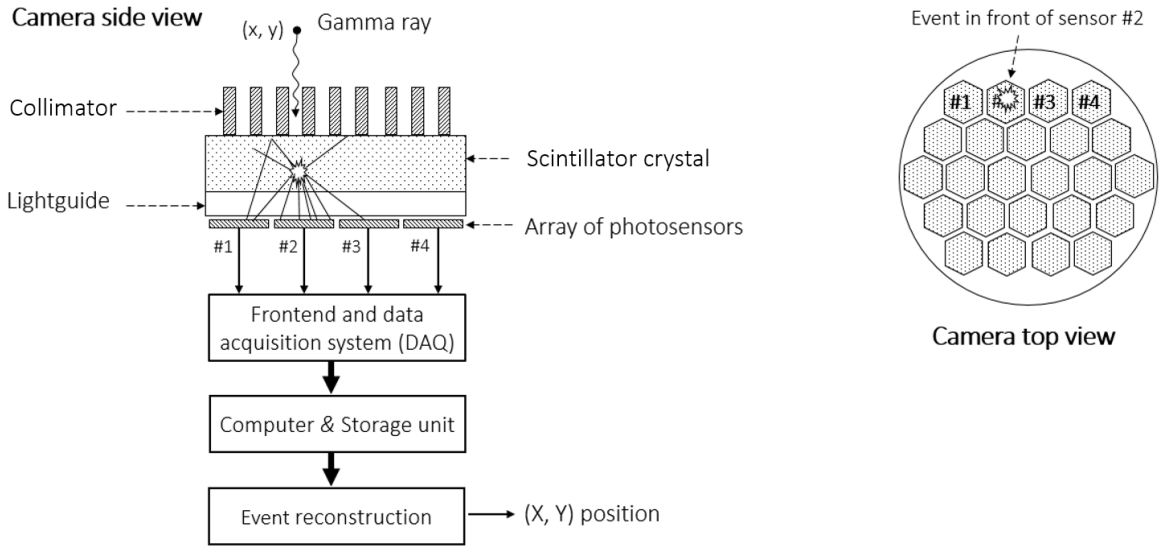

Figure 2.12: Functional diagram of a gamma camera. One scintillation event occurs inside the crystal (represented by a star). The signal in the photosensors are read by the DAQ and used to reconstruct the (X, Y) event position.

Gamma rays pass through a collimator that projects the distribution of the gamma activity onto a scintillator crystal. In a scintillation event a γ-ray interacts with the scintillator and light is emitted isotropically. The number of emitted photons is roughly proportional to the energy deposited in the crystal. The optical photons are detected by an array of photosensors connected to an acquisition system. The geometry of the photosensor array (and the type and number of sensors) depends on the purpose of the gamma camera. The sensor outputs are processed by the front-end electronics (FEE), which amplifies and shapes the signals, and then fed to the data acquisition system (DAQ) which digitizes the analog signals. The digitized signals are used by the reconstruction algorithms to find the position of each scintillation event. The following sections present in more detail the gamma camera components listed above.

2.2.1 Collimator

To obtain the projection of the source onto the scintillation crystal, a collimator is placed between the crystal and the imaged object. The materials used to make collimator are chosen among materials with high atomic number and density, such as lead or tungsten.

Collimators can be classified by the type of focusing. There are four classes of collimator depending on the focusing type: pinhole, parallel-hole, converging and diverging (**Fig.2.13**). When the size of the detector is bigger than the organ to image, converging collimators can be used to magnify the image and, on the contrary, diverging collimators are applied to fit inside the field of view of the camera big organs, like the lung. However, the most used collimator types in medical imaging are the parallel-hole and pinhole collimators. Parallel-hole collimator offers a one-to-one projected image. It consists of a plate of a γ-ray absorbing material with a honeycomb structure of closely packed, parallel holes of the same size. The hole shape can be square, circular or triangular, but the most common is the hexagonal shape. The pinhole collimator consists of a small aperture in a plate of a γ-rays blocking material. The object to be imaged is projected through the aperture onto the crystal plane. This pinhole collimator allows to increase or decrease the size of the source object in the detector plane (magnification and de-magnification, respectively) depending on both the source-to-aperture distance and the distance from aperture to the image plane. Note that distortions are present in images obtained with collimators that magnify or de-magnify [6].

The geometry of the holes have a crucial influence in both sensitivity and spatial resolution of the parallel-hole collimator. In the pinhole collimator, this role is played by both the acceptance angle and the diameter of the pinhole. The penetration of γ-rays through the collimator material must be considered in the design. The equations commonly used for the design of both collimators are now presented.

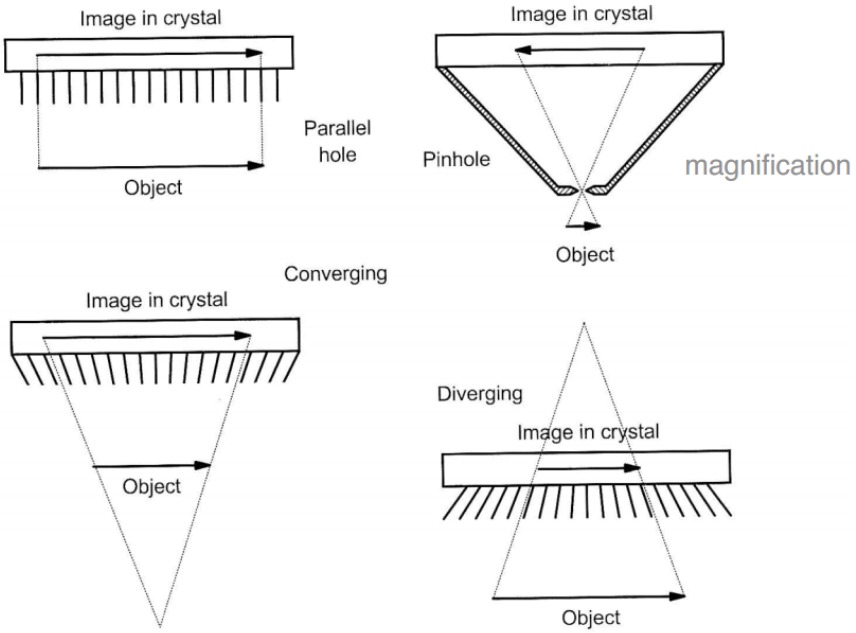

Figure 2.13: Four main types of collimators used in medical imaging. Image taken from [28].

2.2.1.1 Parallel-hole collimator

A parallel-hole collimator can be designed as follows, considering the dimension from **Fig.2.14**. The minimum septa (space between holes) thickness t for $< 5\%$ septal penetration on a collimator made of a material with absorption coefficient μ should be [29]:

$$t \geq \frac{\frac{6d}{\mu}}{a - \left(\frac{3}{\mu}\right)} \tag{2.24}$$

where d is the distance between two consecutive septas and a is the height of the septa.

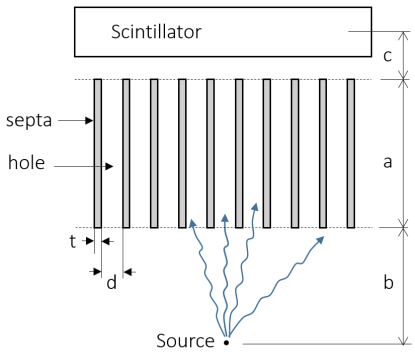

Figure 2.14: Section view of parallel-hole collimator showing γ-ray pathway and irradiated areas of scintillator. Image taken from [30]

Spatial resolution Sorenson describes the collimator spatial resolution as the "sharpness or detail of the γ-ray image projected onto the detector" [29]. The collimator spatial resolution is usually described by the FWHM of the line spread function of the projected radiation profile. The further the distance to the source, the larger is the line spread function and, so, the lower is the spatial resolution (see **Fig.2.15**).

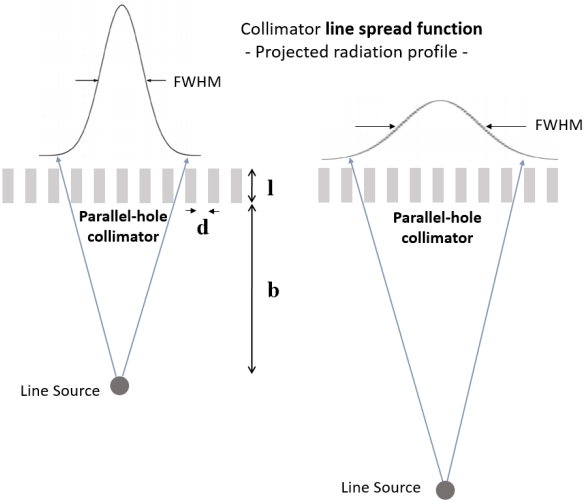

Figure 2.15: Collimator resolution illustrated for a parallel hole collimator. FWHM of the radiation profile projected onto the detector (line spread function, LSF) is the numeric value that expresses the collimator resolution. The FWHM of the LSF increases linearly with the distance from the source to the collimator.

Collimator resolution (also named extrinsic resolution) is mainly influenced by the design of the collimator and its material. The dimensions and orientation of the collimator holes play a crucial role. For parallel-hole collimator the extrinsic resolution (R_{coll}) is given by:

$$R_{coll} = \frac{d(a+b+c)}{a_e} \tag{2.25}$$

where d is the hole diameter, b the distance between the point or line source to the collimator, c the distance between the collimator and the center of the scintillator, a the collimator length and a_e the effective length (**Eq.2.26**), which accounts for the septal penetration at the edges of the collimator holes [31]. Penetration can happen when the rays pass from one hole to the neighbor one through the septa.

$$a_e = a - \frac{2}{\mu} \tag{2.26}$$

Extrinsic resolution can be improved by decreasing the hole diameter or increasing the "channel" height a. The thickness of the collimator septa also influences the collimator resolution.

Commercial collimators are designed for specific γ-ray energies. For instance, in low-energy collimators (for use with radionuclides emitting γ-rays with energies up to 150 keV) the septa is a few tenths of mm thick, while medium-energy collimators (up to 400 keV) have a few millimeter septal thickness.

Usually, a collimator with many holes of small diameter is called a high-resolution collimator. A collimator with fewer holes of larger diameter, or with short holes of small diameter, is called high-sensitivity collimator, because it allows more γ-rays to reach the crystal [32]. The spatial resolution for the high-sensitivity collimator decreases rapidly with the increase of source-to-collimator distance (**Eq.2.25**) [6].

In clinical cameras with field-of-view of about 500 $\times$ 500 mm^2, typical values of resolution (FWHM for a source-to-collimator distance of 10 cm) are about 8 mm for low-energy high-resolution and general purpose parallel-hole collimators and about 13 mm for high-sensitivity collimators [6]. A detailed description of analytical calculation and experimental measurement of the resolution of a gamma camera can be found in [33].

Sensitivity Collimator sensitivity (efficiency) g is the fraction of γ-rays passing through the collimator per γ-rays emitted by the source [29]. For holes of hexagonal shape,

$$g_{hex} = \frac{\sqrt{3}}{8\pi {a_e}^2} \frac{d^4}{(d+t)^2} \tag{2.27}$$

where a_e is the effective length (**Eq.2.26**), d is the hole characteristic dimension[1] and t is the septa thickness.

The square root of the factor $\sqrt{3}/8\pi = 0.2625$ is the K factor in many sensitivity equations found in the literature, for example the following from H. Anger's paper from 1964 [30]:

$$g = \left[\frac{Kd^2}{a(d+t)}\right]^2 \tag{2.28}$$

That constant K depends on the shape of the holes (hexagonal, round, square or triangular). The preferred hole shapes are round and hexagonal, because they maximize the area of the collimator surface without γ-rays blocking material [29].

In parallel-hole collimators, a gain in sensitivity is accompanied by a loss of resolution and *vice-versa* [32]. Common trade-off curves will be presented further on in the **section 3.4.1**. General purpose collimators are designed with intermediate values of resolution and sensitivity.

[1] In this document, whenever hexagonal "hole characteristic dimension", "hole dimension" or "hole size" is written, it refers to the distance between opposite faces of the hexagonal hole. Sometimes in the literature it is called simply "hole diameter", although it is not an accurate term.

Geometric efficiency g is unitless and, in order to be more clinically relevant, it is often converted to sensitivity with units of counts per minute per micro Curie ($cpm/\mu Ci$) using the equation:

$$S = 2.2 \times 10^6 \eta g \tag{2.29}$$

where η is the number of γ-rays emitted per nuclear decay (for ^{99m}Tc, $\eta = 1$).

It should be noted that the efficiency g does not depend significantly on the distance source-to-collimator in air (uniform "depth response"). This is true for sources located in a cone-shaped region within a source-to-collimator distance range (≈2 cm to ≈150 cm for large FOV cameras), providing that the source is not too close to the collimator to strongly reduce the detected counts due to the γ-rays blocking in the septa and that it is close enough to be completed image within the boundaries of the crystal [30, 34, 35]. Gunter explains this uniform depth response in more detail [35]. For the propagation of γ-rays from the source to collimator through tissues or organs, the sensitivity is modified for different depths due to attenuation and absorption.

Weinmann *et al.* define a minimum distance between source and collimator b_{min} for validity of both efficiency and resolution equations [36]:

$$b_{min} = \frac{a}{2} + \frac{at}{d} \tag{2.30}$$

2.2.1.2 Pinhole collimator

Fig.2.16 a shows a scheme of the pinhole collimator geometry, where α is the acceptance angle, d is the pinhole diameter, f is the focal length, z is the distance from the source to the aperture and θ is the angle of incidence of the γ-ray measured from the plane of the pinhole aperture. Magnification can be achieved with the pinhole collimator. The magnification factor $M(z)$ is given by the ratio between the focal length and the source distance, $M(z) = \frac{f}{z}$.

Spatial resolution The equation for the spatial resolution of the pinhole collimator accounts for the magnification factor and is given by:

$$R_{pinh}(z,\theta) = \sqrt{\frac{{R_i}^2}{M(z)^2} + \left(d_{Reff}(z,\theta)\left(1 + \frac{1}{M(z)}\right)\right)^2} \tag{2.31}$$

R_i is the detector intrinsic resolution. The effective diameter d_{Reff} is larger than the diameter d of the physical aperture, because some γ-rays can penetrate the cone edges. Near the edges of the cones, the thickness along the direction parallel to the pinhole axis is gradually decreased until the knife-edge (**Fig.2.16 b**), being the decreasing rate given by the acceptance

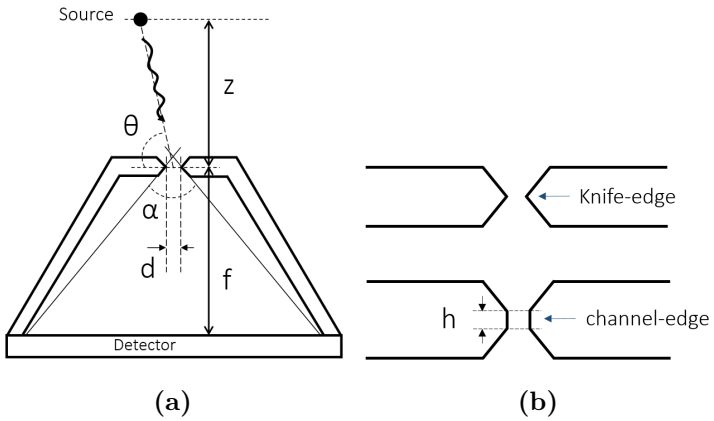

Figure 2.16: Drawing of the pinhole collimator. **a**: Geometry and dimensions: α is the acceptance angle, d is the pinhole diameter, f is the focal lenght, z is the distance from the source to the aperture and θ is the angle of incidence of the γ-ray measured from the plane of the pinhole aperture. **b**: Two alternative apertures: knife-edge (top) and channel-edge (bottom).

angle. The larger the acceptance angle α, the thinner are the pinhole edges and, consequently, the more is the number of γ-rays that pass through the material (with attenuation coefficient μ), enlarging the effective pinhole diameter:

$$d_{Reff}(z,\theta) = d + \frac{ln2}{2} tan\frac{\alpha}{2} \tag{2.32}$$

Sensitivity Considering the pinhole dimensions from **Fig.2.16 a**, a simplified approach can be used to calculate the efficiency, that does not account for the penetration near the pinhole aperture. The source is assumed to emit isotropically. If z is the distance from the source to the aperture, the sensitivity is given by the ratio between the aperture area a and the area of the surface of a sphere with radius z, A_s. Thus,

$$g_{geometrical} = \frac{a}{A_s} = \frac{\pi d^2/4}{4\pi z^2} = \left(\frac{d}{4z}\right)^2 \tag{2.33}$$

where r is the radius of the hole and d is the hole diameter.

A more comprehensive equation is presented by Audenhaege in his review article on collimators [37], referring to [38] and [39]:

$$g_{pinh}(z,\theta) = \frac{d_{Seff}^2 sin^3\theta}{16z^2} \tag{2.34}$$

where

$$d_{Seff} = \sqrt{d(d + \frac{2}{\mu} tan\frac{\alpha}{2}) + \frac{2}{\mu^2} tan\frac{\alpha}{2}} \tag{2.35}$$

And z is the distance from the source, the angle θ is the angle of incidence and μ is the attenuation coefficient (cm^{-1}). Note that the effective diameter might be almost twice the physical dimension [38]. It should be highlighted that different "effective diameters" are applied in the resolution (d_{Reff}) and sensitivity (d_{Seff}) equations [37]. On the other hand, for $\theta = \frac{\pi}{2}$ in **Eq.2.34**, g is equal to the last expression on **Eq. 2.33**, which often appears in the literature [37].

Pinhole collimators are often used in small-animal imaging due its magnification capability, that allows to achieve spatial resolutions below 1 mm. The sensitivity of the pinhole collimator can be improved, if the detector is large enough, by combining multiple pinholes (MP) into a multi-pinhole collimator [40, 41, 42, 43]. For instance, Jaekeon Bae et al. [44] presented recently (2017) a study of a high-throughput eight-hole collimator (2 mm diameter each hole) for a region of interest of 90 mm diameter. For SPECT[1] (coverage of 180°), the scanning time can be reduced from 30-45 minutes using a parallel holes (PH) collimator (5 mCi of I-123) to 20 min with a MP. Note that using a single pinhole, the scanning time would be higher than for a parallel-hole collimator. There are also other types of collimators, such as cone and fan beam (convergent) collimators, coded aperture collimators, multi-slit, slit-slat, rotating-slat and hybrid collimators. A brief review on this collimator types can be found in [37].

2.2.1.3 Collimator materials and manufacturing techniques

Materials and γ-rays penetration The shielding material against gamma radiation has been lead for decades, despite its toxicity. It is also the material of choice for collimators, which have the role of absorbing the ionizing radiation that is emitted towards the detector from outside of the acceptance angle. As lead is a very dense material (11.4 g/cm^3) and has a high atomic number (Z = 82) it has an adequate attentuation capability for thicknesses of material in the order of mm, when irradiated with low energies. For instance, for the energy of 140 keV used for SLN and thyroid imaging, the attenuation coefficient is 27.25 cm^{-1}, which means that 2 mm of lead are sufficient to absorb 97.8% of 140 keV γ-rays.

However, other materials, as tungsten (19.3 g/cm^3) and tungsten carbide alloys (doped with niquel, cobalt, copper and/or iron) are being increasingly used as alternatives to lead, considering, for instance, RoHS (Restriction of Hazardous Substances) directive of the European Union, that aim at reducing the usage of lead, due its toxicity.

Gold, uranium and platinum are also highly adequate due to their high attenuation coefficient. The price, and (radio)toxicity in the case of uranium, is the main limitation for the widespread use of these materials. However, they can be sparingly applied, for instance, in the edge of a pinhole, to reduce the penetration of γ-rays in that thinner region.

[1] SPECT stands for Single-photon emission computed tomography.

Manufacturing techniques The manufacturing method depend on the material and dimensions of the collimator. The most used techniques for collimator manufacturing are listed below. More details on the manufacturing processes can be found in [37]:

1. Stamping and stacking lead foils (paralle-hole, converging and diverging collimators)
2. Material casting in a mold (e.g lead for parallel-hole collimator).
3. Milling and drilling (e.g. tunsgten alloys)
4. Electric discharge machining (EDM) (e.g. pinhole collimator made of tunsgten alloys)
5. Cold casting (tungsten powder mixed with epoxy resin, which results in a composite with a density $\approx 9\ g/cm^3$, much less then the pure tungsten density).
6. Additive manufacturing (3D printing): selective laser melting (SLM) of tungsten powder.

2.2.2 Scintillator

Currently, there are five types of scintillator materials being used in gamma cameras: inorganic crystals, organic crystals, organic liquids, plastics and glasses [19]. Inorganic crystals are widely used as scintillators for medical imaging, as they provide strong attenuation (due to the higher density and higher atomic number) and high light yield, which results in better energy resolution [19]. Inorganic crystals are usually grown in high temperature furnaces often with a small amount of activator admixture. The most widely used is sodium iodide doped with thallium NaI(Tl), first applied in radiation detection in 1948 by Robert Hofstadter.

Table 2.1 lists several inorganic materials often used as scintillator crystals, presenting their main characteristics: density, emission wavelength, refractive index, decay time, light yield and intrinsic energy resolution. The density of the material combined with its mass attenuation coefficient defines the material thickness required to achieve a high detection efficiency (typically $> 80\%$) at a certain energy (see **Fig.2.30** from **section 2.4.1**). From the wavelength of the emitted light one have to choose the most suitable photosensors. NaI(Tl), for instance, has a maximum emission wavelength of 415 nm, which is typically within the range of maximum efficiency of bialkaly photomultipliers (PMT). This is one of the reasons for the usage of NaI(Tl) from the beginning of gamma cameras.

The transmission through the interface between the scintillator and the lightguide depends on the refractive indices of the two materials. The scintillator refractive index n should be considered when selecting the materials for the lightguide and the optical grease. It should be as close as possible to $n = 1.5$ to better couple with typical low n lightguide and low n photosensor entrance window ($n \approx 1.5$). The longer the decay time τ is, the lower is the

Material	**Density** (g/cm^3)	λ_{max}	**Refractive Index,** n	τ ns	**Light yield** (Photons/MeV)	**Energy resolution** at 622 keV (%)
$NaI(Tl)$	3.67	415	1.85	250	38000	6.6
$CsI(Tl)$	4.51	550	1.79	1000	54000	5.2
$Bi_4Ge_3O_{12}$	7.13	480	2.15	300	8200	12
BaF_2	4.89	220, 310	1.54	0.6, 630	1500, 9500	11 (511 keV)
CeF_3	6.16	340	1.62	30	4400	20 (511 keV)
$LaBr_3(Ce)$	5.08	350	1.9	27	49000	3
$CdWO_4$	7.9	475	2.2 – 2.3	14000	13000	8.3
$LYSO$	7.4	420	1.81	$40/36^a$	$28000/32000^b$	8
$GAGG$	6.63	520	1.93	88	50000	5.2

Table 2.1: Scintillator crystals - Example of some inorganic materials widely used as scintillator crystals. λ_{max} is the wavelength of maximum probability in emission spectrum and τ is the scintillator decay time. The materials properties were taken from three manufactures: Saint Gobain, Advatech and Epic Crystals.

[a]Saint Gobain crystals company, around 2016, have produced a new LYSO with shorter decay time (36 ns) than the previous generation of that crystal (40 ns).

[b]Saint Gobain crystals company, around 2016, have enhanced its LYSO light yield from 28 ph/keV to 32 ph/keV [45].

maximum acquisition rate obtainable with the detector (not to have pile-up) and the longer is the time window required to acquire all photons that form one event. As a consequence, the amount of noise which is collected is higher, and the signal-to-noise ratio is worse. The light yield is a scintillator parameter that gives the average number of emitted photons per unit energy deposited in the scintillator. The higher it is, the more the light collected by the readout and so the better the signal-to-noise ratio, which will result in a better energy and spatial resolution. A comparison is given below on three alternative scintillators, starting by two crystals frequently used in the nuclear imaging area: the NaI(Tl) and the Ce doped Lu_2SiO_5 (LYSO).

NaI(Tl) has higher light yield (38 ph/keV against 28 ph/keV) and better intrinsic energy resolution (6.6% against 8% at 611 keV) than LYSO. Both crystals have a similar maximum emission wavelength (415 nm for NaI(Tl) and 420 nm for LYSO). However, NaI(Tl) has a relatively slow decay time (230 ns) compared with that of LYSO (40 ns). It has also a longer attenuation length[2] than LYSO at 140 keV, so it should be more than twice thicker than LYSO to achieve a comparable level of γ-ray absorption [46]. The increase of the scintillator thickness can negatively affects the spatial resolution when there is no information on the depth of iteration. Other disadvantage of NaI(Tl) is that it get damaged when exposed to moisture in the air (hygroscopic), which implies encapsulation in a hermetically sealed container, resulting

[2]The attenuation length is the reciprocal of the attenuation coefficient and it is also known as "mean free path".

in a less flexible option for design of a compact gamma camera. For instance, the lightguide thickness can not be lower than the encapsulation material thickness. However, despite the LYSO advantages over NaI(Tl), LYSO is intrinsically radioactive due to the presence of ^{176}Lu [47, 48]. A crystal that have been reported in the last decade as an alternative to LYSO is cerium-doped $Gd_3Al_2Ga_3O_{12}$ (GAGG) [49, 50, 51, 52], due its attractive light yield (≈50 ph/keV) and the absence of intrinsic radioactivity. GAGG has an intrinsic energy resolution (5.2%) even better than NaI(Tl) and a decay time of 88 ns, which is about two times slower than LYSO but significantly faster than NaI(Tl). On the negative side, GAGG has a index of refraction $n = 1.93$, which is the highest of the three crystals ($n = 1.85$ for NaI(Tl) and $n = 1.81$ for LYSO) and a maximum emission wavelength of 520 nm, which is far from the maximum detection wavelength of common photosensors. It should be noted that both LYSO and GAGG have non-linearity of the light output over the γ-ray energy, which affects the energy resolution.

Monolithic *vs* pixelated scintillators Monolithic or continuous crystals have predominantly been used in the design of scintillator-based imaging detectors, although other configurations have been also employed [8]. One of those alternative configuration is to pack an array of small crystal columns, commonly with a reflective material filling the gaps between them in order to confine as much as possible the visible photons to the individual column in which the scintillation occurs. Some crystals, as CsI(Tl), CsI(Na) or GOS (Gd_2O_2S:Pr) can be either grown as a continuous volume (monolithic crystal) or in columns that can be used as elements of a pixelated scintillator [53, 54]. The usage of pixelated crystals can offer higher spatial resolution in thick crystals, because in the columnar structure the light is guided along the columns by internal reflections to the photosensor, preventing resolution loss due to light distribution in the scintillator, as occur in monolithic crystals. On the other hand, in pixelated scintillators the cross-sectional area of the individual crystal columns defines the hard limit on spatial resolution. Other disadvantages of pixelated-crystal cameras are lower sensitivity due to the unavoidable presence of space between pixels, higher assembly cost than monolithic crystal based cameras and usually worse energy resolution due to reduced light collection by the photosensors [8, 55, 56, 57]. Monolithic scintillators allow to collect more light and distribute it more evenly by the array of photosensors, which is beneficial for statistical reconstruction.

Interestingly, optical micro-structures (optical barriers) can be created in a monolithic crystal using laser-induced optical barriers (LIOB) technique, also known as subsurface laser engraving (SSLE). A laser is focused inside the crystal and microcracks forming semitransparent walls are created [58]. It was confirmed that the optical barriers contribute to the light channeling and reflect the scintillation light back to the pixel volume, as expected for pixelated

scintillators [58, 59]. It should be noted that the crystal light output is not changed by the LIOB process and that the crystal regions affected by the laser pulses remain sensitive to the γ-ray radiation [60]. LIOB has being increasingly used [58, 59, 60]. For instance, Sabet et al. [60] have fabricated CsI:Tl crystals (3, 5, and 10 mm thick) with an optical barrier pattern with 0.625 $\times$ 0.625 mm^2 pixels, which can be effectively resolved using CoG. Konstantinou et al. [58] have engraved a honeycomb design with hexagones with an area of approximately 1.42 mm^2 in a 12.8 $\times$ 12.8 $\times$ 6 mm^3 LYSO:Ce scintillator. The laser processed scintillators are, hence, an alternative to monolithic and pixelated scintillators that can provide the high sensitivity, the low cost and the capability to calculate the depth of interaction (DOI) given by monolithic crystals as well as the high intrinsic spatial resolution of finely pixelated scintillators. The micro-structured scintillators can also mitigate the so-called edge effect, the worsening in reconstruction quality in the periphery of the detector when centroid reconstruction is used. A review on scintillators used for γ-rays imaging can be found, for instance, in [8] and [61].

2.2.3 Lightguide

The lightguide is the component of a gamma camera that couples the scintillator to the photosensors window. It is transparent to light and it is optically coupled to the scintillation crystal on one side and to the photosensors array on the other side. The purpose of the lightguide is to increase the distance between the crystal and the sensor array. This way the light is distributed over a larger number of photosensors, so that CoG performs better and higher spatial resolution can be achieved. For example, for clinical medical cameras ($\sim$500 mm crystal diameter) the lightguide usually has a thickness of about 10 mm. The materials typically used in the lightguide are glass, PMMA (Plexiglas) and quartz [62]. The optical coupling is performed by an optical grease, which helps to avoid air bubbles and decrease the loss of photons in the interfaces between the scintillator, the lightguide and the photosensor windows.

2.2.4 Photosensors

For gamma cameras the main parameters to take into account when choosing the photosensors are the following: light detection efficiency, amplification gain, dark current and dark count rate and wavelength sensitivity range. They will be discussed in this section along with a brief review of the two types of photosensors commonly used nowadays in gamma cameras: photomultiplier tubes and silicon photomultipliers. A comprehensive information on PMTs and SiPMs can be found in [63] and [64, 65, 66], respectively.

2.2.4.1 Photomultiplier tubes

Photomultiplier tube (PMT) is extremely sensitive detectors of light in the UV, visible, and near-infrared. **Fig.2.17** shows a simplified scheme of a photomultiplier tube. The incident light passes through a transparent window and interacts with the photocathode. Each photon has a probability to eject a photoelectron from the photocathode (quantum efficiency). The photoelectrons are directed by an electrostatic focusing system to an electron multiplier: a chain of dynodes where a multiplication process takes place. In **Fig.2.17** one can see the resistive voltage divider responsible to feed each dynode with the required voltage. PMTs typically operate with high voltages in the range from 750 V to 3 kV.

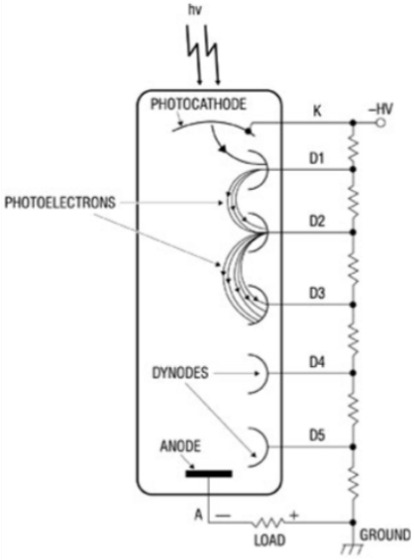

Figure 2.17: Scheme of a photomultiplier. The voltage is distributed to the dynodes through a voltage divider, built with a resistive chain. Note that the scheme only represents the amplification process until the third dynode. In reality the amplification process continuous exponentially until the electrons reaches the anode, in the end of the dynode chain.

Properties of PMTs

- Quantum efficiency

  Quantum efficiency QE is the ratio of the number of produced photoelectrons and the number of photons hitting the photocathode (see **Fig.2.17**). Quantum efficiency is strongly dependent on the wavelength of the incident light. For this reason, the photocathode selected to work in a scintillation detector should have a high quantum efficiency for the wavelengths of the light that the scintillator emits. Typical maximum values of QE are between 25% and 35%, but they can go up to 40%.

- Photon detection efficiency

  Photon detection efficiency (PDE) is the product of the quantum efficiency of the photocathode and the collection efficiency, which is the probability of the photoelectron released from the photocathode to generate the avalanche through the dynodes chain.

- Gain

  Each PMT has its specific amplification factor, the gain. For a given voltage applied to a PMT the "PMT gain" or "multiplication gain" is the signal amplification factor and it is usually in the order of 10^5 or 10^6 (the more recent can provide a gain of 10^7).

  PMTs cannot be assumed to be identical (their gains are different), even if they come from the same batch. Each sensor has its own "fingerprint", due to some physical features like:

  1. Photocathode shape differences between sensors
  2. Slightly different electric field configuration
  3. Slightly different dimensions of the dynodes (due to the manufacture process)

  Also, thermal expansion leads to changes in the field geometry, which affects the response of the dynodes. Magnetic field (including Earth magnetic field) strongly influences the collection efficiency which limits the possibility to apply PMTs in imaging detectors combining, for instance, SPECT and magnetic resonance imaging (MRI).

- Dark counts

  Even placed in complete darkness, PMT will generate some signals. This signals are due to thermal emission of electrons from the photocathode (and the dynodes). Dark counts are typically strongly dependent on the PMT temperature.

- Single photoelectron spectrum

  Single photoelectron spectrum (SPS) is the distribution of the output signals of the PMT in response to a single detected photon. **Fig.2.18** gives an example of the SPS recorded for the photomultiplier Hamamatsu R11410-10, at room temperature and a voltage of 1750 V.

  The peak close to zero in the SPS is due to electronic noise and the ejection of electrons from the dynodes (not from the photocathode). These electrons have less amplification than the ones that follow the entire dynodes chain. The contribution of the electronic noise can normally be represented as a Gaussian with a small standard deviation (**Fig.2.18**). A threshold can be used to filter out the low amplitude peak.

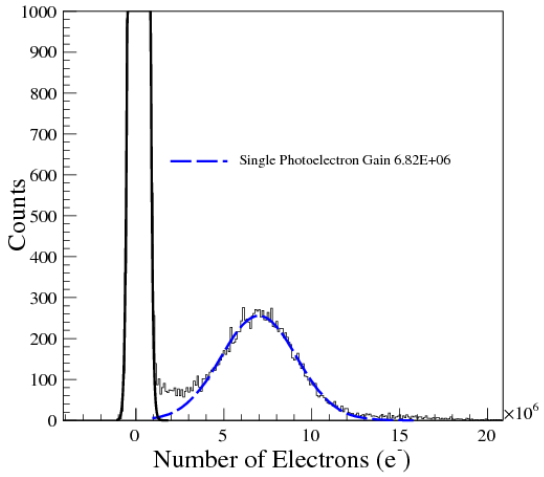

Figure 2.18: Example of a single photoelectron spectra recorded for the photomultiplier Hamamatsu R11410-10. Measurement performed in UCLA University at room temperature and a voltage of 1750V. Image taken from [67].

- Dynamic range

  Dynamic range of a sensor is the range of input signals where it works in linear mode. PMTs have good linearity in anode output current for a large range of incident light levels (have a wide dynamic range).

Position sensitive PMTs Position-sensitive PMTs (PSPMTs) is a modified version of the conventional PMT with compact size, that gives information on the photocathode position of the detected light. PSPMTs have a focusing mesh after the photocathode and then a grid of metal channel dynodes for the photoelectron amplification. The two main types of PSPMTs differ in the layout of the readout of the amplified signals. It can be either the reading of the individual anodes signals of a multianode structure (**Fig.2.19 a**) or the single reading of the photocathode position of the light incidence given by the center-of-gravity of the multianodes signals (**Fig.2.19 b**) [63].

2.2.4.2 Silicon photomultipliers (SiPM)

An alternative to PMTs are the silicon photomultipliers (SiPM), which exhibit a superior optical photon detection efficiency (up to 45%). Besides, SiPM are compact and mechanically robust, fast, operate at much lower voltage than PMTs, have gain of the same order as that of PMTs ($\approx 10^6$) and can operate in environment with strong magnetic field.

SiPMs are bi-dimensional arrays of avalanche photodiodes (APD). These APDs operate

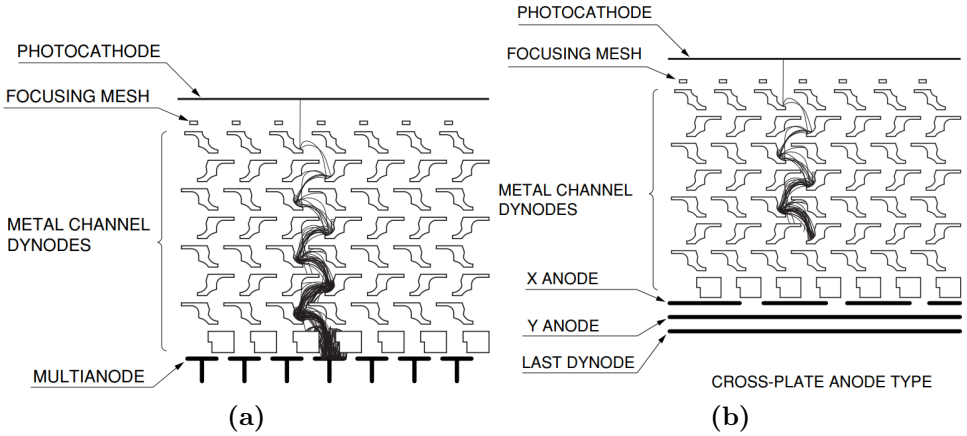

Figure 2.19: Schemes of PSPMTs types of electrodes structures. The images were copied from [63]. **a**: Multianode readout. Scheme of the electrodes structure and electrons trajectory. **b**: Center-of-gravity readout. Cross plate anode type. The avalanche amplification process in not represented until the end of the dynodes chain.

in Geiger mode, biased slightly above the breakdown voltage. In Geiger mode[1], when a sufficiently high electric field ($> 5 \times 10^5$ V/cm) is applied to the depletion region, the created charge carrier is accelerated until it carries sufficient kinetic energy to create secondary charge pairs, through a process called impact ionization. Hence, a single absorbed optical photon can trigger a ionization cascade (avalanche) that will spread throughout all the depletion region under the influence of the electric field. The depletion region, then, become conductive, effectively amplifying the original electron-hole pair into a measurable current flow [65]. In the Geiger mode the avalanche is auto fed and the current increases exponentially, being limited by a resistor (quenching resistor) placed in series with the APD. **Fig.2.20 a** shows the equivalent circuit of an APD working in Geiger mode, where C_d is the diode capacitance, R_s is the series resistance of the silicon substrate and R_q is the quenching resistor ($R_q >> R_s$). The circuit have three operation modes: quiescent, discharge and recovery mode. In quiescent mode, the diode is reverse biased slightly above the breakdown voltage (V_{brk}). The bias voltage (V_{bias}) defines the overvoltage (ΔV), which is the difference between V_{bias} and V_{brk}. The switch in **Fig.2.20 a** circuit is open and the diode remain in quiescent mode with no current flow until a photon is absorbed or a dark noise event occurs. In these two cases, the switch in the equivalent circuit closes and C_d discharges from V_{bias} to V_{brk} through R_s. The quenching resistor R_q limits the current drawn by the diode during breakdown. The reverse voltage seen by the diode is, thus, lowered to a value below its V_{brk}, stopping the avalanche. Then, C_d recharges back to V_{bias} through R_q and so, the APD returns to the quiescent mode, being available again to detect an other photon [68].

[1]The "Geiger mode" term comes from the "Geiger discharge", the name given to the APDs amplification ionization cascade, in analogy to the ionization discharge observed in a Geiger-Müller tube.

The avalanche produced in the photodiode (and the corresponding collected charge) does not depend on the number of photons that arrive at a specific microcell, because a single photon will saturate the photodiode output. This means that the response linearity of the photodiode is lost: there is no more a proportionality between the number of incoming photons and the electrical signal readout of the single photodiode. To overcome this significant limitation on linearity, many (several thousands) photodiodes - microcells - are packed together, typically in a density of 100-2000/mm^2 and connected in parallel, so the signal output of SiPM is the sum of the individual discharge currents of all triggered photodiodes. The resulting quasi-analog pulse has the desired information on the magnitude of photon flux that impinges on the SiPM. **Fig.2.20 b** shows a possible implementation scheme to obtain the summed output.

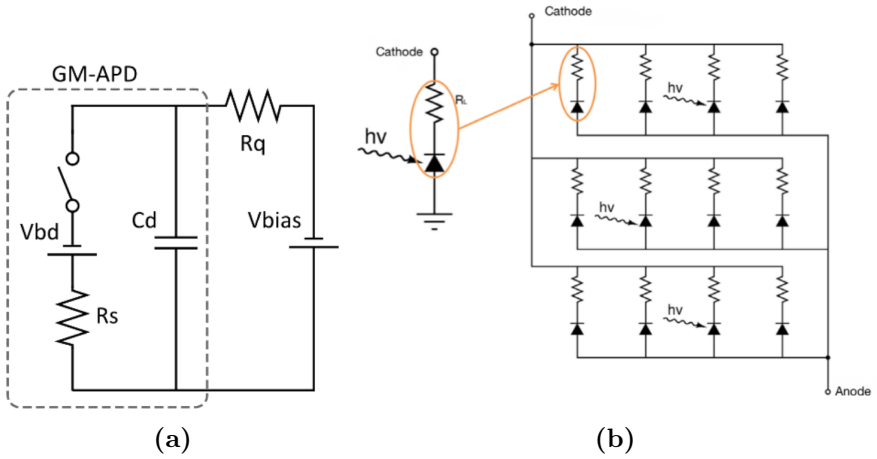

Figure 2.20: A silicon photomultiplier consists of an array of avalanche photodiodes working in Geiger mode. **a**: Equivalent circuit of an avalanche photodiode working in Geiger mode. The image was taken from [68]. **b**: Schematic of an array of microcells, each one containing a photodiode and a quench resistor. The image was taken from [65].

The amplitude seen in an oscilloscope for low level light pulses and the corresponding amplitude spectrum is illustrated below in **Fig.2.21**. Quantized output pulses corresponding to different number of detected photons can be easily distinguished.

The distance between the peaks in the spectrum is constant and corresponds to the charge from a single Geiger discharge. Thus, the average distance between the centers of two consecutive peaks can be assumed to be the SiPM gain (or signal per single photoelectron).

Properties of SiPMs

- **Photon detection efficiency**

  The photon detection efficiency (PDE) is a product of three factors: quantum efficiency of silicon $\eta(\lambda)$, avalanche initiation probability $\varepsilon(V)$ (or Geiger efficiency) and geometric

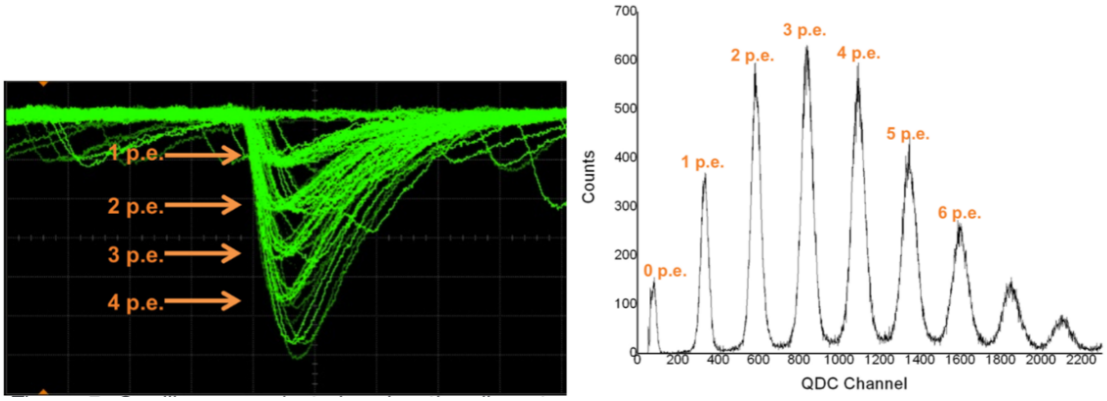

(a) (b)

Figure 2.21: The number of photoelectrons (ph.e.) can be estimated from the amplitude of the pulse. These images are taken from [65]. **a**: Oscillospope snapshot showing the temporal evolution of a signal from one SiPM. Multiple events can be seen. It is possible to identify the discrete number of photoelectrons generated in the SiPM that resulted in the waveforms plotted in the oscilloscope; **b**: Histogram of photoelectrons counts. The peaks correspond to a discrete number of photoelectrons.

efficiency (or fill factor) F:

$$PDE = \eta(\lambda) \cdot \varepsilon(V) \cdot F \tag{2.36}$$

where λ is the photon wavelength and V is the overvoltage.

The **quantum efficiency** is the product of the intrinsic and the extrinsic quantum efficiency. Intrinsic quantum efficiency is the fraction of incident photons that generate an electron-hole pair and the extrinsic quantum efficiency is the fraction of photons that reach the depletion region.

The **Geiger efficiency** (avalanche probability) is the fraction of electron-hole pairs that give rise to an avalanche. This factor increases with the overvoltage.

The **geometric efficiency** (fill factor) is the ratio of the active and full area, where inactive area is comprised of the gaps that exist between the photodiodes. These non-sensitive spaces form what is known as dead region. The larger is the number of micro-cells, the larger is the dead region fraction.

The PDE of a SiPM detector can reach 40% - 45% [69].

- **Gain**

The gain of a microcell, and hence the SiPM detector gain, is the ratio of the output charge and the electron charge. The output charge is calculated multiplying the microcell

capacitance C by the overvoltage ΔV which is the difference between the bias and the breakdown[1] voltage:

$$G = \frac{C \cdot \Delta V}{e} \tag{2.37}$$

Gain increases with bias voltage, but dark count increases as well. A typical relation between the SiPM gain and the overvoltage is plotted in **Fig.2.22**.

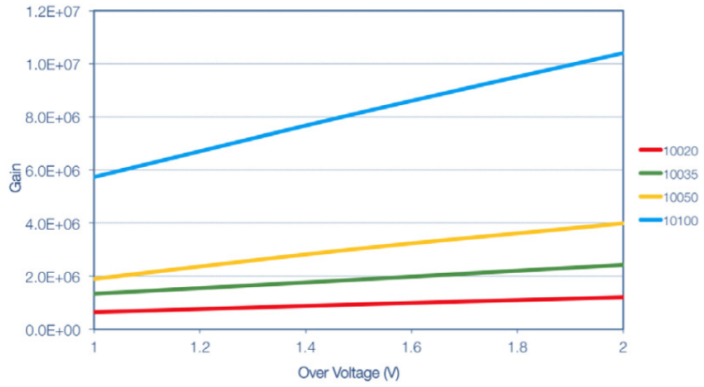

Figure 2.22: SiPM gain as a function of the overvoltage for different microcells sizes (20 μm, 35 μm, 50 μm, 100 μm), represented with different colors. The last two digits in the legend labels correspond to the microcells size in μm. This plot is available in a technical note on SiPMs from the manufacturer SensL [65].

- **Dark counts, afterpulsing and crosstalk**

  The main cause of noise in SiPMs are the dark counts, which are signals generated without any incidence of a photon on the SiPM. These signals are a consequence of the thermal generation of electron-hole pairs in the photodiode depletion region. When a pair of charge carriers is generated in that region, there is a large probability (given by the Geiger efficiency) of an avalanche to be produced. The typical dark count rate for SiPMs is in the range from 10 kHz to 1 MHz per mm^2.

  The dark current depends on the temperature, bias, microcell size and the overall area of the detector. **Fig.2.23** presents the dark current as a function of the bias voltage for different microcells sizes. Smaller microcells have less noise. Typically, reducing the temperature one can decrease the rate of dark counts.

  Another cause of noise in SiPMs is the afterpulsing: the appearance of signals after the cell discharge is already finished. These may occur when some semiconductor impurities

[1]The breakdown voltage is the voltage applied to the SiPM (bias voltage) at which the strength of the electric field generated in the depletion region is sufficient to create a Geiger discharge [65].

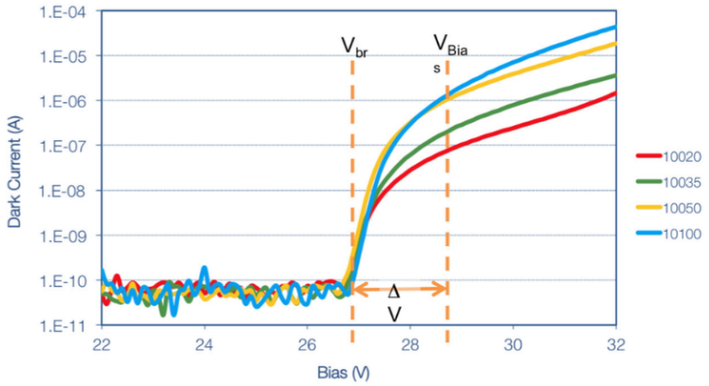

Figure 2.23: SiPM dark current as a function of the bias voltage for several microcells sizes (20 μm, 35 μm, 50 μm, 100 μm), represented by different colors. The last two digits in the legend labels correspond to the microcells size in μm. This graphic is available in a technical note on SiPMs from the manufacture SensL [65].

catch one electron from an avalanche and release it within some time, initializing a new avalanche, and thus producing a new signal.

In the avalanche process infrared photons are emitted. When these photons are absorbed by the neighbor microcells, optical crosstalk (OCT) occur. The signals generated in the neighbor microcells produce signals in the SiPM similar to that produced by photons from scintillation, resulting in the increase of the output signal fluctuations. The probability of such phenomenon increases with overvoltage. To minimize OCT an opaque material is often placed between the microcells.

SiPMs are being increasingly used in position sensitive scintillation detectors (PSSD), gradually replacing the photomultiplier tubes. One example are the modern gamma imaging detectors, especially where compactness (e.g. thyroid or prostate imaging) or magnetic field immunity (e.g. combined MRI-PET[1] devices) is required. In a typical configuration of a gamma detector, one or more arrays of SiPMs are used to read out the light produced by a γ-ray interacting with a scintillation crystal.

The main disadvantage of SiPMs is the high dark rate caused by the thermal generation of carriers. This problem can in general be mitigated choosing a short acquisition time window and a high threshold in the pulse discriminator [70].

2.3 Readout systems

In gamma cameras, the light emitted inside the scintillation crystal is converted by an array of photosensors into electric signals. The (x, y) location of the source is found from the

[1]MRI stands for magnetic resonance imaging and PET stands for positron emission tomography.

distribution of light over the array of light sensors. The sum of the signals in all sensors is typically proportional to the deposited energy of the γ-ray.

Originally, gamma cameras had an analog readout that provided the event (x, y) position and the signal sum. More recent cameras allow individual readout of each photosensor. This way, advanced techniques may be used in position reconstruction, estimating the most likely event position using statistical methods. Below, a review is given on the typical electronic circuits used both for traditional and for individual PMT readout.

2.3.1 Traditional readout

From the beginning of gamma cameras and in many cameras nowadays, the reconstructed energy and position of the events is calculated in an analog manner, with a resistive chain. Preamplifiers make the pulse shaping and after this the signals enter the summing amplifiers through a resistor matrix. There are four amplifiers, one for each direction, $-X$, $+X$, $-Y$, $+Y$. For each single scintillation event, five signals come out of the camera with the -X, +X, -Y, +Y values and the sum of the signal in all photosensors (energy-signal E), as depicted in **Fig.2.24**. The values of $-X$, $+X$, $-Y$ and $+Y$ are determined by splitting the signals from each PMT into four output lines. The fraction of the current that flows through each line ($+X$, $-X$, $+Y$ and $-Y$) is determined by the values of the circuit resistors ($R_X{}^+$, $R_X{}^-$, $R_Y{}^+$, $R_Y{}^-$), since the current is proportional to 1/R (Ohm's law). **Fig.2.25** presents a schematic of the resistive circuit, showing the resistors values for different PMTs. It can be seen as the signals on each PMT are multiplied by a factor which depends on the position of the PMT center relatively to the center of the crystal.

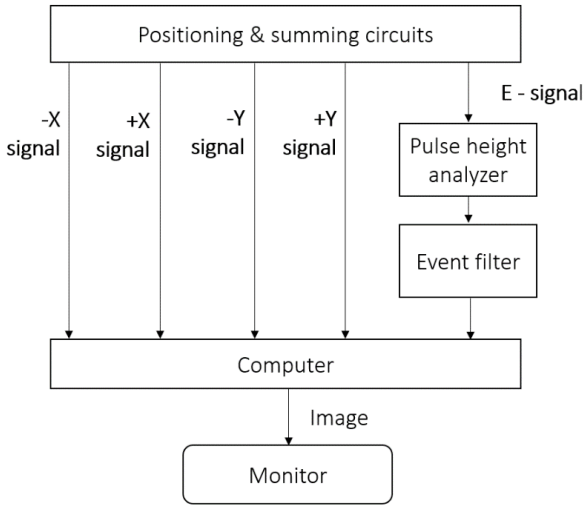

Figure 2.24: Original readout system of the gamma camera. Five signals come out of the camera: -X, +X, -Y, +Y position signals and energy signal (E-signal). These signals correspond to a single event.

The coordinates origin is assumed to be in the center of the camera. The event position is calculated as follows:

$$X = \frac{(+X) - (-X)}{E} \tag{2.38}$$

$$Y = \frac{(+Y) - (-Y)}{E} \tag{2.39}$$

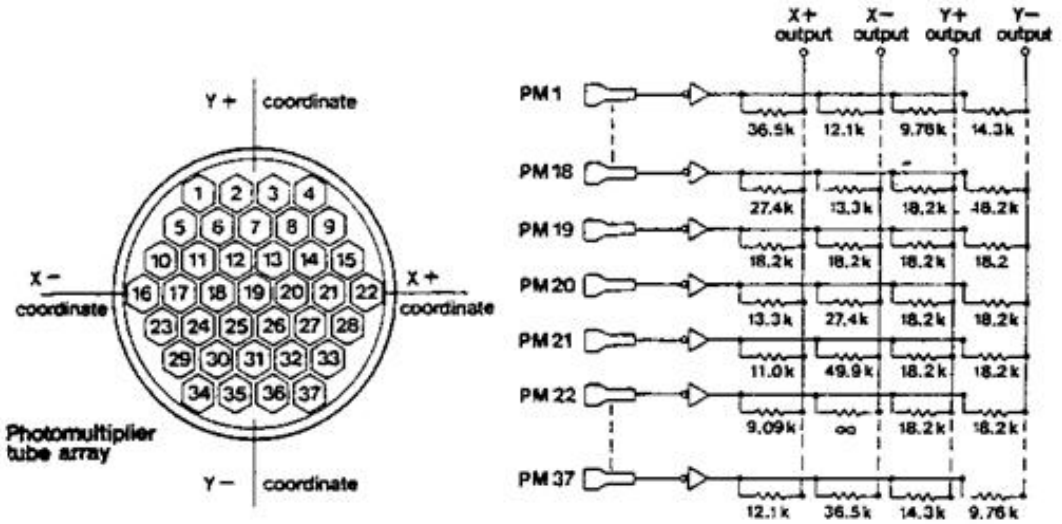

Figure 2.25: Individual PMTs signals are split into four lines using a resistive chain. The output lines are designated by X+, X-, Y+ and Y-. The energy output is not represented. The image was taken from [71].

Frame mode *vs* list mode

The X and Y signals are calculated by the analog circuitry are digitized by analog-to-digital converters (ADCs) and can be stored in two possible forms: frame mode and list mode. In the frame mode the data structure that is used to store the recorded event data is a matrix in which each element ((p_x, p_y) pixel) corresponds to a range of (x $\rightarrow$ x + dx, y $\rightarrow$ y + dy) positions in the field of view of the detector. If the new arriving X and Y signals fall within the (x $\rightarrow$ x + dx, y $\rightarrow$ y + dy) range, a new count is added to the corresponding (p_x, p_y) pixel. The size and depth of the matrix must be chosen, as well as the time of acquisition per frame (or the desired total counts) and the number of frames per study. With this mode the images are immediately available.

In list mode, X and Y signals are stored sequentially with associated timestamps. After acquisition is finished, data can be processed. For example, matrix size and acquisition time per frame can be manipulated or discrimination of some frames can be performed using some selection criteria. List mode is quite flexible, but needs large storage space and, frequently, longer processing times before the image can be displayed.

2.3.2 Individual readout mode

In the individual mode, for every channel the signal after being preamplified is sent to two circuits: **trigger circuit** and **signal circuit**. The first shapes the signal in order to make possible to identify that an event occurs. The trigger circuit has, hence, the function to initialize the digitalization of the signal that flow through the signal circuit. This signal circuit shapes the photosensor signals to allow the integration of their complete charge.

The hardware modules which deal with analog signals before the digitalization constitute what is usually called the **front-end electronics (FEE)**. The front-end module commonly consists of a preamplifier that feeds both a slow shaper (charge signal) and a fast shaper (event trigger signal), which have as the main component an amplifier. Digitalization and data transfer to a processing unit is performed by a **data acquisition system (DAQ)**.

Preamplifier The signal read out of a photosensor has to be amplified. The preamplifier amplifies weak signals from the photosensor and feeds them to the rest of the acquisition system. The preamplifier also works as an impedance adapter, matching the high impedance of the photosensor and the low impedance of coaxial cables to the amplifier.

There are four basic types of preamplifiers, classified according to the type of signals they work with: voltage sensitive, current sensitive, charge sensitive and transimpedance amplifiers (TIA), being the latter the most popular in the SiPM readout frontends.

Transimpedance amplifier

Transimpedance amplifier (TIA) is a current-to-voltage converter, frequently implemented using an operational amplifier. TIA is a good choice for photosensors that have a current response more linear than the voltage response, which is the case of photodiodes. **Fig.2.26** shows a basic transimpedance amplifier configuration.

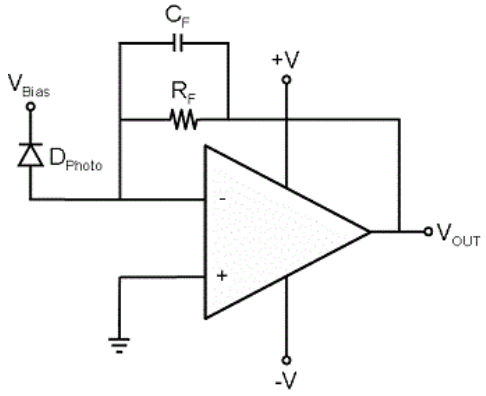

Figure 2.26: Schematic configuration of a basic transimpedance amplifier. Image taken from [72].

TIA input has low impedance and isolates the sensor from the output voltage of the operational amplifier. A feedback resistor R_f is used to convert the input current to the required output voltage range. A capacitor C_f is sometimes placed in parallel with that feedback resistor in order to stabilize the circuit. Note that because the amplifier is in an inverting configuration, the amplifier gain has the value of $-R_f$.

Amplifier and shaper The output of the preamplifier is fed to an **amplifier**. It is also part of the function of the amplifier to shape the pulse and to feed it to the analyzer. The signal-to-noise ratio of the pulse is improved before amplification with a pass-band circuit that filters out the highest frequencies, mainly from electronic noise, and the low 50/60 Hz frequency from the AC power supplier. The amplifier should be linear, showing a proportionality between its input (pulse from the photosensor) and output (shaped pulse) in the current, voltage or charge, depending on the amplifier.

Typically, there are two shaper circuits: the fast shaper and the slow shaper. The **fast shaping** prepares the signal to be used in the trigger circuit. The main requirement of the fast shaper is to have small *jitter*[1]. Due to the electronic noise there is an uncertainty (jitter) in the time at which the analog pulse crosses the discriminator threshold [73, 74]. The rising edge (usually very short in time) must be detected, so a broad bandwidth is also required.

The signal **slow shaping** aims to optimize the signal-to-noise ratio for the event amplitude reading. This means to shape the signal in order to be digitized. The slow shaper also limits the signal duration in order to avoid pile-up at high counting rates. The slow-shaper signal output is fed to the DAQ. The signal shaping is typically done with one of two techniques: RC differentiation-integration (CRRC shaping circuit) or delay line shaping.

In CRRC shaping, the most commonly used technique, the signal is sent through a cascaded CR differentiator, filtering low frequency noise and through an RC integrator, filtering high frequency noise, and thus optimizing the signal-to-noise ratio. This shaper generates unipolar signals. A typical CRRC circuit is presented below, along with the output signal (shaped) for a step function pulse.

Delay line shaping is an alternative to the previous shaping circuit. The reflection of the pulse in a delay line of the well-defined length placed in parallel with the output produces the destructive interference of the pulse tail. This allows to reduce the pulse width without changing the rising time. The signal-to-noise ratio of the signals formed by this method is

[1]Ideal devices always trigger with the same delay in respect to the "trigger feature" of the signal. Jitter characterizes the trigger time variability on non-ideal devices. Commonly a constant threshold is used for triggering and so, the trigger time depends on the signal amplitude. An alternative method is the constant fraction discrimination. It consists in the comparison of the threshold with the signal level at a fixed fraction of the maximum amplitude.

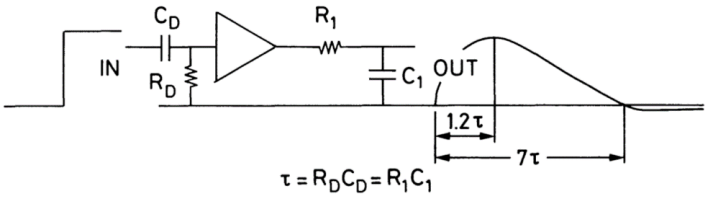

Figure 2.27: CRRC shaping circuit. Image taken from [19].

inferior to signal-to-noise ratio obtained with RC shaping, and so it is mainly used to prevent signal overlap [19].

2.3.3 Event triggering and DAQ

Trigger The trigger signal (logical signal) can be generated either analyzing the fast signals of individual photosensors (**Fig.2.28 a**) or applying some criteria based on a mathematical or logical operation to select what photosensor signals will be used by the discriminator (**Fig.2.28 b**). In the first case, each individual photosensor signal is fed to a discriminator and the output signals enter a disjunctive gate (OR). If at least one of the fast signals pass the defined discrimination criteria the trigger will the generated. In the second case, only the result given by the selected mathematical or logical operation (e.g. the sum of all photosensor signals) enters the discriminator. The schematics of **Fig.2.28** show the two alternatives.

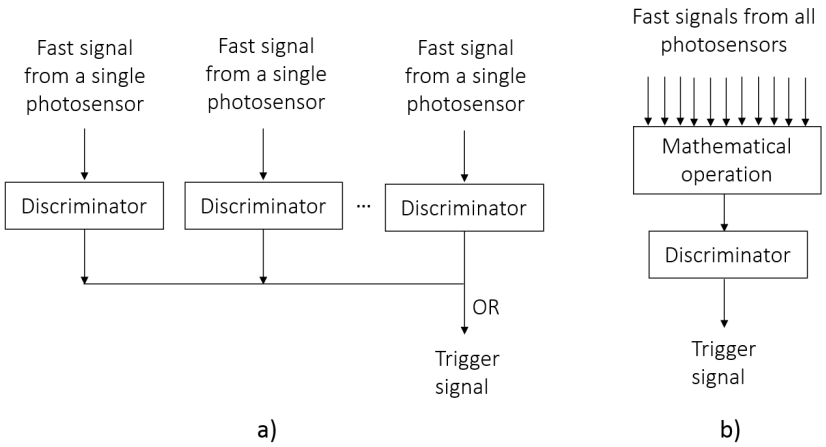

Figure 2.28: Schematic with two alternative trigger circuits. **a)** The signal of all photosensors is compared with a trigger threshold level by individual discrimators. **b)** A group of photosensors is selected to be analyzed by the discriminator through a mathematical criteria.

If a group of photosensors is used for trigger, the signal-to-noise ratio will be typically higher than using individual channels. The simplest approach using grouping is to analyze the sum of the fast signals of all photosensors. As alternative, before the sum, the photosensors with signals lower than certain value can be suppressed. Other criteria can be found, for

instance, filtering photosensor signals by relative hit positions in the detector. For example, if two photosensors far away from each other have both similar high signals it may indicate that it is a double event, which should not be recorded.

Data acquisition (DAQ) The slow signal, the photosensor signal shaped by the front-end module, needs to be digitized. This is the purpose of the data acquisition module: record for each photosensor a value proportional to the signal generated by that photosensor. Since the signal is distributed over a certain time (e.g. defined by the scintillation decay time), the photosensor signal has to be integrated. Along with the integration of the signal the electronic noise is also integrated. Higher integration time results both in more signal charge collected and more noise. Signal-to-noise ratio must be optimized by tuning the integration time. There are three common ways to sample the slow signal: peak sensing, gated integration and continuous sampling.

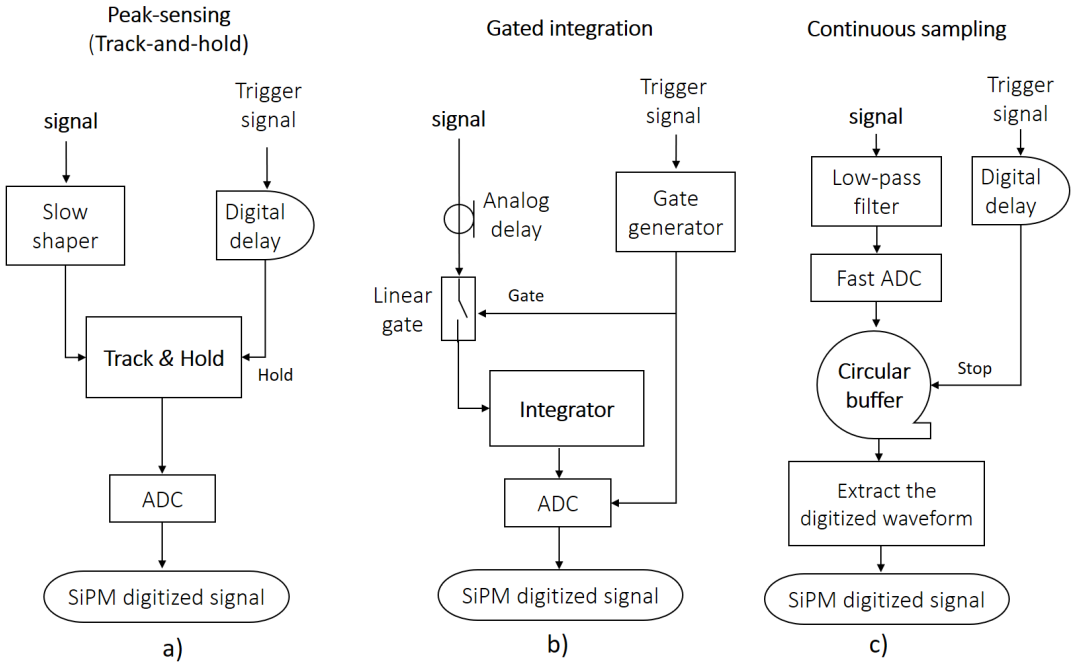

Figure 2.29: Three alternative digitization methods. **a)** peak sensing. **b)** gated integration. **c)** continuous sampling.

In the peak sensing approach (**Fig.2.29 a.**) the trigger signal needs to be delayed (the required time for the slow signal to reach the peak minus the delay from the trigger circuit) to read the highest amplitude (peak) of the slow signal. After the delay time, a hold signal is sent to a circuit which is keeping the instantaneous amplitude of the slow signal ("track & hold" block in **Fig.2.29 a**). From that moment the slow signal is held and the ADC digitize its value, corresponding to the signal peak. In the gated integration mode (**Fig.2.29 b**) the principle is not to record the peak but instead to integrate the signal waveform. The signal is

analogically delayed, using a long cable, to guarantee that the integration of the signal does not start too soon, but only when the trigger signal has arrived to the gate generator circuit and the gate generator circuit has generated the gate signal (integration window).

Nowadays there is a trend to perform all processing of the signals digitally. For that purpose, the signal is continuously sampled (digitized using a very fast ADC) and transferred to a processing module (commonly an ASIC or a FPGA) where the desired method can be used to read the signal from the digitized waveform: either peak sensing or gated integration. Digital filters can also be used once the signal is already digital. This third alternative (continuous sampling) is schematically represented in **Fig.2.29 c.** A low-pass filter is required to remove high frequencies from the slow signal to guarantee that the sampling at the ADC rate is sufficient to capture all the information of the continuous signal, according with the Nyquist–Shannon sampling theorem (the filter cutoff frequency should be half of the ADC frequency). The digitized signal enters a circular buffer and when a stop signal arrives from the digital delay, the buffer freezes and the samples corresponding to a certain time window are extracted and sent to a processing module.

From the presented digitalization possibilities, peak sensing has the advantage to be cheaper than gated integration and continuous sampling. Note that in peak sensing the same ADC can be used to digitize in series all photosensor signals, if the time of that operation is compatible with the required acquisition rate. Gated integration requires one ADC per channel (photosensor) as continuous sample does.

2.4 Gamma camera performance assessment

There is a set of parameters that characterizes the performance of a gamma camera. The most important parameters are the detection efficiency, the spatial resolution, the energy resolution, the linearity and the uniformity.

2.4.1 Gamma rays detection efficiency

Typically, for a gamma camera the total detection efficiency is defined as the fraction of γ-rays emitted by the source which is registered by the camera [19]. Note that cameras with high efficiency give the possibility to inject smaller doses in the patients. For a gamma camera one is only interested in the photopeak events because they are the ones that correspond to the events which carry information on the γ-ray emission position (see **section 2.4.3** for details). Thus, for a gamma camera the intrinsic efficiency (without collimator) is the ratio between the number of photopeak events and the number of γ-rays that have impinged the sensitive

region. The intrinsic efficiency $\mathcal{E}_{int}$ corresponds to the γ-ray interaction probability, which is defined by the γ-ray energy E_γ, the scintillator thickness l and the attenuation length $L(E_\gamma)$[1]:

$$\mathcal{E}_{int}(E_\gamma, l) = 1 - exp(-l/L(E_\gamma)) \times \zeta \tag{2.40}$$

Where ζ is the photo-fraction, i.e., the fraction of incident γ-rays which undergo full-absorption.

As an example, the curve in **Fig.2.30** shows the dependence of the detector efficiency on the crystal thickness for a commonly used scintillator, LYSO. The emission of one hundred thousand 140 keV γ-rays was simulated in a Monte Carlo simulation package for ten different crystal thickness (from 1 mm to 10 mm). The curve shows that the detection efficiency is nearly 100% for crystal thicknesses above 5 mm.

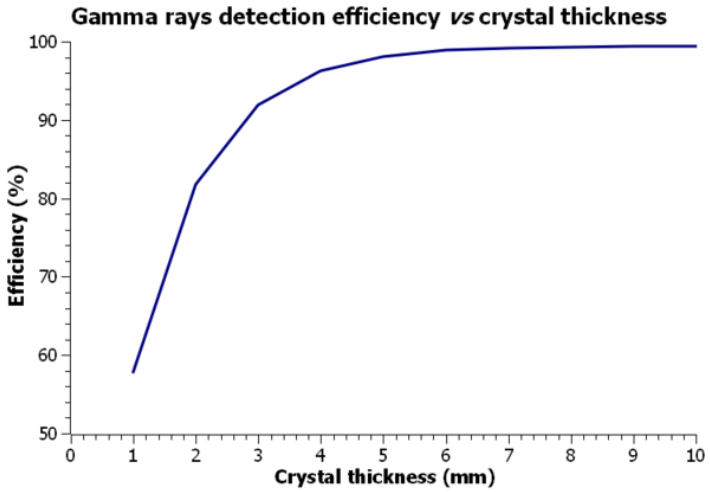

Figure 2.30: Gamma rays detection efficiency as a function of the LYSO crystal thickness. For crystal thicknesses of 2 mm and 3 mm, the efficiency is higher than 80% and 92%, respectively.

2.4.2 Spatial resolution

In medical diagnosis physicians need to clearly distinguish organic features in the images acquired by a gamma camera. For an imaging system, spatial resolution characterizes the ability to discriminate between adjacent high-contrast objects. **Fig.2.31** shows examples where two objects can (**a.** and **b.**) and cannot (**c.**) be resolved. The bottom part of the figure plots the projection of the event density along the vertical axis on the imaging device.

The spatial resolution of a scintillation camera is, therefore, a parameter that describes the ability to resolve closely situated objects in the image. There are two contributions for the overall system spatial resolution: intrinsic and extrinsic resolution.

[1]The attenuation length is the reciprocal of the attenuation coefficient, $\mu(E_\gamma)$.

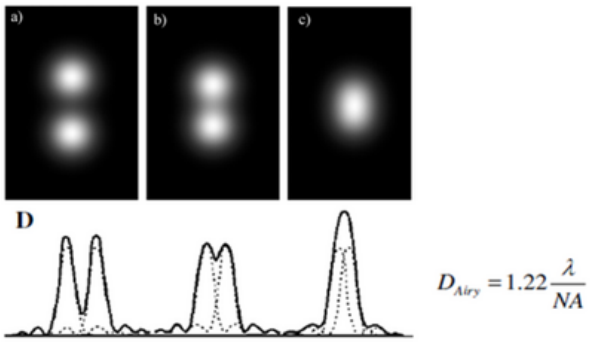

Figure 2.31: Three examples of two adjacent objects to illustrate the concept of spatial resolution. The bottom part of the figure shows the projection of event density along the vertical axis on the imaging device. Images a) and b) present two objects that can be resolved, while image c) is an example of non-resolved adjacent objects. Figures taken from [75].

2.4.2.1 Intrinsic resolution

Intrinsic resolution (R_{int}) refers to how well the position of the γ-ray interaction within the scintillator is localized by the gamma camera system. It is affected by many factors, most importantly the γ-ray energy and the photon yield of the scintillator (number of optical photons emitted per unit of deposited energy). Therefore, one can only refer to the resolution for a specific energy. For instance, for 140 keV γ-rays of ^{99m}Tc interacting with NaI(Tl) crystal, typical values of intrinsic resolution for a clinical camera of traditional design are between 3-4 mm [6, 62]. For lower energies from ^{201}Tl decays (68–80 keV) the usual resolution are about 5-6 mm [76]. Less energetic γ-rays produce less photons per scintillation event, which results in larger relative statistical fluctuation in the photosensor signals. From statistics it is known that the intrinsic spatial resolution is proportional to $1/\sqrt{E}$, where E is the energy of the γ-rays [29]. This rule assumes that the energy E is proportional to the number of produced photons N, and that N can be described by a Poisson distribution, for which the fluctuations are given by $1/\sqrt{N}$.

Other factors that influence the intrinsic resolution are the reconstruction technique and the detector design. The intrinsic resolution is limited due to fluctuations in the photosensors signal amplitudes registered by the detector. There are three main causes for fluctuations in the signal from a photosensor irradiated by a fixed source with constant intensity, which can result in different reconstruction positions, degrading the spatial resolution:

1. Statistical fluctuations (of both detected photoelectrons and dark current)

2. Fluctuations of single photoelectron response (including afterpulsing and crosstalk)

3. Electronic noise

Spatial modulation of the intrinsic spatial resolution Anger cameras typically exhibit spatial modulation of the spatial resolution. The degree of this modulation depends on the sensor array geometry, the distance between the source and the array, the spatial response of the sensors and the position reconstruction method.

As an example, the modulation of the spatial resolution is shown in **Fig.2.32** for a clinical gamma camera. The results are obtained using a simulation of the camera: the emission and reconstruction of one hundred thousand events was performed for three different source positions (C1, C2, C3), using a statistical method (maximum likelihood). **Fig.2.32.a** shows these positions in respect to the array of PMTs. **Fig.2.32.b** show the XY density plots of the reconstructed positions. Note that as the number of events is the same for all points (100 000 events), the collection of points C2 looks darker, because the events are spread through a larger area than in the collections C1 and C3. **Fig.2.32.c** shows the profile along the X direction of the XY density plots of the reconstructed events for the three source positions. The profile with the largest FWHM corresponds to the position C2, while the profile with the narrowest FWHM corresponds to the position C1.

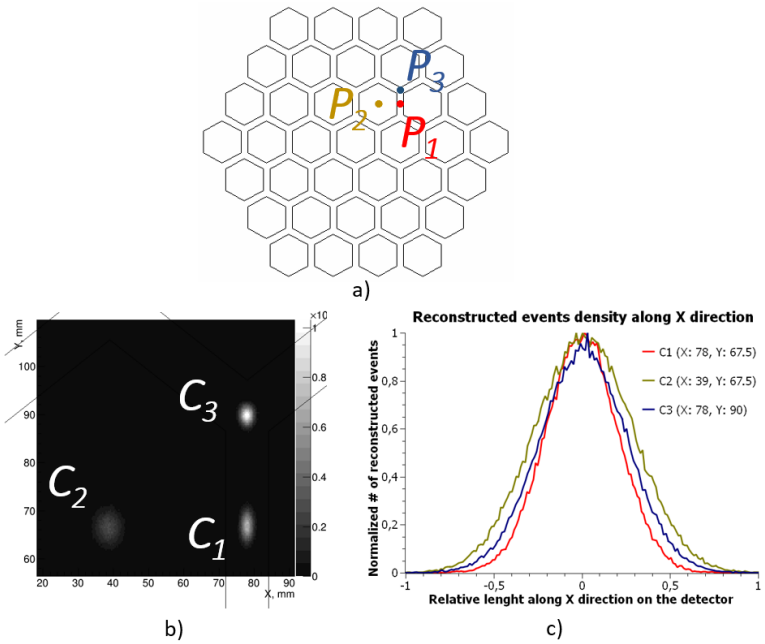

Figure 2.32: Quantitative demonstration of the modulation of spatial resolution with the coordinates. **a)** Top view of the array of PMTs (round camera for clinical imaging) showing three positions (P1, P2 and P3). **b)** Collections of reconstructed events (C1, C2 and C3), each one corresponding to one of the three emission positions. The region of interest is zoomed. **c)** Profiles along the X direction of the XY density plots of the reconstructed events for the three emission positions.

2.4.2.2 Extrinsic resolution

Extrinsic resolution (R_{ext}), also called collimator or geometric resolution, refers to how well the collimator localizes the γ-ray source in the patient and it is affected by the diameter and length of the holes and by the distance from the collimator to the patient [77]. The spatial resolution equations for both the parallel-hole and the pinhole collimator were presented in **section 2.2.1**.

Considering the intrinsic (R_{int}) and extrinsic (R_{ext}) spatial resolution, the global system resolution (R_{sys}) can be expressed as a combination of the two:

$$R_{sys} = \sqrt{R_{int}^2 + R_{ext}^2} \tag{2.41}$$

How to measure spatial resolution

The two resolution components can be measured using bar phantoms, which allow the γ-rays to pass between the lead bars. The width of the bars (and holes) are chosen for a particular camera size and expected intrinsic resolution (see a drawing and a picture of a phantom in **Fig.2.33**).

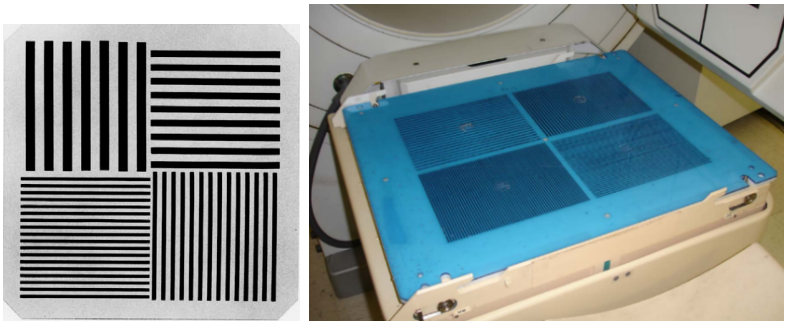

(a) **(b)**

Figure 2.33: Examples of bar phantom. **a**: Scheme of a four-quadrant bar phantom; **b**: Real four-quadrant bar phantom placed on the top of a rectangular medical camera.

Fig.2.34 represents two different setups for the measurement of the two contributions to the spatial resolution. The intrinsic resolution is measured with the collimator removed and using a quasi-parallel beam (point source placed at a distance of 4 or 5 fields of view of the camera). With this configuration parallax does not affect the image. For extrinsic resolution measurements, the gamma source is usually placed close to the camera, irradiating uniformly the entire camera field of view and the collimator is present.

However, there are other methods of measuring both the intrinsic and extrinsic resolutions. The intrinsic resolution can be calculated as the FWHM of the transverse profile of the reconstructed projection of a source (parallel beam) through a slit placed in contact to the

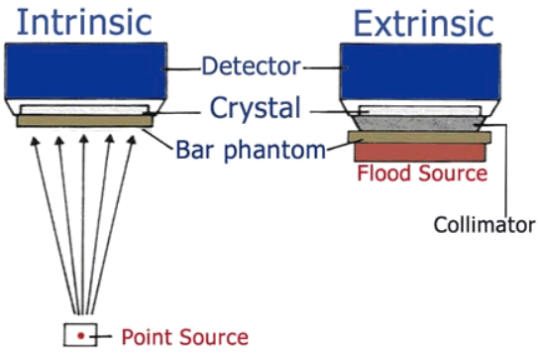

Figure 2.34: Comparison between setups for intrinsic resolution and extrinsic resolution measurement. For the extrinsic resolution measurement the collimator is present.

camera. The extrinsic resolution can be calculated as the FWHM of the transverse profile of the reconstructed projection through a collimator of a capillary tube filled with a radioactive source. The tube is placed at several distances from the collimator and the extrinsic resolution is given as a function of the distances.

2.4.3 Energy resolution

Energy resolution characterizes the detector capability to distinguish γ-rays with similar energies. Energy resolution is essential for the discrimination between γ-rays absorbed by photoelectric effect and γ-rays that undergo scattering in the patient's body before entering the gamma camera. **Fig.2.35** shows a typical γ-ray energy spectrum for ^{99m}Tc, presenting both the *primary* contribution from γ-rays hitting directly the detector and the *scatter* contribution due to Compton effect in the path of a fraction of the γ-rays towards the detector.

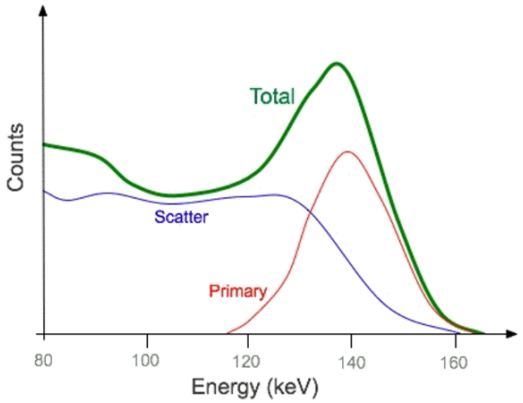

Figure 2.35: Energy spectrum for ^{99m}Tc. *Total* curve (green) shows the contribution of γ-rays absorbed after Compton scattering in the patient's body (*scatter* curve - blue) and γ-rays that hitting directly the detector (*primary* curve - red).

The contribution of γ-rays absorbed after Compton effect is reduced by properly tuning the pulse height discriminator. *Peaking* is the name given to the procedure of adjusting the

energy discrimination window to center it on the photopeak of the radionuclide of interest. However, as one can see from **Fig.2.35**, a non-negligible amount of events from scattering will still be selected in the discriminator as events corresponding to photoelectric absorption.

The commonly used parameter to measured the energy resolution d_e is the width of the photopeak of the energy spectrum (FWHM), which for a Gaussian distribution is given by:

$$d_e = 2\sigma\sqrt{2ln2} \simeq 2.35\sigma \tag{2.42}$$

Where σ is the standard deviation.

The relative energy resolution can be calculated dividing d_e by the average energy of the photopeak E_γ [78]:

$$E_r = \frac{d_e}{E_\gamma} \tag{2.43}$$

As an example, in NaI(Tl) detectors, the energy resolution for ^{99m}Tc (140 keV photopeak) is in the range of 10% - 14%, while for ^{137}Cs (662 keV) it is in the range of 7% - 10%.

2.4.4 Uniformity

The degree of non-uniformity in the gamma camera response to uniform irradiation can be defined in terms of global and local variations in uniformity over the field of view: integral and differential uniformity, respectively [79, 80]. The **integral uniformity** IU is given by:

$$IU = \frac{max - min}{max + min} \tag{2.44}$$

where *max* and *min* are the minimum and maximum number of reconstructed events (counts) in each position (pixel in the XY density plot of the reconstructed event positions) over all field of view.

The **differential uniformity** DU is given by:

$$DU = \frac{high - low}{high + low} \tag{2.45}$$

where *high* and *low* are the highest and lowest count difference in any continuous set of pixels (∼5 pixels) along a row or column for each row or column of pixels in the reconstructed image. The uniformity percentage should be higher than 96% [77, 81].

2.4.5 Linearity

Linearity characterizes the ability of the detector to reconstruct straight lines in the image. It can be assessed as the deviation of the reconstructed line from a straight line at the true line

source emission position [82]. The spatial linearity assessment aims at obtaining two distinct quantities: differential spatial linearity and absolute spatial linearity.

The **differential spatial linearity** is reported as the average standard deviation in both X and Y directions of all the differences between the best-fit line and the peaks of the line spread functions along rows perpendicular to the reconstructed line. The **absolute spatial linearity** corresponds to the maximum displacement of any peak from the best-fit line. The fitted lines should be found fitting equally spaced lines to the reconstructed lines [82].

Fig.2.36 presents two images of a linearity assessment. In this case two orthogonal orientations were chosen. Frequently, a third orientation (45 degrees in respect with the others) is also used. Some non-linearities can be seen, mainly in the right image. Nevertheless, the deviation from a straight line is less than 1.0 mm (absolute spatial linearity).

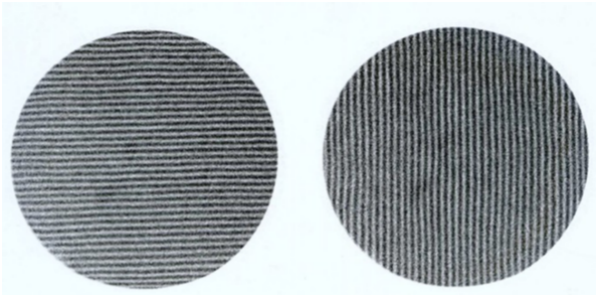

Figure 2.36: Linearity check images. Images obtained with a parallel line equal spacing (PLES) phantom with ^{99m}Tc source. Deviation from straight line is less than 1.0 mm for useful FOV (UFOV).

2.4.6 Maximum acquisition rate

The acquisition rate (counting rate) is the number of events readout by the data acquisition system per unit time. It should be as high as possible to allow calibration and imaging in the shortest possible time. In a medical examination, for instance, if the patient moves, the reconstructed image is blurred. The acquisition rate should be sufficiently fast to digitize and transfer to the processing unit the events registered by the detector. The maximum acquisition rate can be limited at least by three factors: 1) the maximum rate allowed by the data acquisition system; 2) the gamma camera physics, for instance if the scintillator decay time is long and the signal have to be integrated for a long time (e.g. if the scintillator light yield is low) and 3) the amount of data to be transferred (e.g. depending on the number of photosensors, on the number and lenght of the digitized frames). Nuclear imaging exams with small FOV gamma cameras typically require acquisition rates lower than 10 kHz.

2.5 Position and energy reconstruction of scintillation events

2.5.1 Traditional position reconstruction technique

After the signal amplitudes are recorded, the next step is to reconstruct events. Traditionally center-of-gravity (CoG) algorithm is used. This section briefly reviews CoG technique widely used in medical gamma cameras. The main advantages and limitations of CoG will be also pointed out.

The average value of the sensor signal depends on the event position (typically, the closer it is to the sensor the higher is the signal), the detection efficiency of the sensor, the gain of the sensors and the properties of the readout electronics.

To obtain the position of the scintillation event, CoG gives the event position (x, y) as the centroid of the sensors centers (x_i, y_i), weighted by the sensor signals:

$$x = \frac{\sum_i A_i x_i}{\sum_i A_i} \text{ and } y = \frac{\sum_i A_i y_i}{\sum_i A_i} \tag{2.46}$$

where x_i and y_i are the coordinates of the sensor i center and A_i is the signal amplitude of the i^{th} sensor.

Center-of-gravity algorithm only needs the positions of centers of the sensors and the measured signals in each sensor to reconstruct the position of a scintillation event. Typically, the energy is calculated as the value proportional to the sum of the signals in all sensors. The position can be calculated in an analog fashion, using a simple resistive chain (**section 2.3.1**). This CoG method has, however, several significant drawbacks, namely:

(a) **Sensitivity to gain drift**

CoG assumes that the relative gains of photosensor are the same. In reality they are not the same and they change with time (see **section 2.2.4.1**). To deal with the differences between PMTs and gain drifts with time, a periodic calibration procedure is used to normalize the gains.

(b) **Systematic spatial distortions**

Distortions appear in CoG because a photosensor response is generally not a linear function of coordinates. Special look-up tables are needed to correct those distortions. These tables establish the connection between the true position and the result of CoG reconstruction for that true position.

(c) **Limited capabilities to discriminate multiple events**

All events should be single events, corresponding to γ-rays which deposited all their energy by photoelectric effect. Double events occur when part of the energy carried

by a γ-ray is deposited after it undergoes Compton effect, followed by the photoelectric deposition of the energy carried by the scattered ray. As full energy deposition is registered by the readout system despite it does not correspond to a single deposition position, a double event results in a wrongly reconstructed event position. Thus, double events must be filtered out. However, in CoG the discrimination of events which not correspond to a single event can only be performed by energy. As the reconstructed energy of some double events may fall within the total absorption peak spectral range (see **Fig.2.7**) they will be wrongly considered as events corresponding to a single γ-ray full energy deposition.

2.5.2 Methods relying on the model of detector response

When working with individual mode readout (see **section 2.3.2**), the detection of a scintillation event results in a vector of signals from the photosensors. These signals need further processing to reconstruct the position and energy of the event.

From the 80's several methods are being applied to reconstruct the event positions which result in distortions-free images, without the use of correction tables, but rather a model of the detector response. Two examples of those methods are statistical reconstruction (SR) and k-nearest neighbors search.

In order to estimate the scintillation event position, the SR methods compare the photosensor signals with those given by the model of the detector response. They can, in principle, give more accurate position reconstruction compared to the centroid and offer significantly better capability to discriminate noise and multiple events [7]. However, the application of SR requires the knowledge of the detector response model that consists of: (i) a set of functions, characterizing the spatial response (average response as a function of the source position) of each photosensor [83] and (ii) the probability distribution function (PDF) for the statistical fluctuations of the photosensor response. In the following text, it is always assumed that the sensor response can be described by the Poisson distribution. The reason is related with the isotropic emission of light in a scintillation event. A portion of the photons are emitted towards the sensor and other portion is not. Each photon has a probability of hitting the sensor that is independent from the other photons. Hence, the probability density function of the random variable that gives the number of detected photons in the sensor can be well described by a binomial distribution, from which the Poisson distribution can be derived, as shown in **appendix A**.

All statistical reconstruction methods have the model parameterized in some way, being analytical functions or spline based techniques, for example. There are also different approaches in how to "populate the model", i.e., to obtain a correspondence between the photosensor

signals and the scintillation position, using either experimental or simulated data (calibration data). It can be done scanning the entire field of view of the camera with a pencil beam source and registering the signals in each photosensor for each position. Another possibility is to use the sensor responses obtained on simulations. A third alternative is to find a procedure that can reconstruct automatically the sensor responses to light from flood field irradiation[1] of the detector. This possibility was successfully exploited. An iterative algorithm was developed to obtain the light response functions (LRF) of gamma cameras, one per photosensor [11, 12]. In this case, "populate the model" has a more precise meaning, which is to use data from flood field irradiation of the camera to calculate, for each photosensor, the coefficients of the function (LFR) that gives the photosensor signal as a function of the scintillation positions. The details of the LRFs and of the iterative algorithm working principles are explained in the **section 2.6.1**.

2.5.3 Model (light response)

The parametrization scheme of the spatial response of the detector must be selected before populating the model. The model used in this work for gamma cameras is a set of **light response functions (LRFs)** $\eta(x, y)$, one per each sensor, as proposed by [84] and already used in [11, 12, 83, 85]. A LRF provides the average signal of the sensor as the function of the position (x, y) of a monoenergetic point source. If a sensor response has axial symmetry, a (x, y) position can be converted to a radial distance from the sensor center. The expected signal value a_i for the sensor number i which has a LRF $\eta_i(x, y)$ can be described as

$$a_i = C_i E \eta_i(x, y) \tag{2.47}$$

where C_i is a proportionality constant (normalization constant) and E is proportional to the deposited energy.

2.5.4 Statistical reconstruction

Statistical methods applied to image reconstruction aim at finding, for a single event, the position and the energy that result in the best match between the vector of measured signals A_i and the vector of expected values a_i given by the model. Two procedures are required: one to characterize the difference between the two sets of data and the other to find the position that gives the best match between the two datasets (optimization technique).

[1] By flood field irradiation it is meant that the events are distributed over the entire active area of the detector.

Fig.2.37 presents a flowchart for a generalized algorithm for statistical reconstruction methods. For a detector (e.g. gamma camera) with a certain number of photosensors (represented in the figure as a set of hexagons) depending on the position where the scintillation event occurs (star in the image) there will be a distribution of signals through photosensors, as can be seen in the color encoded representation.

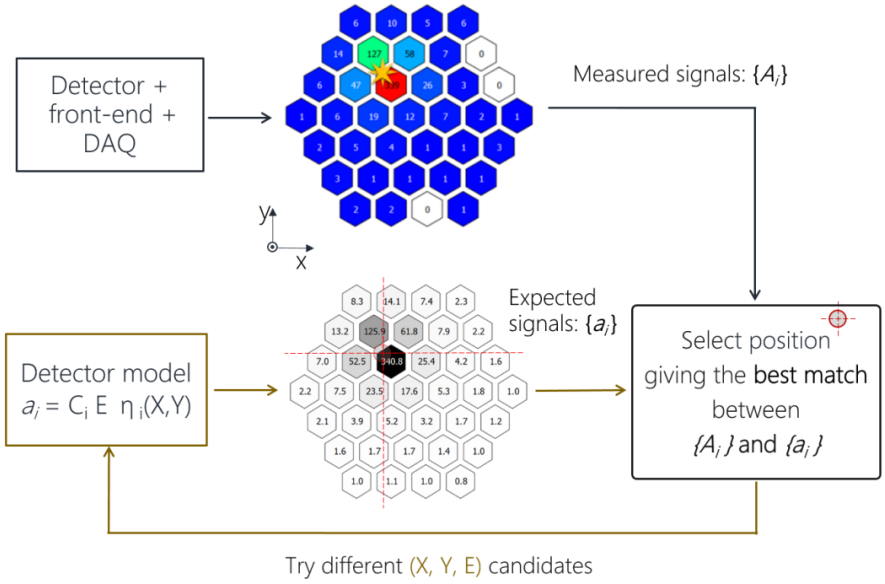

Figure 2.37: Statistical reconstruction representation. The optimization algorithm selects the position that gives the best match between the vector of measurements and the vector of expected values.

2.5.4.1 Characterisation of the difference between the expected and observed values

The characterization of the differences between the expected and observed values is commonly performed using either maximum likelihood or least squares method.

- **Maximum likelihood**

  Maximum likelihood method (ML) is based on the maximization of the likelihood of obtaining the vector A of measurements when the scintillation event occurred in the detector position (x, y) emitting N photons. In event reconstruction, if the number n_i of photons registered in each sensor i is known, the likelihood function L can be found as the product of the probabilities for each sensor to read n_i photons, assuming that n_i is an independent variable:

$$L = \prod_i P(n_i, \mu_i) \tag{2.48}$$

The probability of the i-th photosensor to detect n_i photons can be assumed to follow the Poisson distribution (**section 2.5.2**):

$$P_i(n_i) = \frac{\mu_i^{n_i} e^{-\mu_i}}{n_i!} \tag{2.49}$$

where μ_i is the expected number of photons detected by the photosensor i when N photons are emitted:

$$\mu_i = NC_i\eta_i(x, y) \tag{2.50}$$

where C_i is a proportionality factor.

The parameters that maximize the function L (**Eq.2.48**) are the same that maximize $\ln L$, because the logarithm is a monotonically increasing function. As the logarithm of a product is the sum of the logarithms, one can write, using **Eq.2.48** and **Eq.2.50**:

$$\ln L = \sum_i \ln P(n_i, \mu_i) = \sum_i (n_i \ln \mu_i - \mu_i) - \sum_i \ln(\mu_i!) \tag{2.51}$$

As $\mu_i = NC_i\eta_i(x, y)$ and the last member of **Eq.2.51** is a constant and does not affect the position of the maximum, maximization of the product given by **Eq.2.48** is equivalent to the maximization of:

$$\sum_i [(n_i \ln(NC_i\eta_i(x, y)) - NC_i\eta_i(x, y)] \tag{2.52}$$

It should be mentioned that the maximum likelihood method to estimate the position of a scintillation event was first introduced by Gray and Macovski [84].

- **Least squares**

  In the limit of very high photoelectron statistics, the Poisson distribution that describes the number of detected photons n_i is identical to the Gaussian distribution, and so the maximum likelihood method is equivalent to the least squares (LS) method. In the LS method the position and energy parameters can be found minimizing the weighted sum of the squared differences between A_i and the vector of expected values a_i for all m sensors.

$$\sum_{i=1}^{m} \frac{(A_i - a_i)^2}{\sigma_i^2} \tag{2.53}$$

where σ_i^2 is the weighting factor, which is the squared standard deviation of the expected signal.

For more details on maximum likelihood and least squares see [10, 86, 87].

In this work LS was only used when the distribution of the variable n_i (number of detected photons in the sensor i) is not known. This happened in the beginning of this work for experimental data, when there were no calibration of the readout system, so the photosensor signals were quoted in arbitrary units, rather than in number of detected photons. Both in simulations, where the number of detected photons was always known, and when the calibration of the readout system was performed, Poisson distribution for the probability of detect n_i photons in a photosensor was assumed, because the average number of detected photons is quite low (less than 10 photons). Hence, maximum likelihood was used, since the statistics of photon detection were known.

2.5.4.2 Optimization techniques

Optimization is the process of finding the position which gives the best match between the vector of measured signals and that with the predicted signals. The simplest (and the slowest) optimization approach is the *brute force*. In this method, the vector of the predicted signals is calculated for positions forming a dense grid over the detector field of view. The grid step is chosen according to the resolution of the camera.

An alternative approach is to use the "contracting grids" technique, which is faster than *brute force* because it does not perform high resolution search over the entire parameter space. A grid is defined around a certain region and the search is performed. Depending on the required precision, a new, finer grid is defined around the optimal position and the search starts again. The new optimal position is calculated and this process can iterate, decreasing the step between the grid nodes until the finest grid, which is usually smaller than the spatial resolution. This technique can be very fast if a parallel computing resource is available, for instance a graphics processing unit, as all the grid nodes can be evaluated independently.

The best match can also be found using minimization methods, like *Migrad* and *Simplex*. In these methods the parameter space is not scanned. Migrad is a gradient descent algorithm with step control. The *Simplex* method is an iterative procedure that solves in each iteration a system of linear equations and stops when either the optimum parameters are reached or the solution proves to be infeasible [88, 89, 90]. Both methods are available, for instance, in CERN ROOT library (Minuit2 package) [91, 92].

As not all the photosensors carry the same amount of useful information, in some situations it is beneficial to use only the signals of a subset of the available photosensors. The spatial response far away from the sensor is not important for reconstruction, because it is mostly

dependent on the scattered light and dark counts, rather than in the scintillation position. For each event, a possible way of selecting the photosensors to be used in the reconstruction is to define a maximum radius from the starting (x, y) position of the optimization algorithm to the center of the photosensors. In this work, a parameter called *active radius* was used to select the sensors considered as *active* in the event reconstruction, as opposed to those considered as *passive*. The passive photosensors does not enter into account in the optimization functions that compare the photosensors signals dataset with the model dataset with the expected photosensors signals.

2.6 Calibration and self-calibration: estimation of the detector model

Usually, to populate the model, a scan of the camera field of view (FOV) is performed with a pencil beam source and the sensor signals are recorded in a look-up table (LUT) for each source position. In some cases, this requires a complex setup with robotic control and takes significant time, depending on the FOV area and the pitch of the source positions. For example, Bouckaert et al. [93] made a calibration scan with a ^{99m}Tc pencil beam source for which a 32×32 points grid with 1 mm pitch was acquired. The measurement time per position was corrected for the decay of ^{99m}Tc and it started as 15 seconds. The complete acquisition took about 11 hours.

Traditional medical cameras require a periodic calibration procedure due to the drifts in the photosensor gains. The standard calibration procedure contain several steps, need highly qualified technical personal and it is also time consuming. The need for such periodic calibrations increase downtime and significantly increase running costs, which could be avoided for cameras with self-calibration.

2.6.1 Adaptive algorithm for LRF reconstruction

A technique to populate a scintillation based detector response model from flood field irradiation, without knowledge of the source position, was first developed for a dark matter detector, where a scan was impossible to be performed [10], and later the same technique was successfully applied to thermal neutrons Anger-type gaseous detectors and medical Anger cameras by Morozov et al. [11, 12]. In this section it is assumed that the detector model is the set of LRFs of the array of photosensors. **Fig.2.38** plots a typical LRF shape for axial-symmetric case, which is typically a monotonically decreasing function. Axially symmetric response can be expected for a PMT because the signal is only dependent on the distance between the PMT center and the projection of the scintillation event position onto the PMT photocathode.

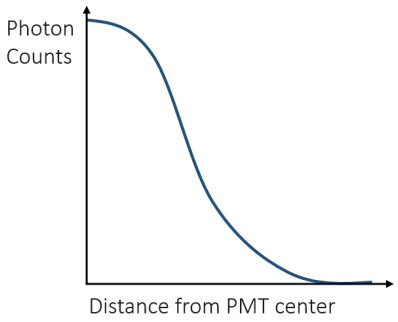

Figure 2.38: Typical shape of the photosensors light response function (LRF). The curve is a monotonically decreasing function.

An iterative algorithm, presented below, uses flood field illumination data to reconstruct the LRF for each photosensor of the detector [10]. Starting with an initial assumption on the LRFs, the positions of the scintillation events are reconstructed using a statistical method (**section 2.5.4**). These new positions and the signals on the PMTs are used to obtain the new LRFs. The process iterates until a stopping criteria is reached.

Two sets of data are required as input for the LRF iterative reconstruction method:

(a) Vectors of measured photosensor signals A_i – fixed during the iterative process.

(b) Estimated positions and energy (x, y, e) – updated at each iterative step.

In the first iteration an initial guess must be taken on the LRF (e.g. given by CoG). The following cycle is iteratively performed:

1. Event reconstruction: statistical reconstruction is applied (using the available LRFs) to find the position and energy (x, y, e) of each event in the dataset.

2. Evaluation of new LRFs using the event positions obtained in step 1.

3. Check for convergence of LRF. If LRFs have not converged yet, go to step 1.

In the end of each iteration (step 3) the stopping criteria must be inspected to see if the iterative method is converging, and if so, the process should stop and return the evaluated LRFs. To monitor the progress, a parameter proportional to the *chi-square* value of event reconstruction, averaged over all events is used. Alternatively, the difference between the LRFs resulting from successive iterations can be used to evaluate convergence.

There are additional steps, that can be optionally used:

(i) **Filtering**: after the reconstruction, events can be filtered out, for example, if its reconstructed energy is out of a defined energy range, if its reconstructed position is out of a

defined spatial area and if the *chi-square* of the reconstruction is above certain threshold can be.

(ii) **Blurring**: every reconstructed position is shifted randomly by a small value after the reconstruction of all events. Since LRFs are typically slow-changing functions, this procedure does not introduce large errors, and allows to populate the regions with no events due to inadequate LRF shape during several iterations in the beginning of the iterative procedure. The procedure was empirically verified to accelerate the LRF convergence [12].

The iterative algorithm can start both from step 1) or step 2). If it starts from step 1), an initial guess on LRFs is required. It can be given by CoG method. Alternatively, when estimating LRFs for experimental data, the initial guess can be the LRFs given by simulation data. If the algorithm starts from step 2), an initial guess on event positions has to be made. This can be done using, for instance, CoG method.

It should be noted that the iterative algorithm does not impose strong requirements on the spatial uniformity of the event distribution of flood field irradiation. For more details on the iterative method for reconstruction of detectors response refer to [12].

The described adaptive algorithm was implemented in the simulation and experimental data processing package ANTS2 [94]. In this implementation, LRFs are parameterized using cubic B-splines and assumed to be axially symmetric functions. The estimated LRF curve should have three features that can be imposed during the LRF evaluation: be a monotonically decreasing function, have zero derivative in the origin and to be non-negative. For implementation details and a description of the parametrization procedure see [83].

At the first glance, the axially symmetric approach seems to pose a problem for compact camera with a square scintillator and square shape of the sensors. It should be noted, that the large amount of scattered light on the periphery of the compact camera and the square shape of the photosensors can break the axial symmetry of the LRF. This could be a serious problem for the iterative reconstruction method, which relies on this symmetry. However, recently, the iterative reconstruction of the photosensors light response functions in a square shaped compact camera was experimentally validated [85].

2.7 State-of-the-art on SFOV gamma cameras

Small field-of-view (SFOV) gamma cameras are devices of small sizes when compared with traditional clinical gamma cameras. They are well-suited for small animal imaging, which is extensively used in genetic research and in the drugs development cycle [95, 96]. Portable cameras are also adequate for some medical examinations and surgeries. For instance, the

usage of compact cameras as hand-held scanners for thyroid, parathyroid, urological and gynecological functional characterization studies and to be used during surgeries, e.g., for the sentinel lymph node biopsy (in melanoma and breast tumor staging). The compact cameras, when assembled in a complete imaging system, are being called "mobile cameras", "handheld cameras" or "imaging probes" and the respective surgeries as "radio-guided surgeries" or "intraoperative scintigraphy" [97, 98].

The developement of small size devices was leveraged by the growing importance of specific imaging applications, mainly those which do not need to image a large FOV [8, 55]. Another factor was the increasing use in the last 20 years of *in-vivo* small-animal imaging for preclinical studies of animal models of human diseases, with SPECT modality being vastly applied along with PET ([57, 99]). The small size of mice organs requires spatial resolutions lower than 1 mm (typically in the 0.3 mm - 0.9 mm range) [100, 101, 102, 103, 104, 105, 106], which is $\sim$10 times better than those usually given by large FOV cameras, with sufficient sensitivity to achieve good contrast images in a practical time period for a reasonable amount of injected dose activity [8]. These demands have contributed for the innovation in both detection and collimation technologies.

The technologies behind the SFOV cameras can be divided in the same branches as for large FOV cameras. There are two main groups: semiconductor-based cameras, which directly detect γ-rays and scintillator based cameras, in which the light produced in the scintillation process is collected by photosensors (**section 2.1.2**).

Scintillator based cameras can be divided by the type of crystal they feature, either pixelated (or columnar) or monolithic (or continuous), as presented in **section 2.2.2**. In pixelated scintillators, reflective material (e.g. Teflon, MgO powder) usually covers the crystal lateral sides in order to guide the light through the crystal column, minimizing the transition of light to the neighbor columns. For some methods, as center-of-gravity, this collimation technique can be beneficial for reconstructing the scintillation positions, but the spatial resolution is always limited to the pitch between crystal pixels (or columns). Monolithic crystals are not limited in the spatial resolution as pixelated crystals are, due to the insulating space between pixels. Besides that, they are less expensive than pixelated crystals, feature a better light collection and for statistical reconstruction algorithms they allow the necessary distribution of light by the array of photosensors.

Another division can be made among the scintillator based detectors depending on the type of photosensor to collect light (**section 2.2.4.1**), that can be: photomultiplier tubes (PMTs), position sensitive photomultilpier tubes (PSPMTs), silicon photomultipliers (SiPMs), avalanche photodiodes (APD) or simple photodiodes. Photodiodes are almost not used because they have a limited signal-to-noise ratio due to the absence of amplification and a significant

capacitance of the electrodes [8]. In APDs a relatively high reverse bias voltage (100-200 V in silicon) is applied and amplification is achieved due to impact ionization. The amplification is rather low ($\sim$ 100), but it can be improved (up to $\sim$1000) in some silicon APDs employing alternative doping and beveling techniques that allow the usage of greater reverse bias voltage (>1500 V) before the breakdown voltage is reached. Typically, the amplification factor increases with the reverse voltage. However, it is challenging to obtain gain uniformity in the APD active area and maintain stability over time and temperature variations [8]. Comparing with gamma cameras using PMTs, which need a bias voltage of at least $\sim$750 V, SiPMs and photodiodes have the clear advantage of not requiring high voltage for their operation. Another advantage of SiPM, photodiode and APD based cameras is that they are not affected by magnetic fields, which allows the magnetic resonance imaging (MRI) to be applied in close proximity or the integration of the gamma camera in a multimodal imaging system which uses MRI. In **section 2.2.4** the main features of PMTs, PSPMTs and SiPMs were presented.

Each year new studies on SFOV gamma cameras of each type are published, either presenting new designs, experimental characterizations, reconstruction methods, or solving limitations from previous camera designs. In the **appendix B** several scintillation based cameras with different readout types are presented, namely those using SiPMs, digital SiPMs and PSPMTs. In this section, a brief overview is made on the main scintillation event reconstruction methods being used, with focus on an automatic and iterative procedure to build the detector response. Several studies that have compared the performance of the pinhole collimator with that of parallel-hole collimator for the same detector are described. Then, intraoperative gamma cameras are presented with emphasis in sentinel lymph node detection, being either research prototypes or commercially available equipment. The performance of a large set of compact gamma cameras is summarized in a table.

2.7.1 Event reconstruction methods and detector response models

Center-of-gravity (Anger-logic) is by far the method most used to reconstruct positions and energy of scintillation events, although it has a number of limitations (**section 2.5.1**). It was demonstrated that statistical algorithms can overcome those limitations, potentially offering a more accurate reconstruction [7, 10, 107, 108, 109]. However, a model of the detector response is required in statistical reconstruction methods. This model has been typically built by scanning the entire detector FOV with a pencil-beam source and registering the sensor signals in each irradiation position. Interpolation techniques were also introduced to obtain a continuous position dependence of the light response (e.g. [110]).

The adaptive algorithm described in **section 2.6.1**, can also be used to build the model of the detector response [10, 11]. In 2017, Morozov et al. have verified both with simulations

and experimentally that the iterative method can be applied to a square-shaped SFOV camera featuring a 30 × 30 × 2 mm^3 LYSO:Ce scintillator (Epic-Crystal company) and an array of 8 × 8 SiPMs (SensL MicroSB-30035) for 140 keV γ-rays [85]. The spatial response (LRFs) of the SiPMs was parameterized as a set of axially symmetric functions obtained iteratively from flood field irradiation data. The square shape of the SiPMs can be a problem due to the non-axiallity of the LRFs. However, Morozov et al. verified that relatively low level of distortions was achieved assuming an axial symmetry of the sensor LRFs. The average difference between the reconstructed positions and true positions are around 0.2 mm in a central FOV of 22 × 22 mm^2 and 0.4 mm in the peripheral region of the camera. It was also shown that there is no strong requirements on the uniformity of the distribution of events over the detector FOV.

Alternative methods, namely k-nearest neighbor (k-NN) and artificial neural networks (ANN) machine learning approaches are also being applied to reconstruct the scintillation positions [111, 112, 113, 114]. For example, it has been shown that a high spatial resolution can be achieved by using a monolithic crystal coupled to an array of digital SiPMs and using k-NN search [115]. Ulyanov et al. [116] have reconstructed the 3D positions of γ-rays interaction points using ANN trained with experimental data. Their setup was mainly intended to be used in a Compton telescope for γ-ray astronomy, but the event position reconstruction method can be also used in gamma cameras. Three independent ANNs were implemented for the calculation of the three Cartesian coordinates of the interaction point based on the signals of 16 SiPMs (6 × 6 mm^2 SensL MicroFB-60035-SMT). The ANN training data were collected scanning the detector (2.3 mm steps) with a collimated ^{133}Ba source (356 keV). Two scans were performed. A XY scan covered the entire face of the crystal and the acquired data were used to train the ANN for reconstruction of x and y-coordinates, being the corresponding coordinates of the γ-ray interaction approximately given by the beam position. With the XZ scan, one lateral side of the crystal is illuminated along the Z direction, and the acquired data was used for the ANN training in reconstruction of z coordinate. For a 20 mm thick $CeBr_3$ crystal (25 × 25 mm^2 main face size), the imaging system showed a spatial resolution of about 5.4 mm FWHM (x and y coordinates) and 7.8 mm FWHM for the z coordinate.

k-NN and ANN methods perform their training phases using calibration data: information on the γ-rays emission positions (output parameters) associated to the respective photosensor signals. The photosensor signals are the input parameters and the event positions are the output parameters in the reconstruction phase of both methods. When there are no tools available to populate a model based on a set of LRFs from calibration data, k-NN can be used rather than statistical reconstruction algorithms, because it has a direct correspondence between the photosensor values and the reconstructed positions. However, besides the limitation of not being a continuous model of the detector response, k-NN reconstruction can

be very slow, depending on both the dimension of the calibration data set and the strategy for storing those data. If data are saved as a tree structure, the reconstruction of new event positions is faster than if it is saved as a tri-dimensional array (a grid with a vector with the sensor signals), where brute force approach need to be used. In this case, all training events are compared with the signals of the event to be reconstructed. It should be noted that the reconstruction based on a k-NN tree is not precise. Moreover the training phase itself can be very time consuming depending on the calibration array dimension and on the number of events used per array node during the training. When the array size is small, the precision of the reconstructed positions can be low.

ANN has always a slow training phase, but it is very fast in reconstruction and can be very precise if a good data set is used for training. When compared with statistical methods, the speed of reconstruction is a factor to select the ANN reconstruction, when no parallel computing (e.g. GPU or FPGA) is available. However, when parallel computing resources are available, SR methods can perform also very fast. However, the well defined ANN layer structure pose an important limitation to ANN. If any value is missing in the neural network input layer (e.g. a photosensor signal is zero), the reconstruction process can work, but results in strongly distorted reconstructed positions, because the network was not trained for that input set of signals. If SR reconstructed is used instead, the switched off sensor can be simply excluded from reconstruction with no impact on the linearity. The reconstruction result can be close to that given when all photosensors are switched on, although degradation in spatial resolution can be expected in the vicinity of the excluded sensor. ANN will require a complete training cycle to update itself to the new camera configuration.

Espana et al. [114] used a ANN with only two layers to build a self-organizing map (SOM) and reconstruct the event positions. The network (map) was built from experimental training data using unsupervised learning. The authors reported a fast calibration of a SPECT monolithic scintillation detector using static un-collimated sources, since it does not require robotic stages.

2.7.2 Collimation of γ-rays in SFOV gamma cameras

The type of collimators used in SFOV gamma camera depend on the application. Parallel-hole collimator has higher sensitivity than pinhole collimator for equivalent spatial resolution. Pinhole collimator gives a SFOV camera a capability to image objects that are larger than the field-of-view. This can be achieved placing the pinhole aperture at a distance from the object which is larger than the distance aperture-scintillator, resulting in a de-magnification effect on the detector plane. However, the reconstruction of the event positions of γ-rays reaching the

scintillator with diagonal direction are inaccurate ("parallax error" or "depth-of-interaction (DoI) effect"). Other factor that cause misreconstruction of γ-rays in pinhole imaging is the edge penetration at the aperture. Together with parallax error it causes broadening of the point spread function (PSF), as represented in **Fig.2.39**.

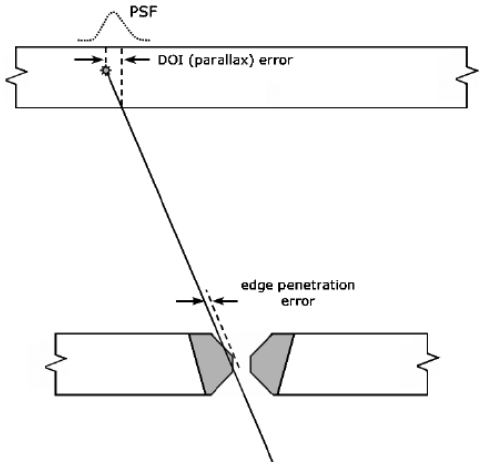

Figure 2.39: Main factors that cause mis-reconstruction of γ-rays in pinhole imaging: edge-penetration and parallax error. Image was copied from [57].

Several groups have optimized the collimator for particular gamma camera designs and applications.

For example, Baek et al. [117] have optimized a large view (120°) pinhole collimator to a camera with a 50 × 50 × 6 mm^3 monolithic CsI(Tl) scintillator and an array of PSPMT (Hamamatsu H8500). The focal length (distance from aperture to detector) is 14.5 mm. The main applications envisioned by the authors are nuclear survey and environmental monitoring in medical fields, due to the large acceptance angle of the collimator. The intrinsic spatial resolution and sensitivity were calculated for simulation data, where the pinhole diameter and channel edge were changed in the range from 0.5 mm to 4.0 mm and 0 mm (knife-edge) to 3.0 mm, respectively. From spatial resolution and sensitivity trade-off curves (see **Fig.2.40**), the optimal pinhole diameter was found to be 1.5 mm, while the channel height was 0.5 mm to get a resolution below 2 mm FWHM with a reasonable sensitivity for the system configuration in the study. Increasing the channel height, the spatial resolution improves, because the penetration and scattering of γ-rays in the aperture edges decrease. On the other hand the sensitivity for grazing angles is reduced. The authors noted that a shortcoming of large-angle pinhole is the non-uniform spatial resolution over the FOV, due to the parallax error.

Yujin Qi [118] has optimized both a pinhole and a parallel-hole collimator for a 110 × 110 mm^2 pixelated CsI(Na) detector for pre-clinical imaging when a desired object resolution, a given pixel size (1.0×1.0 mm^2), a target intrinsic resolution and a given object-to-collimator distance were specified. The required object resolution was 1.5 mm FWHM at 30 mm from

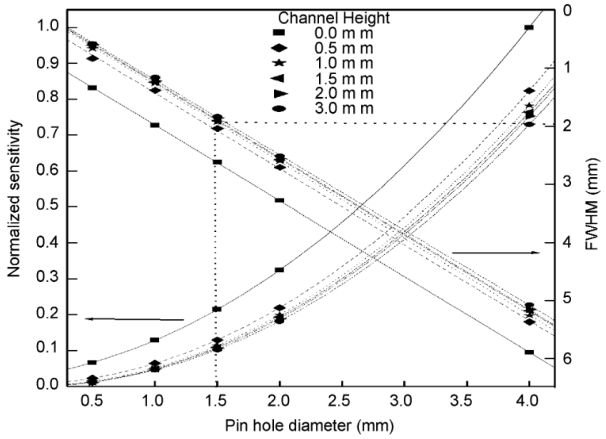

Figure 2.40: Trade off curves from [117] work on the optimization of a large view pinhole.

collimator (for mice) and 2.0 mm FWHM at 50 mm from collimator (for rats). A parallel-hole collimator with hexagonal holes with 1.2 mm size, 40 mm hole-length and septa thickness of 0.2 mm was found to be the optimal design for object resolution of 2.5 mm at the object-to-collimator distance of 30 mm. For a pinhole collimator acceptance angle of 60 degree and a focal length of 100 mm, the spatial resolution and detection sensitivity were determined for a range of aperture diameters from 0.6 mm to 2.0 mm. Simulations have shown that a 0.5 mm height channel edge improves by 18% the spatial resolution, compared with the knife-edge aperture. This can be attributed to the lower contributions of γ-rays penetration and scatter in the aperture edges. As can be seen from the sensitivity *vs* resolution trade-off curves (see **Fig.2.41**) for several aperture diameters, the pinhole collimators with 1.0 mm and 0.6 mm diameter can provide resolutions better than 1.8 mm FWHM for an object-to-collimator distance of 30 mm. The best trade-off is obtained for pinhole diameter of 1.0 mm: spatial resolution of 1.5 mm and relative sensitivity about 2 times higher than that of the parallel-hole collimator.

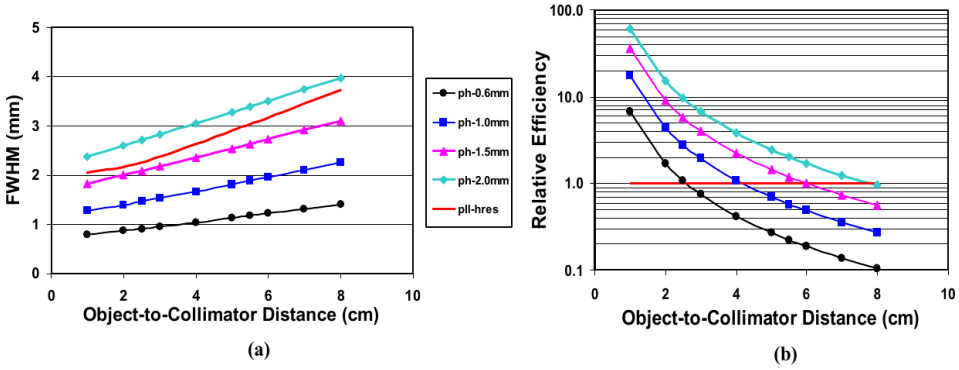

Figure 2.41: Trade-off curves (sensitivity *vs* spatial resolution) as a function of the aperture diameter. Image taken from [118]. **a.** Spatial resolution (FWHM) **b.** Relative efficiency.

Berthot et al. (2003) used Geant4 to simulate a gamma camera with monolithic NaI(Tl) scintillator for small animal imaging. The simulation model was first validated comparing the collimator performance to that of the analytical equations. Both pinhole and parallel-hole lead collimators were used. The pinhole aperture has a diameter of 4.0 mm and a focal length of 30 mm. The parallel-hole has 1.9 mm diameter holes and 0.5 mm thick septum. The authors have simulated the emission of 500 thousand γ-rays from a source 100 mm apart and aligned with the center of the collimator. A good agreement between simulation and analytical results was achieved for both collimator types. The simulated resolution was 6.5 mm for the parallel-hole collimator, for both simulation and analytical cases. For the pinhole collimator, the simulated resolution was 5.0 mm, slightly better than the 5.2 mm resolution given by the analytical equation. The simulated sensitivity of the pinhole collimator was 0.00013, while the analytical sensitivity was 0.00010. The simulated sensitivity was 0.00011 for parallel-hole collimator and the corresponding analytical sensitivity gives 0.00013.

Other comparative study on the performance of pinhole and parallel-hole collimator for SFOV cameras was carried out by Jeong et al. [119], using Monte Carlo simulations. The authors have considered the three most used types of parallel-hole collimators: low-energy high-resolution (LEHR), low-energy general-purpose (LEGP) and low-energy high-sensitivity (LEHS). The detector is a 128 $\times$ 128 $\times$ 1 mm^3 pixelated CdTe semiconductor, with pixels size of 0.35 $\times$ 0.35 mm^2. It has 32% efficiency for γ-rays with energy of 140 keV. The authors simulated a point source and a hot-rod phantom to evaluate the sensitivity and spatial resolution of each collimator. The results are summarized in **table 2.2**, along with the collimator dimensions. The hole diameters for the LEHR, LEGP and LEHS collimators are 1.2 mm, 1.6 mm and 2.0 mm, respectively; the septal thickness is 0.2 mm, 0.25 mm and 0.3 mm; the collimator thickness is 30 mm, 25.4 m and 25.4 mm. The pinhole collimator had an aperture of 50° with 1.2 mm diameter. The ratio between the source-to-aperture and aperture-to-detector distances resulted in a magnification factor of 3.0. The authors confirmed that the sensitivity of all parallel-hole collimators is independent of the source-to-collimator distance. The highest sensitivity was achieved when using LEHS, followed by LEGP, LEHR and pinhole. The spatial resolution at an object-to-collimator distance of 20 mm was 1.63 mm, 2.05 mm, 2.79 mm and 3.45 mm using pinhole, LEHR, LEGP and LEHR, respectively. The reconstructed hot-rod phantom images showed that the 2 mm thick rods were clearly resolved with pinhole and the LEHR collimators.

Several studies were published presenting multi-pinhole collimator ([120, 121, 122, 123, 124]). Converging [125] and diverging [126] collimator solutions have been also developed.

	LEHR	LEGP	LEHS	Pinhole coll.
Hole diameter (mm)	1.2	1.6	2.0	1.2
Septal thickness (mm)	0.2	0.25	0.3	-
Hole length (mm)	30	25.4	25.4	-
Aperture angle (°)	-	-	-	50
Spatial resolution (mm)	2.05	2.79	3.45	1.63
Sensitivity (cps/kBq)	0.09247	0.23441	0.36773	0.00393

Table 2.2: Spatial resolution and sensitivity of the collimators studied by [119].

2.7.3 SFOV gamma cameras for specific applications

Small FOV gamma cameras allowed a close proximity (less than 3-4 cm) to the organs to be imaged (e.g. thyroid, SLN, breast, prostate, heart), improving the sensitivity in several clinical procedures and the spatial resolution of the reconstructed images. In order to further improve the sensitivities and spatial resolutions required for specific clinical examinations, application-specific imagers have been developed driving the innovations of technology related with SFOV gamma cameras, such as SiPMs, PSPMTs or new scintillators with high light yields and low decay times.

The Society of Nuclear Medicine and Molecular Imaging (SNMMI) and the European Association of Nuclear Medicine (EANM) have approved the guidelines presented in 2013 by Giammarile et al. for lymphoscintigraphy and sentinel node localization, in order "to promote the use of nuclear medicine procedures with high quality" [127]. In the radioguided surgery section, portable gamma cameras and SPECT/CT imaging systems are considered as devices that can help to localize the nodules of activity. Several small gamma cameras dedicated to sentinel node detection were developed (see **table 2.3** and **appendix B**), to substitute or complement the conventional gamma probe during the surgeries for the removal of sentinel lymph nodes.

A review of 13 small intraoperative gamma cameras for radioguided surgery is given in [128]. The camera with the best performance has 6.9% of energy resolution, 1.59 mm of intrinsic spatial resolution and 3.4 mm system resolution at 50 mm from the source [129]. A vast number of references to SFOV gamma cameras used in interventional and intraoperative imaging can be found in the book edited by Perkins and Lee, published in 2017 by CRC press [130].

Another imaging application that has been the focus of detector technologies innovation is scintimammography. Small FOV devices have the ability to be placed closer to the breast and to provide better spatial resolutions, compared to large-area gamma cameras ([8, 131]). Peterson states that planar scintimammography using ^{99m}Tc-Sestamibi potentially provides

sensitivity and specificity for the malignancies detection, particularly for women with radio-opaque breasts for whom mammograms are often inconclusive [8]. In [132] a review on mobile gamma cameras used in breast cancer treatment and SNL biospy is given. The authors have analyzed 14 articles published from 2000 to 2012. Further details on a comparative study of cameras dedicated to breast imaging can be found in [133].

Intraoperative surgery SFOV gamma cameras - Sentinel lymph node detection The reduction in size and weight given by SFOV relatively to conventional LFOV cameras opened the possibility of integrating SFOV cameras in portable imaging systems, either hand-held or mobile trolleys with articulated arms. The trolleys can be small enough to be accommodated in regular surgical suites and the arm holder makes easier to maintain stability of the camera position. Hand-held devices offer the freehand advantage whenever the weight is comfortable to be held by a person during the required imaging time (up to 1 minute for SNL). Besides that, freehand devices are more easily sterilized and covered with soft bag protective materials in the operating room. A brief history of the use of intraoperative small and large field-of-view gamma cameras for radioguided surgery in given in the book edited by Herrmann et al. (chapter 3) [97]. The first prototype hand-held gamma camera, called imaging probe (IP) was patented by Soluri et al. in 1997 [134].

Hand-held gamma cameras are intraoperatively used in sentinel lymph node (SLN) detection and removal. SLN is the first regional lymph node that drains from the primary tumor. It is potentially the first node to receive the seeding of lymph-borne metastatic cells. Lymphoscintigraphy easily identifies and allows the surgical biopsy of the SLN, but can not determine if it is involved with cancer. An anatomo-pathological analysis is performed, during the surgical procedure, with that objective in mind. If the SLN is not involved by the tumor, the physician can be confident that the downstream ganglia are also negative, and a lymph node dissection can be avoided. If the SLN is positive, a lymph node dissection is performed for N-staging purposes, that is, to evaluate the extension of the lymph node disease.

Both the signalization of the SLN before the surgery (usually one day before) and the localization of the sentinel nodes during surgery should be done as accurately as possible. Radioactive tracers, able to map the lymphatic system and accumulate in the lymph nodes, are administered. For the signalization phase, scintigraphy images are performed and the region of the SLN is marked on the patient's body with the help of an gamma-counting probe. This probe is a commonly available detector for the localization of the radioactive nodules. The probe emits an acoustic signal with frequency proportional to the detected source activity. This method cannot distinguish nodes situated very closely from each other or nodes that overlap at different depths. Moreover, in the close vicinity of the injection site a significant amount of radiotracer is accumulated, making it hard to discriminate any potential lymph

node in the proximity using only the gamma-counting probe. To overcome these limitations, a portable gamma camera could be very useful, as suggested in [135, 136]. The portable gamma camera could improve the accuracy of the SLN localization, both in the signalization phase and during surgery. Three examples of hand-held cameras being used in SLN detection and surgical removal are given below.

The sZSCOPE detector, from Anzai Medical (Japan), is a relatively lightweight (∼820g) hand-held CZT-based semiconductor gamma camera with 32 × 32 mm^2 FOV, which features an energy resolution of 9% (140 keV, ^{99m}Tc) and an external spatial resolution (using low-energy high-resolution LEHR collimator) of 2.3, 8.0 and 15 mm at 10, 50 and 100 mm, respectively. Heller et al. noted, however, that the camera size remains limited because a single lymph node occupies almost half of the field of view, which means that searching the surgical field can be time-consuming [137]. The same author, who had personally evaluated sZSCOPE, recommends a slightly diverging collimator that would double the field-of-view at 50 mm from the gamma sources or a pinhole collimator which would give a variable FOV to the camera, depending on the ratio between aperture-to-detector and aperture-to-source distances.

Other intraoperative commercial camera is the hand-held Sentinella 102 based on a continuous CsI(Na) scintillator, a flat panel of PSMPTs and a high-resolution interchangeable lead collimator with pinhole apertures of 1.0, 2.5 and 4.0 mm. The camera dimensions are approximately 150 mm×80 mm×90 mm [138]. Its performance was measured for a 140 keV source. The camera has 13% energy resolution and an intrinsic spatial resolution of 1.6 mm. For a source at 100 mm from the pinhole, the system resolution is 10 mm and 18 mm, respectively, for aperture sizes of 2.5 m and 4 mm. Ortega et al. [138] have successfully tested the hand-held version of Sentinnella 102 for minimally invasive parathyroidectomy (MIP) procedures. Five patients diagnosed preoperatively with primary hyperparathyroidism underwent MIP. A gamma probe and the camera were consecutively used intraoperatively for the localization of the pathological glands. The camera had located all the parathyroid single adenoma, even the most difficult case that the probe did not detected. It was also useful to confirm the complete resection of pathological tissues. Sentinella 102 evolved to a commercial gamma camera with an articulated arm, commercialized by Oncovision company and it is also used for SLN biopsy.

Popovic et al. [139] reported the usage of a larger gamma camera (200 × 200 mm^2 FOV) for preoperative identification of nodal basins that contain SLNs and the establishment of the overall surgical plan. They consider a useful balance for the needs of the various stages of melanoma SLN biopsy, the preoperative survey imaging performed with the larger camera, followed by the intraoperative spot imaging for the localization of sentinel nodes and post-excision assessment performed with the small FOV camera. The same authors present a table

of devices used for clinical trials of SLN biopsy.

Fig.2.42 shows three commercial hand-held cameras: CGC, CrystalCam and MiniCam II. **Fig.2.43** shows another two SFOV cameras, a hand-held (eZ-Scope) and an arm-mounted (Sentinella 102).

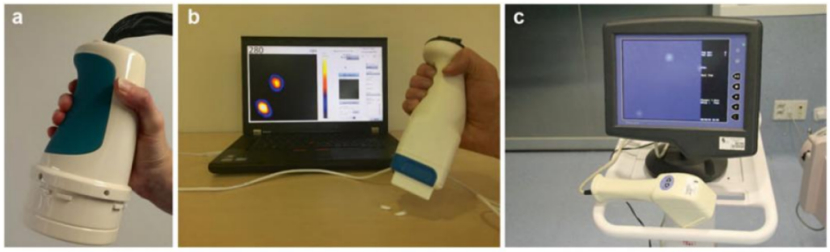

Figure 2.42: Photographs of three comercial hand-held SFOV gamma cameras. **a.** CGC, **b.** CrystalCam, **c.** MiniCam II. The image was taken from [97].

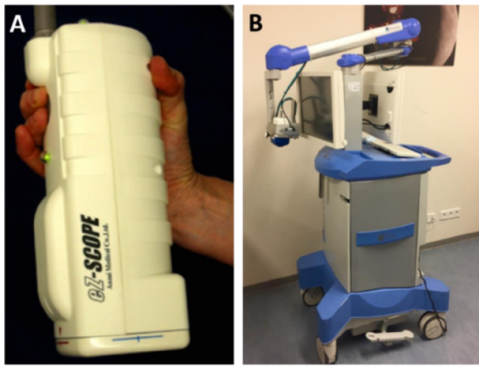

Figure 2.43: Photograph of a hand-held (eZ-Scope) and of a arm-mounted (Sentinella 102) SFOV gamma cameras. **Left:** eZ-Scope, **Right:** Sentinella 102. Image taken from [140].

* * *

Table 2.3 summarizes the performance of a set of SFOV gamma cameras, the majority of which were presented in this section. The performance of the two versions of the gamma camera prototype developed in this work (**section 6.1.1**) is also included (the cameras are named as *GAGG prototype* and *LYSO prototype*).

It should be noted that semiconductor based gamma detectors can generally offer better energy resolution than scintillators based detectors (e.g. from **table 2.3**: Tsuchimochi, Ge(Haifa), CrystalCam, MiniCamII). High energy resolution is often a requirement, because a good resolution allows discrimination of events not belonging to the photopeak. With statistical reconstruction, however, high energy resolution is not needed for the events discrimination, because SR can be achieved comparing the sum over all sensors of the difference between the sensor signal and the expected signal for the reconstructed position (*chi-square*). Scintillator

based cameras are a cost-effective solution and they offer a γ-rays collection efficiency one order of magnitude higher than that of semiconductors detectors at 140 keV. Among scintillators, the monolithic ones allow to collect more light and are less expensive than those with pixellated crystals (**section 2.2.2**).

Several cameras in **table 2.3** use CsI(Tl) scintillator due to its high light-yield (60 keV/ph) and good intrinsic energy resolution (5.2%). Moreover, CsI(Tl) is only slightly hygroscopic, while NaI(Tl) and $LaBr_3$ are highly hygroscopic, requiring airtight containers to protect them from the moisture. However, CsI(Tl) has a long decay time (1000 ns), which means more electronic noise collected by the readout system, with the consequent degradation of the signal-to-noise ratio (see **section 2.2.2**). Long readout time windows give also higher probabilities of reading pile-up events.

For the light collection, the use of SiPMs gives several advantages comparing with other light detection technologies (e.g. PSPMTs, CCD). SiPMs have high gain ($\sim 10^6$) and good quantum efficiency (up to 40%), require no high voltage (personal safety) and no cooling system, and they can be used in close proximity of equipment generating strong magnetic fields, as magnetic resonance imagers.

As regards the event reconstruction method, as in this work the event reconstruction should be fast (allowing real-time imaging) and a method to build a continuous model of the camera is available, k-NN approach was not considered. Additionally, the monitoring of the quality of the detector response model with the subsequent model reconstruction if the quality degrades was set as an objective. Rebuild a model given by an ANN would take significantly more time than that required by the adaptive algorithm. The continuous model obtained with the adaptive method can be used for very precise event reconstruction by SR methods, as maximum likelihood and least squares. Maximum likelihood (ML) was selected for the reconstruction of the scintillation events in this work, because the statistics on the number of collected photons can be described by a Poisson distribution.

An additional outcome of SR methods, namely ML, is the capability to reconstruct scintillation events that have occurred beyond the center of the most outer "ring" of sensors in the edges of the camera. CoG, for instance, cannot reconstruct events in these regions. For cameras with small FOV that possibility means a significant advantage. The drawback of SR is that it usually requires the knowledge of the source position to obtain the detector response model. This problem was addressed in this thesis by using an adaptive algorithm (see **section 2.6.1**) that is capable of building the model only from flood field irradiation data, offering to the camera a self-calibration capability.

The gamma camera developed in this work should be compatible with the features described above, namely, it should allow 1) the usage of fast statistical reconstruction to allow

real-time imaging, 2) the monitoring of the model quality and 3) the application of the self-calibration method, which highly relies on the parameterization of the light response functions (see **section 2.6.1**). Other features that should be taking into account are the non-hygroscopy of the scintillator (e.g. LYSO, GAGG, BGO, YAG(Ce) are possible choices) and the possibility of use both a parallel-hole and a pinhole collimator in a interchangeable system. The details on the camera optimization are given in **section 3** and the prototypes design and characterization are presented in **section 6**.

Camera name (or researcher)	Detector type	FOV (mm^2)	Photosensors type	Energy resolution (140 keV)	Intrinsic spatial resolution (mm)	Extrinsic spatial resolution (mm)[a]	Collimator
GAGG prototype	Scintillator Monolithic GAGG:Ce	28×28	SiPM	29%	0.90	1.57 @ 5.8 mm	Parallel-hole
						3.90 @ 50 mm	Parallel-hole
						1.65 @ 47 mm	Pinhole ($M^b = 1$)
LYSO prototype	Scintillator Monolithic LYSO:Ce	28×28	SiPM	29%	0.72	1.48 @ 5.8 mm	Parallel-hole
						3.90 @ 50 mm	Parallel-hole
						1.65 @ 47 mm	Pinhole (M = 1)
Nakanishi GAGG [141]	Scintillator Pixelated GAGG	20×20	SiPM	23% (122 keV)	0.5	-	
Nakanishi LYSO [141]	Scintillator Pixelated LYSO	20×20	SiPM	30% (122 keV)	0.6	-	
Fujita [142]	Scintillator Pixelated GAGG:Ce	10×10	SiPM	14% (122 keV)	0.48	-	-
Goertzen [143]	Scintillator Pixelated CsI(Tl)	13.2×13.2	SiPM	40.2% (122 keV)	-	6.24 @ 50 mm	LEHR
Deprez [46]	Scintillator Monolithic LYSO:Ce	49×49	PSPMT	21.3%	0.93	-	-
Sentinella 102 (Oncovision) [144]	Scintillator Monolithic CsI(Na)	40×40	PSPMT	13%	2.0	∼9 @ 50 mm	Pinhole
CGC (Univ. Leicester) Bugby [14]	Scintillator Pixelated CsI(Tl)	40×40	EMCCD	58%	0.63	1.28 @ NI[c]	Pinhole
CarollReS Mathelin [145]	Scintillator Monolithic GSO:Ce	50×50	PSPMT	45%	3	10 @ 50 mm	Parallel-hole
Olcott [146]	Scintillator Pixelated NaI(Tl)	50×50	PSPMT	12.1%	1.8	1.8 @ 60 mm	Parallel-hole
2020tc imager MiniCam II [147]	Scintillator Pixelated CsI(Tl)	212×212	SiPM	14%	-	18 @ 150 mm	LEAP[d]
Popovic [139]	Scintillator Monolithic LaBr3	60 mm diameter	SiPM	21%	4.2	10.3 @ 50 mm	Parallel-hole 1mm hole
IP-824	Scintillator Monolithic CsI(Tl)	36×36	PSAPD	7%	0.9	-	
Guardian 2 [148]	Scintillator Pixelated CsI(Tl)	44×44	PSPMT	20%	-	-	
HiReSPECT (Moji) [149]	Scintillator Pixelated CsI(Tl)	46 × 89	PSPMT	19%	≈2.0	3.5 @ 50 mm	LEHR
Jong-Ho Kim [150]	Scintillaor Monolithic NaI(Tl)	60 × 60	PSPMT	12.9%	≈3.1	3.5/3.9 @ 0 mm	Parallel-hole/Diverging
eZSCOPE [151]	Semiconductor Pixelated CZT	32×32	-	9.0%	-	8.0 @ 50 mm	LEHR
Tsuchimochi [152]	Semiconductor Pixelated CdTe	44.8×44.8	-	7.8%	1.56	6.3 @ 50 mm	Parallel-hole squared hole
GE (Haifa)	Semiconductor Pixelated CZT	40×40	-	8.0%	-	5.0 @ 50 mm	Parallel-hole
CrystalCam [153]	Semiconductor Pixelated CZT	40×40	-	7.0%	-	5.4 @ 35 mm	LEHR
MiniCam II Eurorad [154]	Semiconductor Pixelated CdTe	40×40	-	5-7%	2.46	-	

Table 2.3: Performance parameters of several SFOV gamma cameras.

[a]The extrinsic resolution is given for a specified distance source-to-detector.

[b]M is the magnification factor.

[c]NI: "No information" given by the authors on the source-detector distance used to measure the extrinsic spatial resolution.

[d]LEAP stands for "low energy all-purpose" parallel-hole collimator.

3

Simulation and Optimization

To achieve the optimal performance of a camera for a certain budget, the components should be carefully selected, considering their physical properties, dimensions and costs. One of the objectives of this work is to optimize the design of a compact gamma camera through simulations. The design should result in a camera that at the same time permits to: 1) successfully apply the adaptive algorithm presented in **section 2.6.1**, 2) optimize the efficiency of scintillation light collection 3) achieve intrinsic spatial resolution of 1 mm or better and 4) have a useful field-of-view (FOV) that covers the SiPMs array until at least the half of the most outer "ring" of SiPMs. In traditional center-of-gravity reconstruction, this is the best FOV commonly achieved. With this minimum requirement on the FOV, the optimization will be performed in order to achieve the best spatial resolution and the lowest level of distortions.

In this work a gamma camera detector was simulated in order to evaluate its performance for different designs and parameters selection. For instance, 1) to find the lightguide thickness that results in the best trade-off between spatial resolution and level of distortions within the camera FOV and 2) to study the performance of statistical reconstruction methods for gamma cameras.

3.1 Compact gamma camera design and components selection

3.1.1 Specifications of the proposed compact gamma camera

The target imaging objects of the camera studied in this work are small organs, either for clinical (e.g. sentinel lymph nodes, thyroid, prostate) or pre-clinical studies (e.g. mice brain and heart). To be better suited for small organ molecular imaging, cameras of reduced size, when compared with the conventional 500 mm diameter cameras, were developed in the last two decades, as presented in **section 2.7**. They are commonly known as small field-of-view (SFOV) gamma cameras.

The **table 3.1** summarizes the specifications defined in this work for the small gamma camera system. They are based on the features of several of SFOV cameras dedicated to sentinel node detection and thyroid scintigraphy. The target values for the main performance parameters are listed.

Compact camera feature		Requirement
Energy detection		122 keV and 140 keV
Intrinsic Efficiency		> 80%
Photosensor type		SiPM
Scintillator	Type	Monolithic or Pixelated
	Face area	50 × 50 mm^2
	Hygroscopic	No
Intrinsic energy resolution	(@120 keV)	<25%
	(@140 keV)	<20%
Uniformity[a]		>90%
Spatial linearity (UFOV)	Absolute	< 0.35 mm
	Differential	< 0.2 mm
Useful FOV		48 × 48 mm^2
Readout type		Individual mode
Intrinsic spatial resolution		<= 1 mm
Extrinsic spatial resolution	Pinhole coll. (@50 mm)[b]	< 2 mm
	Parallel-hole coll. (@50 mm)[c]	< 5 mm
Acquisition rate		up to 10 kHz
Sensitivity (extrinsic)		100 cps/MBq

Table 3.1: Requirements of the compact gamma camera

[a] In this work the uniformity it is given as the percentage of uniformity, rather than the percentage of non-uniformity, as it often occurs.

[b] Total distance source-to-pinhole plus pinhole-to-detector and no magnification.

[c] Source-to-collimator distance.

The objective of the work was to optimize the performance parameters of a SFOV camera, starting by computational simulations. Afterwards, to experimentally confirm the camera performance, a prototype was assembled and characterized (**section 6**). Due to budget restrictions in the purchase of the camera components[1], the size of the camera to be optimized was set to be equal to the size of the SiPMs array already available in the group: 33.2 × 33.2 mm^2. A camera prototype of that size is sufficient for research purposes, although not adequate for some molecular imaging exams, when using a parallel-hole collimation. It allows, however, to characterize the performance of a real camera, that can be further built with a larger detection area, which fits the size required for pre-clinical and clinical studies.

[1] The more expensive components are the scintillator crystal and the array of photosensors.

Research SFOV camera specifications Although the main goal of the envisioned SFOV camera was to be used for clinical and pre-clinical applications, it was also designed having in mind its application in research context. In fact, the prototype used for the validation of the clinical camera design will be later used for other studies in the university laboratory where it was first tested. This laboratory will take advantage for research works not only of the basic gamma camera structure, but also of the developed workbench and the in-house implemented data processing and reconstruction software. For instance, different scintillators can be coupled to the array of SiPMs to study their properties and gamma radiation data can be recorded with the camera to build research datasets to test reconstruction algorithms and calibration procedures.

The specifications of the SFOV camera studied with research purposes are the same as those summarized in the **table 3.1**, except the dimension of the crystal, that affects the useful field-of-view (UFOV). As typically the reconstruction is worse near the camera borders, I had the objective of reach an UFOV of 28 × 28 mm^2 out of the total crystal area of 33.2 × 33.2 mm^2.

In case of compact cameras, SiPMs offer several advantages over photomultiplier tubes, such as lower operating voltage (two orders of magnitude below than PMTs), compactness, immunity to magnetic fields and robustness.

Three reasons, however, have contributed for the SiPM choice over PMTs, having the secondary usage for research in perspective: 1) personnel safety, because high-voltage is not required, 2) robustness, as SiPMs do not break so easily on fall and do not got damaged on accidental excessive light exposure and 3) easiness of calibration, as the signal per photoelectron can be easily obtained from the photoelectron peak positions in the pulse height spectra. Also, the results obtained with data recorded with SiPM can be easily extrapolated to data that would be obtained with PMTs, for example in the estimation of light response functions.

In clinical examinations, namely sentinel node detection, the event rate is not expected to exceed 1 kHz, because the uptake by the sentinel node is at maximum a few percent of the injected dose. However, to reduce time required for calibration, a higher acquisition rate is strongly advised, thus 10 kHz was defined as the target acquisition rate in a sustainable individual mode readout of 64 channels (**section 2.3.2**). The sensitivity of the camera for parallel-hole collimator usage should reach 100 cps/MBq. This sensitivity is compatible with the minimum acquisition rate of 10 kHz for sentinel node detection exams. Even the maximum activity of ∼37 MBq (1 mCi) used in injected dose studies [155, 156] would result in a rate of 2.5 thousand γ-rays reaching the crystal per second (2.5 kHz), assuming 100% uptake.

3.1.2 Compact camera geometry and components

Fig.3.1 depicts the typical geometry of a compact gamma camera which comprises an optical part with the four main layers (array of SiPMs, lightguide, scintillation crystal and reflector) optically coupled with thin layers of optical grease, and a collimator.

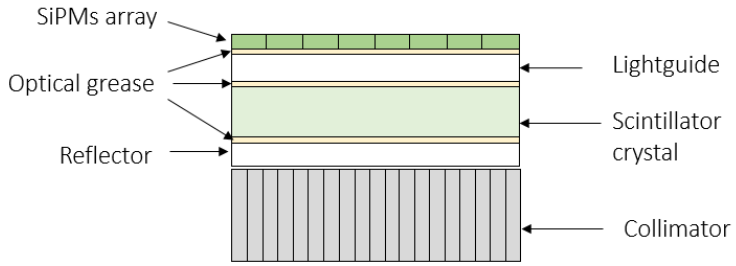

Figure 3.1: Compact camera typical geometry. The scheme represents a gamma camera with a parallel-hole collimator attached. The dimensions are not to scale, rather they serve for clarity purposes (the optical grease layer, for instance, has a thickness of ∼0.1 mm, while the lightguide is ∼1 mm thick).

The optimization of the camera was performed in two stages: 1) optimization of the optical part of the camera in terms of the intrinsic spatial resolution and the level of distortions and 2) optimization of the system spatial resolution and the γ-ray detection efficiency for the complete system, with the collimator. In the following, each component of the compact camera is discussed, with the focus on the defined specifications, existing constraints and parameters to optimize.

Scintillator crystal The scintillator has the important function of converting the energy of γ-rays into light. It should be selected according to the desired camera performance, in conjunction with the photosensor detection features. The scintillator γ-rays absorption efficiency should be maximized without compromising other performance parameters, as the spatial resolution. A thicker scintillator would have higher efficiency but also worst resolution due to larger fluctuations of the depth of γ-ray interaction, which results in a larger number of events for which the SiPMs light responses are far from the light responses given by the model. Additionally, scintillators without intrinsic radioactivity are preferred.

The collection of the light emitted by a scintillation event should be maximized, to improve the spatial resolution. Depending on the energies of the γ-rays (122 keV and 140 keV in this work), the scintillator light yield (photons per energy keV) should be sufficient for the emission of the amount of light required for the good performance of the reconstruction methods. However, not all the emitted light is registered by the photosensors. To maximize the measured signal, the overlap between the scintillation emission spectrum and the photosensors photon detection efficiency should be maximized. Reflections should be minimized in the interface

between the scintillator and the lightguide in the light path to the photosensors. Usually scintillators have high refractive index. The lower the index, the better the coupling with the lightguide, usually made of glass (n≈1.5). From the side of the acquisition system, the decay time of the scintillation should be not too long to not compromise the acquisition rate and to minimize the dark counts (**section 2.2.4.2**) in the data acquisition window.

In respect to mechanical properties, the crystal should be monolithic, rather than an array of smaller columnar crystals. The adaptive algorithm for LRFs estimation developed in the laboratory works only with data from gamma cameras using monolithic scintillators, as it relies on simultaneous measurement of the scintillation signal by several photosensors (**section 2.6.1**). Besides this, monolithic crystals are simpler to handle and mechanically resistant. A non-hygroscopic crystal is also desirable, because it does not need any encapsulation, so its application is more flexible. The area of the crystal face should cover the detection window formed by an array of 8 × 8 squared SiPMs, each one with an area of 3 × 3 mm^2. That array of SiPMs has a total area of 33.2 × 33.2 mm^2 and was already bought by the group.

The choice of the crystal ultimately depends on the options available on the market, including the sizes viable to be manufactured and would fall on the most cost-effective solution (features, price and lead time). In the **table 2.1** are listed some of the most used scintillators in nuclear medicine at the time of this work. LYSO was selected as the scintillator for the studies on the validation of the simulation model (**section 3.2.4**). However, LYSO has two important limitations: 1) intrinsic radioactivity [47] and 2) light-yield dependence on energy (non-linearity) [157]. The intrinsic radioactivity comes from the ^{176}Lu radioactive isotope, which has a beta decay emission followed by a cascade of gamma decays (307 keV, 202 keV, 88 keV). The radioactive decay is represented in the diagram of **Fig.3.2**. The expected activity from ^{176}Lu radionuclide for a 33.2 × 33.2 × 2 mm^3 LYSO crystal[1] was estimated as 390 Hz, considering the half-file measured by [158] using γ-ray spectrometry.

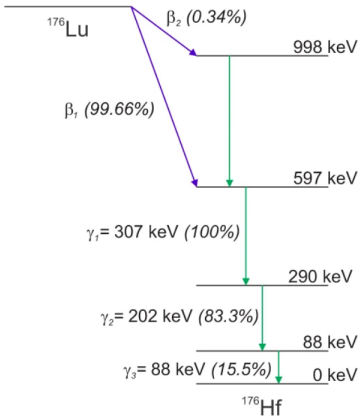

Figure 3.2: Simplified ^{176}Lu decay diagram. The image was taken from [47] .

[1] A 33.2 × 33.2 × 2 mm^3 LYSO crystal was already available in the group.

The GAGG scintillator is a possible alternative to LYSO. Compared to LYSO, GAGG has a smaller gamma detection efficiency in the energy region of interest, so requires a crystal of about 1.5 times larger thickness to achieve the same efficiency as a LYSO crystal. GAGG emission spectrum does not match very well the sensitivity curve of the SensL SiPMs used in this work, resulting in a similar response to γ-rays, despite having much higher light yield than LYSO. Nevertheless, it was considered that the absence of intrinsic radioactivity and a better energy resolution than LYSO justify the use of GAGG in the SFOV gamma camera.

SiPMs When selecting the SiPMs for a gamma camera, the photon detection efficiency is one of the first parameters to consider. The overlap between the photon detection efficiency spectrum and the scintillator emission spectrum should be maximized. Additionally, the dark count rate should be as low as possible. Dark noise cannot be neglected when it is comparable with the total number of detected photons in the SiPM (e.g. around 10%). The important properties of SiPMs were discussed in **section 2.2.4.2**.

In order to be able to compare the behavior of a simulated detector with that of a real camera, the modelling of the SiPMs should follow the specification of commercially available sensors. Some of the most relevant SiPM manufactures are Hamamatsu, SensL and Fondazione Bruno Kessler (FBK). By 2016, SensL had the SiPMs with the lowest level of dark counts (30 kHz/mm^2 at an overvoltage ΔV = 2.5 V, e.g. model 30035 of C-series) [159]. Although Hamamatsu some time later released the model S13361-3050NE-08 with dark count rate of the same order (50 kHz/mm^2 at ΔV = 3.0 V) [160] as the SensL 30035, it was significantly more expensive, as for the FBK model with the lowest dark count rate at 2016, which was 50 kHz/mm^2 at ΔV = 2.0 V (FBK NUV-SiPM model) [161].

Fig.3.3 shows the photon detection efficiency spectrum of the SiPMs from the three manufacturers, as well as the emission spectrum of LYSO and GAGG. The effective PDE, PDE_{eff}, which is the photon detection efficiency weighted by the crystal emission spectrum, is used for not wavelength-resolved simulations, rather than the PDE spectrum peak. Both the crystal emission spectrum $S(\lambda)$ and the PDE spectrum $PDE(\lambda)$ of the SiPMs are needed to calculate the PDE_{eff}:

$$PDE_{eff} = \frac{\int PDE(\lambda) \times S(\lambda) d\lambda}{\int S(\lambda) d\lambda} \tag{3.1}$$

Table 3.2 presents the PDE_{eff} for the three SiPMs models considered in this study, weighed by both LYSO and GAGG emission spectra. FBK and Hamamatsu SiPMs have the highest PDE_{eff} for LYSO (35.3%) and for GAGG (33.0%) light detection, respectively. However, the SensL model, among the three alternatives, was the most cost-effective solution: the cheaper one, with the lowest dark count rate and a detection spectrum compatible to

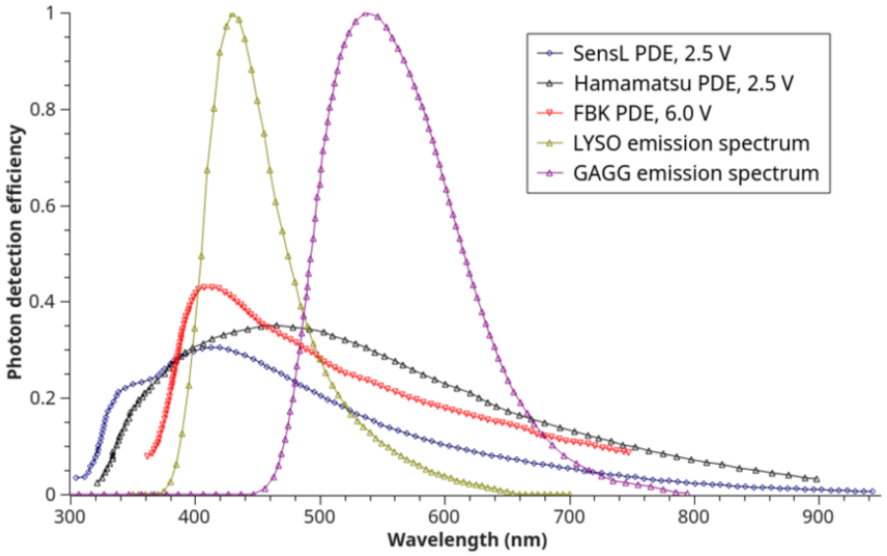

Figure 3.3: Photon detection efficiency spectrum of SiPMs from three manufacturers overlapped with the emission spectrum of GAGG and LYSO. SiPM models: SensL 30035 (dark blue), Hamamatsu S13361-3050NE-08 (black) and FBK NUV-SiPM (red).

work with either the LYSO and GAGG crystals, although the PDE_{eff} is not so good as for Hamamatsu and FBK sensors. The PDE_{eff} for LYSO is ∼25% and for GAGG ∼14% when the SensL SiPMs working overvoltage is $\Delta V = 2.5$ V. Our group have acquired SiPMs of the model 30035 from SensL, which are modeled in our simulation software (**section 3.2.3.2**).

SiPM manufacturer	PDE_{eff}, % (LYSO)	PDE_{eff}, % (GAGG)	Overvoltage (V)
SensL	25.8	13.9	2.5
Hamamatsu	33.0	26.8	2.5
FBK	35.3	21.4	6.0

Table 3.2: Effective PDE of SiPMs from three manufacturers weighed by LYSO and GAGG emission spectra.

Lightguide A lightguide material couples the scintillator and the array of photosensors, creating a distance between them, given by its thickness. Lightguide is traditionally used in gamma camera design to improve linearity of CoG-reconstructed images, as a consequence of a more even distribution of the light emitted from the scintillator to the photosensors array. In case of statistical reconstruction, the role of the lightguide in linearization is less important, while there is notable degradation in the spatial resolution with increase of the lightguide thickness. Another point to consider is that a thicker lightguide can reduce dependence of LRF shape on DoI and improve the convergence of LRF reconstruction.

On the other hand, if the SiPMs array is larger than the crystal, lightguide of the same size as the array is used, for better coupling. The most important parameters of the lightguide are

the thickness, which was optimized by simulations (**section 3.3.3**), and the refractive index, defined by the material choice (typically glass or plexiglass, with indexes ≈1.5).

Reflector To improve light collection, a reflector is usually attached to the crystal, in the opposite side of the array of photosensors. The improvement in light collection leads to improved spatial and energy resolutions. The reflector thickness must be kept as low as possible as the increased distance between the crystal and the collimator can degrade the collimator resolution. One material which is typically used as reflector is Teflon, because it has very high reflectivity which, however, is only achieved for a rather thick layer (∼1 mm). Another possible option is aluminium, with mostly specular reflection, which results in less broad light scattering. Other alternative would be to use a thin Teflon layer followed by an aluminium foil.

Optical coupler Three optical interfaces exist in a typical gamma camera: crystal – lightguide, lightguide – photosensor window and crystal – reflector. Optical grease is used to enhance the optical coupling by eliminating the air gaps between optical surfaces. The key parameter of the optical grease is its index of refraction n. Grease with $n \approx 1.5$ is normally chosen to match as best as possible the index of refraction of the several gamma camera components, namely those of the scintillator and of the lightguide. However, to maximize the light transmission in the optical interfaces, an index close to the mean value between the indexes of the two components to be coupled should be used. A simulation study was performed to verify that an improvement in the light collection can be achieved by using for each interface an optical grease with refractive index in between those of the components to couple (**section 3.3.2**).

Collimator The type of collimator typically used for small organ imaging is the pinhole collimator [120, 162, 163, 164]. It offers the magnification possibility and increasing the distance from the aperture to the source, the useful FOV at the source place can be expanded (**section 2.2.1.2**). Comparative studies recommend pinhole for the imaging of specific organs, as for thyroid and parathyroid exams [165, 166, 167]. However, when increasing the distance from the source to collimator, the resolution deteriorates more for pinhole collimator than for parallel hole collimator [168], besides a stronger decrease in sensitivity. Parallel-hole collimators are being used in hand-held gamma cameras for the detection of sentinel lymph nodes [135, 139, 143]. The two collimators can be attached to the same single-head detector, one at a time, using a easy to handle switching mechanism or in a dual-system with two camera heads, each one with its collimator type [169].

3.2 Simulation tools and models

In general, the simulation process for a gamma camera can be subdivided in five stages listed below.

1. Emission and tracking of γ-rays until their escape or capture in the scintillator crystal or surrounding materials
2. Conversion of the γ-ray energy deposited in the scintillator crystal into the scintillation photons
3. Emission and tracking of scintillation photons until their detection in the photosensors, absorption or escape from the detector
4. Generation of photosensor signals based on the number of detected photons, dark noise and the properties of electronics and the data acquisition channel.
5. Event reconstruction from the acquired signals

Geant4, the well known toolkit for the simulation of interaction of particles with matter, can simulate the generation, emission and tracking of γ-rays until they are absorbed in the scintillator material or escape it. In the simulation of γ-rays interaction with matter, Geant4 takes into account the photoelectric, Compton and pair production effects and also accounts for three secondary effects: coherent scattering (also known as Rayleigh or elastic scattering), X-ray fluorescence and Auger electron emission (**section 2.1.1**).

When energy is deposited in the scintillator, Geant4 can generate light, simulating the scintillation process. The amount of emitted optical photons is proportional to the deposited energy. These photons can be tracked by Geant4. In the case of Anger type detectors, optical photons can 1) be absorbed inside the material they are crossing, 2) suffer reflections in interface between materials, 3) escape the detector or 4) can be detected by photosensors that can be also modeled in the simulation.

ANTS2, a software package developed at LIP-Coimbra [94], can also perform the processes referred before. However, it must be highlighted that ANTS2 cannot simulate the γ-rays interaction with matter in the same detail as Geant4. ANTS2 does not simulate the emission of secondary γ-rays and Auger electrons. ANTS2 has the tools to add dark noise and electronic noise to the simulated recorded photosensor signal. Moreover, ANTS2 has also already implemented the algorithm for LRFs estimation and the reconstruction of scintillation event positions and energy used in this work (**section 2.6.1**). ANTS2 has the additional advantage of providing tools for interactive detector design, with the possibility of exporting detector geometry and material description into GDML, a Geant4-compatible format [170]. Thus, I

used ANTS2 for the detector design and models configuration, Geant4 to simulate the emission and deposition of γ-rays in the scintillator and ANTS2 again to simulate the scintillation process in the positions where energy was deposited, and the subsequent light detection and reconstruction of event positions.

3.2.1 Geant4 toolkit

Geant4 is a comprehensive toolkit for the Monte Carlo simulation of particles interaction with matter. High energy, nuclear and accelerator physics as well as investigation in space science and medical devices are among the applications fields of this simulator. Geant4 is written in C++, exploiting the object-oriented paradigm [171, 172, 173].

The toolkit comprises modules for the distinct simulation processes: system geometry design, materials specification, generation of particles and tracking them through materials and electromagnetic fields, generation of several types of events (e.g. gamma and optical photons emission), calculation of the detector response, storage of events and tracks, post processing and visualization of particle trajectories and detection results and also the analysis of simulation data [174].

Because of the broad range of areas that take advantage of the toolkit, Geant4 supplies an extensive list of the relevant physics processes that handle different interactions of particles with matter for a wide energy range. The user has to activate the desired processes. For instance, for the simulations described in this section Geant4 was used to study the effects of the physical processes yet unavailable in ANTS2 toolkit (Rayleigh scattering, X-ray fluorescence and Auger electron emission) on the gamma camera performance. Thus, "QGSP_BIC_HP" standard physics list was used and three relaxation processes were activated, to be used for processes producing vacancies in atomic shells: fluorescence ("/process/em/fluo"), Auger effect, including Auger cascades ("/process/em/auger" and "/process/em/augerCascade") and particle induced X-ray emission ("/process/em/pixe"). Auger cascades are simulated as series of occurring vacancies in inner-shells of an atom, leading to multiple emission of Auger electrons. A range cut of 10 micrometers was set for secondary particles ("/run/setCut 0.01 mm") [175, 176, 177].

3.2.2 ANTS2 computational package: simulation tool

ANTS2 is a C++ open source and multiplatform package, developed at LIP-Coimbra using CERN ROOT and Qt frameworks. The package is intended for the following applications [94]:

- Optimization of detector design and geometry using Monte Carlo simulations
- Optimization and development of event reconstruction techniques

- Adaptive reconstruction of detector response using flood field illumination data
- Reconstruction and filtering of events from experimental data

Successful use of ANTS2 for simulation of a compact gamma camera with SiPM readout was demonstrated in [178] with a good agreement between simulations and experimental results. However, additional validation of the ANTS2 simulation results by comparing them with those from Geant4 was included into the plan of the current work. The average number of collected photons per event, the energy resolution and the spatial resolution will be the parameters to compare between the two packages.

ANTS2 has a scripting engine that I have used to automatize several routines and the gamma camera optimization cycle. The validation of ANTS2 as a software well suited for simulation and experimental data processing of Anger camera-type detectors was demonstrated in [94], [179] and [178]. For a comprehensive presentation of ANTS2 package please refer to [94].

Geant4 simulations called from ANTS2 As using Geant4 for simulating γ-ray interaction with matter permits to implement more realistic particle model than in ANTS2, the developers of the later package added the possibility of calling an external application to trace particles in Geant4[1]. **Fig.3.4** presents a diagram with data flow between ANTS2 and Geant4.

The camera geometry (in GDML format) is passed to Geant4 along with the chemical composition and density of all the materials specified in the ANTS2 detector model. The particles to simulate are supplied as a separate file, where the initial position, direction and energy are specified for each particle. Once the simulation of the requested number of events finishes in Geant4, the information on each deposition node per primary γ-ray is sent back to ANTS2, namely: the deposited energy and position (x, y, z) and the deposition time. Based on the received information and on the scintillator light yield, ANTS2 generates optical photons, simulates their tracing and counting of the photons that reach each SiPM.

3.2.3 Assumptions and models in ANTS2 simulations

Emission of γ-rays In this study, two γ-ray sources were simulated: ^{99m}Tc and ^{57}Co. The nuclide ^{99m}Tc is a metastable isomer of the Technetium isotope ^{99}Tc. Its half-life is 6.0067 hours, which allows it to be used for radiopharmaceutical (radiotracer) production, in conjunction with some biochemical tracer. **Fig.3.5** presents the decay scheme of ^{99m}Tc isotope.

[1] A dedicated software (called G4ants[2]) was developed in LIP-Coimbra as an interface between ANTS2 and Geant4 package. G4ants uses the Geant4 library directly. It is called by ANTS2, which sends the relevant simulation data and receives the resulting deposited energies and respective positions.

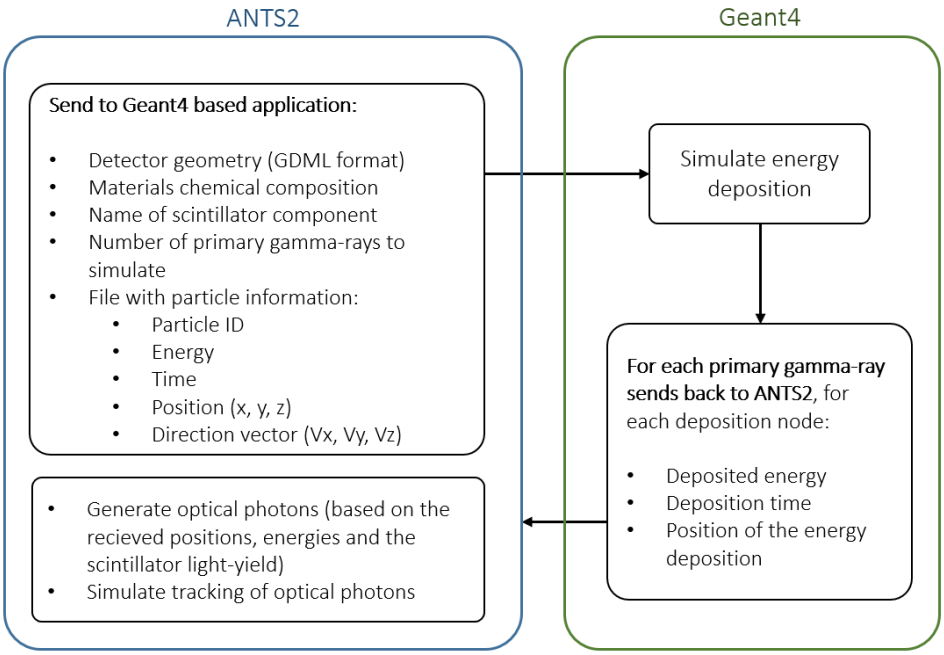

Figure 3.4: ANTS2 and Geant4 exchange of data scheme. **Left**: ANTS2, **Right**: Geant4.

The blue arrows indicate that the nucleus decays by β^- emission. The metastable state ^{99m}Tc decays by isomeric transition (IT). The metastable state at 143 keV decays initially to the 2 keV deeper-lying level at 141 keV. The most important transition is from the 141 keV level to the ground state with the emission of a 141 keV γ-ray. As an alternative to this transition, a weak emission of conversion electrons is observed ($\alpha_T = 0.113$). Direct transition from the 143 keV level to the ground state also occurs, with low probability [180, 181]. Emissions from the decay product, ^{99}Tc, can be safely ignored in the simulations due to its much longer half-life of 2.1×10^5 years.

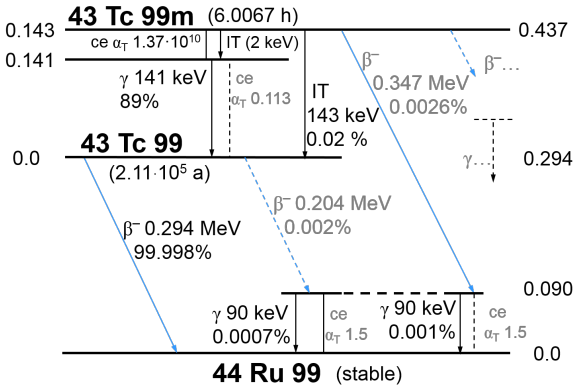

Figure 3.5: Reduced decay sheme of the isotope ^{99m}Tc. The figure was taken from [181].

The ^{57}Co nuclide is radioactive with an half-life of 271.80 days, which makes it well suited

for experiments in laboratory. **Fig.3.6** presents the decay scheme of ^{57}Co isotope. The red arrow indicates that the nucleus decays by electron capture (ϵ). The most probable transition of the ^{57}Co nuclide is to an excited state of ^{57}Fe at 136 keV, through electron capture. The nuclide de-excites from this level by emitting either 122 keV (85.51%) and 14 keV (9.15%) γ-rays consecutively or directly 136 keV γ-rays (10.71%) leading to the ground state of ^{57}Fe. The fact that ^{57}Fe is stable guarantees the absence of posterior decays [182, 183]. **Table 3.3** lists the energy weights of the two isotopes used in simulations, ^{57}Co and ^{99m}Tc.

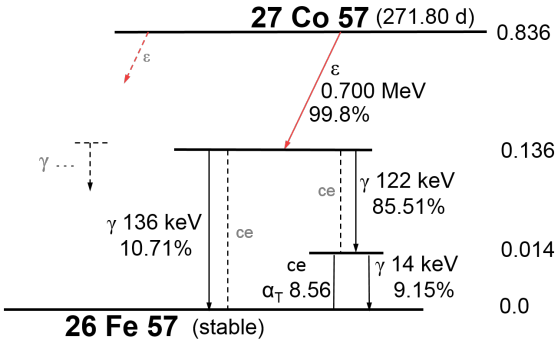

Figure 3.6: Reduced decay scheme of the isotope ^{57}Co. The figure was taken from [182].

Isotope	Energy (keV)	Statistical weight (normalized to unit)
^{57}Co	122	0.889
^{57}Co	136	0.111
^{99m}Tc	141	0.986
^{99m}Tc	143	0.014

Table 3.3: ^{57}Co and ^{99m}Tc energies statistical weights used in ANTS2

In ANTS2 a γ-ray source is defined by specifying its geometry and position as well as its emission lines with corresponding probabilities. To improve simulation efficiency, the collimation direction of the emitted particles (with a specified maximum emission angle - cone opening) can be specified as well.

Gamma-rays propagation and interaction with matter In ANTS2 simulation, γ-rays propagate through detector geometry in a straight line until they undergo photoelectric capture, Compton scattering or pair production. For each crossed volume, the path length to each process is randomly sampled from the exponential distribution with the mean free path (MFP) for the corresponding interaction as a parameter and the shortest path is selected. If the interaction point lays within the volume in question, the interaction occurs, otherwise propagation continues through the next volume. ANTS2 uses data imported from NIST XCOM database [16] to calculate the MFP.

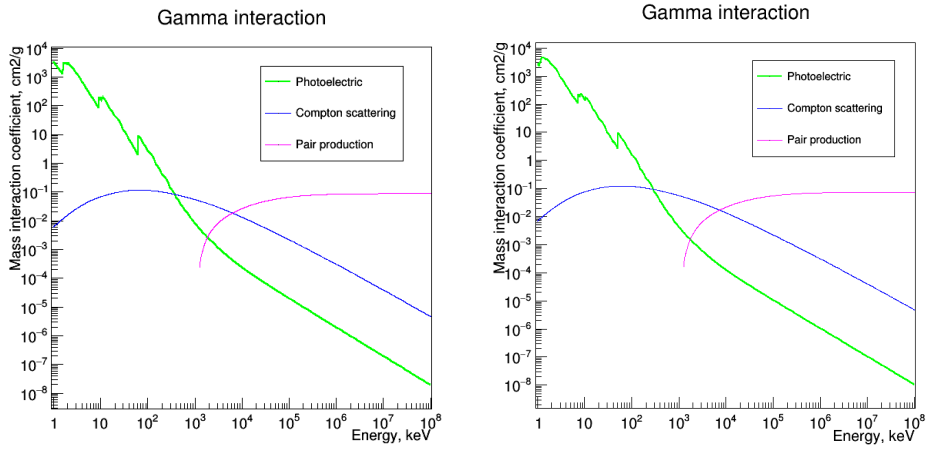

(a) **(b)**

Figure 3.7: Mass interaction coefficient (cm^2/g) of two scintillation crystals **a.** LYSO:Ce **b.** GAGG:Ce.

The thicknesses of the crystals were selected according to the desired γ-rays detection efficiency. Below the properties of the simulated crystals (LYSO and GAGG) relevant for its interaction with γ-rays are presented. The same is done for tungsten carbide (WC) and pure tungsten (W), the materials used for collimators, both in simulations and experimental measurements.

- **LYSO:Ce γ-rays interaction properties**

  As the exact LYSO chemical composition can vary depending on the manufacturer, the simulations used the composition of the crystal employed in our experimental studies (Prelude420^{TM} from Saint-Gobain), namely $Lu_{1.8}Y_{0.2}SiO_5$ doped with 0.5% (molar) of cerium (Ce). The crystal density is 7.1 g/cm^3. **Fig.3.7 a** presents the LYSO mass interaction coefficient. The total attenuation without coherent scattering (thus, accounting for photoelectric effect and Compton scattering) is 1.2 cm^2/g for 140 keV.

- **GAGG:Ce γ-rays interaction properties**

  Also for GAGG, the chemical composition varies with the vendors. I have used the composition of the crystal used in the experimental work, which was supplied by Kinheng Crystal Material Co. (Shanghai): $Gd_3Al_2Ga_3O_{12}$ doped with 0.5% (molar) of Cerium (Ce). The GAGG crystal density is 6.63 g/cm^3. **Fig.3.7 b** presents the mass interaction coefficient of GAGG:Ce. The total attenuation of GAGG without coherent scattering is 0.72 cm^2/g for 140 keV.

- **γ-rays interaction properties of collimator materials**

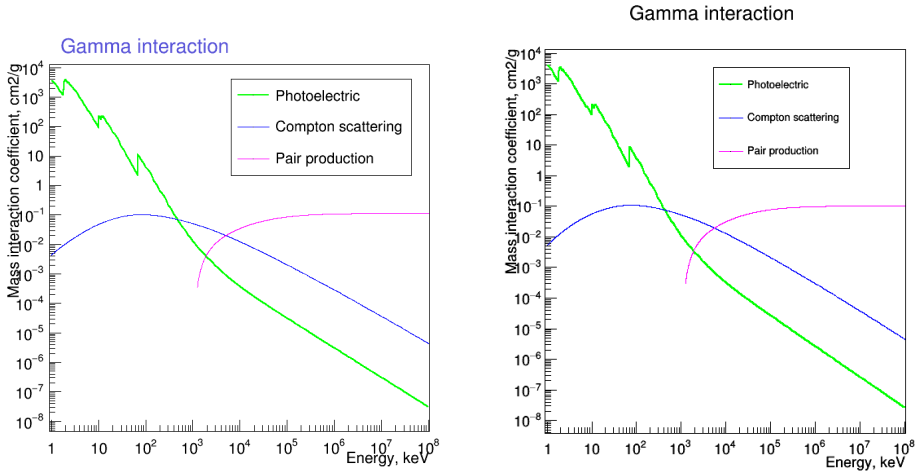

(a) **(b)**

Figure 3.8: Mass interaction coefficient (cm^2/g) of two highly γ-rays absorptive materials **a.** Tungsten (W) **b.** Tungsten carbide (WC) doped with Cobalt (Co).

One of the collimators used in simulations and experimental work (of parallel-hole type) is made of pure Tungsten (W). The other, of pinhole type, is made of an alloy of 94.5% of Tungsten carbide (WC) and 5.5% of Cobalt (Co). The mass interaction coefficients for W and WC are presented in **Fig.3.8**.

3.2.3.1 Conversion of the deposited γ-rays energy into scintillation photons

The average number of emitted scintillation photons is typically found multiplying the deposited energy by the scintillator light yield. However, for some crystals, the light-yield is not constant for all energies. Some years ago, the non-linearity in the LYSO light output has been reported, for instance by Pidol *et al.* [184] and Swiderski *et al.* [157]. From those measurements, for ≈125 keV the light yield is ≈0.85 that at 662 keV (^{137}Cs). Based on this data and the LYSO light yield of 32 ph/keV reported by manufacturer for 662 keV, the light yield for 140 keV was estimated to be 27.2 ph/keV.

The manufacturer of the GAGG:Ce crystal reports light yield of 50 ph/keV for 662 keV. As the non-linearity factor for 140 keV is 0.92 according to recent studies [51, 185, 186], the light yield of the GAGG:Ce crystal was estimated to be 46 ph/keV.

3.2.3.2 Emission, propagation and "end-of-life processes" of scintillation photons

For each energy deposition in a scintillator, the scintillation process is simulated as described below. Light is emitted isotropically, randomly sampling the direction of each photon in 4π and randomly sampling the wavelength weighted by the scintillator emission spectrum. The number of emitted photons is given by the product of light yield and the deposited energy.

The photon path length is randomly sampled from an exponential distribution with mean free path calculated from the bulk attenuation coefficient of the material. According to the path length and the photon direction, it is verified if the photon crosses the material interface towards another material. If not, the photon is considered to have been absorbed. If the photon reaches an interface between materials, two options exist: either Fresnel and Snell laws are applied (**section 2.1.3**) or a custom optical rule ("override") is applied, presented further on. In the first case, to simulate the processes in the interface between materials, the incidence angle is calculated and it is used in Snell's equation to calculate the transmission angle. These two angles and the materials refraction coefficients are used to calculate the reflection probability according to Fresnel equations, which will define the probability for the photon to be transmitted to the second material. If the photon is refracted, the propagation continues through the next volume until eventually the photon is absorbed in its path, reaches some photosensor or escape the detector. When the photon arrives to the photosensor from the lightguide coupled with optical grease, it enters the epoxy material, following Fresnel rules between the grease and the epoxy. The optical properties of silicon SiPM surface are not disclosed by the manufacturer (being regarded as a trade secret), so it was assumed that photons which enter the photosensor through the epoxy layer are detected with the probability equal to the sensor photon detection efficiency (PDE) for its wavelength. For not wavelength-resolved simulations, the effective PDE calculated according to **Eq. 3.1** was used. For wavelength-resolved simulation the dispersion curve (index of refraction *vs* wavelength) of all camera materials that interact with light must be known.

Table 3.4 lists the wavelength-independent optical properties of all materials considered in the gamma camera model.

Material	Density (g/cm^3)	Refractive index	Attenuation coefficient (mm^{-1})	Dispersion curve available?
Air	1.20×10^{-3}	1.00	0.0	-
Acrylic	1.19	1.50	0.0	Yes
LYSO:Ce	7.1	1.81	4.8×10^{-3}	Yes
GAGG:Ce	6.63	1.91	5.0×10^{-3}	Yes
Epoxy	1.3	1.59	0.0	Yes
Optical grease	1.3	1.47	0.0	Yes

Table 3.4: List of material wavelength-independent optical properties and density.

Custom rules in materials interfaces: *overrides* Before describing the optical properties of the gamma camera components assumed in ANTS2, the *override* concept of ANTS2 must be presented. When an *override* is defined in the interface of two materials it means that some other optical rule will override the Fresnel law in that interface. By other words,

custom rules are defined for the optical processes in some materials boundaries. For the simulations studies presented further ahead (**section 3.2.4**), the used overrides are referred in the respective sections.

LYSO and GAGG optical properties The simulation used the optical properties of LYSO and GAGG listed in the **table 3.4**. The emission spectra of both crystals was simulated from the curves shown in **Fig.3.3**. As the GAGG manufacturer did not provide its emission spectrum, one that was reported in [50] was used. I have calculated the absorption spectrum based on the data that the authors of [50] sent me on their published absorbance and transmission curves, as well as the sample thickness for the two measurements. **Fig.3.9** presents both the emission spectrum and the absorption spectrum of GAGG.

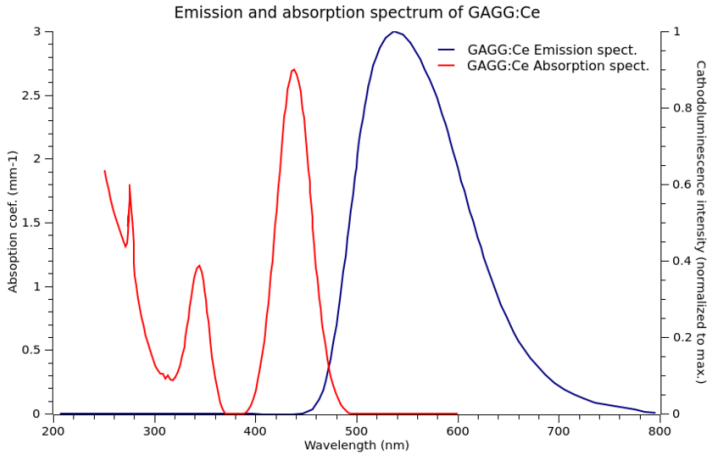

Figure 3.9: GAGG:Ce emission spectrum and absorption spectrum. Red: absorption spectrum; Blue: emission spectrum.

The dispersion curve of LYSO:Ce, provided by the manufacturer is depicted in **Fig.3.10 a**. **Fig.3.10 b** depicts the GAGG:Ce dispersion curve. A Sellmeier curve was fitted to three index of refraction points kindly sent by other vendor of GAGG crytals (Furukawa Co.) for three wavelengths: 485.9 nm (n = 1.9336), 587.1 (n = 1.9191) and 656.3 (n = 1.9128).

Optical coupling The optical coupling material was an optical grease (Saint Gobain BC-630) with index of refraction quoted by the manufacturer as n = 1.465, close to the index of the plexiglass (n = 1.49). However, Saint Gobain does not specify the exact wavelength, so a sample was sent to Metricon company, which measured the index for four wavelengths: 448.2 nm (n = 1.4767), 532 nm (n = 1.4677), 632.8 nm (n = 1.4615) and 826.7 nm (n = 1.4558). Then, a Sellmeier curve was fitted to that data. The dispersion curve can be seen in **Fig.3.11 c**.

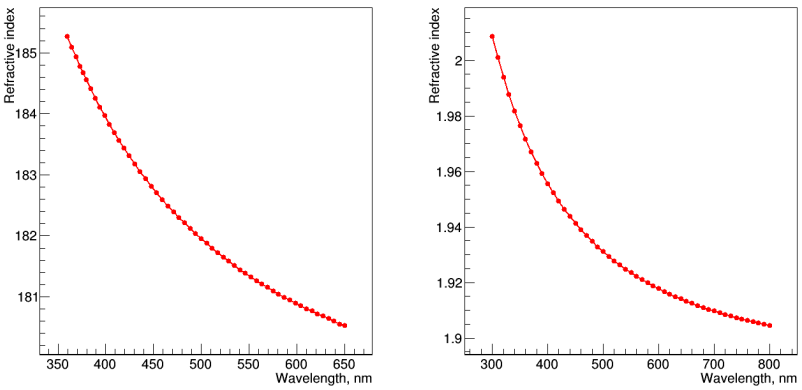

(a) **(b)**

Figure 3.10: Dispersion (refractive index *vs* wavelenght) curves of LYSO and GAGG crystals **a.** LYSO:Ce **b.** GAGG:Ce.

Lightguide acrylic The lightguide material is plexiglass to allow the light to propagate into the array of SiPMs. The plexiglass density is 1.18 g/cm^3 and its index of refraction is 1.49 (λ = 590 nm).

Crystal lateral sides covering: reflective and black materials The main sides (those facing the SiPM array and the reflector) of the scintillator used in experimental work are polished, but the lateral sides are unpolished or "ground" (**section 6.1.1**). A black ABS plastic was applied as wrapping material in the lateral sides of the scintillator to simulate low reflectivity. In the design of the geometry of the camera, a thin layer of optical grease (0.1 mm) was added to the lateral sides of the crystal, followed by a layer of the black plastic. The thickness of those layers is not important for the simulation, once overrides are applied in their interface with the optical grease.

Teflon Reflector PTFE (Teflon) can be considered an ideal diffuse reflector [187, 188, 189, 190]. Consequently, an override between the optical grease and Teflon was defined so that Teflon scatters back 95% of the incident photons, following Lambert's emission law [187, 190]. The remaining 5% of the photons are absorbed.

SiPMs epoxy resin All around the silicon, the photosensors have an epoxy resin. The epoxy has a density of 1.3 g/cm^3 and an index of refraction n = 1.57. The dispersion curve was provided by the manufacturer. The dispersion curves of the epoxy resin, acrylic glass, optical grease and ABS plastic are shown in **Fig.3.11**.

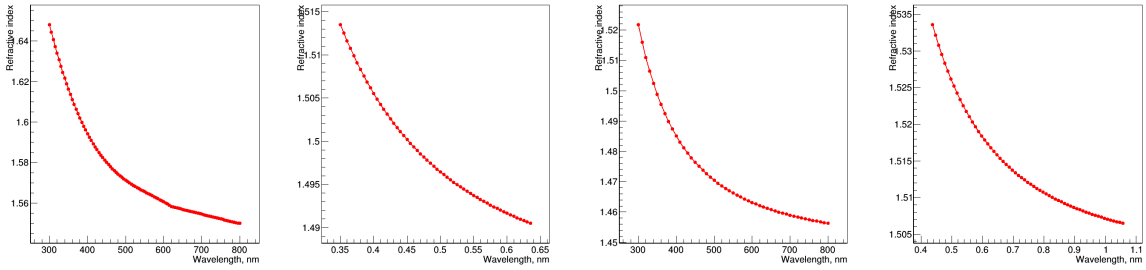

(a) Epoxy resin dispersion **(b)** Acrylic glass dispersion **(c)** Optical grease dispersion **(d)** ABS Plastic dispersion

Figure 3.11: Dispersion (index of refraction *vs* wavelength) of several materials. **a**: Epoxy resin dispersion **b**: Acrylic glass dispersion **c**: Optical grease (Saint Gobain BC-630) dispersion **d**: ABS Plastic dispersion.

SiPMs modelling The SiPMs model was implemented according to the SensL datasheet [159]. I have used all parameters at the overvoltage $\Delta V = 2.5$ V. The geometry of the array of SiPMs was implemented according to [191]. The size of the SiPM active area was set to 3 $\times$ 3 mm^2. The 30035 model has an epoxy resin as coating material. As neither the optical properties of the SiPM surface nor angular response were provided by the manufacturer, the SiPM interface was modelled as a uniformly and isotropically absorbing surface. The number of microcells (Geiger cells) is 62 $\times$ 77, hence 4774 in total. This number defines the dynamic range of the sensors. For a single scintillation event, if two or more photons arrive to the same microcell, only the first is registered as detected.

3.2.3.3 Generation of photosensors signals

Part of the photons that reach a SiPM are registered with probability equal to the PDE. Each registered photon triggers an avalanche process in the microcell where it impinges, creating an electric charge. That charge is summed to other charges created by photons in other microcells. However, there is another source of electric charge. With certain probability, optical crosstalk (OCT) occurs (**section 2.2.4.2**), resulting in a new avalanche within a neighbor microcell (or even two or more microcells). This phenomena is quite fast, so as the microcells are connected in a resistive chain, the total voltage drop in the SiPM terminals corresponds to the sum of the photon generated photoelectrons and the photoelectrons generated due to OCT [65].

The signal at the SiPM output enter the readout electronics circuitry to be integrated. The dark counts that occur during the integration time are added to the initial signal. The average dark counts number expected in the integration window is given by the integration time multiplied by the dark count rate. For example, for the experimental camera described in **section 6** it was 650 ns $\times$ 300 kHz $\approx$ 0.2 dark count photoelectrons.

All the above processes can be simulated in ANTS2. The number of photons detected by a SiPM is simulated according to its PDE. Additional photons can be added depending on the defined OCT probability and dark count rate. Dark counts are sampled from Poisson distribution with the expected value μ equal to the average dark count in the integration window.

3.2.4 ANTS2 models validation

The objective of this section is to validate the gamma camera simulation models, by comparing the simulation results with that of experimental measurements. While considerable effort was invested in making the simulation model as realistic as possible, information regarding a few parameters was not readily available (e.g. PTFE reflectivity, the reflectivity in the unpolished crystal lateral sides). As boundary values are roughly known for that parameters, I have used middle values or values which result in no significant impact on the performance results. For example: the reflection between the ground crystal lateral sides and the coating material was set to be of Lambertian type with a probability of 40%.

3.2.4.1 Gamma camera design and configurations

The camera models were build in a way to reproduce the experimental designs as closely as possible. The base prototype is comprised by the elements listed below, coupled with Saint Gobain BC-630 optical grease. All the elements have the same area, defined by the array of photosensors: 33.2 × 33.2 mm^2.

- An array of 8 × 8 photosensors formed with four 4 × 4 arrays from SensL (C-Series 30035 [159]).
- A 1 mm thick plexiglass lightguide
- A 2 mm thick LYSO crystal (Prelude 420^{TM}) from Saint Gobain
- A 2 mm thick reflector plate (Teflon)

A black (ABS plastic) frame wraps around the listed elements, to absorb light exiting the camera. In between the camera elements and the black frame there is a layer of optical grease with tickness of 0.2 mm. When a reflector was used, it was a 2 mm thick Teflon plate coupled to the crystal with 0.1 mm optical grease. The design of the camera model followed that of the prototype presented further in **section 6.1.1**. The design of the camera model is presented below in **Fig.3.12**. Overrides were defined for the following interfaces:

- Grease → Teflon (Absorption: 5%, 2π Lambertian back scattering: 95%)

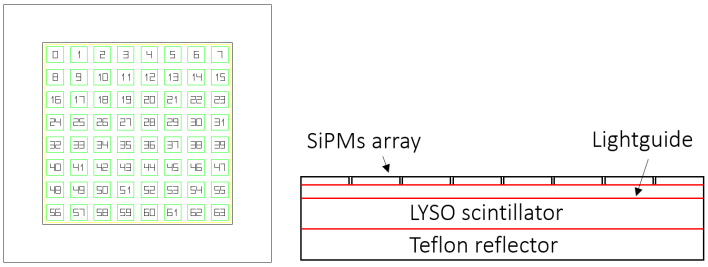

(a) **(b)**

Figure 3.12: Camera geometry for the models validation study. **a**: Top view of the camera plus the plastic frame around **b**: Camera side view (not to scale). The top layer is the array of SiPMs. Then, the lightguide, the LYSO scintillator and the Teflon reflector are represented. The red lines represent the thin layers of optical grease.

- Grease → Black material (Absorption 95%, 2π Lambertian back scattering: 5%)
- Lateral sides of LYSO → Grease (Absorption 60 %, 2π Lambertian back scattering: 40%)

In the interfaces where no override was defined, a Fresnel reflection/refraction was assumed. Between the grease and the Teflon plate (highly diffusive material, PTFE) it was assumed a high lambertian reflective component (95%). Contrary, when the PTFE reflector was replaced with one made of a black material, the override was defined as 95% of absorption and only 5% of diffuse reflection. Some reflection should be simulated because in the assembled camera the black material was black paperboard. The assumption on the light reflections in the interface between the unpolished LYSO lateral sides and the grease that makes the optical coupling with the black covering material was that it is also diffusive, due to the random orientation of the micro-facets of the crystal rough surface. This internal diffuse reflection on LYSO was modeled in a simplistic way. As LYSO has a high refractive index (n = 1.81), in its interface with the grease (n = 1.465) a great amount of back reflections are expected, and due to the unpolished finishing a stochastic angular distribution of the reflected photons directions are also expected. The photons that pass the "Lateral sides of LYSO - Grease" interface will be absorbed in the black frame. Hence, for the sake of simplicity, the optical rule at the interface "Lateral sides of LYSO - Grease" was set as 40% of lambertian back-scattering and 60% of absorption.

3.2.4.2 Simulations *vs* experimental

Two camera configurations were studied:

1) with the reflector plate made of light-absorbing material (black ABS plastic)
2) with the reflector plate made of highly reflective material (PTFE)

The total number of collected photons in the camera and the LRF shape of a central and a peripheral SiPM obtained for flood irradiation of whole camera field-of-view with γ-rays were compared. When the reflector is not present in the camera (black plate), other optical parameters can be better observed, as the reflections on the crystal lateral sides. With the first study, the assumptions on the photon reflections in the crystal lateral sides (simulated with the optical rules in the interface between materials) can be validated, mainly analyzing the LRF of one of the outer SiPMs of the sensors array. However, as the gamma camera imaging systems that use statistical reconstruction benefit a lot from the presence of a reflector (reflection of "escaping" photons to the SiPMs array), a second study was performed with the reflector to validate the simulations assumptions for a complete camera modeling. In the two studies, the energy deposition was simulated using Geant4, as explained below in **section 3.2.5**.

Wavelengh-resolved simulations Another objective was to verify if the wavelength-resolved (WR) simulation is required in order to correctly reproduce the experimental results. For the two camera configurations, both WR and not-WR simulations were performed. The WR simulation required the optical dispersion curves, as well as the LYSO scintilator emission spectrum and the SiPMs PDE wavelength dependence.

1. Study with no reflector on the camera This study helped to validate the crystal lateral sides finishing assumptions. A simulation of 450 thousand events produced in the scintillator by the γ-rays from a ^{57}Co source.

The histogram of the total charge in photoelectrons collected from all the SiPMs per one event (*sum* signal) is plotted in **Fig.3.13**. The red curve is the WR simulated sum signal, the green curve is the not-WR simulated sum signal and the blue one is the experimental sum signal. This color code applies to other plots in this section. The average WR simulated sum signal is 123 photons, the No-WR sum is 120, while the average experimental sum signal is 103 (16% difference). The uncertainties in the SiPMs PDE and crystal light yield (around 10% for both) are the most likely reasons for the difference between experimental and simulation results. It should be noted that the second peak on the simulation spectrum (sum signal $\approx$ 70) does not appear in the experimental spectrum. This second peak corresponds to escape of Lu K-shell fluorescence (**section 2.1.1**). It is not present in the experimental spectrum because the trigger threshold of the acquisition system was set too high and so the events that correspond to the escape peak were not acquired.

Fig.3.14 shows the simulated and experimental LRFs for one of the central (#28) and one of the peripheral (#5) SiPMs. Please see **Fig.3.12 a** with the SiPMs mapping. Note that in the peripheral SiPM the tail of the LRF curve is above zero for both experimental and simulated data. The comparison between the exprimental and simulated LRFs, confirmed

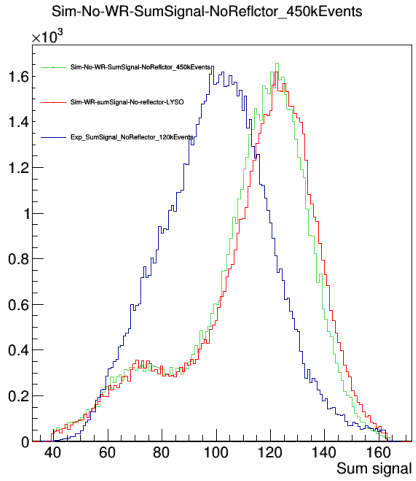

Figure 3.13: Sum signal from WR simulated data (red), No-WR simulated data (green) and experimental data (blue). The γ-rays source is ^{57}Co (122 keV).

that the assumption that motivated the choice of that override was correct: more reflections on crystal sides would result in more collection of photons in the SiPMs far from the scintillation event (positions corresponding to the LRF tail).

2. Study with the back reflector The idea was to further validate the assumptions for the reflectivity model of Teflon reflections. In the camera prototype a 2 mm thick Telfon plate was coupled with optical grease to the LYSO crystal, instead of the black paperboard. To reflect the change in the experimental prototype, the following change in the simulation model was made:

- Override grease $\rightarrow$ reflector (Teflon material): Absorption 10 %, 2π Lambertian back scattering: 90%

The **Fig.3.15 a.** shows the sum signal spectrum and the LRF profiles for simulated and experimental data. The peak in the experimental spectrum (average sum signal) is 191 photons while the spectrum peak for the simulated data is 195 and 200 photons for No-WR and WR respectively (difference of $\approx$4%). **Fig.3.15 b** and **c** present the LRF for a SiPM in the center of the camera (#28) and for a SiPM in the periphery of the camera (#5), respectively. The LRFs for both WR and no-WR simulation data are presented. They are very similar, except in close vicinity of the radial distance equal to zero, where the WR simulation results are closer to the experimental results. The agreement between the experimental and simulated LRFs is even better in this study with the reflector than in the previous without the reflector in the back of the camera.

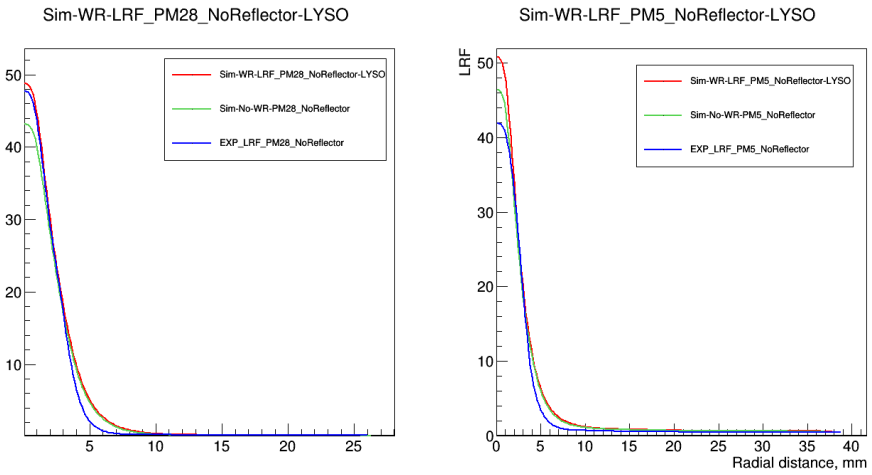

(a) **(b)**

Figure 3.14: LRFs of a central SiPM (#28) and a peripheral SiPM (#5)(no reflector on the LYSO crystal back). Red: LRFs from simulation (wavelength-resolved), Green: LRFs from simulation (not wavelength-resolved) and Blue: "Experimental" LRFs. **a**: LRF of a central SiPM (#28) **b**: LRF of a peripheral SiPM.

It can be assumed that the models of the camera components are adequate, because they contribute for the reconstruction of light response functions in close agreement with that from experimental data. As WR and No-WR simulations give very similar results, No-WR simulation was used in the following studies to speed up simulations.

3.2.5 Geant4 simulations of energy deposition

A comparison is presented between two cases: 1) when the energy deposition is delegated to Geant4 and 2) when it is simulated in ANTS2. The gamma camera configuration is the one shown in **Fig.3.12**, with LYSO crystal (2 mm thick), plexiglass lightguide (1 mm thick), Teflon reflector (2 mm thick) and a black frame around the crystal sides. A linear source (infinitesimal slit) was simulated, emitting 140 keV γ-rays perpendicularly to the detector face. The line source was diagonally oriented in order to cover different regions of the camera.

Fig.3.16 a. and **b.** show the reconstructed linear source projection on the crystal. **Fig.3.16 c** shows the profile of the linear source projection along the direction perpendicular to the line, for the two cases: Geant4 and ANTS2 simulation of energy deposition (**Fig.3.16 a.** and **b.**). When the energy deposition is simulated in Geant4, the FWHM of the profile is ≈0.64 mm, while when only ANTS2 is used the FWHM is ≈0.52 mm. This difference of 23% is attributed mostly to K-shell fluorescence of Lu (53-63 keV), which is only simulated in Geant4.

The simulation of 500 thousand ^{99m}Tc flood field events was also performed for the two cases. The energy spectra when the energy deposition is delegated to Geant4 and when it is

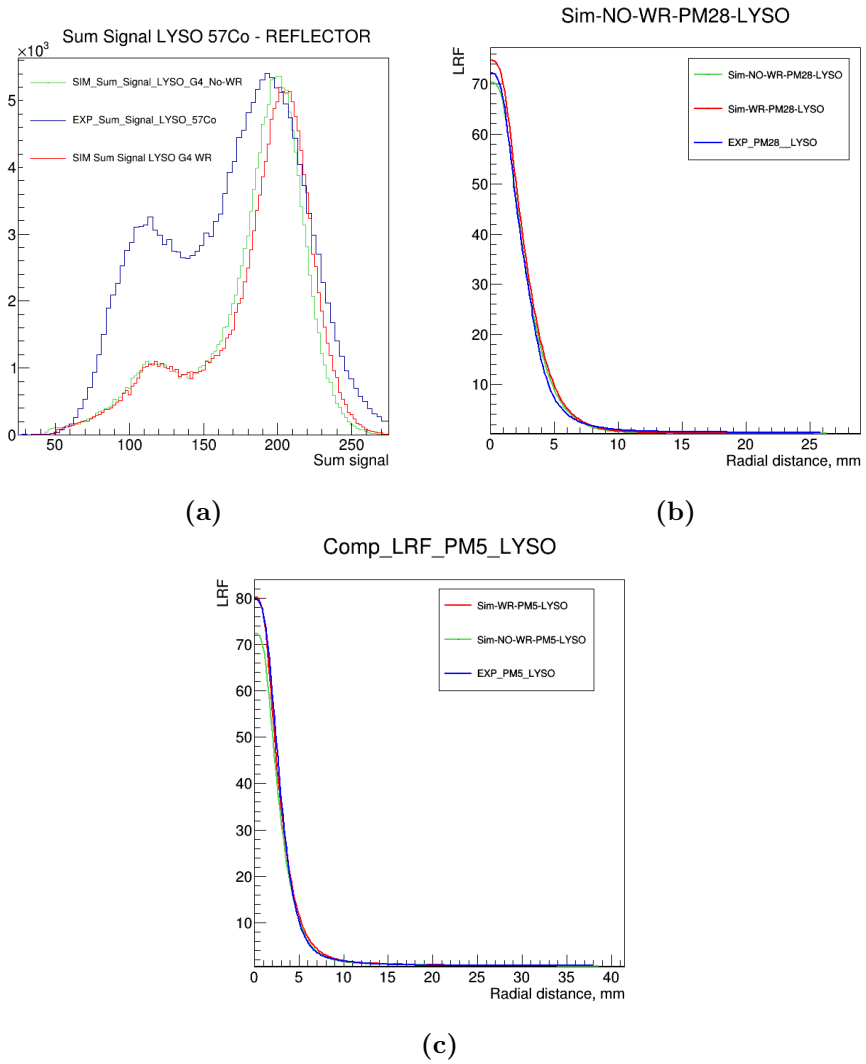

Figure 3.15: Comparison between experimental and simulated sum signal spectrum and LRFs of a peripheral SiPM (#5)(reflector on the crystal backs). The red and green curves show respectively the results from WR and Not-WR simulated data and the blue curve the results for experimental data. **a**: Sum signal spectrum **b**: LRF of a central SiPM (#28) **c**: LRF of a peripheral SiPM (#5).

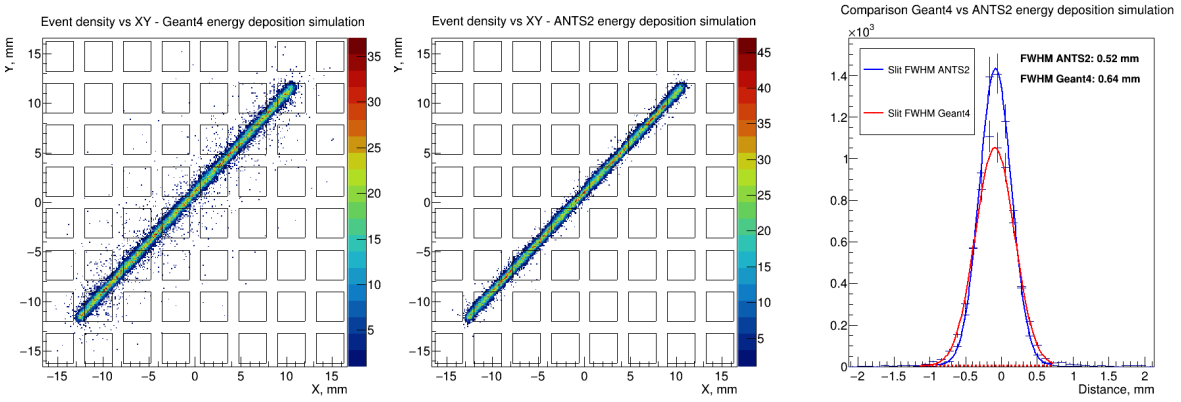

(a) **(b)** **(c)**

Figure 3.16: Comparison between the simulation of gamma-rays (140 keV, ^{99m}Tc) energy deposition using Geant4 and ANTS2 softwares. Simulation of the irradiation of a gamma camera with a linear source (infinitesimal slit). **a**: XY density plot of the reconstructed positions of the slit projection on the crystal (Geant4) **b**: XY density plot of the reconstructed positions of the slit projection on the crystal (ANTS2) **c** FWHM of the transverse profile of the reconstructed events from a linear source.

simulated in ANTS2 are compared in **Fig.3.17**. In Geant4 simulation the escape peak at ≈84 keV[1] due to fluorescence phenomenon is quite visible.

The more accurate simulation of the absorbed energies by Geant4, considering also secondary γ-rays and Auger electrons, results in a higher variability of the absorbed energies and, consequently, in a worsening in the energy resolution. It is 18.5% for the case when Geant4 simulates the energy deposition, compared to 18.0% for ANTS2. This represents an increase of only ≈2.8% when using Geant4, which is a sign that the assumption made in ANTS2 on the point-like deposition of the energy absorbed by photoelectric effect is a fair approximation when there is no special concern in the accuracy of the positions of the energy deposition. Nevertheless, the decision of using or not Geant4 should also rely on the requirement on the spatial resolution, because it was verified that the difference between Geant4 and ANTS2 simulation is around 23%, for the particular case of the LYSO camera.

Along with the Compton scattering, the fluorescence phenomena is the other major contributor for the shift in the reconstructed position of the photoelectric energy deposition. The X-ray emitted in the relaxation of an electron previously ejected from the K-shell will cross some space within the material, characterized by its mean free path. Thus, in order to decide if the spatial resolution will be affected by X-ray fluorescence, the expected spatial resolution should be compared with the mean free path (MFP) of a X-ray emitted in fluorescence process by the heaviest chemical element that constitute the scintillator. For instance, in the case of LYSO, Lu is the heaviest element and the MFP of its K-shell fluorescence is around 0.62 mm.

[1]The escape peak is centered at ≈84 keV because it corresponds to the absorbed energies given by the energy of the incoming γ-rays (140 keV) minus the energy of the Lu K-shell (53-63 keV.

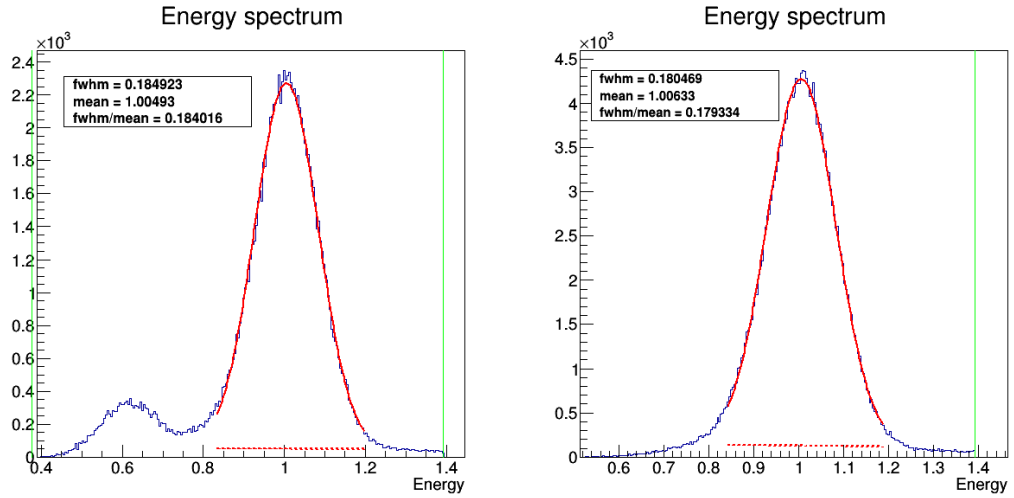

(a) (b)

Figure 3.17: Energy spectrum from simulated events (140 keV, ^{99m}Tc). **a**: Energy spectrum when the energy deposition in simulated in Geant4. **b**: Energy spectrum when the energy deposition is simulated in ANTS2.

This is a value close to the expected spatial resolution for the camera with the LYSO scintillator, which is in the range of 0.60 - 0.65 mm. Hence, as the limits of the intrinsic resolution were tested in this work, the energy deposition should be simulated with Geant4.

3.2.6 Validation of collimator models: numerical *vs* analytical comparison

I wanted to design a small FOV gamma camera system that can be used for pre-clinical and clinical exams. Collimators should be designed for the desired spatial resolution and γ-rays collection efficiency (sensitivity). Formulas to calculate the sensitivity and spatial resolution as a function of the collimator geometry and dimensions are available in the literature for decades, but mostly for large FOV cameras (LFOV). Only recently those formulas are being applied to SFOV cameras, which are typically one order of magnitude smaller than LFOV in their width. Before using straightforwardly the standard equations in the design of small FOV collimators and send them for manufacturing, I wanted to verify if there is some possible non-linearity effect due to the scale-down on the collimator dimensions, e.g., increased septal penetration, relatively to those of large FOV.

The validation of the formulas was performed comparing simulation results obtained using ANTS2 with the analytical results given by the literature formulas (**sections 2.2.1.1** and **2.2.1.2**). Two collimator types were analysed: parallel-hole collimator and pinhole collimator.

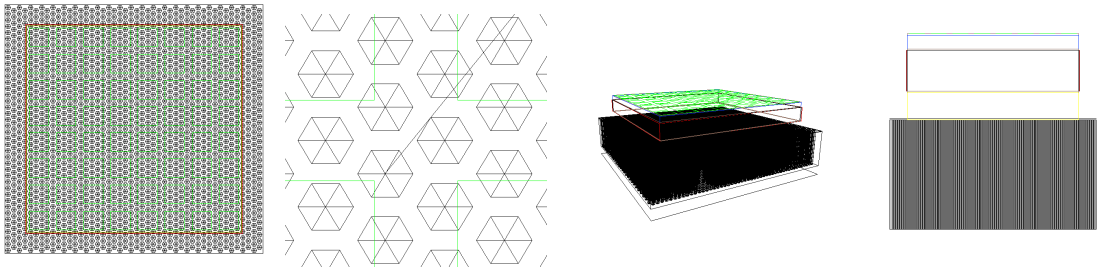

(a) **(b)** **(c)** **(d)**

Figure 3.18: Parallel-hole collimator design in ANTS2. Holes characteristic dimension: 0.5 mm; septa thickness: 0.3 mm. Hole lenght: 10 mm. The SiPMs are represented with green lines. **a**: Top view; **b**: Zoom of the top view. The green lines represent the SiPMs positions; **c**: Perspective view; **d**: Side view.

3.2.6.1 Parallel-hole collimator sensitivity and spatial resolution

Fig.3.18 shows an overview of the parallel-hole collimator simulated in ANTS2. It is slightly larger than the camera and it was attached to the camera reflector, so the camera side opposite to the SiPMs array (**Fig.3.18 d**). The collimator material was pure tungsten W ($19.3\ g/cm^3$)[1]. The simulated collimator has an area of 40×40 mm^2 with hexagonal holes. Two characteristic dimensions of the hole (distance between to opposite faces of the hexagon) were used for the same septa size of 0.3 mm: 0.5 mm and 0.8 mm, resulting in hole pitch of 0.8 mm and 1.1 mm, respectively. Simulations were performed with collimator thickness varying from 7 mm to 20 mm.

In ANTS2, planar "monitors" can be placed in any detector region to monitor the number of γ-rays that cross those planes. In order to estimate the collimator sensitivity, a monitor was placed at the boundary between the camera reflector and the collimator. In this position, the number of particles that effectively reach the detector window can be counted.

The sensitivity was calculated as the ratio between the number of γ-rays hitting the monitor and the total number of emitted γ-rays (point source emitting isotropically in 4π), which were 25 million. To obtain the simulation spatial resolution, a diagonal line source (tilted by 30° relatively to the X axis) was defined, crossing all the collimator area, as shown in **Fig.3.19a**. The FWHM of the projection of the density plot of the reconstructed positions along the direction orthogonal to the slit was measured and considered as the collimator (or extrinsic) spatial resolution. More accurately, it is the system resolution, because it includes the intrinsic resolution due to reconstruction. However, the intrinsic resolution was not removed from the system resolution to obtain a purely extrinsic resolution, because the intrinsic resolution is much narrower than the extrinsic one, which means that the extrinsic resolution is very

[1]The manufacturing of parallel-hole collimator in tungsten is available on the market. The fabricated parallel-hole is presented in **section 6.1.2**.

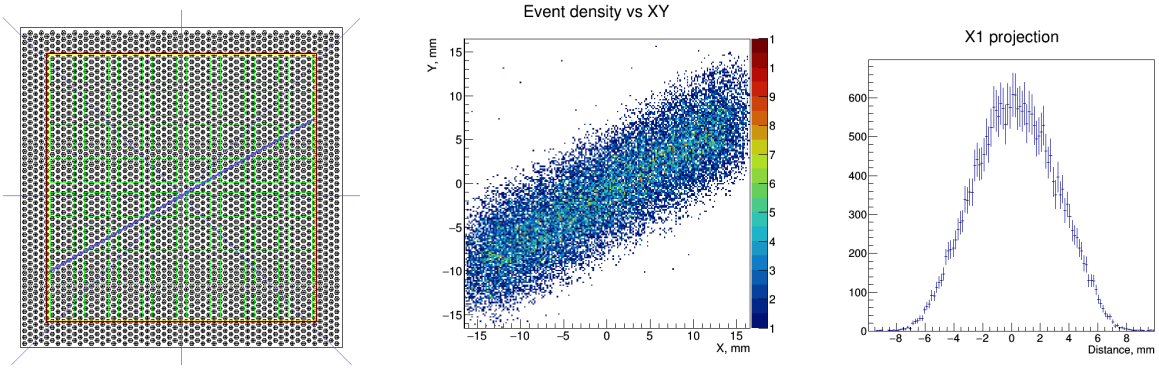

(a) (b) (c)

Figure 3.19: Diagonal slit used to measure the simulation spatial resolution of the parallel-hole collimator. The collimator hole diameter is 0.5 mm, the septa thickness is 0.3 mm and the holes length is 8 mm. The line source was placed 100 mm away from the collimator face. **a**: Position of diagonal slit source (top view); **b**: XY density plot of the reconstructed positions of a slit projection; **c**: Transversal profile of the density plot projection along the direction orthogonal to the slit.

similar to the system resolution (see **Eq.2.4.2.2**). **Fig.3.19 b** is the XY density plot of the reconstructed positions of the events that correspond to γ-rays that pass through the slit and **Fig.3.19 c** is the projection of that density plot along the direction orthogonal to the slit (FWHM = 7.5 mm).

Fig.3.20 presents the comparison between the sensitivity calculated analytically (using **Eq. 2.27**) and with data from simulations for the parallel-hole collimator. The comparison was done for two holes diameter, 0.5 mm and 0.8 mm, demonstrating in both cases a good agreement between the simulation and the analytical sensitivity.

Fig.3.21 presents the comparison between simulated and analytical spatial resolution for the same parallel-hole geometries used for the sensitivity measurement (septa of 0.3 mm and two different hole diameter: 0.5 mm and 0.8 mm). The simulation results have a good agreement with the analytical results, confirming that **Eq.2.25** correctly predicts the spatial resolution of the parallel-hole collimator with hexagonal hole geometry and dimensions in the order of a few millimeters.

3.2.6.2 Pinhole collimator sensitivity and spatial resolution

Besides validating the adequacy of the analytical formulas for the design of the pinhole (**section 2.2.1.2**), this study was performed in a view of manufacturing the optimized collimator. Two materials were simulated: 1) an ideal γ-rays absorber (100% efficiency) and 2) WC alloy (90% WC + 10% Co) as a feasible manufacturing option. **Fig.3.22** shows an overview of the pinhole design.

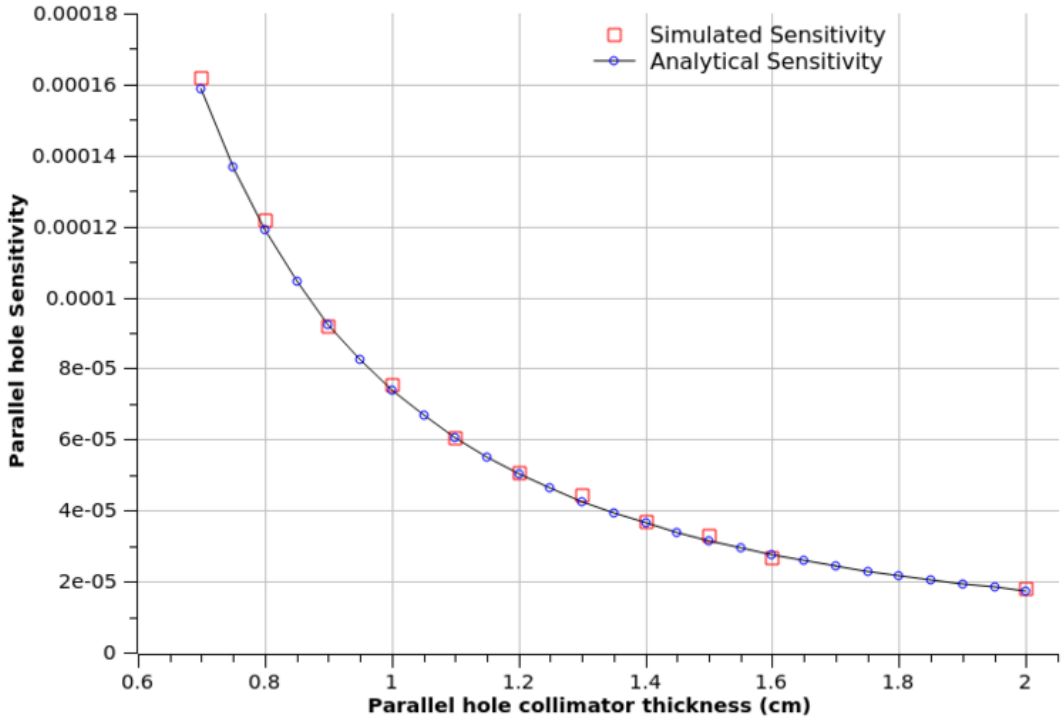

(a)

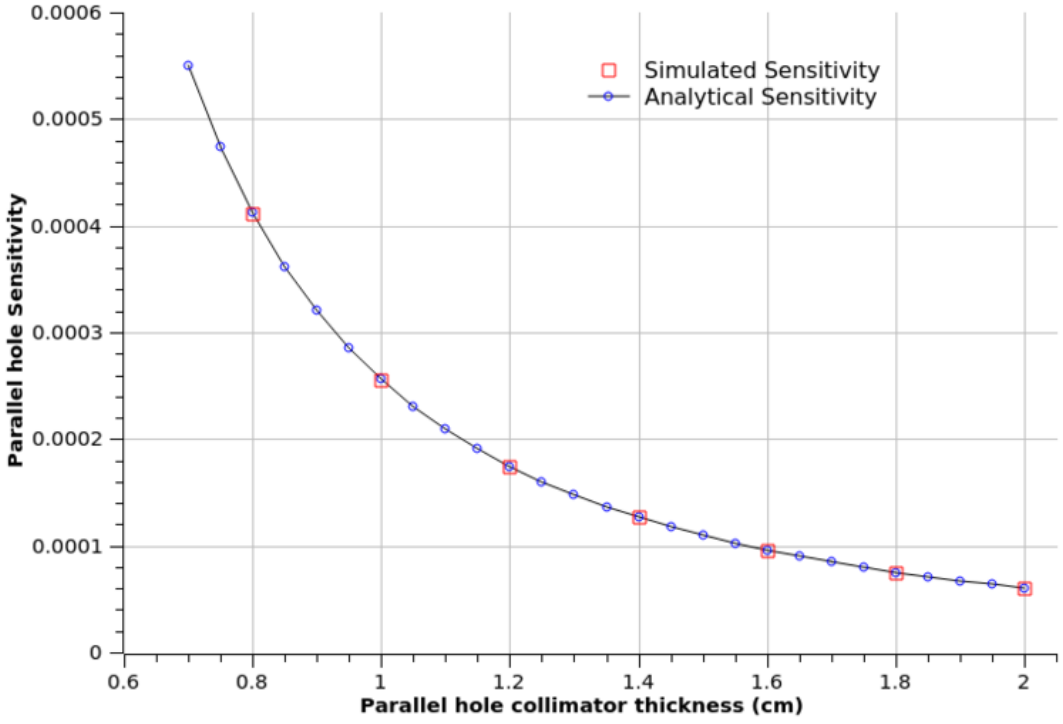

(b)

Figure 3.20: Parallel-hole sensitivity as a function of holes length: simulated *vs* analytical **a**: Hole diameter: 0.5 mm; **b**: Hole diameter: 0.8 mm. The source was placed at 20 mm from the collimator.

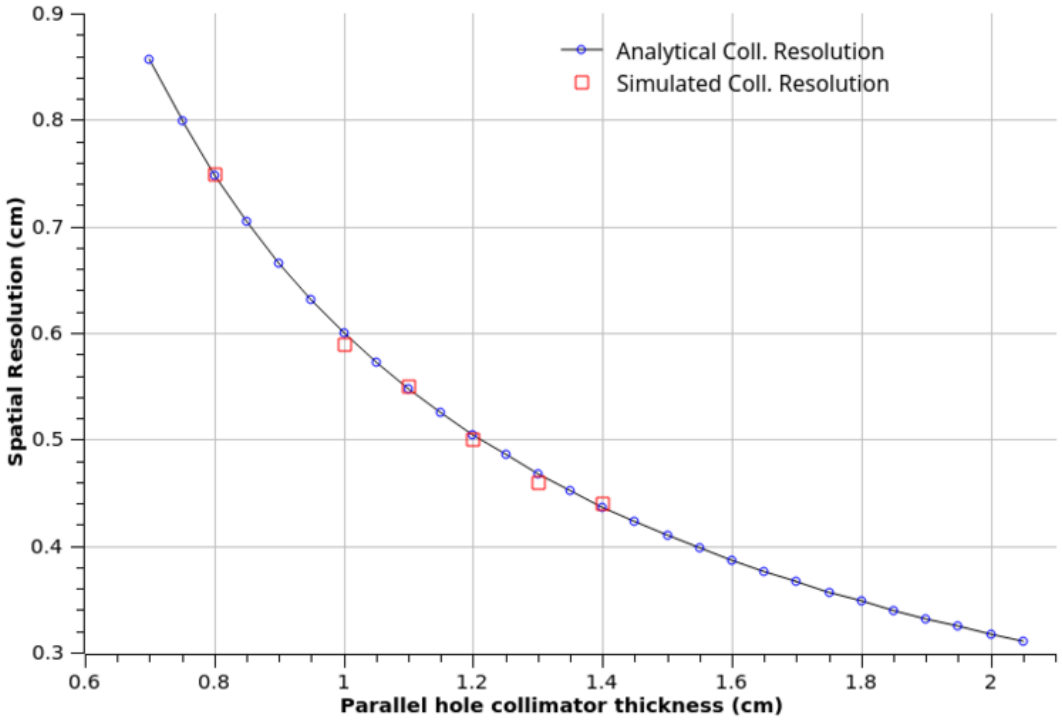

(a)

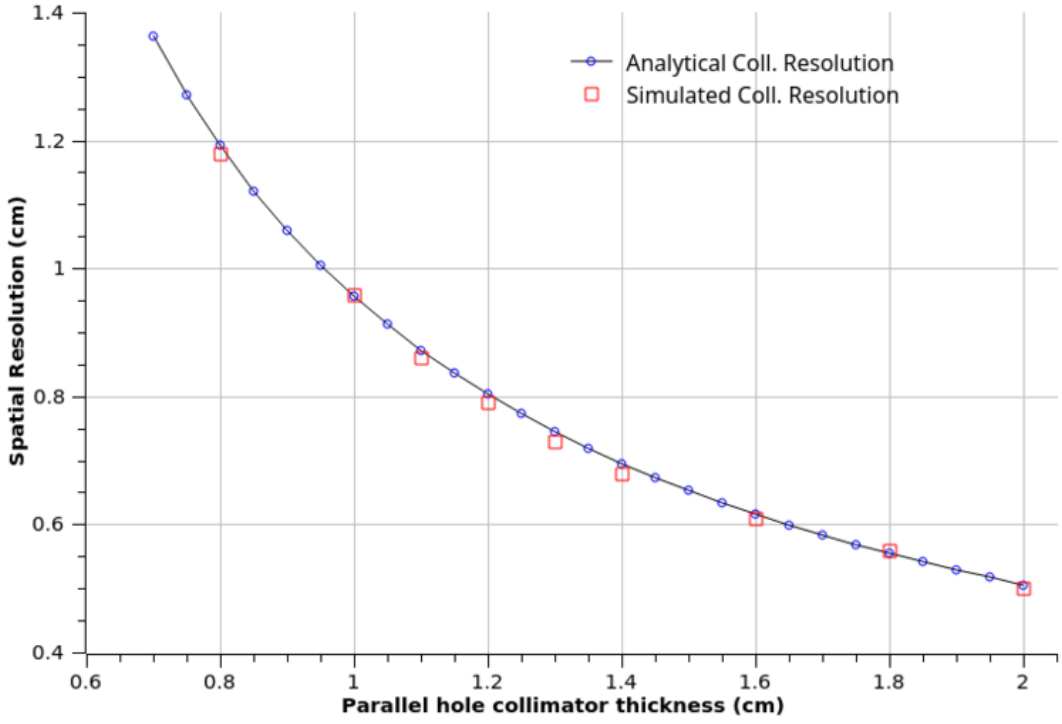

(b)

Figure 3.21: Parallel-hole spatial resolution as a function of holes length: simulated *vs* analytical **a**: Hole diameter: 0.5 mm; **b**: Hole diameter: 0.8 mm. The source was placed at 100 mm of the collimator.

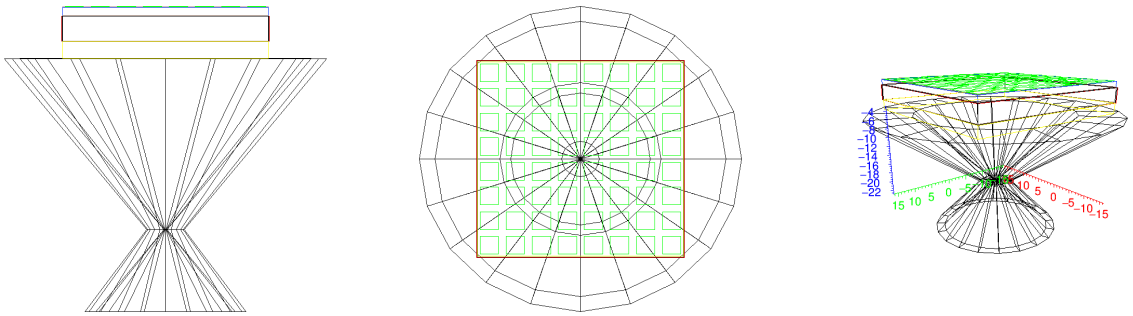

(a) (b) (c)

Figure 3.22: Pinhole collimator design in ANTS2. Hole diameter: 0.5 mm; acceptance angle: 90°. The camera is also represented. **a**: Side view; **b**: Top view; **c**: Prespective view.

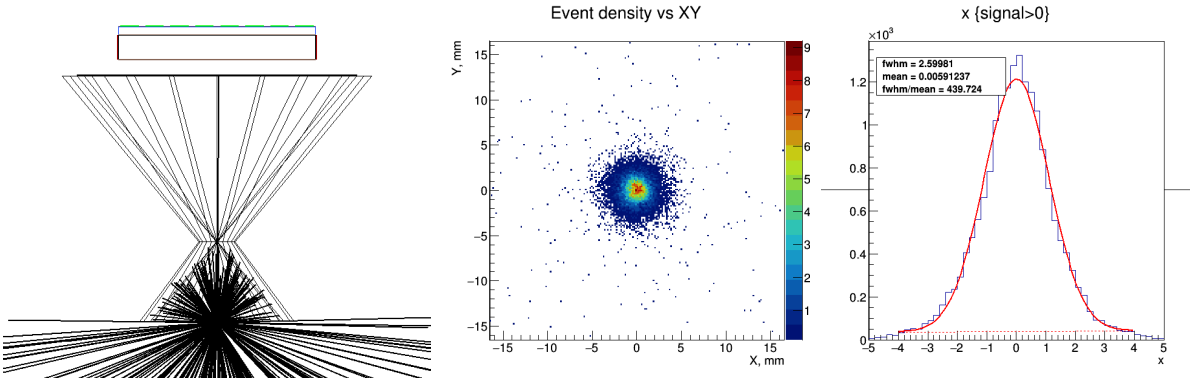

(a) (b) (c)

Figure 3.23: Point source imaging with a pinhole collimator made of WC alloy. Hole diameter: 0.5 mm; acceptance angle: 90°; magnification factor = 2. **a**: Point source position; **b**: XY density plot of the point reconstructed image; **c**: Profile of the point source density plot projection along the Y direction with a Gaussian curve fitted to it.

The geometry used in simulations is shown in the **Fig.3.23 a**. The acceptance angle α is 90°, the hole diameter d is 0.5 mm and the focal length f is 23.5 mm. A ^{99m}Tc source was placed on the collimator axis at half the distance to the detector in order to obtain magnification factor of 2. **Fig.3.23 b** and **c** show the XY density plot of the reconstructed positions and its profile along X, respectively, for the pinhole collimator made of WC alloy. **Fig.3.24 a** and **b** show the same, but for the pinhole made of 100% blocking material. Note that the reconstructed simulated point source image (e.g. **Fig.3.23 b**) is the image reconstructed in the detector plane, which is a magnification of the source image. The FWHM of the simulated point source profile must be divided by the magnification factor to obtain the resolution in the source plane, also called object resolution. This way a comparison can be made with the analytical object resolution, which was also calculated for the source plane.

Fig.3.25 shows the comparison between simulation and analytical spatial resolution. When

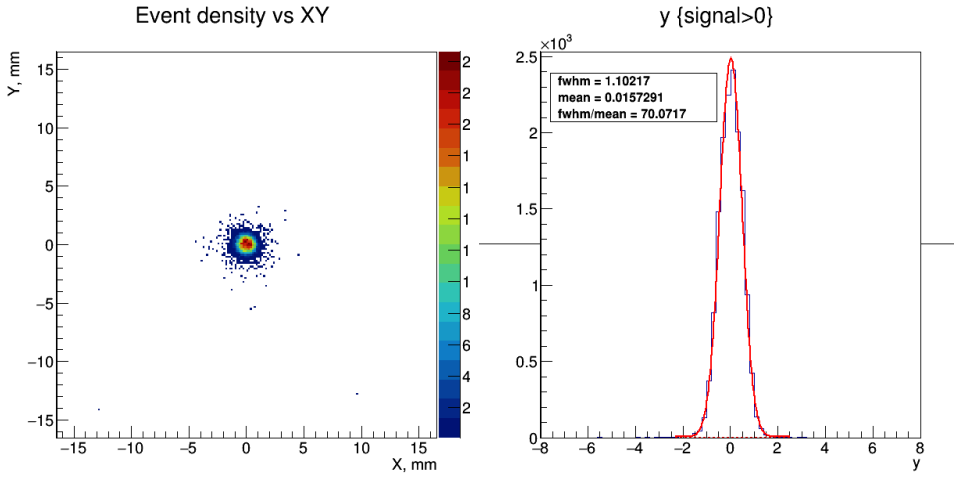

(a) (b)

Figure 3.24: Point source imaging with a pinhole collimator made of 100% γ-rays blocking material. Hole diameter: 0.5 mm; acceptance angle: 90°; magnification factor = 2. **a**: XY density plot of the point reconstructed image; **b**: Profile of the point source density plot projection along the Y direction with a Gaussian curve fitted to it.

WC alloy is used (open symbols in the figure), the effective pinhole diameter is enlarged when compared with that of the ideal absorber material (**see section 2.2.1.2**). This explains the worse resolution of the former, as expected from the dependence of spatial resolution on the hole diameter. Regarding the comparison between simulation and analytical resolution, they are relatively close, with differences lower than ≈0.2 mm for resolutions in the order of few millimeters.

Fig.3.26 shows the comparison between the collimator efficiency obtained analytically and from simulations. The agreement between the simulation efficiency and the one given by the analytical formula is quite good. As expected, the pinhole made of 100% blocking material has a lower γ-rays detection efficiency than the pinhole made of WC alloy. It can be concluded that the models of the collimators are valid and can be used to simulate the complete gamma camera.

3.3 GAGG:Ce based camera optimization through simulations

This section describes the GAGG:Ce based camera optimization studies, performed through simulations. The optimizations aim to obtain a camera configuration that results in the best collection of light by the photosensors array, in the lowest possible level of distortions and in the best possible spatial resolution (preferably below 1 mm FWHM). At the same time, the camera design should allow the reconstruction of LRFs through the iterative algorithm that relies on the axial-symmetry of sensors response to light. Some alternatives for the two

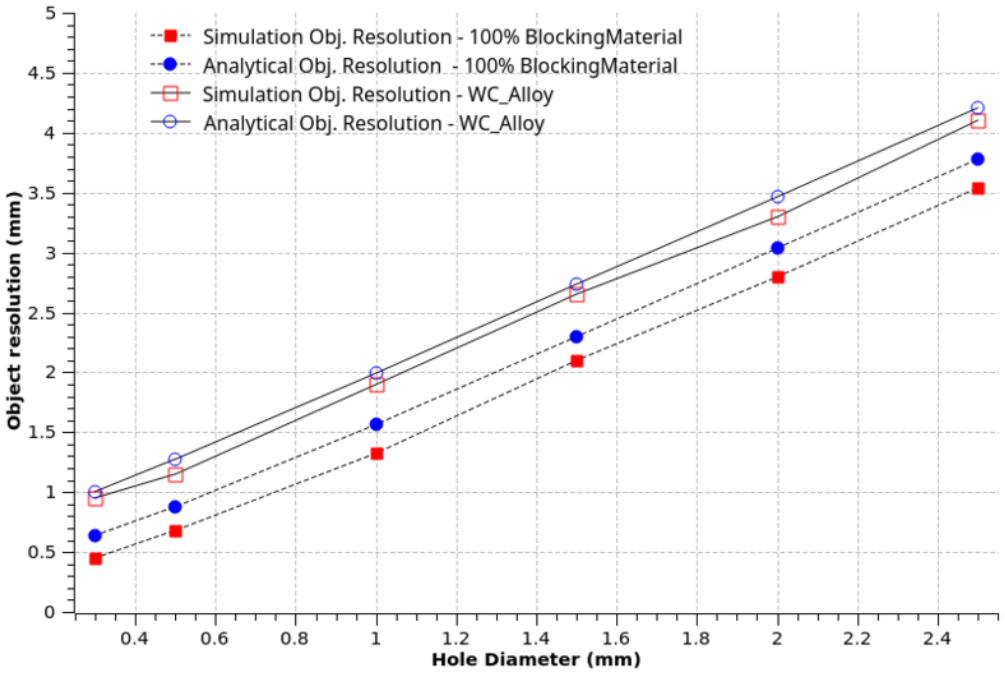

Figure 3.25: Simulation and analytical object resolution of a pinhole collimator with an aperture angle = 90°. The circles are the analytical results, while the squares are the simulation ones. The filled symbols correspond to the ideal blocking material and the opened symbols correspond to the WC alloy collimator material.

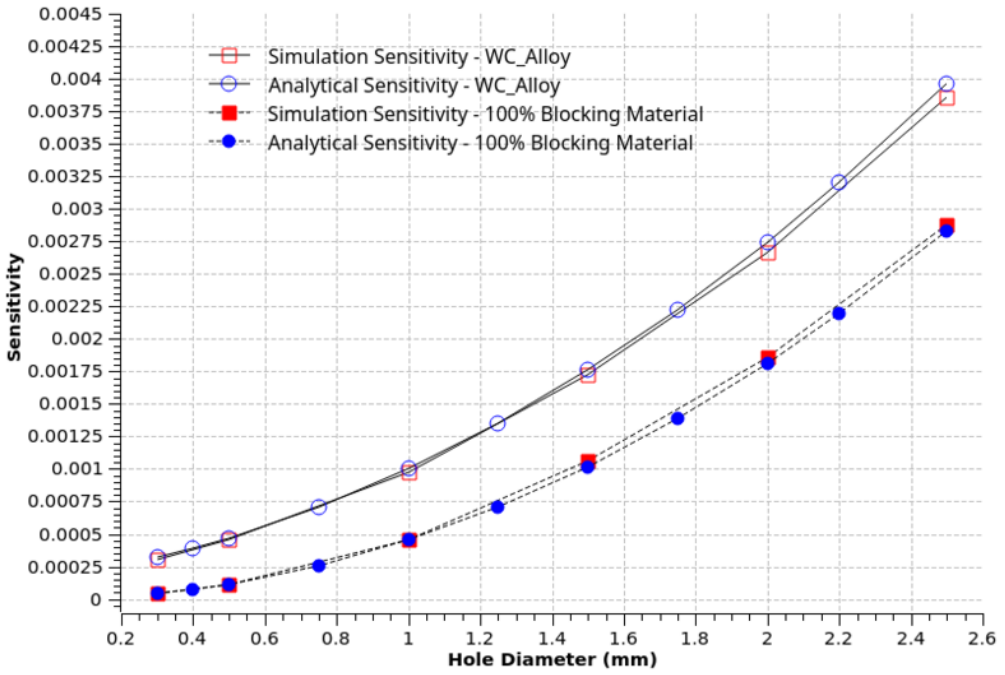

Figure 3.26: Simulation and analytical efficiency (sensitivity) of a pinhole collimator with an aperture angle = 90°. The circles are the analytical results, while the squares are the simulation ones. The filled symbols correspond to the ideal blocking material and the opened symbols correspond to the WC alloy collimator material.

following components were studied:

1. **Coupling material**: one single "standard" optical grease (n = 1.465) or three "high index" (higher than n = 1.5) coupling compounds

2. **Lightguide (for 3 mm thick crystal)**: thickness from 0.2 to 1.5 mm

The camera "base design" was the same used for the simulation models validation (see **section 3.2.4.1**), but the crystal was replaced for a 3 mm thick GAGG:Ce. The material chosen to cover the lateral sides of the crystal was again the black ABS plastic used before, because the objective is to improve as much as possible the spatial resolution (rather than the energy resolution, that would be optimized with a reflective material). For all camera configurations the simulation of the energy deposition in the crystal was performed with Geant4, through the ANTS2 interface, presented in **section 3.2.5**.

3.3.1 Criteria and method to evaluate the camera performance

The performance of a particular camera configuration was evaluated through the average and maximum values of two parameters, calculated for the camera central field-of-view of 29 × 29 mm^2: 1) spatial resolution and 2) distortions.

As the optimization study was done through simulations, the true positions of the events were known and so the distortions were calculated as the difference between the reconstructed positions and the true positions, separately for X and Y coordinates. The reconstruction performance was verified to be symmetric relatively to the vertical and horizontal central axis of the camera detection window. This symmetry allowed to only evaluate the camera performance for a quarter of the camera and to consider only the parameters for one direction (X, for instance). As an example of symmetry, the **Fig.3.27** presents the distortions along X (left image) and along Y (right image).

Method The method to calculate the distortions and the spatial resolution along X was the following:

1. Simulate the emission of 250 thousand γ-rays of 140 keV (^{99m}Tc) evenly distributed over the entire camera FOV (flood field irradiation). The energy deposition in the scintillator were simulated with Geant4.

2. Estimate LRFs using the adaptive method.

3. Reconstruct flood data with the LRFs and calculate distortions level.

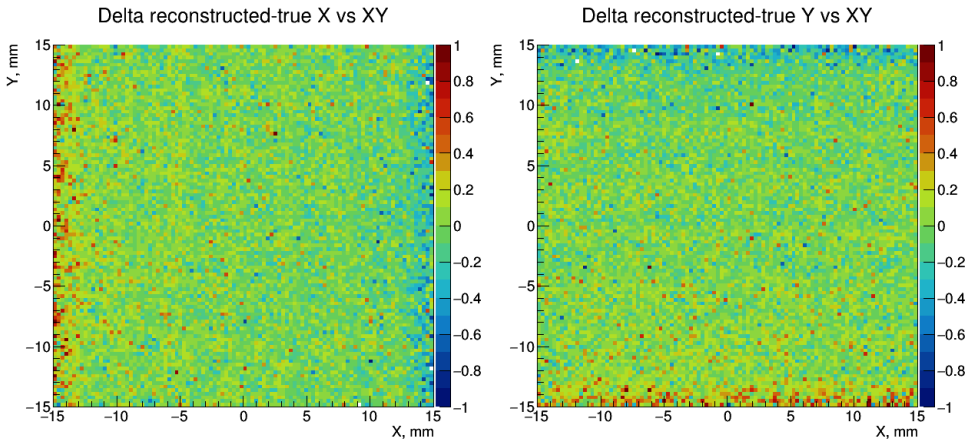

Figure 3.27: Distortions along the horizontal (X) and vertical (Y) directions of the GAGG camera (FOV 28 × 28 mm^2). **a**: Distortions along X (reconstructed X - true X); **b**: Distortions along Y (reconstructed Y - true Y).

4. Simulate a grid of 15 × 15 pencil-beam sources in the upper-right corner of the camera (1250 ^{99m}Tc events in each point), reconstruct events and calculate the FWHM of the Gaussian curves that fit the histograms of the reconstructed X positions.

3.3.2 Alternative coupling elements

One problem associated with many inorganic scintillator materials is the high refractive index (n > 1.8). It makes optical coupling using traditional optical grease with refractive index about n = 1.5 considerably less efficient than desired for the collection of light in the photosensors plane. For example, GAGG:Ce has an index of refraction of approximately n = 1.9 at emission peak. The critical angle at the interface between GAGG:Ce and the optical grease with index n = 1.47 is 44.3°, which means a significant amount of reflections back to the crystal, higher or lower depending on the scintillation position along the crystal thickness.

There are commercially available optical coupling materials with refractive index as high as n = 1.73. In the interface between GAGG (n = 1.93) and a material with n = 1.73 the critical angle would be 63.7°, which means a reduction of about 60% in the fraction of the photons that would be reflected in that interface, when compared with the case in which the critical angle is 44.3°. Lightguide materials with index n = 1.73 (high index) can be produced [192]. The "standard" camera configuration (**Fig.3.28 a.**) has an interface GAGG → optical grease with a steep change in the reflective index (n = 1.93 → n = 1.465). The objective of this study was to check to what degree a sequence of smaller changes in the reflective index from the scintillator to the SiPMs epoxy (n = 1.93 → n = 1.73 → n = 1.57 → n = 1.47), as shown in **Fig.3.28 b.**, would be beneficial to the camera performance. Three "high index"

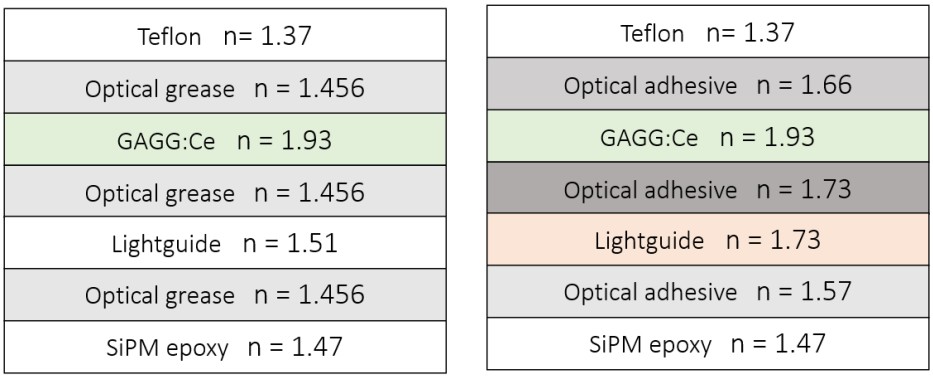

Figure 3.28: Schematic representation of the refractive indices of the gamma camera components for two alternative configurations. The thickness of the layers (∼0.1 mm) are not represented at scale. The GAGG:Ce crystal is 3 mm thick and the lightguide is 1 mm thick. **a**: layers scheme of a standard camera with a single "low index" optical grease (n = 1.465); **b**: layers scheme of the advanced camera with three "high index" optical adhesives (n = 1.57, n = 1.73, n = 1.66).

coupling components have been used in simulations to have as much as possible a gradual transition, applying commercially[1] available materials (optical adhesives) of different indexes. This configuration, shown in **Fig.3.28 b**, should permit to collect more photons per event (less reflections, due to a better coupling) and thus to improve the quality of event reconstruction. This section presents the comparison between this "advanced" alternative and the standard alternative of using the same optical coupler (n = 1.465) in all interfaces.

Total light collection and spatial resolution The comparison between the standard and the advanced camera configurations was performed based on two parameters: 1) the mean number of total collected photons per scintillation event and 2) the spatial resolution. Spatial filter was applied: only the reconstructed events inside a FOV of 29 × 29 mm^2 were used in spatial resolution calculation. The results are summarized in the **table 3.5**. As expected, in the advanced configuration the optical coupling is better than in the standard configuration. In the first case more photons arrive directly from the scintillation position to the SiPMs plane, because less reflections occur in the interface between components. The average total number of photons detected by the SiPMs for one scintillation event is 227 in the advanced configuration, while it is 163 photons for the standard one. The average and worst spatial resolutions are 0.728 mm and 0.842 mm for the advanced configuration, while they are 0.758 mm and 0.870 mm for the standard configuration.

[1]The optical adhesives with the indices used in the simulations are supplied by AMS Technologies (AT#3728E (n = 1.57), AT#6205 (n = 1.73), AT#18166 (n = 1.66)).

Parameter	Advanced configuration	Standard configuration
Total number (mean) of collected photons	227	163
Average spatial resolution (mm)	0.728	0.758
Worst (over area) spatial resolution (mm)	0.842	0.870

Table 3.5: Performance results of the two configurations for coupling the gamma camera components: Three optical "high index" adhesives ("advanced" configuration) and one single optical grease ("standard" configuration).

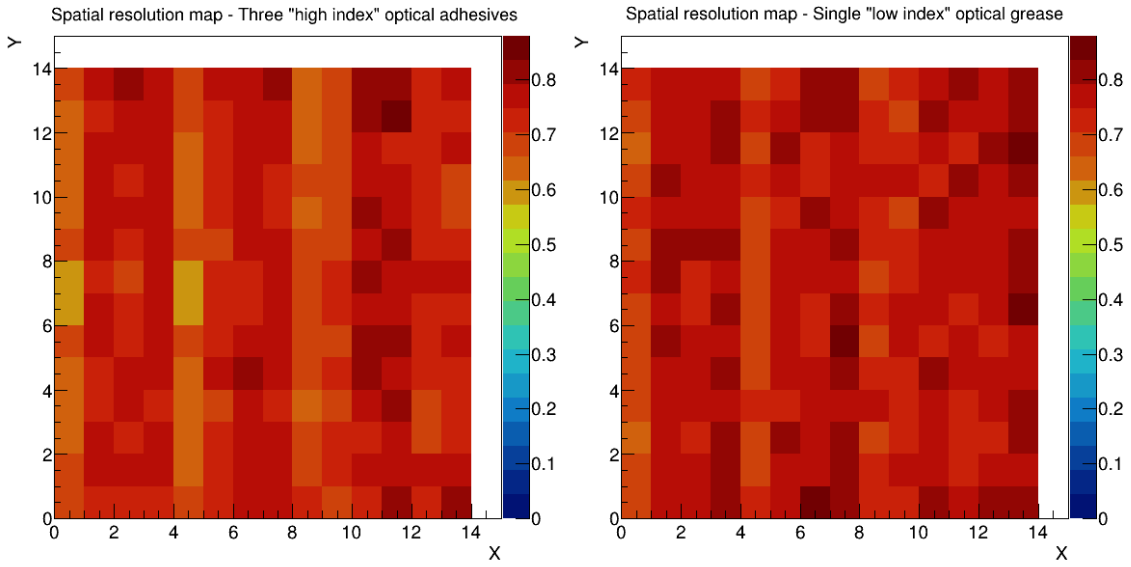

(a) **(b)**

Figure 3.29: Spatial resolution color-coded map of a grid of pencil-beam sources reconstructed events. **a**: Camera with three "high index" optical adhesives (n = 1.57, n = 1.73, n = 1.66); **b**: Camera with a single "low index" optical grease (n = 1.465).

Fig.3.29 shows the spatial resolution color maps for the two camera configurations calculated from the reconstructed grid of pencil-beam sources in the upper-right corner of the camera. The spatial resolution was obtained for each square in the image - corresponding to a single point source - measuring the FWHM of the Gaussian curve fitted to the histogram of that point source reconstructed positions (X coordinate).

The improvement given by the advanced configuration does not compensate the drawbacks of such solution. High index elements pose a technological problem due to issues related with toxicity and long-term stability of such compounds. They are also more expensive than the low index optical grease. The advanced configuration may be interesting for mass produced cameras, but the use of adhesives is really inconvenient for a research device (hard to remove after applied to the surfaces), so I have decided to use the standard design ("low index" n = 1.465 optical grease was used in all camera interfaces) in the experimental work, in which two

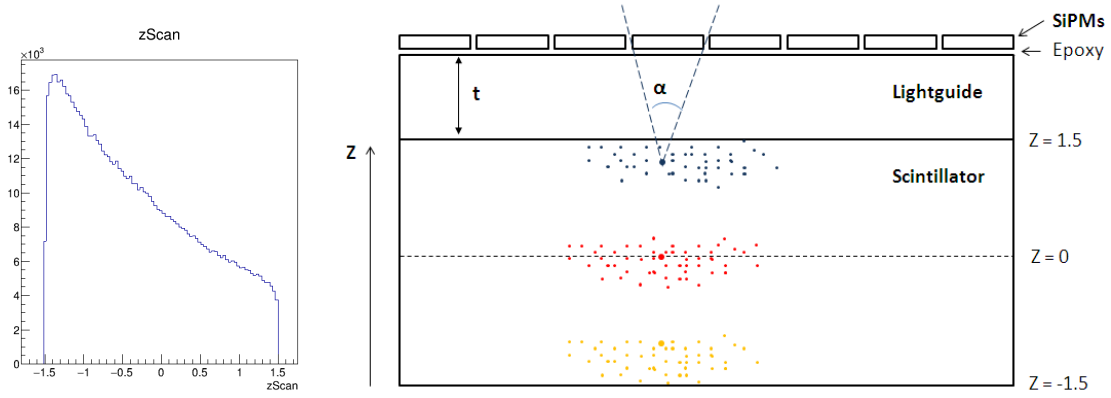

(a) (b)

Figure 3.30: Depth of interaction of γ-rays in a 3 mm thick GAGG scintillator. **a**: Histogram of γ-rays interaction depth within a 3 mm GAGG crystal (from Monte Carlo simulations); **b**: Scheme illustrating three possible regions of interaction with DoI positions represented in three different colors.

gamma camera prototypes were prepared.

3.3.3 Optimization of the lightguide thickness in the GAGG camera

The lightguide thickness initially selected for the 3 mm thick GAGG based compact gamma camera was 0.5 mm, following the recommendation on [178], in which this lightguide dimension was found to be the optimal for a compact gamma camera with a 2 mm thick LYSO. The first simulations showed, however, that a 0.5 mm thick lightguide results in a significant level of distortions in the positions of the reconstructed events in the GAGG camera, as can be seen below in this section. For this reason, the optimization of the thickness of a plexiglass lightguide was carried out. The lightguide thickness that results in the best performance of the gamma camera with a 3 mm thick GAGG scintillator was investigated, starting by the analyzes of the γ-rays depth of interaction (DoI) within the scintillator crystal and its implication on the SiPMs light response functions. The accuracy of the LRFs determine the event reconstruction quality.

Note that a 3 mm thick scintillator was selected to ensure a γ-rays collection efficiency of more than 80%, as a significant amount of 140 keV γ-rays have a depth of interaction within the crystal which goes up to 3 mm. **Fig.3.30 a** shows the histogram of the interactions depth. It was defined that Z = -1.5 mm is the entrance face of the GAGG crystal (so, the "bottom" region is the range -1.5 mm $<$ Z $<$ -0.5 mm), Z = 0 mm is the crystal center (the "central" region is the range -0.5 mm $<$ Z $<$ 0.5 mm) and Z = 1.5 mm is the crystal edge closer to the SiPMs (the "top" region is the range 0.5 mm $<$ Z $<$ 1.5 mm). The larger fraction of the interactions occur in the first third of the crystal depth, the bottom region.

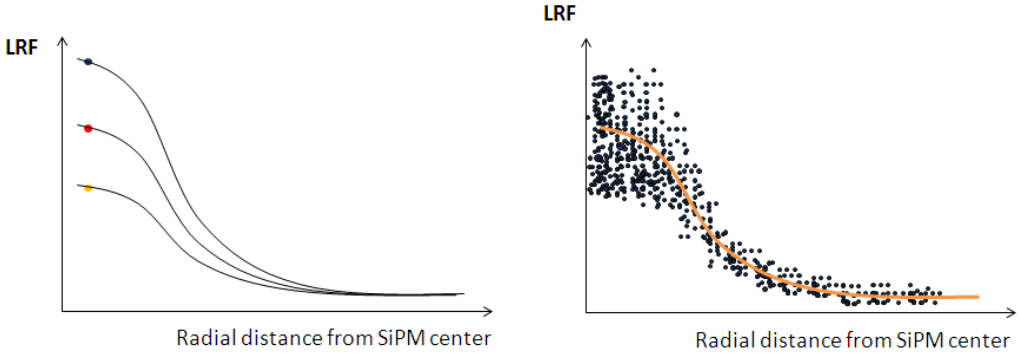

(a) (b)

Figure 3.31: Depth of interaction of γ-rays in a 3 mm thick GAGG scintillator. **a**: LRFs curves that could be estimated from data from three different scintillator regions (identified with colored dots). The yellow is the region most far from the SiPMs, the red is the central region of the scintillator and the blue is the scintillator edge closer to the SiPMs. **b**: Representation of the data points corresponding to reconstructed positions of events along all the scintillator depth which are used to fit the LRF curve.

The lightguide thickness t allows to control the distance between the interaction positions and the SiPMs, defining also the solid angle α subtended between the two, as shown is in **Fig.3.30 b**, a schematic cut of part of the gamma camera, only representing the scintillator, the lightguide and the SiPMs array. **Fig.3.31 a** shows a representation of the LRF curves that could be estimated from the reconstructed positions if they correspond exclusively to the interaction positions of each one of the three regions represented in **Fig.3.30 b**. The colored points in the curves indicate what are the correspondent scintillator regions of the reconstructed positions which would result in that particular LRF (illustrative examples). The LRF is strongly dependent on the DoI. However, commonly there is no information on the scintillation events DoI in the gamma camera systems. **Fig.3.31 b** represents the LRF and the data used to estimate it, for the case in which there is no information on the scintillation events DoI, so all the events are used without any filtering based on the interaction depth. In this case, the LRF curve fits better the data which corresponds to events in the center of the scintillator than for that in the edge regions.

This was verified with simulation data, filtering out events from the bottom and top regions (in a 3 mm thick GAGG and using a 1.0 mm thick lightguide). The LRFs were obtained from data from the uniform irradiation of the entire camera field-of-view (33.2 $\times$ 33.2 mm^2) with 100 thousand 140 keV γ-rays. The analysis on the reconstruction performance was only performed for a quarter of the camera area (16.6 $\times$ 16.6 mm^2 in the upper-right corner). The emission of one million 140 keV γ-rays uniformly distributed over that area was simulated. The XY density plot of the reconstructed positions using the LRFs estimated with all events but filtering out the scintillation positions out of the central region is shown in **Fig.3.32 a**.

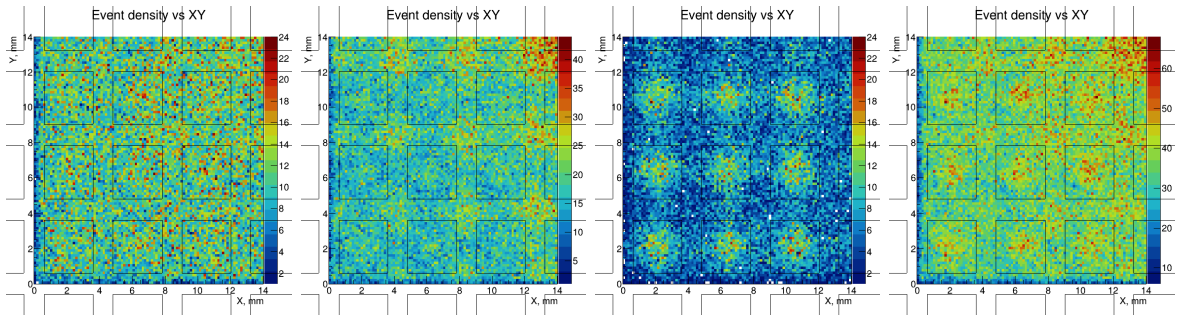

(a) (b) (c) (d)

Figure 3.32: Density plot of reconstructed positions (3 mm thick GAGG and 1.0 mm thick lightguide). **a**: Using only events from the central region of the scintillator; **b**: Using only events from the bottom region of the scintillator; **b**: Using only events from the top region of the scintillator; **d**: Using all events.

In this case, the resulting image is uniform, with a low degree of distortions. On the other hand, when only the bottom or top events are reconstructed, the modulation of the events density plot is quite noticeable, as can be seen in **Fig.3.32 b** and **c**. A pattern is apparent: for the bottom events, there is a higher events density around the SiPMs edges, rather than in the SiPMs centers (**Fig.3.32 b**), while for the top events the opposite occurs (**Fig.3.32 c**). The image which results from the reconstruction of all interaction positions in the scintillator is shown in **Fig.3.32 d**. The event positions wrongly reconstructed due to inaccurate LRFs either due to bottom or top events compensate each other and the resulting image has a lower degree of distortions than that with only bottom or top events.

The estimated LRF taking into account all scintillation events in the 3 mm thick GAGG crystal is not so precise as for a thinner GAGG crystal or for a crystal with higher attenuation coefficient, in which a large fraction (vast majority) of the interactions would occur in the bottom region. The lightguide thick t can be used to control the LRFs quality, which is particularly influenced by the distance between the top events and the SiPMs array. This distance defines the solid angle α from the top scintillation positions into the SiPMs. The larger the angle α is, the more the photons collected by the SiPMs in the proximity of the scintillation position are. If the lightguide is too thin and so α is too large, the number of collected photons is much higher than the expected number of photons given by the LRF estimated using events from all DoIs, and consequently the reconstructed position would be far from the real scintillation position. **Fig.3.33** shows the average difference between the reconstructed positions and the true positions (”delta” along X direction, ”delta X”) for a lightguide thickness of 0.3 mm, for bottom, central and top events separately and also when all events are included. It can be observed that the top events result in higher distortion than the bottom ones, what is explained by the reasoning on the solid angle given above.

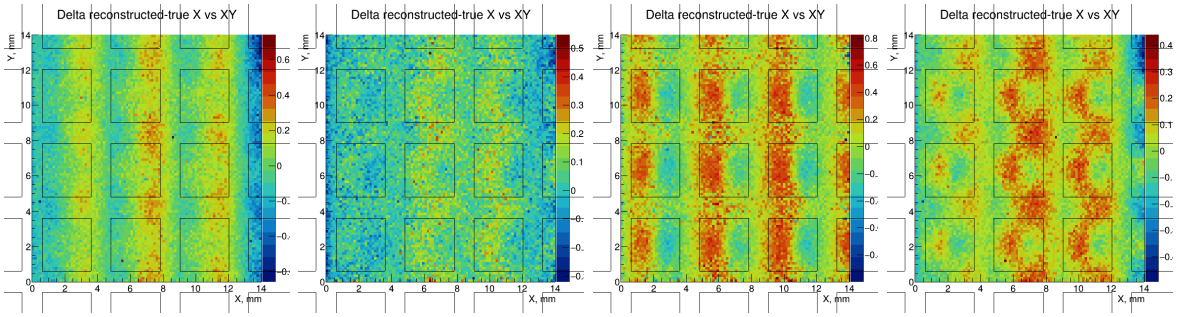

(a) **(b)** **(c)** **(d)**

Figure 3.33: XY density plot of the average differences between the X coordinate of the reconstructed and true positions (3 mm thick GAGG and 0.3 mm thick lighguide). **a**: Using only events from the bottom region of the scintillator; **b**: Using only events from the central region of the scintillator; **c**: Using only events from the top region of the scintillator; **d**: Using all event.

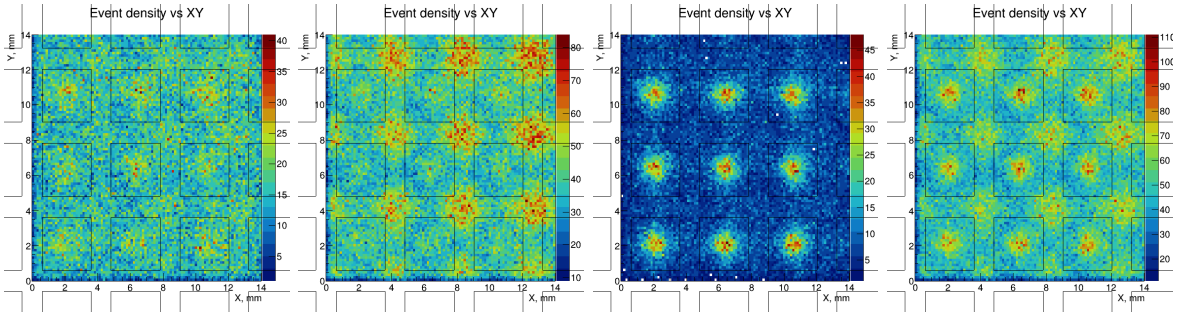

(a) **(b)** **(c)** **(d)**

Figure 3.34: Density plot of reconstructed positions (3 mm thick GAGG and 0.3 mm thick lightguide). **a**: Using only events from the central region of the scintillator; **b**: Using only events from the bottom region of the scintillator; **c**: Using only events from the top region of the scintillator; **d**: Using all events.

Fig.3.34 shows the reconstructed positions from simulation data for the 3 mm GAGG and a lightguide with thickness of 0.3 mm. The reconstructed positions that correspond to the bottom, central and bottom events are shown separately in **Fig.3.34 a, b** and **c** and all together in **Fig.3.34 d**. When comparing with **Fig.3.32** (for lightguide of 1.0 mm) it is apparent that the use of a thinner lightguide results in a higher degree of distortions (non-uniformity of the flood field image).

Other simulation was performed to further demonstrate that thinner lightguides result in stronger distorted reconstructed positions. The irradiation of the camera through a diagonal slit was performed for two lightguide thicknesses, 0.3 mm and 0.8 mm. **Fig.3.35** presents the XY density plot of the reconstructed positions. Even visually one can realize that the distortions are stronger for 0.3 mm thick lightguide. For the 0.8 mm thick case, if only the bottom and top events are reconstructed separately, distortions are apparent, as one can see in **Fig.3.35**. However, when using all events, the number of misreconstructed events from the

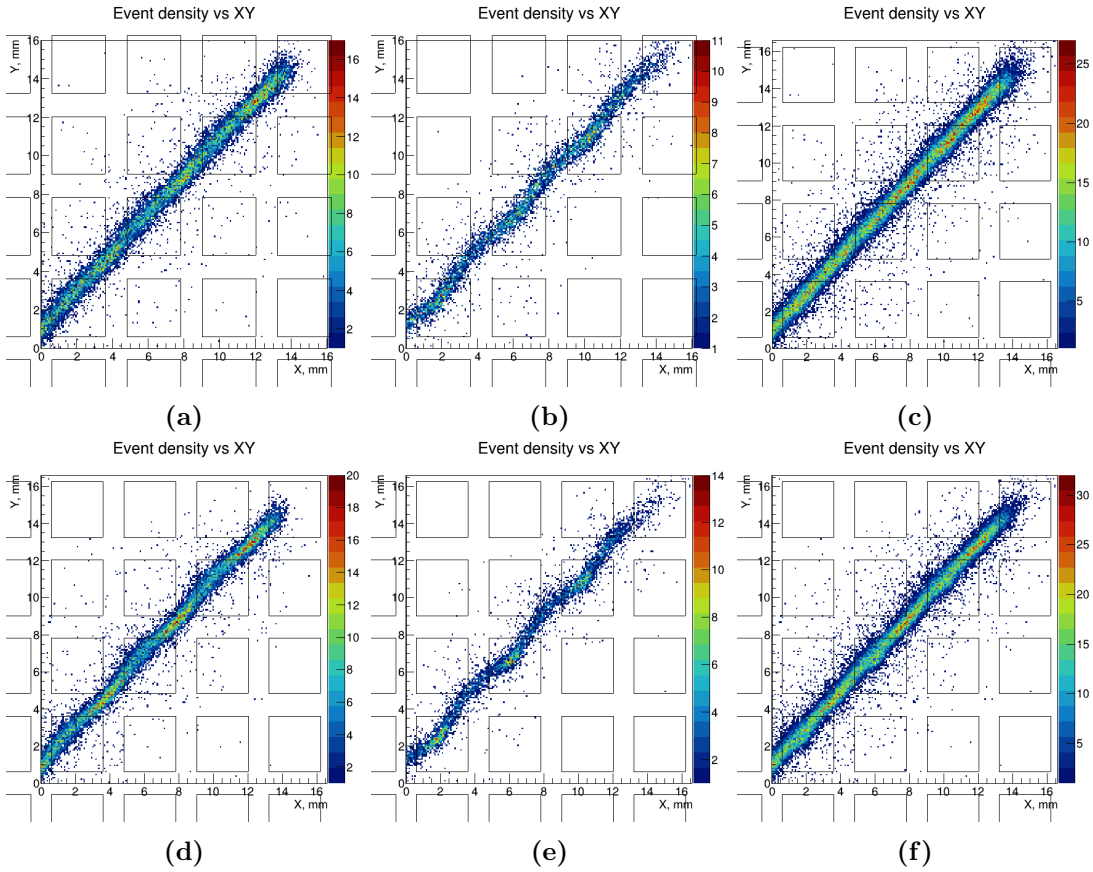

Figure 3.35: XY Density plot of reconstructed positions of a ^{99m}Tc source projection through a diagonal slit (3 mm thick GAGG). **a**, **b** and **c**: 0.8 mm thick lightguide; **d**, **e** and **f**: 0.3 mm thick lightguide; **a** and **d**: Using only events from the bottom region of the scintillator; **b** and **e**: Using only events from the top region of the scintillator; **c** and **f**: Using all events.

bottom and top region cancel out each other, resulting in a quasi uniform image of the XY density plot of the reconstructed positions (**Fig.3.35 c**). Contrarily, for the 0.3 mm lightguide the distortions are still strong when reconsctruction events from all DoI, as one can observe in **Fig.3.35 f**.

Simulations were performed for the range of thicknesses between 0.2 mm and 1.5 mm in order to find the lightguide thickness for which the distortions induced by the top and bottom events start compensate each other to give an uniform density plot of the reconstructed positions. That thickness value would be the optimal to improve the image uniformity, which is a very important parameter for the physician analyzing clinical nuclear images. Other parameter that was taken into account was the spatial resolution, which should be the best possible whenever a good uniformity is guaranteed.

A set of scripts were run to automatically perform the procedures to measure the performance of the gamma camera for several thicknesses of the lightguide. The parameters that were optimized were the distortions and the spatial resolution in a 29 x 29 mm^2 FOV area.

The optimization cycle has the following steps:

- Configure the camera: set the lightguide (LG) thickness
- Configure source shape/size: squared for flood irradiation
- Flood field simulation (250 thousand γ-rays of 140 keV over the entire camera FOV)
- Produce LRFs and save them
- Calculate distortions
  - Irradiate uniformly the upper-right quarter of the camera (16.6 $\times$ 16.6 mm^2) with 140 keV γ-rays
  - Save in a 100 $\times$ 100 matrix (100 bins in both X and Y direction) the differences between the reconstructed X coordinate and the true interaction X coordinate ("delta X"). In each (X, Y) bin is saved the average delta X for all simulated emission positions which belong to that bin.
  - Calculate the average delta X in the 100 $\times$ 100 matrix.
- Calculate spatial resolution map:
  - Cycle to simulate and save 1250 pencil-beam sources of 140 keV per node in a grid of 15$\times$15 nodes (1 mm pitch)
  - For each node: create histogram of the reconstructed positions (projection along X) and fit a Gaussian curve to that histogram
  - Calculate the FWHM

The scatter plot in **Fig.3.36** shows the average distortions along the X direction (delta X) and the average spatial resolution for the gamma camera configurations with different lightguide thicknesses. It can be seen that the thinner the lightguide is, the higher is the delta X (higher level of distortions) and the better is the spatial resolution (lower FWHM). Commonly, the best possible spatial resolution is desired, however, the choice of the lightguide thickness should be based on the acceptable level of distortions. In the case of the 3 mm thick GAGG crystal, it was verified that thinner lightguides (e.g. 0.3 mm or 0.5 mm) offer higher distortion level than thicker ones (e.g. 1.0 mm or 1.2 mm) due to higher misreconstructions of the event positions in the top of the crystal.

Fig.3.37 shows the XY events density plot of the reconstructed grid of 15 $\times$ 15 pencil-beam sources for three lightguide thicknesses: 0.3 mm, 0.5 mm and 0.8 mm. For all cases, a significant amount of distortions is visible to the naked eye all over the camera, mainly for

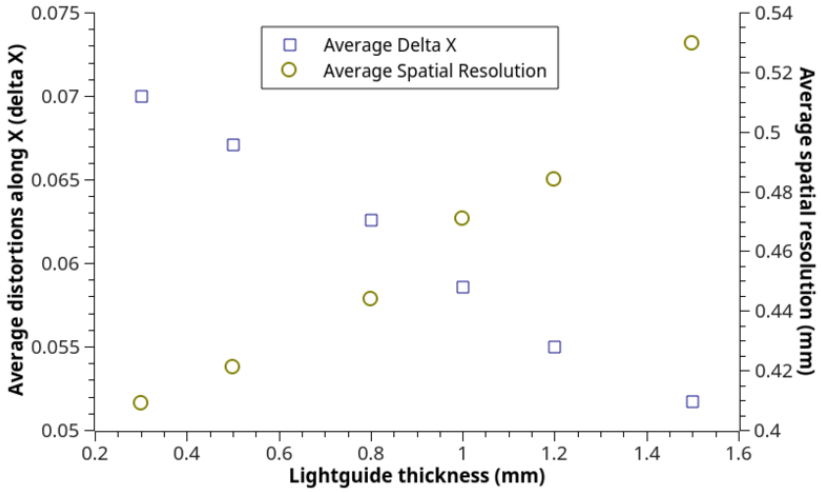

Figure 3.36: Average distortions (mm), delta X, and average spatial resolution along X (mm) of a 3 mm thick GAGG based gamma camera for different thicknesses of the lightguide. The presented results are for the thicknesses: 0.3 mm, 0.5 mm, 0.8 mm, 1.0 mm, 1.2 mm and 1.5 mm.

the two thinner lightguides. The distortions are more intense in the periphery of the FOV under analysis (29 x 29 mm^2), but even in the central region several reconstructed pencil-beam sources appear with elliptic shapes instead of the expected circular shape. Note that the images show the upper-right corner of the gamma camera. The zero represents the center of the camera. The red circles indicate the true positions.

Fig.3.38 shows the reconstructed grid of pencil-beam sources for the lightguide thicknesses of 1.0 mm, 1.2 mm and 1.5 mm. For the three thicknesses, the reconstructed pencil-beam sources have a circular shape for the whole FOV, except in the most outer line of pencil-beam sources (either in X and in Y). Although the lightguide thicknesses of 0.3 mm and 0.5 mm give the best spatial resolutions, for the experimental prototype it was selected the lightguide 1.0 mm thick. There are two reasons for this choice. One is that for 0.3 mm and 0.5 mm cases the distortions are significant (even visually - several elliptic shapes instead of circles). The other reason to select 1.0 mm lightguide is that the standard dimensions of plexiglass plates in the interested thickness range are 0.5 mm and 1.0 mm. If 0.8 mm was available, it would be also a good choice.

3.4 Collimators design optimization

The collimators should be designed according to the requirements of specific imaging applications. The protocols of clinical exams, namely the radiotracer dose, should be taken into account, for instance to estimate the time needed to acquire high contrast images for different collimator designs. The organ uptake percentage for the particular radiotracer is also an

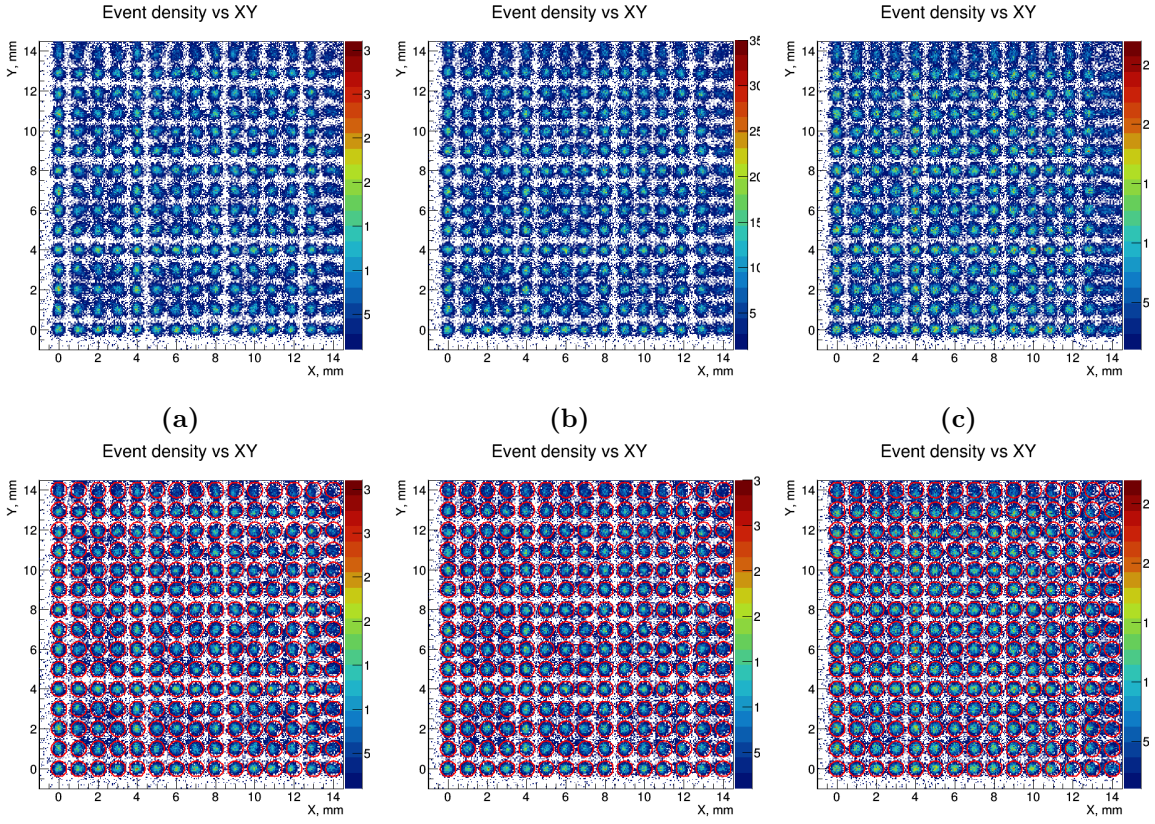

Figure 3.37: XY Density plot of the reconstructed grid of 15 × 15 pencil-beam sources (lightguide thicknesses: 0.3 mm to 0.8 mm). **a**: Lightguide thickness = 0.3 mm; **b**: Lightguide thickness = 0.5 mm; **c**: Lightguide thickness = 0.8 mm; **d**: Lightguide thickness = 0.3 mm with true positions (red circles). Note that besides the elongation of the circles, from X = 11 and Y = 11, the reconstructed events are out of the true position circle; **e**: Lightguide thickness = 0.5 mm with true positions (red circles); **f**: Lightguide thickness = 0.8 mm with true positions (red circles).

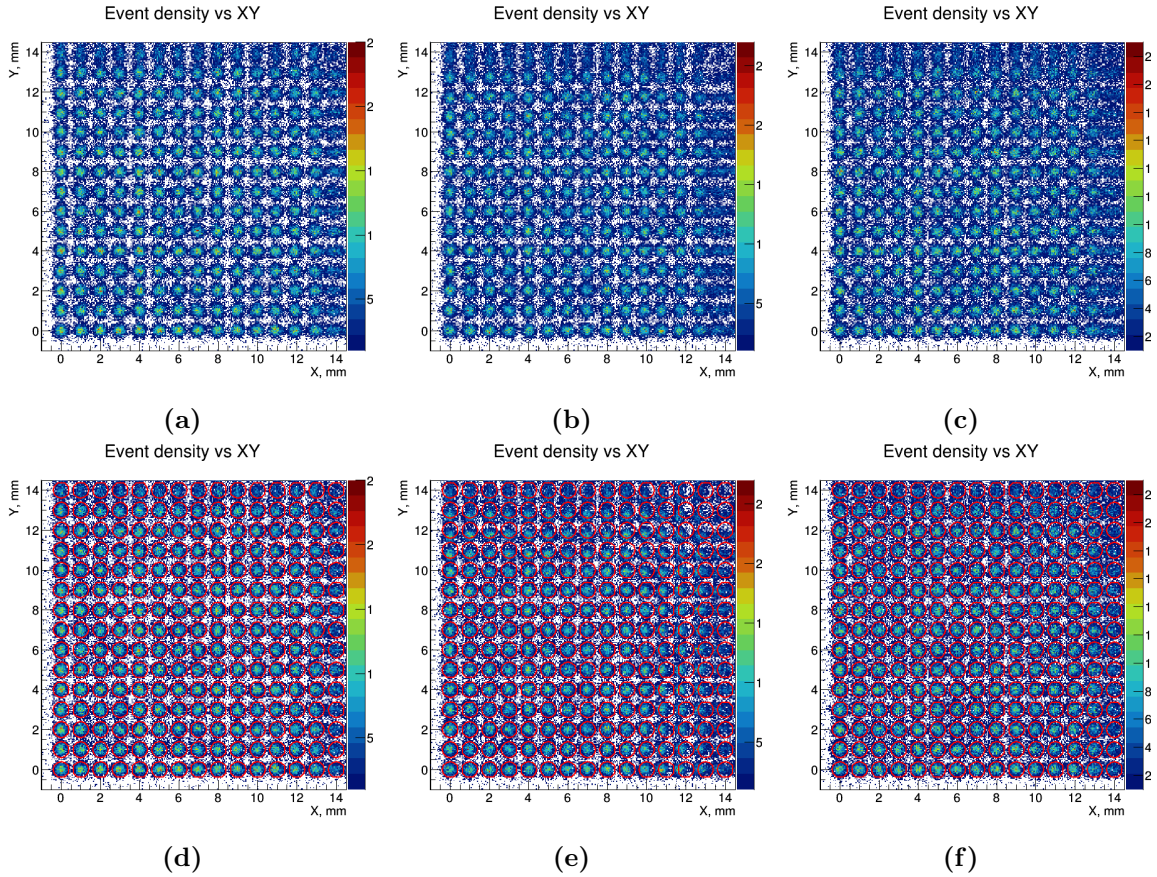

Figure 3.38: XY Density plot of the reconstructed grid of 15 × 15 pencil-beam sources (lightguide thicknesses: 1.0 mm to 1.5 mm). **a**: Lightguide thickness = 1.0 mm; **b**: Lightguide thickness = 1.2 mm; **c**: Lightguide thickness = 1.5 mm; **d**: Lightguide thickness = 1.0 mm with true positions (red circles); **e**: Lightguide thickness = 1.2 mm with true positions (red circles); **f**: Lightguide thickness = 1.5 mm with true positions (red circles).

important information to know, as well as the working distance from source to collimator and distance from the collimator to the detector. With that information, spatial resolution and sensitivity of the collimator can be calculated and optimized for particular imaging scenarios.

For sentinel node detection and thyroid imaging (radiotracer with ^{99m}Tc) the required system spatial resolution (which would improve the capabilities of the cameras commonly available at nuclear imaging clinical departments) is 5 mm for a distance of 50 mm from the source to collimators face [193]. The sensitivity should be at least 220 cpm/μCi, which is the same as 100 cps/MBq ($g = 0.0001$), with "high-resolution collimator" in order to keep the acquisition times in the sub-minute range. This value is also above the sensitivity specified in **table 3.1**, 150 cpm/μCi, which is the same as 67.5 cps/MBq.

3.4.1 Design and optimization of a parallel-hole collimator

Fig.3.39 presents the collimator sensitivity *vs* spatial resolution trade-off curves as a function of the collimator thickness (hole height) for a pure tungsten parallel-hole collimator with septa of 0.3 mm. The hexagonal hole characteristic dimension d, which refers to the cross section of the hole, varies from 0.5 mm to 0.9 mm with 0.1 mm step. Each hole dimension has its respective trade-off curves, identified with different symbols. Septa widths smaller than 0.3 mm and hole dimensions below 0.5 mm were not considered as viable, after the conversation with the representatives of some tungsten transformation companies. The source is assumed to be at 50 mm from the collimator face. Superimposed to the trade-off curves, regions of acceptable spatial resolution and sensitivity were defined using transparent colors, based on the requirements stated above (resolution better than 5 mm at 50 mm from the collimator and sensitivity higher than 0.0001).

To accomplish with the requirement of a system resolution better than 5 mm (with the source at 50 mm) several options can be selected, depending on how thicker one wants the collimator to be. The thicker, the better the spatial resolution. For example, for a hole height longer than 11.5 mm, even the larger hole can lead to resolutions below 5 mm. On the other hand, collimators with thinner hole have an acceptable sensitivity only for short hole heights. For example, for $d = 0.6$ mm, the maximum hole height is 11 mm and for $d = 0.5$ mm the hole cannot be longer than 8.6 mm. Furthermore, with shorter holes size the collimator thickness can be thinner for the same spatial resolution, which means lighter and more compact, which is important for a hand-held gamma camera.

Table 3.6 presents seven parallel-hole collimator configurations (hole size and length, always for 0.3 mm septa) that result in the maximum sensitivity, for a spatial resolution no larger than 5 mm at 50 mm. **Table 3.7** presents for each hole size, the hole length required to

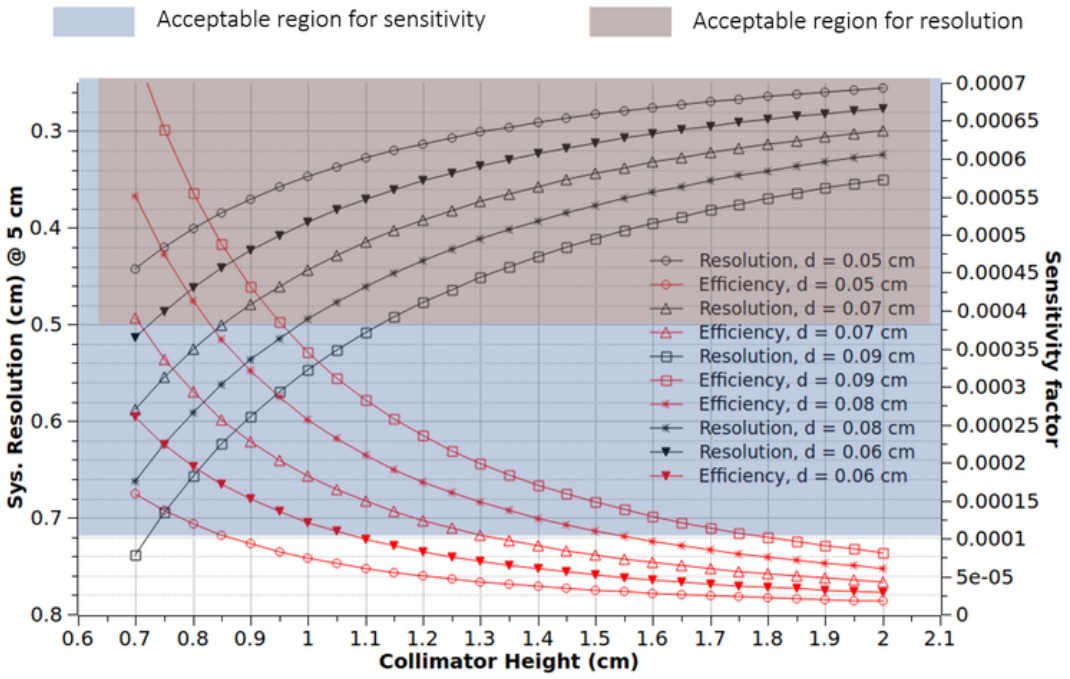

Figure 3.39: Trade-off curves for a pure tungsten parallel-hole collimator. The sensitivity and the system resolutions is plotted for 5 hole dimensions (distance between opposite faces of the hexagonal hole): 0.5 mm , 0.6 mm, 0.7 mm, 0.8 mm and 0.9 mm.

achieve the best possible spatial resolution, guaranteeing the minimum acceptable sensitivity of 100 cps/MBq.

Hole diameter d (mm)	Hole length a (mm)	R_{sys} (mm)	Sensitivity (cps/MBq)
0.5	6.5	4.9	186.5
0.5	8	4.1	119
0.5	16	2.2	27.7
0.6	8	4.9	194.9
0.7	9.5	4.8	202.7
0.8	11	4.9	209.6
0.9	12.5	4.9	215.7

Table 3.6: Spatial resolutions and sensitivities for six parallel-hole configurations. For different hole diameters were chosen the hole lengths that result in the highest sensitivity for the worst acceptable resolution.

The interest in a compact camera defined the choice of the hole dimension d for the parallel-hole collimator prototype. Hence, $d = 0.5$ mm was selected. After the trade-off curves analysis, the selected hole length a was 8 mm, which provides 4.1 mm spatial resolution and a sensitivity of 119 cps/MBq, both values respecting the defined requirements. A slightly better resolution of 3.8 mm could be achieved with a hole lenght of 8.5 mm, decreasing the sensitivity to the minimum acceptable value of 100 cps/MBq. To work within some margin above the minimum

Hole diameter d (mm)	Hole length a (mm)	R_{sys} (mm)	Sensitivity (cps/MBq)
0.5	8	4.1	119
0.5	8.5	3.8	100
0.6	10.5	3.8	100
0.7	13	3.7	100
0.8	15	3.7	100
0.9	17.5	4.9	100

Table 3.7: Spatial resolutions and sensitivities for six parallel-hole configurations. For different hole diameters were chosen the hole lengths that result in the best spatial resolution for the minimum acceptable sensitivity (100 cps/MBq).

sensitivity, this option was not chosen. It should be noted that if for a particular application a spatial resolution better than 4.1 mm is desired with no special restrictions on the sensitivity, two 8 mm thick collimators can be attached, doubling the hole height (16 mm). This solution provides a resolution of 2.2 mm and a sensitivity of 27.7 cps/MBq for a source at 50 mm from the collimator face.

Clinical imaging studies (thyroid) When ^{99m}Tc is used for clinical thyroid exams, an activity of 370 MBq (10 mCi) is frequently injected into the patient [194, 195, 196, 197]. The radionuclide uptake by the thyroid 20-30 minutes after injection varies typically between 0.3% and 3% [193]. For the parallel-hole collimator with $d = 0.5$ mm and $a = 8$ mm (the prototype), it means a maximum detection rate of 132.1 cps and 1321 cps respectively.

The maximum detection rate at an activity of 370 MBq is presented in **table 3.8** for more collimator geometries, to give an idea of the rates that can be achieved during thyroid examination depending on the collimator design. The table presents the spatial resolution (with the source at 50 mm from the collimator), the sensitivity and the maximum detection rate (cps) for six collimator geometries. Three collimators have $d = 0.5$ mm and three $d = 0.8$ mm hole sizes. For the two cases, three hole lengths a were considered: 8 mm, 12 mm and 16 mm.

For the same collimator geometries, **table 3.9** shows the time (in seconds) required to acquire 100 thousand events for a relatively low activity of 3 mCi. With 100 thousand events a high quality image can be produced. For all cases in the table, the time required to acquire 100 thousand events is clearly below 60 seconds, which was indicated by the hospital imaging experts as the upper limit for the acquisition time in lymphoscintigraphy. For the dimensions chosen for the parallel-hole prototype, 7.6 seconds are required. The "double" collimator ($a = 16$) requires 32.6 seconds. All the collimators with the larger hole $d = 0.8$ mm in **table 3.9** require less than 10 seconds to acquire 100 thousand events (e.g. 2.18 seconds when $a =$

8 mm), with the drawback of worsen the spatial resolutions when compared with collimators with $d = 0.5$ mm for the same hole lengths (**table 3.8**).

Coll. Config	System Res. (mm)	Sensitivity (cps/MBq)	If injected 370 MBq (10 mCi)	
			cps for Thyroid uptake 0.3%	**cps** for Thyroid uptake 3%
d = 0.5 mm a = 8 mm	4.1	119	132.1	1321
d = 0.5 mm a = 12 mm	2.84	49.9	55.39	553.9
d = 0.5 mm a = 16 mm	2.2	27.7	30.75	307.5
d = 0.8 mm a = 8 mm	6.54	408.6	453.5	4535
d = 0.8 mm a = 12 mm	4.54	172.9	191.9	1919
d = 0.8 mm a = 16 mm	3.57	95	105.5	1055

Table 3.8: Parallel-hole spatial resolution (at 50 mm), sensitivity and counts per second (cps) for some collimator configurations and example activities. An activity of 370 MBq (10 mCi) is given as an example of a clinical dose for thyroid imaging. The cps rates achieved by the parallel-hole when the radionuclide uptake is 0.3% and 3% (typical uptake percentages) are presented.

Coll. Config	Time(s) required to acquire 100k events
d = 0.5 mm a = 8 mm	7.6
d = 0.5 mm a = 12 mm	17.9
d = 0.5 mm a = 16 mm	32.6
d = 0.8 mm a = 8 mm	2.18
d = 0.8 mm a = 12 mm	5.2
d = 0.8 mm a = 16 mm	9.4

Table 3.9: Time (minutes) required to acquire 100 thousand events for six configurations of the parallel-hole and for a radionuclide activity of 3 mCi.

3.4.2 Design and optimization of a pinhole collimator

The optimization of the pinhole collimator was made considering that a magnification of about twice ($M = 2$) would be useful for the imaging of small sentinel nodes and that for the FOV of the designed gamma camera, de-magnification of about an half ($M = 0.5$) would be useful in thyroid imaging. The requirement of a spatial resolution better than 5 mm for a source 50 mm far from the detector was also taking into account, as well as the requirement on a minimum sensitivity factor g of 0.0001 (or 100 cps/MBq).

The pinhole collimator design was the same used in the **section 3.2.6.2**, with acceptance angle of $\alpha = 90°$. This angle was selected to reduce the influence of the parallax effect on event position reconstruction (**section 2.7.2**) when compared with the influence that higher angles would have. On the other hand, $\alpha = 90°$ offers a reasonable trade-off between the sensitivity and spatial resolution, in comparison with other acceptance angles in the range $\alpha = 60°$ to $\alpha = 120°$, as can be seen in **table 3.10** for a hole diameter of 1 mm. The considered collimator material was WC alloy doped with cobalt (94.5% WC + 5.5% Co), with density of 14.95 g/cm^3, which was available for the pinhole collimator prototype production (**section 6.1.2**).

Accep. Angle (°)	60	70	80	90	100	110	120
Sensitivity factor g	0.000118	0.000165	0.000211	0.000247	0.000269	0.000273	0.000257
Spatial Res. (mm)	2.50	2.57	2.64	2.73	2.84	2.97	3.14

Table 3.10: Pinhole collimator sensitivity and spatial resolution as function of the acceptance angle. The magnification factor is $M = 1$.

Fig.3.40 shows the pinhole collimator trade-off curves (sensitivity *vs* spatial resolution) as a function of the aperture diameter for three source-to-aperture distances ($z = 47.0$ mm, $z = 23.5$ mm and $z = 11.75$ mm) and a fixed focal length ($f = 23.5$ mm). The three ratios $M = f/z$ result in three magnification factors: $M = 0.5$, $M = 1$ and $M = 2$.

For $M = 1$, the overall distance source-to-detector is 47 mm, close to 50 mm, the limit distance established to check the spatial resolution (should be < 5 mm). As can be seen in the trade-off curves (**Fig.3.40 b**), hole diameters below $d = 2.2$ mm can offer a resolution better than 5 mm. The sensitivity factor is higher than the limit of 0.0001 for all represented hole diameters except $d = 2.5$ mm. A magnification of $M = 0.5$ is achieved when the distance source-to-detector is 70.5 mm. In this case d should be thinner than 1.25 mm to accomplish the resolution criteria, but also larger than 1.5 mm to have a sensitivity higher than 0.0001 (**Fig.3.40 a**). This means that for the used focal length $f = 23.5$ mm, $M = 0.5$ is not convenient to be used. However, if the focal length is reduced to $f = 18$ mm, $M = 0.5$ is achieved with $z = 36$ mm and a overall distance source-to-detector of 54 mm. For this geometry, if the hole diameter is 1 mm, the sensitivity is already above 0.0001 and the resolution is 4.26 mm, within the acceptable limit. For $M = 2$, keeping the focal length $f = 23.5$ mm, the overall distance source-to-detector is 35.25 mm. As can be seen in the trade-off curves (**Fig.3.40 c**), the hole diameter can be anywhere in the presented range (0.3 mm to 2.5 mm) to accomplish the stated limits. From the trade-off curves analysis a hole diameter $d = 1$ mm was selected for the prototype of the pinhole collimator.

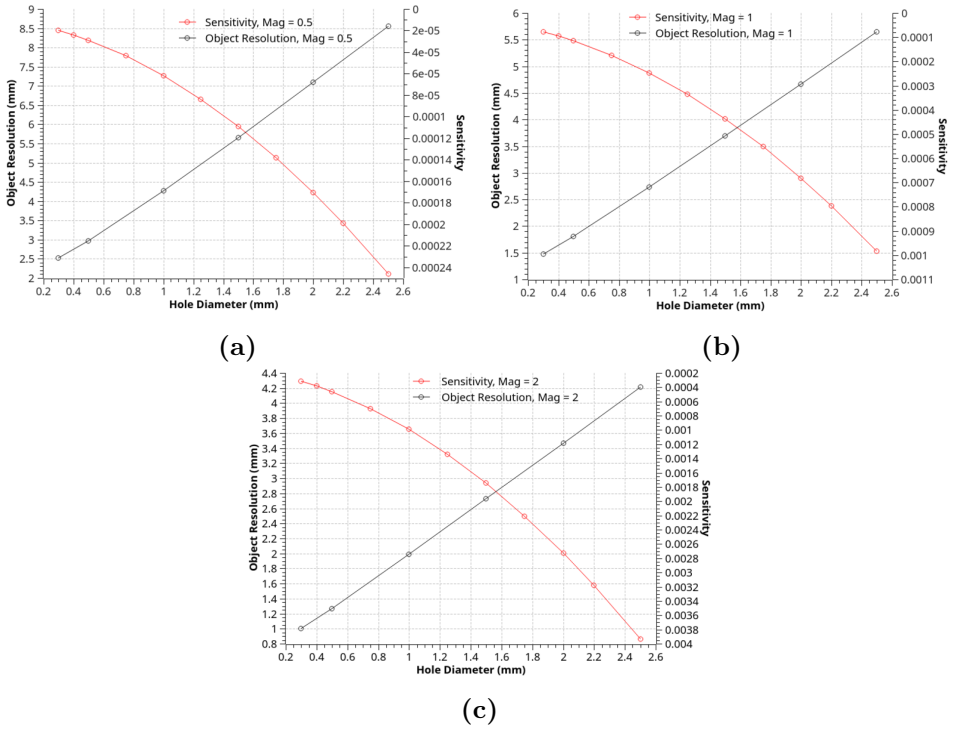

Figure 3.40: Sensitivity and spatial resolution trade-off curves of the pinhole collimator (as function of the aperture diameter) a: Magnification = 0.5; **b**: Magnification = 1; **c**: Magnification = 2.

Keeping the focal length $f = 23.5$ mm, for a overall distance source-to-detector of 50 mm (the distance of interest to evaluate the collimators performance acceptability in this work), z must be 26.5 mm. At this distance the magnification factor is $M \approx 0.89$. For a hole diameter $d = 1$ mm, the resulting 2.92 mm spatial resolution is clearly below 5 mm and the resulting sensitivity factor of 0.000195 (195 cps/MBq) is also above the minimum sensitivity requirement.

Table 3.11 presents the object resolution, the sensitivity (cps/MBq) and the time required to acquire 100 thousand events for pinhole collimators with hole diameter varying from 0.3 mm to 2.5 mm and an activity of 3 mCi. Only for the diameter of 1 mm three different magnification factors are considered. For a fixed magnification, the thinner the pinhole diameter, the better the resolution and the worse the sensitivity, as expected.

It is known that the pinhole collimator sensitivity is decreased when the source is shifted from the collimator central axis to the edges [198]. A common way to minimize this angle-dependence sensitivity is to use a channel-edge instead of a knife-edge (**see Fig.2.16**). However, the channel-edge can block γ-rays from the cone edges, if the acceptance angle is too large, reducing the useful field-of-view of the camera. Other groups found that a 0.5 mm channel height offers a good trade-off between the improvement in the resolution and a decrease in the sensitivity, while minimizing the sensitivity angle-dependence and maximizing the useful

FOV [118, 199, 200]. Thus, the pinhole collimator that was ordered to be manufactured has an acceptance angle $\alpha = 90°$ and a hole diameter $d = 1$ mm with a channel-edge 0.5 mm height.

Pinhole diameter (mm)	Magnification factor	Obj. spatial resolution	Sensitivity (cps/MBq)	Time (s) to acquire 100 k events
0.3	2	0.99	321	2.81
0.5	2	1.27	470	1.92
1	0.5	4.28	63	14.37
1	1	2.74	251	3.59
1	2	2.0	1002	0.89
1.5	2	2.73	1761	0.51
2	2	3.47	2746	0.33
2.5	2	4.22	3958	0.23

Table 3.11: Pinhole spatial resolution, efficiency and time to acquire 100 k events for eight different pinhole configurations and a radionuclide activity of 3 mCi.

4

Readout system

4.1 Features of the required front-end and DAQ electronics

The readout system selected for this work should be suitable for small field-of-view gamma cameras (e.g. sentinel node detection or thyroid imaging), which commonly use dozens of photosensors. There are solutions available in the market that contain all the required components of a readout system (**section 2.3.2**): the front-end electronics (FEE) for signal amplification and shaping, the trigger circuit and the data acquisition system (DAQ) for the recording of a value proportional to the signal generated in each photosensor. Either the complete solution or the individual components (FEE, trigger circuit and DAQ) are sold as Application-Specific Integrated Circuits (ASICs). There are vendors that allow to customize the components. In this case, the implementation is not made in an ASIC but, instead, in a Field-Programmable Gate Array (FPGA) which has several programmable logic blocks, in the hardware level. Evaluation boards are frequently made available by vendors in order to make easier to start using and to test their chips. Those boards typically consist of: 1) a DAQ chip, sometimes with the trigger circuit included, 2) ports to connect either the FEE circuit or directly the sensors, if the FEE is also included in the board, and 3) a communication protocol and respective ports to export data for a processing unit.

The most relevant features considered in the selection of the readout system are summarized in **table 4.1**. The first parameter in the table is the number of channels. As the camera was designed to have 64 SiPMs, at least 64 channels are needed. If later a 3D reconstruction is desired, two layers of SiPMs (one in the top and other in the bottom of the crystal) should be considered and in that case a minimum of 128 would be required. The number of analog-to-digital converters (ADCs) can be either 64, one per SiPM, or less, depending on the digitization strategy. For example, some solutions use only one ADC to digitize the signals from all sensors. The signal should be coded at least with 10 bits to have 1024 quantisation levels.

Requirements	Required	Desirable
Number of channels	64	64 + Sum signal channel
ADC	10 bits	12 bits
Sustainable rate with 64 channels	10 kHz	20 kHz
Integration time	Adjustable in range: 50 ns - 500 ns	10 ns - 10μs
Trigger	sum channels fast output + external trigger	Sum or individual, CFD[a]
Imput polarity	"+" and "-"	"+" and "-"
Electronic noise	< 100 000 e	< 100 000 e
Crosstalk	< 1%	< 1%
Driver	C++	Opensource, Windows + Linux
Firmware	Not hardware protected	Open source
Connection	USB 3.0	Ethernet

Table 4.1: Readout system requirements

[a] "CFD" stands for "constant fraction discrimination.

This value was selected considering the dynamic range of the expected signals. The electronic noise, so the lower limit in the range of expected signals, should be at most 100 kilo-electrons (10^5e). For the energy of γ-rays (140 keV) used in this work, and for the light yields of the scintillators (see GAGG and LYSO in **table 2.1**) and photon detection efficiencies of the photosensors (see SensL 30035 SiPM in **Fig.3.3**) used in the prototypes, one can expect no more than ≈100 photons collected by a photosensor[1]. As the photosensors have a gain of 10^6, the maximum expected output signal is 100 mega-electrons (100 Me). The required dynamic range is, thus, 10^5e - 10^8e. Each quantisation level should be higher than the noise level. Hence, the ratio between the two limits of the dynamic range (10^8e / 10^5e) which is 1000 gives the number of required quantisation levels. The number of bits need to code at least 1000 levels is 10 (1024 levels). If possible, 12 bits is a better choice, especially if the detection of higher energy γ-rays may be of interest in the future. In the case of waveform acquisition systems like TRB3, the requirement on the number of bits is relaxed as many samples are summed to get the integral. For small FOV gamma cameras an acquisition rate of 10 kHz gives a large margin for the typical activities used in the imaging examinations, so the new system should have this minimum counting rate, but preferably 20 kHz.

An adjustable integration time in the range of 50 ns – 500 ns was set as a requirement for research systems, in order to enable the system to use gamma cameras with a wide range

[1] The photons are emitted isotropically, from an optimistic estimation. The fraction F of the photons that reach the photosensor depends on the solid angle subtended by the photosensor window in respect to the scintillation position. The maximum number of collected photons can be roughly calculated multiplying the number of photons given by the factor "light yield × energy" by the fraction F and by the PDE of the photosensors.

of scintillators. The decay time of scintillators typically used in small FOV gamma cameras are in the order of dozens of *n*s (e.g. see $LaBr_3$, CeF_3, LYSO and GAGG in **table 2.1**). Ideally, the readout should be prepared to be used for laboratory studies (research work) that might require an adjustable integration time of the scintillation signal, for instance when large cameras are used, because these cameras commonly have scintillators with decay times of hundreds of *n*s (e.g. see $Bi_4Ge_3O_{12}$, CsI(Tl) and NaI(Tl) in **table 2.1**). Using a fixed large integration time is not convenient because more noise would be included in the integrated signal and the pile-up probability also increases.

The event triggering can be performed based on the comparison of a threshold value either with the individual SiPM signals or with the sum of all signals (**section 2.3.3**). The constant fraction discrimination method is another possibility.

The system should be prepared to handle both positive and negative input polarities, to be able of work with both common anode and common cathode SiPM arrays. As a typical intrinsic gain of SiPMs is more than 5×10^5, the acceptable level of the electronic noise in the readout system is assumed to be up to 10^5 electrons rms. In this case, the peaks corresponding to a discrete number of photoelectrons (1, 2, 3 and so on) are clearly resolvable, so they could be used to calibrate the readout system in photoelecrons. Crosstalk between electronic channels could lead to distortions in the measured LRF shape. To prevent this distortion, the crosstalk level should be less than 1%. The software drivers should be preferentially written in C++, to be compatible with data acquisition software programmed in that language. The possibility of adjusting the SiPM bias voltage of each individual channel is an additional feature to take into account when searching for a readout system. It allows a fine adjustment of the SiPM gain at the system level, to correct for possible non-uniformities in the detector field-of-view given by SiPMs with different relative gains.

4.2 Solutions available on the market

Five alternative readout system solutions that fulfill many of the specified requirements were identified:

1. MAROC3 evaluation board from Omega
2. Modular data acquisition system based on TOFPET2 ASIC from PETSys
3. TRIROC ASIC from Weeroc
4. VATA64 HDR16.2 ASIC from IDEAS
5. TRB3 evaluation board from GSI

4.2.1 MAROC3

MAROC3 ASIC chip, which is distributed by Omega company, executes both the front-end and digitalization functions. It incorporates in a single chip the modules for analog interface, preamplification, shaping, discrimination and signal digitalization of 64 channels. Omega also makes available a MAROC3 test board, containing all the components necessary for multichannel signal acquisition. A detailed presentation of MAROC3 chip and the test board can be found in [201] and [202].

Fig.4.1 shows the architecture and functional diagram of MARCOC3 ASIC. There is a 1) pre-amplification module, 2) a shaping and charge reading module and 3) a triggering module. The shaper is a $CRRC^2$ (**section 2.3.2**) that is followed by two "sample and hold" buffers. MAROC3 chip is prepared to read 64 input channels and has 64 pre-amplifiers with adjustable gain (up to a factor of 4) set with 8-bit DACs. It has a crosstalk level between channels less than 1%, a dynamic range between 2 fC and 30 pC (non linearity of 2% in charge measurements until 4500 fC), a shaper with an adjustable time constant (30 to 210 ns) and a built-in Wilkinson 12-bits ADC for signal digitalization.

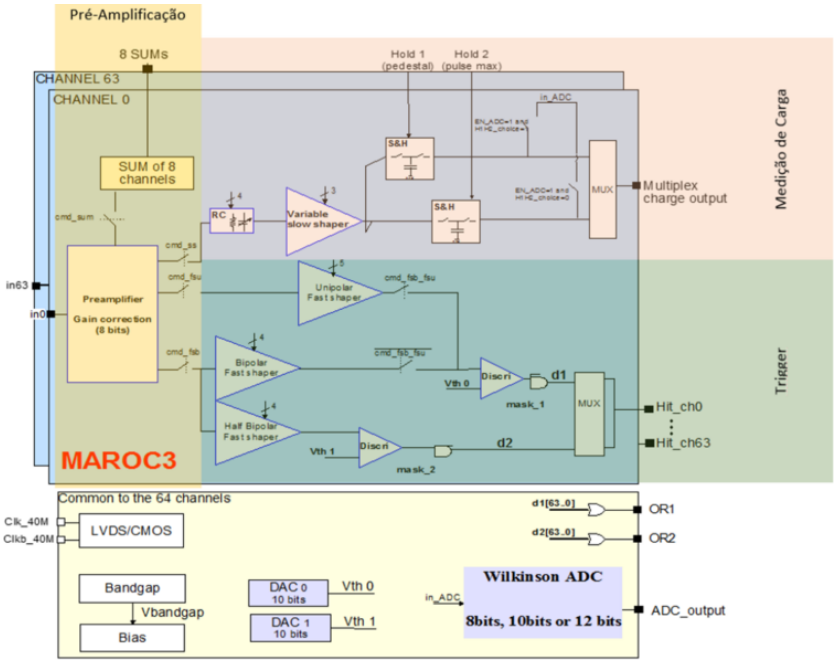

Figure 4.1: Architecture and functional diagram of MAROC3 ASIC. The circuitery for pre-amplification, triggering and charge measurement can be seen. The image was taken from [202]

On the negative side, the MAROC3 test board can not exceed an acquisition rate of 3 kHz (64 channels and signals digitized with 12 bits), although the internal Wilkinson ADC of the MAROC3 chip can achieve 8 kHz if it works at 12 bits [202].

The shaping time (up to 210 ns) is not optimal but still allows the integration of about half of the signal from NaI(Tl) crystal (88% of the decay time). The input polarity is only negative and so, some sensors cannot be used. The signal extraction is performed in track-and-hold mode. As the signal shape is standardized by the shaper, the signal peak appears always with the same time delay from the beginning of the signal. The track-and-hold circuit follows the signal and holds the signal level as soon as it receives the hold signal. This is sent after a fixed time delay from the beginning of the trigger moment. However, as the triggering occurs always for the same amplitude threshold level, the value held by the circuit does not always correspond to the maximum amplitude, due to time jitter (**section 2.3.2**). Thus, non-linearity exist in the maximum amplitude extracted for signals with different amplitudes.

The laboratory where this work was performed had a MAROC3 based readout, but due to its limitations a search for an alternative readout system was performed.

4.2.2 PETsys

The PETsys TOFPET2 ASIC (TOFPET2_2016)[203, 204] is mainly intended for readout and digitalization of signals from photosensors when high data rate and fast timing is required. At the time I did this research (beginning of 2016) this ASIC was not yet commercially available. However, as the company was announcing the upcoming arrival of the ASIC, it was included in the consideration.

It has independent signal amplification and discrimination for each one of 64 channels. The main features of the ASIC are summarized in **table 4.2**.

Feature	PETsys solution
Number of channels	64
Relative gains adjustment	4 levels per channel
Integration time	up to 1 μs
Dynamic range	up to 1500 pC
Electronic noise	10^5 electrons
Crosstalk level	<1%
Input polarity	+ and -
Event rate	up to 600 kHz per channel
Max. output data rate	3.2 Gb/s
Drivers	C++, open source
Firmware	not open source
Connection	Ethernet

Table 4.2: Main features of the PETsystem DAQ

Fig.4.2a presents the readout scheme of one channel, where one can see two preamplifiers, two postamplifiers, two discrimators, one integrator and a block representing the digital control. **Fig.4.2b** presents the simplified preamplifier circuit for positive signals. The negative signal version has the same topology, with the transistors, either NMOS or PMOS, switched

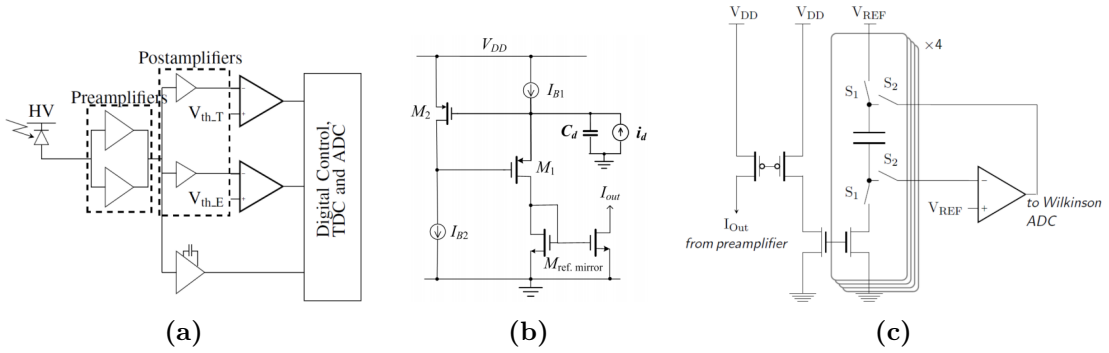

Figure 4.2: PETsys TOFPET2 FEE and DAQ schemes. These figures were copied from [203]. **(a)** Readout scheme for one channel. **(b)** Simplified preamplifier circuit for positive signals. **(c)** Simplified charge integrator scheme.

to the complementary type. They are current conveyors, based on a modified version of the regulated common-gate transimpedance amplifier (TIA). The conveyors provide a low input impedance for the detector and a high impedance current output. The pre-amplifier provides a low-frequency amplification of 25 dB and pass-band of 330 MHz and has power consumption of 2.5 mW. The preamplifier feeds two post-amplifiers and an integrator. The post-amplifiers (one for time measurements and another for triggering) have an adjustable transimpedance gain and provide voltage signals to two discriminators. The output signal of the preamplifier is processed by the charge integrator within a time window that is generated by the digital logic, based on the discriminators output. **Fig.4.2c** depicts a scheme of the simplified charge integrator. Four flipped capacitors sharing a single readout differential amplifier perform the signal integration, allowing de-randomization of the signals. The analogue signals are fed to a 10-bit ADC [203].

TOFPET ASIC is optimized for time measurements, for applications as TOF-PET[1]. Both an overview and a characterization of the TOFPET2 chip can be found at the company website [203, 204]. PETsys company offers the components for a complete readout system: front-end boards, DAQ boards, a trigger module and an evaluation kit[2]. The **front-end board type A** (FEB/A) has two TOF ASICs. It is optimized for positron emission tomography (PET) equipment, allowing to read 128 SiPMs.

The **front-end board type D** (FEB/D-1024) provides power for the ASICs, adjustable bias voltages for the SiPMs, configuration, clock and synchronization signals, and data readout for up to 8 FEB/A boards. It has different output interfaces available: SFP[3] + optical modules or copper cables and Ethernet.

[1]TOF-PET stands for Time-of-flight Positron Emission Tomography.

[2]Information on the front-end boards, DAQ boards, triger module and evaluation kit can be found in the "products" section of PETsys webpage [205].

[3]SFP stands for small form-factor pluggable. SFP modules or mini GBIC (gigabit interface converter), are compact, hot-pluggable optical transceiver modules which are widely used for both telecommunication and data communications application. The SFP ports can be connect to optical modules and copper cables.

The **Clock&trigger module** provides synchronization and time coincidence filtering for the FEB/D modules and it generates the system reference clock and synchronization signal. It can also be prepared for synchronization with external systems. A veto signal can be sent to this module to discard all events across all FEBs when it is active. It allows to implement a coincidence system, which collects coarse time information from all the FEB/D modules and transmits only coincidence events (filtering out the rest). The Clock&trigger module is assembled on the same mother board as the FEB/D board and uses the same communication platform [206]. It supports up to 16 FEB/D and 4 trigger regions per FEB/D.

The **PETsys DAQ board** receives data from the FEB/D boards, and transmits the data to a dedicated computer using a $\times 4$ PCI express port. The maximum event rate to the DAQ computer is 250 MHz. The events in the data frames are chronologically sorted by DAQ board to facilitate the processing by software.

Adequacy PETsys is a spinoff company from LIP-Lisboa. I had a meeting with the chief executive officer, where I was given a full explanation about the existing ASIC at that time (TOFPET) and about the future ASIC in development (TOFPET2). This second generation ASIC fulfills our requirements on the readout, however, when the system was needed it was not yet available. This was the reason to not select PETsys chip.

Nevertheless, PETsys products should be considered whenever a new readout system is envisioned. To implement a 128-channel system with the specified requirements it would be sufficient one unit of each of the following components: DAQ board, FEB/D and FEB/A.

4.2.3 TRIROC

TRIROC is a 64-channels SiPM readout chip aimed for medical imaging applications (namely PET time-of-flight) [207, 208]. As TRIROC has fast and low-jitter trigger, it can be used in applications which require fast and accurate readout of time and charge measurements. Energy and time are internally digitized with an ADC of 10 bits and TDC of 30 bits, respectively.

Having the PET application in mind, the concept behind the ASIC is to measure without interference from each other, both the arrival time of the first incident photon and the signal created as a consequence of the light emitted in the crystal. The main features of the TRIROC[1] ASIC are the following: readout of 64 channels, positive and negative signal polarity handling, 64 input DACs for SiPMs gain adjustment, the peaking time of the shaper is in the range of 10 ns to 160 ns, the dynamic range is from 0 to 480 pC (non linearity of 1% up to 320 pC)[2], the trigger can be internal or external, two 10-bit DACs for trigger threshold adjustment, ADC

[1] An overview of the TRIROC chip can also be seen in the Weeroc company website [209].

[2] 480 pC correspond to 3000 photo-electrons and 320 pC to 2000 photo-electrons, for the SiPM gain of 10^6.

track and hold/peak sensing and maximum acquisition rate of 50 kHz. The vendor gives no information on the crosstalk between channels.

Fig.4.3 depicts an overview of the TRIROC ASIC blocks scheme. The ASIC can be divided in three sections: analog, digital and common/service.

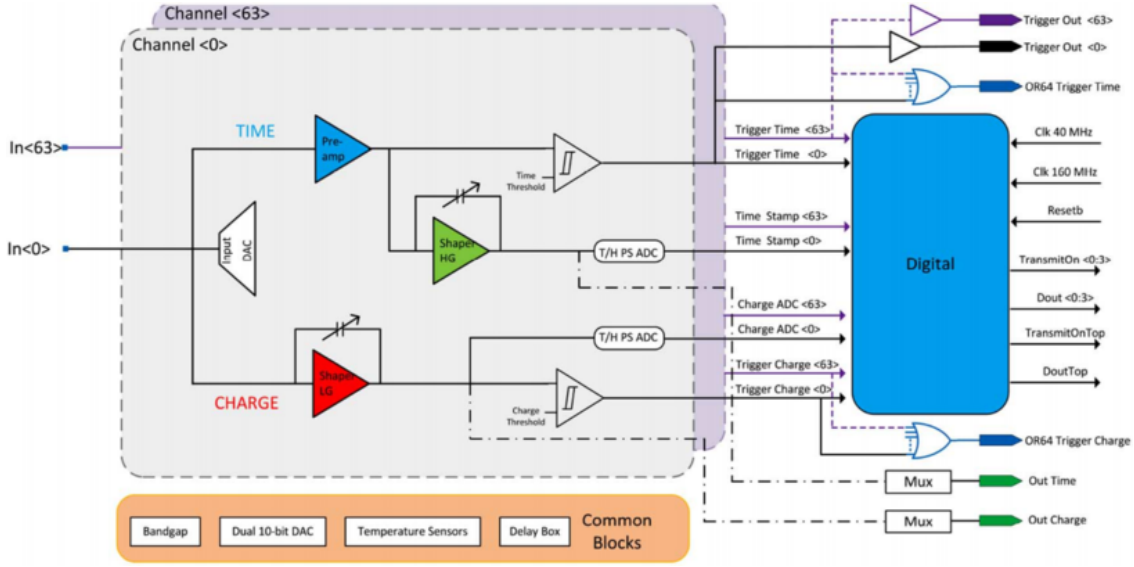

Figure 4.3: Overview of TRIROC ASIC block scheme. This figure was taken from [207].

In the analog section, each one of the 64 channels has an input DAC (8 bits) for the gain adjustment. The analog signal is split in two circuits: 1) the time measurement circuit and 2) the charge measurement circuit.

Time and charge measurement In the time measurement circuit the input signal feeds a pre-amplifier, which output is used by a discriminator to generate a trigger signal, which in turn is sent to the digital part for time-stamping the input signal. The pre-amplifier output is also sent to a high gain (HG) shaper for charge measurement at lower range, namely less than 100 photoelectrons at a SiPM gain $\approx 10^6$.

High dynamic range charge measurement In the charge measurement circuit the signal enters directly a low gain (LG) shaper, which allows measurements up to 2000 photoelectrons. In this section there is also a charge trigger, which is used by the digital part to validate events by the energy level.

Adequacy TRIROC has the attractive feature of allowing the individual adjustment of each channel bias voltage, using a channel-by-channel input DAC. The power consumption is 10 mW per channel, excluding the buffers used to output the signals. This means a total consumption of ≈0.65 W for 64 channels, in our case. A negative feature of TRIROC is the maximum

integration time of 160 ns, which is below the 500 ns specified as a requirement. Another disadvantage is that the driver code is given in Labview, which can not be integrated in a C/C++ custom made acquisition software (a lower level language as C or C++ would be more flexible). An evaluation kit is available, however the provided FPGA must be programmed according to the application, which implies specific programming knowledge not available in the group at the time of this work.

4.2.4 IDEAS VATA64 HDR16.2

IDEAS VATA64 HDR16.2 is an ASIC intended mainly for imaging and spectroscopy. The main features of the chip are the following: it has 64 input channels with individual adjustment of the channel gains, both positive and negative input signals can be used for readout triggering, the integration time is in the range 50 - 300 ns, the dynamic range is the charge window of -20 pC to +55 pC (with up to 300 pF detector capacitance load), the trigger can be internal (adjustable thresholds) or external, the input noise is as low as 8 fC for the input charge in the range -20 pC to +55 pC and <1 fC for input charge in the range -6 pC to +7 pC. The company did not measure the crosstalk level. The acquisition rate is 15.6 kHz, assuming 1 MHz multiplexer clock. The drivers are written in C and the communication with the evaluation kit is performed over Ethernet.

The 64 readout channels and the reference channel from the front-end can be read out via a "back-end" which contains a multiplexer and an output buffer that delivers a differential current and voltage outputs. Voltages and currents for the internal circuits are provided by a programmable bias network [210].

The chip is constituted by a preamplifier optimized for positive input charge, a circuit for amplitude spectroscopy, and a circuit for triggering and timing. The preamplifier can be connected directly to the SiPM and its bias voltages can be adjusted through digital-to-analog converters (DACs). The preamplifier gain can be set via the feedback capacitance to accommodate either a range from -20 pC to +55 pC or a smaller range from -6 pC to +7 pC. **Fig.4.4** presents a high-level circuit diagram of a readout channel in the IDEAS chip.

The shaping of the signal is made with a CRRC noise filter ("slow shaper"). Then, the signal enters a peak-hold (PH) circuit and a sample-and-hold unit (SH). It is possible to choose to acquire either the output of the PH device or SH unit. The amplitude from all channels can be read out sequentially through the first multiplexer. The trigger can be programmed to control the SH automatically and to send an external trigger to initiate a SH for other ASICs.

More information on VATA64 HRD16.2 can be found at the company website [211] and in [212].

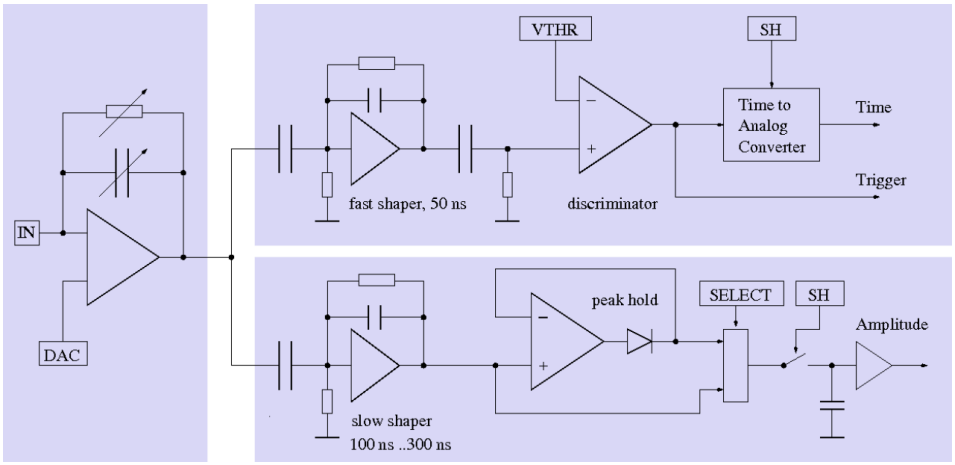

Figure 4.4: High-level circuit diagram of a readout channel in IDEAS VATA64 HDR16.2. The image was taken from [210].

Adequacy The possibility of having individual adjustment of SiPMs bias voltages (8-bit DAC), external triggering and to accept both positive and negative signals are points in favour of VATA64 chip. However, the maximum shaping time of 300 ns is below our requirement, which is 500 ns. The 300 pF detector capacitance load is low, considering that a typical 3×3 mm^2 SiPM has a capacitance of ≈1000 pF. The chip has no internal ADC, which implies the usage of an external one.

4.2.5 TRB3 (GSI)

TRB3 DAQ board was developed for experiments in particle physics (HADES collaboration, GSI laboratory). TRB3 platform was initially designed as a multipurpose FPGA based TDC[1] platform with 64 channels on each FPGA. The board has 5 Lattice ECP3-150EA FPGAs. A central FPGA is responsible for the data acquisition, control and trigger over the "TrbNetwork" [213]. It also controls the gigabit Ethernet (GbE) communication port. Four FPGAs can be individually programmed to serve as controllers for various add-ons developed by GSI. In the original version, each FPGA was configured to manage 64 TDC, resulting in total of 256 channels. Later, an alternative configuration was prepared to manage signals received from ADC devices. Four ADC *add-on* boards developed in GSI can be plugged to the TRB3 board. Each ADC add-on board has 48 10-bits ADCs which operate at 40 MHz, so 48 × 4 channels can be read by the TRB3 board. The ADCs have a differential input voltage with a dynamic range of 1.8 V. The ADC add-on board handles both positive and negative input polarity. The TRB3 trigger can be either internal or external and the trigger rate can achieve 100 kHz [214]. Both the software drivers and the firmware are open source.

[1]TDC stands for "Time to Digital Converter". This device is usually used to measure the time between two electric pulses and convert it to binary format.

Adequacy TRB3 board allows continuous sampling of the signals waveforms. This feature is of great advantage, as post-processing can be performed to optimize the signal-to-noise ratio (e.g. adjust the integration windows, apply filters to the waveform). Open-source drivers are provided[1] and so they can be used to implement a custom made acquisition application. Another benefit of TRB3 board is that it can read up to 192 channels, which makes this DAQ board available for detectors with higher number of sensors, as would be the case of a gamma camera with two arrays of SiPMs coupled to both sides of the scintilator, as a strategy for the measurement of the depth of interaction. Another feature of TRB is that it has an Ethernet port for communication, which can handle higher transfer rates for higher trigger rates or higher number of sensors than the rates listed as minimum requirements for the new readout. Considering the *pros* and *cons* of all five readout system alternatives, the TRB3 board was the selected solution. An additional reason has counted in the selection of TRB3: another group from LIP had already used[2] TRB3 and so our group had the possibility to evaluate the board for our application, including custom made front-end-electronics. TRB3 is presented in more detail in the next section.

Conclusions on the readout system selection MAROC3 is an ASIC with DAQ and FEE incorporated. The vendor provides an evaluation board which has readily available both the ports for the input signals and a USB socket for the readout of the sensors data. It has a single ADC for digitalization of the sensor signals. PETsys is an ASIC with DAQ functions and it can also be ordered with FEE modules, as well as an evaluation kit ready to use. TRIROC and IDEAS VATA64 are ASICs with DAQ and FEE functions included and they are also commercialized with evaluation kits. The IDEAS solution has no internal ADC and it is one of the most expensive from the five readout alternatives, along with PETsys. TRIROC vendor provides a test board with a FPGA that can be used to implement the trigger strategy and communication protocols. TRB3 is an "evaluation board" by itself, which has the DAQ components, a trigger system and Ethernet readout. It has no FEE and no ADCs, but the developers provide an ADC add-on board. From the five readout candidates, TRB3 is the only one that provides continuous waveforms sampling, which gives the possibility of a custom processing of the photosensor signals.

Other solutions available on the market were analyzed but not accepted, because of either not conforming to the established requirements or being prohibitively expensive, for instance:

[1]The firmware code which is running in the FPGAs is also provided. It is written in a hardware description language, VHDL (VHSIC Hardware Description Language).

[2]The group which have experience with TRB3 in LIP uses this board mainly for time measurements in RPC based detectors, e.g. PET systems [215, 216, 217].

Vertilon IQSP482 and IQSP582, CERN NINO chip, Weiner MESYTEC, AiT Instruments MDU40-GI32 and ABL-ARRAYB16P.

4.3 TRB3 based system for real-time readout

The readout system used in this work is comprised of a custom front-end electronics (FEE)[1] and the TRB3 based data acquisition system (DAQ). The FEE is responsible for the amplification and shaping of the signal. The shaped signal enters the ADC to be digitized and sent for the processing unit. Two 48-channel ADC add-ons were required, because 68 channels need to be acquired: 64 SiPM signals and 4 signals with the sums of four separated groups of 16 SiPMs. These sum signals are compared with a predefined threshold for the event triggering.

4.3.1 Front-end electronics (FEE)

The purpose of the FEE is to condition the signals received from the SiPMs to be digitized by the ADCs. The FEE was designed with the following requirements in mind:

- Amplification factor: 10 V/mA (transimpedance) to match the dynamic range of SiPM output to that of TRB input
- Low-pass filter to guarantee correct waveform integration at 20 MHz sampling
- Noise equivalent charge: $< 10^5$ e for an integration window of 650 ns
- Bipolar operation
- Baseline shift to the midscale of TRB's ADC input range (0.9 V)
- Protection of TRB's ADC from voltage excursions below -0.2 V and above 2.0 V

Fig.4.5 presents the scheme of one channel of the FEE circuit.

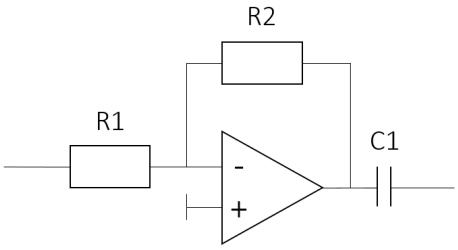

Figure 4.5: Scheme of one channel of the front-end electronics circuit.

[1]The FEE were developed by Vladimir Solovov, based on a design provided by Oleg Morozov.

The circuit amplifies the input signal and also serves as low pass filter. The operational amplifier is a low power, current feedback amplifier, with gain-bandwidth product of 350 MHz. Two amplifiers are available in the integrated circuit AD8012 (SMD), so 32 of these chips were installed on the front-end board.

The dynamic range of the ADCs is 0 V - 1.8 V. Two Zener diodes were used to protect the ADC from voltages above the upper limit of that range. One additional circuit was implemented to shift the baseline voltage from 0 V to +0.9 V. This way, either negative and positive signals can be digitized.

The values of R1, R2 and C1 were selected to confine the signal voltage to the ADC dynamic range and to implement the low-pass filter: R1 = 100 Ω, R2 = 10 kΩ and C1 = 100 nF. The output pulse has risetime of 150 ns allowing for the correct integration at a sampling rate of 20 MHz.

4.3.2 Data acquisition system (DAQ)

Before describing the DAQ system, the TRB3 DAQ blocks and the communication network must be first presented. This architecture has defined the options chosen for the hardware components of the DAQ system.

TRB3 DAQ blocks and TrbNet protocol The architecture of the TRB3 DAQ network is depicted in **Fig.4.6**. TRB3 DAQ has a dedicated network protocol called TrbNet[1] which handles all the communication and data transfer in the DAQ network.

The TrbNet network is divided into three virtual channels for each different type of data: trigger information, event data and slow-control information (represented as the three horizontal stripes in **Fig.4.6**). In the first channel (trigger information) the trigger signals are sent from the Central Trigger System (CTS) to the FPGAs and acknowledgment information is sent in the return path. Both the trigger and readout process are controlled by CTS, which receives fast input signals from all the detectors connected to TRB3, and based on these signals make a trigger decision. The data from the ADCs are stored in the FPGA buffers until a readout request is received on the second channel (event data). The request contains the event number and the identification of the machine where the "event builder" software is running (e.g. IP address of an external computer). This software organizes the incoming data in an event data structure defined in [219] (see **appendix D**). After reception of the readout request, the FPGA fetch the event data from the buffers and send those data to the network communication module where the data from all FPGAs are combined in one single data stream with added UDP and Ethernet headers in order to route the data packet directly to

[1]TrbNet (Trigger and Readout Board Network) was developed in the frame of the HADES project as the communication protocol for the DAQ network. More information can be found in [218, 219].

the "event builder" machine, via Ethernet ("Event Builder" block in **Fig.4.6**) [213, 214, 219]. Each FPGA can be controlled and monitored individually through the "slow control" channel. A 16 bit address bus provides the connection for the registers related with control, status monitoring or debugging.

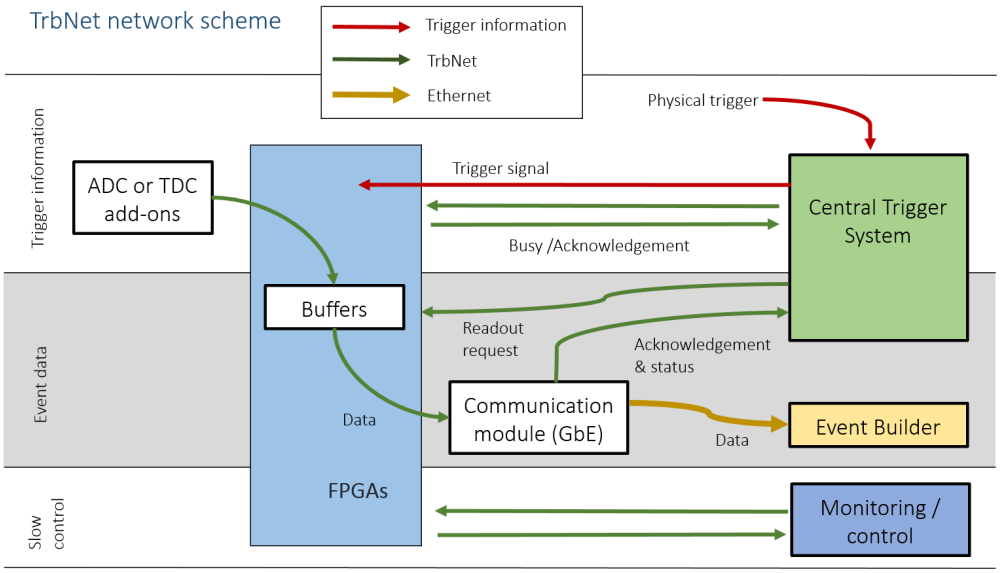

Figure 4.6: TrbNet network scheme. The image is an adaptation of a figure from [219].

DAQ hardware components **Fig.4.7** shows the components of the DAQ system. The main component is the TRB3 DAQ board. Two ADC add-ons are connected to the TRB3 for sampling and digitalization of the signals received from the FEE. Another component is an external computer, where the software required to perfome the acquisition and data storage is installed.

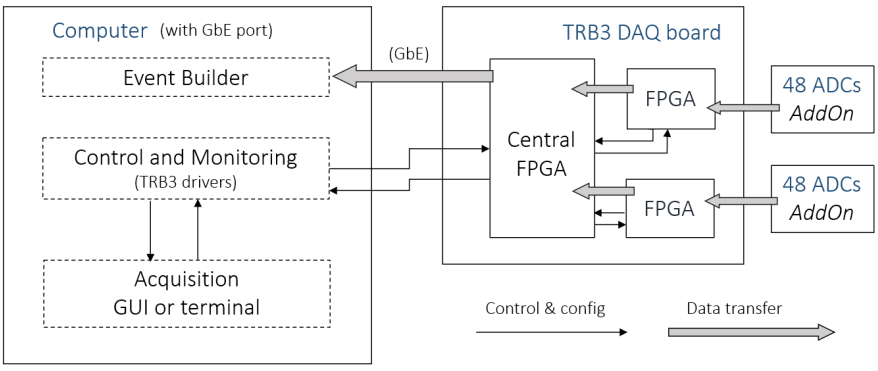

Figure 4.7: Data acquisition components.

1. **TRB3 data acquisition board**

   The TRB3 DAQ board (**section 4.2.5**) was used in the assembled readout system as a multichannel waveform digitizer.

   Triggering Event triggering can be external or internal to TRB3. The implemented solution analyses dedicated sum channels coming from the ADC add-ons for internal triggering. The reason for this decision is that with internal trigger the signal level used in the trigger discriminator is measured from the baseline. This makes the triggering process more immune to noise, compared with an external triggering. For the waveforms of these channels, the baseline is calculated from the current samples (e.g. 8 samples) and the leading edge is compared with the trigger threshold defined by the user.

   To optimize the signal-to-noise ratio of the trigger signal, it was first decided to sum a set of channels, instead of comparing the signal level of each channel in the trigger descriminator. Second, to reduce the noise in the sum channel and to have a discrimination threshold not too high, the 64 channels were divided in four groups of 16 channels that are summed separately to give four "sum" channels with signals that are used for triggering ("trigger channels"). Each trigger channel receives always the digitized sum of the same group of 16 SiPMs. Whenever any of the four sum signals exceed the specified threshold, an event is triggered.

2. **ADCs add-ons**

   Each ADC add-on has twelve AD9219 integrated circuits, each one with four ADCs[1]. The main features of the ADCs are:

   - 40/65 mega samples per second (MSPS)
   - 60 dB signal-to-noise ratio (to Nyquist)
   - 315 MHz full-power analog bandwidth
   - 1.8 V peak-to-peak differential input voltage range
   - On-chip sample-and-hold circuit.
   - Data and frame clock outputs

[1]More information on the AD9219 quad ADC chip can be found in the Analog Devices website: https://www.analog.com/en/products/ad9219.html (available at March 2019).

Fig.4.8 presents the electronic circuit[1] to prepare the signal to be digitized (two differential lines). A low pass filter is implemented with a characteristic frequency of 31 MHz (resistor R13 = 33 Ω, capacitor C268 = 150 pF). This filter protects the system from the interference of surrounding radio-waves, for instance the ubiquitous WiFi (2.4 GHz).

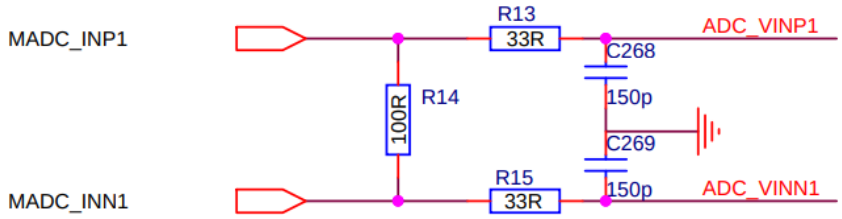

Figure 4.8: Circuit to prepare the 2V peak-to-peak differential input of the ADC. A low pass filter with cutoff frequency of 31 MHz is also included.

When the DAQ system is switched on, the ADCs are continuously digitizing the incoming signals and sending their samples into the FPGA FIFO data buffers. When an event is triggered, the samples which correspond to the event signals are selected according to the predefined number of samples before and after trigger and sent to the communication module. **Fig.4.9 a** shows schematically the FPGA FIFO data buffer. **Fig.4.9b** is an example of a 30 samples waveform digitized in one of the ADCs add-ons. The first 10 samples correspond to the electronic baseline level.

3. **Computer**

A computer is used to run the software for the control, monitoring and data storage of the acquisitions. Three software modules are required:

- TRB3 drivers
- "Event builder" software
- Interface application

The **TRB3 drivers** manage the configuration of the acquisition settings, including the trigger thresholds, the number of samples in the acquired waveforms, and the monitoring the acquisition rate. The slow control messages are sent to and received from the TRB3 central FPGA using the TrbNet protocol. The **"event builder" software** properly packs together and stores the signal waveforms that belong to the same event (data requested from the ADCs at the same timestamp, when an event is triggered) when data arrive to the storage machine (the **appendix D** briefly presents the "event

[1]The complete electronic schemes of the ADC add-ons can be found in the webpage: https://jspc29.x-matter.uni-frankfurt.de/trb/schematics/AddOn_ADC1-ALL.pdf (available at March 2019).

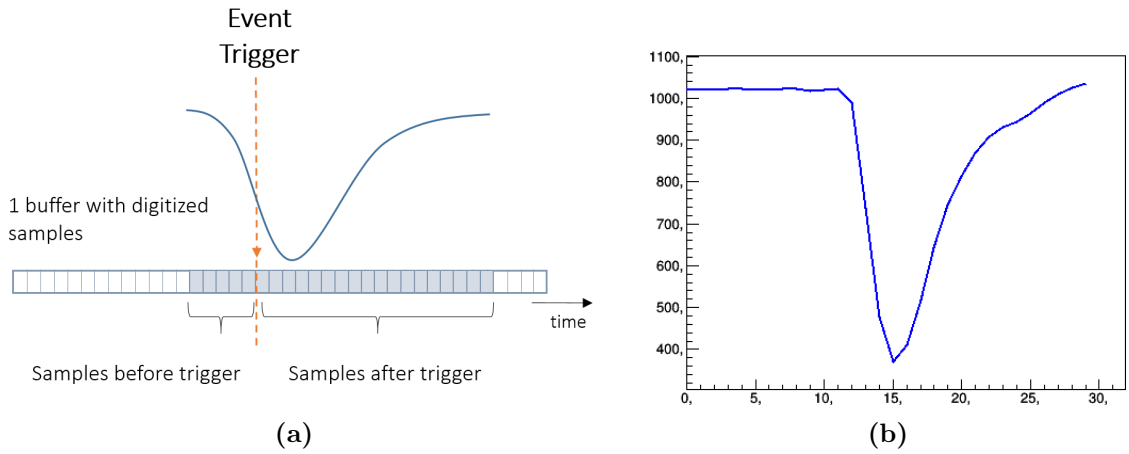

Figure 4.9: ADC digitization in TRB3 DAQ. **(a)** FPGA data buffer schematic representation. The number of samples after trigger that should be taken from the buffer can be configured. **(b)** Waveform digitized by the ADC add-ons. The horizontal axis represent the number of samples and the vertical axis the signal level in number of electronic channels.

builder" software). The **interface application** allows the user to interact with the slow control commands. It allows, for instance, 1) to configure the trigger threshold and the acquisition time, 2) to set the directory and the size of the files where the data should be stored and 3) to start and stop acquisition. The application can be either a graphical user interface, a web page or a terminal.

The three software modules were installed and successfully tested both in a desktop (Ubuntu Mate 18.04 and Kubuntu 14.04) and in a laptop computer (Xubuntu 18.04). The **appendix E** presents the software developed to perform the acquisitions with the TRB3 readout system presented in this section.

The readout system described in this section was first successfully validated in the characterization of a neutron Anger detector. This work was performed at Institut Laue-Langevin (ILL), in Grenoble, and the results were published in the Journal of Instrumentation at March 2019 [220]. In the **appendix C** the details of the neutron detector are presented, as well as the main characterization results.

It should be noted that the software modules can be distributed over different machines, if it is more convenient. For instance, for experimental work performed at the hospital (**section 6**), the TRB3 drivers were installed on a mini-computer (Odroid-C2)[1] running a Ubuntu Mate 16.04 operating system (OS). The "event builder" software as well as the GUI to manage the acquisitions were installed on a laptop running a Xubuntu 18.04 OS. This option of installing the TRB3 drivers on a separated mini-computer gives

[1]More information on Odroid-C2 can be found in this two websites: https://www.hardkernel.com/ko/tag/odroid-c2/ and https://wiki.odroid.com/odroid-c2/odroid-c2

flexibility to the system. For instance, on a previous work performed at ILL for the characterization of the neutron Anger detector, the mini-computer was chosen to be very compact (lightweight), as it does not need much processing power and it can be anywhere in the DAQ network (linked by Ethernet). Before arriving to ILL facility, we did not know if we can stay or not in the cabinet close to the detector (for space and security reasons). In the case we cannot, the computer with the "event builder" software and the interface application should be far from the detector, but it can be connected to TRB3 board and the mini-computer through an Ethernet connection (e.g. using a long Ethernet cable).

The communication between the TRB3 board and the hardware running the required software (e.g. laptop and mini-computer) is done through the gigabit Ethernet protocol. A PT-Link TL-SG105 GbE switch was used to connect all the system components.

5

Data processing chain of the imaging system

In the previous section, the processes necessary for the readout of the photosensor waveforms that correspond to each event were described. Shortly, when a scintillation event is triggered, the signal waveforms are acquired, amplified and shaped to be compatible with the integration windows. Then, the signals are digitized and the waveforms are sent to the processing unit. All these processes are performed by the readout system described in **section 4**.

This section focuses in the data processing chain. The SiPM waveforms are integrated and the resulting values are converted into the number of detected photons in each SiPM per each scintillation event. To perform this conversion a calibration must be performed for each SiPM and it is explained below. Once the photosensor signals are converted into number of detected photons, event position (and optionally energy) reconstruction is performed using the maximum likelihood technique. Then, a XY density plot with the reconstructed event positions is displayed. The set of procedures for the processing of the acquired signals until the data visualization constitute the "real-time processing chain".

Fig.5.1 presents a simplified scheme of the dataflow and the processing chain starting with the SiPM signals acquisition and ending with the reconstruction of the event positions and energies.

5.1 Processing of the digitized photosensor signals

For the processing of the digitized photosensor signals in order to estimate the number of detected photons in each SiPM, two datasets are required. For each photosensor, the electronic baseline must be known as well as the signal that corresponds to the detection of a single photon (signal per photoelectron), given in ADC channels. The electronic baseline is the sensor output signal in dark conditions (no light falls on the sensor), so it must be subtracted from the sensor signal when processing scintillation events. In this work, *pedestal* is the name given to the

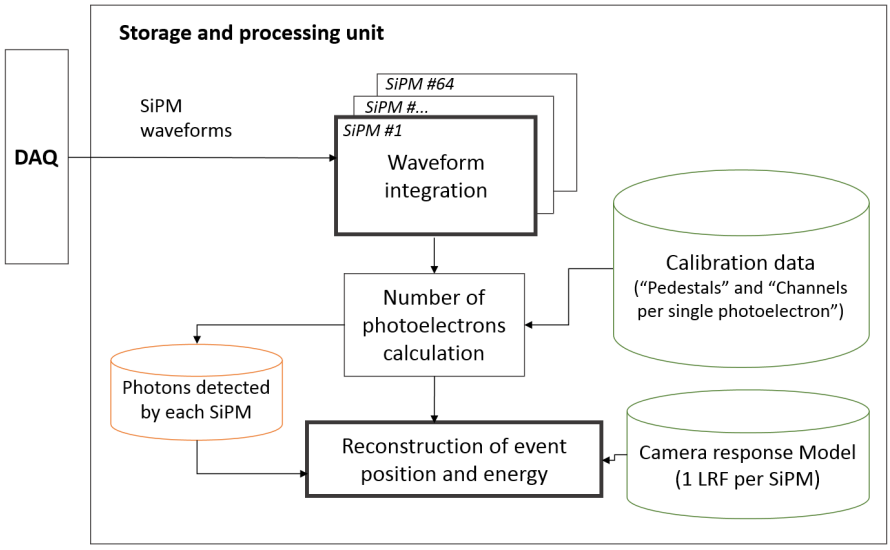

Figure 5.1: Processing chain for reconstruction of events. The SiPMs waveforms are integrated and a calibration is applied (pedestal subtraction and division by the gain).

baseline contribution in the individual SiPM signals. Two alternative methods to calculate the pedestals are explained and compared in this section.

5.1.1 Pedestal calculation and subtraction

The pedestal of the acquired signal waveforms can be calculated by two ways. In the first method, referred below as *local*, it is calculated from each individual waveform. In the second method, referred below as *global*, it is usually calculated as an average from a set of waveforms, in a calibration phase previous to the acquisition. The *local* estimation of the pedestals have the advantage of be able to handle the instantaneous changes that can occur in the electronic baseline, for instance due to interference of the 50 Hz power supply frequency. In the *global* case, the oscillation of the baseline is not taken into account.

Local In the *local* calculation of the pedestal, it is extracted averaging the first samples (pre-trigger window) of the waveform. For example, in this work 30 samples were typically used (see **Fig.5.3**), from which 10 samples can be used to extract the pedestal.

Global To calculate the *global* pedestals, the readout of the photosensor signals must be triggered at time moments when the probability of a scintillation event occur is minimized, thus corresponding to the signals of the photosensor pedestals. Hence, the data used to estimate the global pedestals are acquired with no radioactive source present, to reduce the probability of undesired random coincidences from photosensor readings due to γ-rays deposition. In this work the "pedestal events" were recorded at a periodic rate (e.g. 1 kHz).

The *global* pedestal can be calculated in two ways. The first possibility is to consider as the pedestal the ADC channel corresponding to the first peak of the histogram (zero photons) of the waveform integrals given in ADC channels (pulse height spectrum). The SiPMs bias voltage can be either below or above the breakdown voltage V_{brk} (e.g. the same as for the acquisition of scintillation events), because despite the dark counts when working above the V_{brk}, the first peak can be always identified. Alternatively, an average of the baseline signal (waveform integral) over the set of "pedestal events" can be calculated. In this case, the SiPMs bias voltage must be below the SiPMs V_{brk} to avoid dark counts (**section 2.2.4.2**). The procedure used during the experimental work was to operate the SiPMs slightly below the breakdown voltage and to estimate the pedestals through the identification of the first histogram peak.

Comparison between *local* and *global* pedestal extraction The pulse height spectra (PHS) obtained using pedestals calculated locally and globally are presented in **Fig.5.2** for comparison. The red curve shows the PHS obtained when pedestal value is extracted locally from the first 10 samples of each waveform. The blue curve shows the PHS obtained when the subtracted pedestal is an average value calculated offline, before the acquisition.

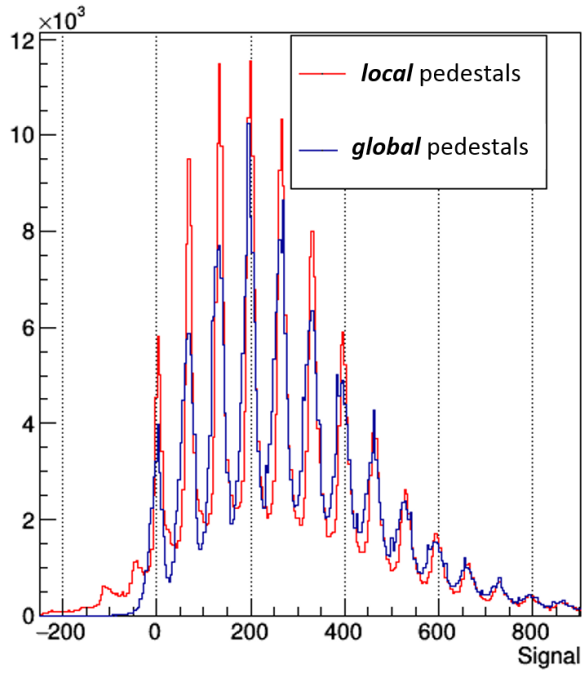

Figure 5.2: Comparison between two pulse height spectra (SiPMs signals). Red curve: local pedestals extraction. Blue curve: global pedestals extraction.

The pulses from the global case (blue) are slightly broader than in the local case (blue), most probably due to the integration of part of the signal from the previous waveform for the

events when the baseline level oscillates relatively to the value obtained in the calibration. Thus, the photon peaks can be better distinguished in the local case, although in both cases the peaks are perfectly separated. The local procedure is able to handle pedestal changes in time, while the global procedure is not. These changes may occur because of temperature variation as well as variations in the bias voltage.

However, when using the *local* pedestal subtraction, an additional calibration step is required in order to obtain the proper number of ADC channels per single photoelectron $C_{p.e.}$. In **Fig.5.2**, two peaks can be seen to the left of the zero peak in the red PHS, corresponding to one and two dark counts accidentally appearing in the pre-trigger window used for pedestal subtraction. These peaks should not be taken into account in $C_{p.e.}$ calculation. To automatically identify the negative peaks, a pre-calculation of $C_{p.e.}$ must be performed taking into account all the peaks in the PHS. That number is given, roughly, by the average distance between each pair of consecutive peaks. Then, the peaks to be excluded are those at negative signals (given in number of ADC channels) which are less then -$C_{p.e.}$/2. This margin accounts for possible fluctuations on the baseline level, which can shift the real pedestal peak to small negative values. After the suppression of the negative peaks, $C_{p.e.}$ should be recalculated as explained below in **section 5.1.3**.

If one estimates the pedestals for different datasets with the two methods (*local* and *global*), the results in both cases are essentially the same. The conclusion is that the two methods can be used for pedestal estimation. However, the *global* pedestals approach results in a simpler data processing.

5.1.2 Signal extraction: waveform integration

The DAQ system presented in **section 4** performs continuous sampling, so the integral of the waveform can be calculated. The waveform integral can be assumed to be a quantity proportional to the SiPM collected charge and thus, proportional to the number of detected photons.

Fig.5.3 shows a waveform with 30 samples acquired with the readout presented in **section 4**. There is a delay of 12 samples before the pulse falling edge and the duration of the pulse goes up to the sample number 27. The integration window should be slightly higher than the pulse duration to always integrate the complete signal, independently of the jitter. On the other hand it can not be excessively long, to minimize the noise contribution. Hence, the selected integration window is in the range of samples between the sample #11 and the sample #28, as indicated in **Fig.5.3**. To perform the waveform integration, TRBReader package (briefly presented in **appendix D.1**) can be used.

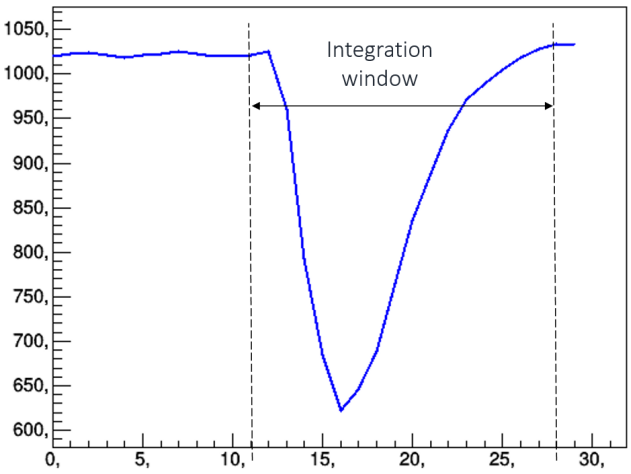

Figure 5.3: Waveform integral window. The waveform has 30 samples. The waveform is integrated from the sample #11 to the sample #28

5.1.3 Calculation of the number of photoelectrons

The waveform integral is given in ADC channels. In order to convert from that units to number of photoelectrons, a calibration factor is required. Note that the conversion of the acquired signal into number of photons is required if the maximum likelihood method (**section 2.5.4.1**) is used for event reconstruction. The calibration factor is the number of ADC channels per single photoelectron $C_{p.e.}$, that should be calculated for each SiPM. The fact that well distinguishable peaks can be obtained in the PHS of SiPMs, gives the possibility of calculate $C_{p.e.}$ analyzing the peak positions. The procedure to find $C_{p.e.}$ for each SiPM is to make a linear regression to the centers of the peaks taken from the pulse high spectrum PHS (ADC channels) and plotted as a function of the peak number (the peak number zero is the most left peak in the PHS). The slope of the fitted line is considered as the $C_{p.e.}$. This procedure was implemented in ANTS2 and it starts by automatically detecting the PHS peaks, using CERN ROOT functions (e.g. GetNPeaks() function from TSpectrum class). **Fig.5.4** shows the identified peaks for two SiPMs PHS. For the PHS on the left (SiPM #5), $C_{p.e.}$ is 28.7 and for the PHS on the right (SiPM #6), $C_{p.e.}$ is 42.8. According to measurements the $C_{p.e.}$ varies about 30% between SiPMs of the same production batch.

After removing the pedestal component from the SiPMs signals, the number of detected photons is obtained dividing the integrals of the SiPM signal waveforms (**section 5.1.2**) by $C_{p.e.}$. **Fig.5.5** show side by side both the acquired waveforms and the calculated number of photoelectrons for the 64 SiPMs array used in experiments, for one scintillation event. The waveforms placement (spatial relation between waveforms that correspond to each SiPM) in the left image is in accordance with the layout of the SiPM array in the right image.

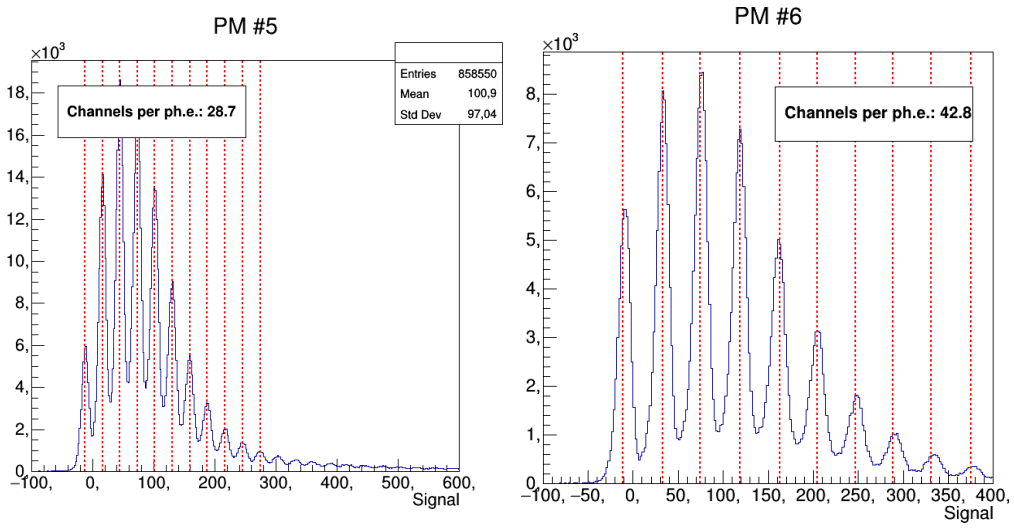

(a) (b)

Figure 5.4: Signal (number of ADC channels) per photoelectron estimated as the average distance between the signals that correspond to the peak centers. The peaks in the pulse hight spectra correspond to the different number of detected photoelectrons. The two images correspond to histograms obtained from data acquired with different SiPMs bias voltages. The data is also from two different SiPMs.

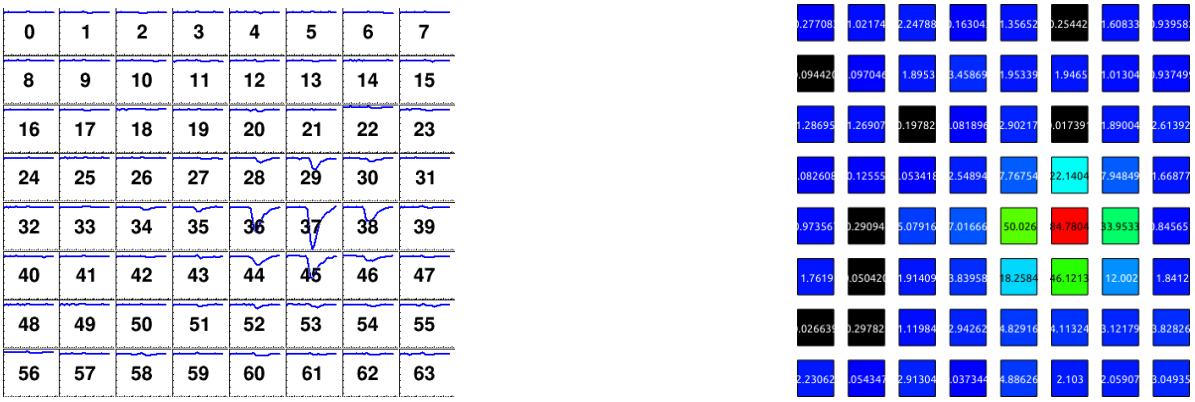

(a) (b)

Figure 5.5: Example of the waveforms and corresponding number of detected photons in the 64 SiPMs array for one scintillation event. **a**: 64 waveforms acquired with the DAQ system. **b**: Number of detected photons calculated dividing the waveform integral by the SiPM gain (signal per one single photon).

5.2 Scripting and automation

Using the software packages and libraries presented in the **appendix D**, namely the ANTS2 scripting engine, a series of processes were automatized: 1) data acquisition procedures, 2) pedestal calculation and 3) light response functions (LRFs) calculation through the adaptive algorithm.

Automation of the acquisition procedures The software presented in **appendix E** is sufficient to initialize the TRB board and to configure and run acquisitions. However, a set of high-level routines were added to make the DAQ system more user-friendly. A set of scripts was prepared in an intermediate layer[1] (bash script) that can be called by the top software layer, the application layer (e.g. in Python, Javascript, C++ GUI, etc). The application layer consists in a set of Javascripts and a GUI interface[2]. The procedures available in the application are 1) the initialization of the TRB3, 2) the starting and stopping of the acquisition, 3) the acquisition of pedestal events, 4) the extraction of the signals from the acquired waveforms.

The procedures to start the acquisition and to process the .HLD files[3] with acquired events data are the bases for the real-time processing cycle. The conversion of the SiPM signals in the processed .DAT files (with the waveform integrals in ADC channels) is then performed in ANTS2 using the $C_{p.e}$ factor (**section 5.1.3**), followed by the event reconstruction and visualization of the XY density plot of the reconstructed positions.

TRBReader[4] is used to process the .HLD files, which contain the waveforms for each SiPM, for each event. According to the TRBReader user configuration (e.g. range of samples that define the integration window), each waveform is integrated and the result is saved in a .DAT file. This file contains one line per event with the result of integration for each SiPM separated with white spaces. The processing of the files can be called from either TRBReader (in GUI or using "hld" scripting unit) or ANTS2 scripting environment. In this scenario, ANTS2 communicates with TRBReader in a client to server protocol (see **appendix D.2**). This allows ANTS2 to be running in a remote machine.

Calculation of the pedestal The method for the calculation of the SiPMs pedestal is based on the SiPM signals histogram, as presented in **section 5.1.1**. A script was developed to make a histogram of the signals (PHS) for each SiPM and to find the first peak in the PHS

[1] The software layers assumed in this work are presented in **appendix E**.

[2] The GUI interface was implemented using the ANTS2 scripting environment. A presentation on the acquisition GUI and the developed script functions can be found in **appendix F**.

[3] The .HLD file is a proprietary format of TRB3 DAQ. This files are created by the *event builder* application and save the acquired events data. The structure of the .HLD file can be found in the TRB3 manual, which is available online, in the section "TRB3 Documents" of the TRB3 GSI website: http://trb.gsi.de

[4] A presentation of the TRBReader application developed in LIP-Coimbra can be found in **appendix D.1**.

of each SiPM. The bin corresponding to the center of the first peak of the SiPM histogram is saved as the pedestal of that SiPM.

Automatic LRFs reconstruction using the adaptive algorithm In this work the adaptive algorithm described in **section 2.6.1** was used to estimate the SiPMs light response functions.

In previous studies (e.g. **section 3.2.5**) the adaptive algorithm was performed manually. This way, one can observe the results of each iteration, make the required changes in the algorithm options, apply filters to the reconstructed positions, decide when to stop and backtrack when needed. An automatic procedure for the estimation of LRFs should iterate through the adaptive algorithm steps towards the convergence of the LRFs curves into a good representation of the average signals as a function of the radial distance to the sensor centers without human intervention. The automatic LRF estimation can be useful coupled to a real-time monitoring of the detector response model (**section 5.3.2**), indicating that the model needs to be rebuild after a new acquisition of flood field data.

I have implemented (in ANTS2) a script[1] to run automatically the adaptive algorithm.

Fig.5.6 depicts a flowchart that summarizes the adaptive algorithm procedures, that are explained below.

Initial configurations on LRFs

The initial parameterization and configuration of the LRF curves must be selected, as well as the source of data for the initial guess on the LRFs. The LRFs parameterization with axial symmetry proved to result in adequate models of the SiPM responses, even for squared-shaped monolithic crystals [85], so it was used when calculating new LRFs. Along with the LRFs parameterization, some configurations can be set for the LRFs, which help the algorithm to converge faster: the LRF function is forced to be a non-negative, monotonically decreasing function, with zero derivative on the origin. These properties of the LRFs are expected from the radial dependence of the solid angle subtended by the SiPM window. To improve convergence, some settings were changing as the iterations progress, for example, the profile of the LRFs was set to be the same for all SiPMs during the first three iterations changing to individual LRF profiles (independent for each SiPM) from the fourth iteration.

Statistical reconstruction of event positions

The event reconstruction algorithm used was the *contracting grids* in GPU (**section 2.5.4.2**), which allows a very fast reconstruction. It was also found that it is advantageous to increase

[1]The ANTS2 script that implements the adaptive algorithm can be found in the online repository: https://github.com/jsmarcos/ANTS2_LRFs_AUTOMATIC_ESTIMATION_SCRIPTS-/blob/master/STEP_2_(and_7)_IterativeAlgorithmForLRFsCalculation.txt.

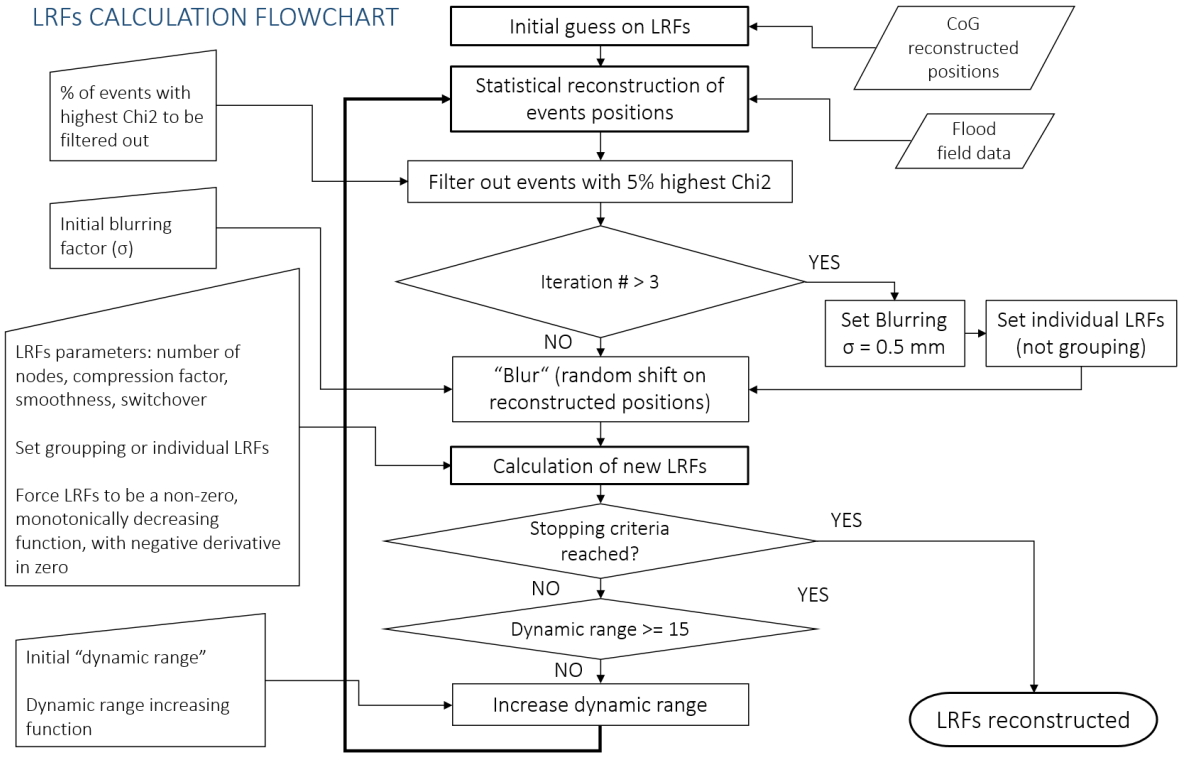

Figure 5.6: Flowchart of the LRFs calculation procedure.

gradually the *active radius* (**section 2.5.4.2**) between iterations. I have used a polynomial grow for the active radius increasing from the iteration i to the iteration $i+1$ until a maximum distance of 15 mm (starting with $DR_i = 9$ mm):

$$DR_{i+1} = DR_i \times (1+b)^{i+1} \tag{5.1}$$

Where b is the decay factor. I have used $b = 0.025$. The b, DR_i and the maximum active radius parameters were found empirically to result in LRFs that converge fast (below 12 iterations) and in reconstructions with low level of distortions. The initial value of DR_i (9 mm) was selected to force the reconstruction algorithm to use at least the 16 SiPMs closest to the scintillation positions (the distance SiPM centers is 4.2 mm).

Application of filters and a random shift on positions

In each iteration, after the reconstruction of event positions, there are events filtered out by the reduced chi-square (χ^2) value:

$$\chi^2 = \frac{1}{\nu}\sum_{i=1}^{M}\frac{(A_i - a_i)^2}{a_i} \tag{5.2}$$

Where M is the number of active SiPMs, ν is the number of degrees of freedom and A_i and

a_i are respectively the measured and expected signal in the SiPM $\#i$. Note that ν = M - 3, when only the (x, y) coordinates are the parameters to be optimized and ν = M - 4 when the energy is also optimized. I have defined a percentage of 5% of the events with highest χ^2 to be filtered out between iterations. A shift in a random direction (*blurring*, see **section 2.6.1**) is applied to each reconstructed position in the end of each iteration. The shift distance is taken from a Gaussian distribution centered in the reconstructed position coordinates. The width of the distribution should be larger in the first iterations, because in these iterations artifacts are present in the density plots of the reconstructed positions, as a consequence of inaccurate reconstructions. Hence, in the first three iterations, the range of the *blurring* procedure is set to σ = 1 mm. From the fourth iteration σ is decreased to 0.5 mm. These values were found empirically to provide the best LRFs convergence.

Calculate new LRFs and check convergence

Optimization techniques (**section 2.5.4**) are used for the LRFs fitting process. In the end of each iteration the LRFs convergence must be verified. The selected stopping criteria for the iterative process was that the difference in reduced χ^2 between two consecutive iterations was below a defined value (e.g. 0.001).

Example of the automatic LRF reconstruction

Simulation tests were performed to evaluate the performance of ML reconstruction using LRFs automatically estimated[1]. An example is given in this section. The idea is to change the initial conditions of a camera design and, firstly, demonstrate that the LRFs estimated for that camera are not adequate to reconstruct events acquired with the new camera conditions; secondly, verify if a new set of LRFs automatically estimated using the script presented above are able to accurately reconstruct events from the new camera. The changes simulated in the camera should result in a new camera response which is described by LRFs with a different profile and also with different maximum average values than those estimated for the initial camera. This way, the capability of the automatic procedure to estimate LRFs in an unsupervised mode can be verified for a challenging scenario. In a real camera, the aging of the optical grease, for instance, can lead to changes in the LRF profiles, while changes in the operating temperature can result in changes in the SiPM relative gains and, consequently in the maximum signal of the LRFs.

A set of γ-rays pencil beam sources placed along a diagonal line in the square camera FOV was used to simulate scintillation events in the two different camera configurations. The LRFs initially estimated for the first camera configuration were used to reconstruct events

[1]The set of ANTS2 scripts used for a particular test, can be found in the web repository https://github.com/jsmarcos/ANTS2_LRFs_AUTOMATIC_ESTIMATION_SCRIPTS-

recorded in the second camera configuration, with poor reconstruction results, that were only improved estimating new LRFs. A gamma camera configuration with a 3 mm GAGG crystal was used. It should be noted that it is not an optimized camera design, but it is sufficiently good to perform the described test. The camera was irradiated with 25 thousand ^{57}Co γ-rays distributed over the entire camera FOV. These flood field events were used by the automatic procedure to estimate the LRFs. To reach the LRFs convergence (LRFs$_1$) eleven iterations were required by the algorithm. The set of pencil beam sources were simulated (350 events per source position) and reconstructed with the estimated LRFs. Then, changes in the camera configuration were manually set, mimicking for instance aging problems and a change in the SiPMs operating temperature. Namely, 1) the optical grease index of refraction of changed from 1.47 to 1.42, 2) the lightguide thickness was changed from 1 mm to 1.2 mm (to force pronounced changes in the camera response and so in the profiles of the required LRFs) and 3) random relative gains were set to the SiPMs (previously all SiPMs had an unitary relative gain) (see the new relative gains in **Fig.5.7 b**). A new simulation was performed with the pencil beam sources in the same positions. The events from the line of sources were reconstructed using LRFs$_1$. New LRFs were required and so, flood field data were acquired for the new camera configuration in order to run the automatic script to estimate new LRFs. The LRFs convergence (into the LRFs$_{new}$) occurred in the end of the seventh iteration. The events from the line of pencil-beam sources (circles in the reconstructed image) were reconstructed with the newly estimated LRFs.

Results Fig.5.7 a shows the reconstructed events for the set of pencil beam sources acquired with the initial camera configuration ("1^{st} line of sources") and reconstructed with LRFs$_1$. The true position of the sources are represented with red circles. Note that the sources positioned until X and Y coordinates equal to 10 are accurately reconstructed. The results of the reconstruction of the line of sources acquired with the changed camera configuration using LRFs$_1$ have strong apparent distortions, as expected, as can be seen in **Fig.5.7 c**. **Fig.5.7 d** shows that the line of sources reconstructed with the LRFs estimated from the flood field acquired for the new camera configuration, LRFs$_{new}$, was well reconstructed, confirming the capability of the automatic algorithm for the estimation of LRFs that faithfully model the camera response.

5.3 Real-time acquisition, reconstruction and visualization of events

One of the ultimate goals of the imaging system described in this work is to be capable of perform event reconstruction and visualization of scintillation event positions as soon as

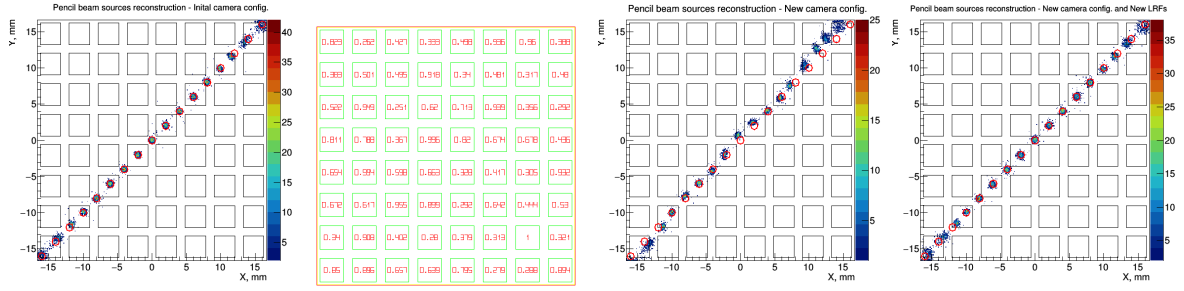

(a) **(b)** **(c)** **(d)**

Figure 5.7: Example of the automatic algorithm capacity to accurately estimate LRFs. **a**: XY density plot of the reconstructed pencil beam sources using LRF_1 (initial camera configuration). The read circles are the true source positions. **b**: Map with the relative gains randomly set to each SiPM (active areas are delimited by a thin green lines). **c**: XY density plot of the reconstructed pencil beam sources using LRF_1 (changed camera configuration). Strong distortions are apparent. **d**: XY density plot of the reconstructed pencil beam sources using LRF_{new} (changed camera configuration).

possible after the events acquisition, processing all the acquired events. This feature was called in this work "real-time imaging" capability. This section describes the infrastructure that I have developed for real-time imaging and presents performance results. The platform that have been used for real-time reconstruction and visualization is a computer with both a multi-core CPU and a general-purpose graphics processing unit (GPU). The system was tested in a laptop with 4 CPU cores (Core i7, 3.5 GHz, 8GB RAM) and a graphic card Nvidia GeForce GTX 850M.

5.3.1 Data structures and procedures

Data structures ANTS2 was used for event reconstruction and visualization of the reconstructed position as a (x, y) density plot. Before explaining the real-time sequence of operations, the required data structures to handle the events data are first presented. For each event, the SiPM signals, the reconstructed position and energy (x, y, e) and the corresponding reduced *chi-square* (χ^2) must be stored. ANTS2 has a data structure called *Event DataHub* which saves all this information. However, the *Event DataHub* is not prepared to work in FIFO mode, as needed for the implemented real-time procedures. I have implemented the necessary C++ data structures and functions and integrated them into ANTS2 scripting engine in order to handle the real-time information associated with the scintillation events. A buffer operating in FIFO mode (***real-time buffer***) was implemented to hold the incoming events. Its size is configurable, and corresponds to the maximum number of events presented in the real-time image.

The C++ functions can be called by the ANTS2 scripting engine. The developed functions include the real-time buffer writing and reading and the events filtering based on χ^2.

Real-time chain procedures Using the ANTS2 scripting module, it is straightforward to perform the reconstruction and visualization of the events when the DataHub contains SiPM signals of these events. If statistical reconstruction is used, the set of LRFs that constitutes the model must be also available. Because in ANTS2 the statistical reconstruction algorithms can be rapidly executed in the GPU[1] ($\sim 10^6$ events are reconstructed in one second for dozens of sensors), in each real-time cycle, all the events in the *real-time buffe*r are copied to the DataHub, then reconstructed and finally plotted. Note that also the events already reconstructed in the previous cycle are reconstructed again in the current cycle.

For clarity, "real-time cycle" refers to one cycle of the real-time operations chain, which has the following steps: 1) monitoring of the directory with the acquired data, searching for new files (.HLD)[2] in a predefined directory, 2) process the acquired data to extract the SiPM signals, 3) load the processed files (.DAT) in ANTS2 (*Event DataHub*), 4) append the new set of events to the *real-time buffer*, 5) clean the *Event DataHub* and copy to it all events in the *real-time buffer*, 6) reconstruct all events in *Event DataHub*, 7) plot the positions of all reconstructed events (XY density plot) and 9) clean the *Event DataHub*.

Fig.5.8 shows a flowchart of the real-time imaging processing chain.

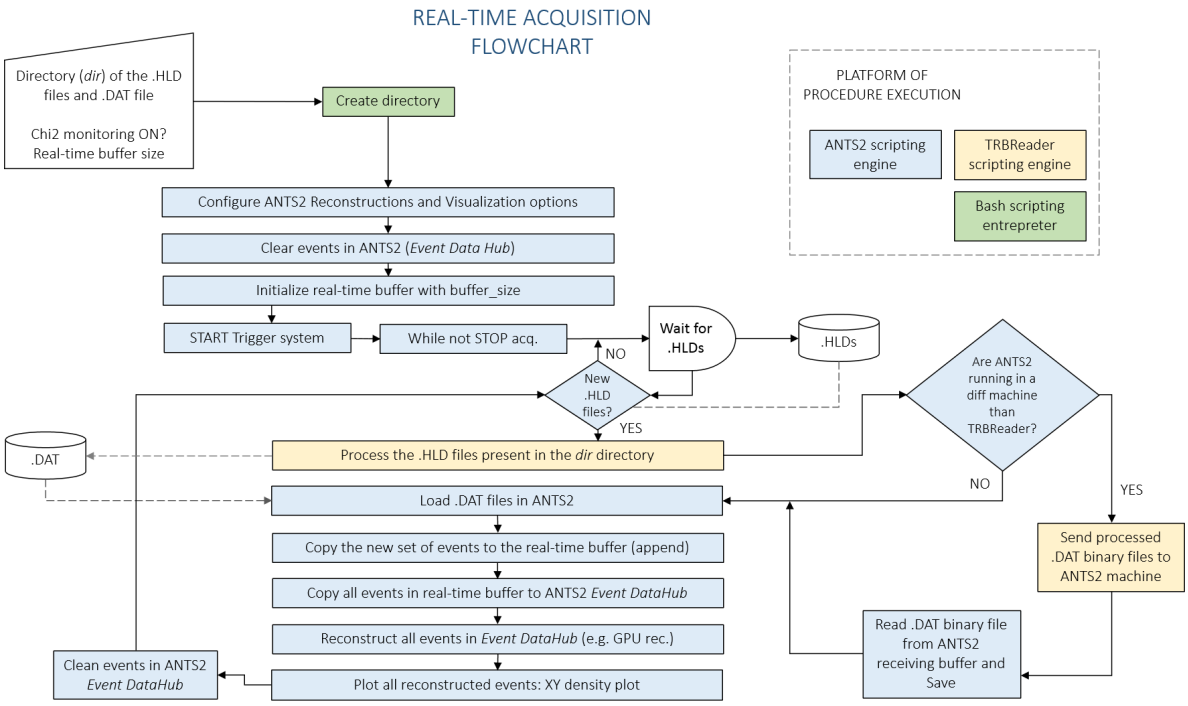

Figure 5.8: Flowchart of the real-time imaging processing chain.

[1]There are two procedures which code runs on the CPU and not on the GPU: the center-of-gravity reconstruction for the initial search position of *contracting grids* method and the calculation of the reduced *chi-square*.

[2]As there is no notification when a .HLD file of the selected size is created with the acquired data, the way to know that new data arrive was to periodically search for new .HLD files.

Alternative handling of events data in buffers An alternative sequence of operations to increase the real-time performance was tested. Instead of copying all the events from the *real-time buffer* to the DataHub in every real-time cycle, only the new bunch of events are copied and immediately reconstructed. The newly reconstructed event positions (and energies) are append to a temporary buffer that saves the reconstructed positions (and energies). The positions of the events in the temporary buffer can then be added to the (x, y) density plot. With this alternative, both redundant copy of events and redundant reconstruction of events are avoided. However, as the reconstruction of all events in each real-time cycle does not considerably affects the real-time performance, this solution was used in the first "prototype" of the real-time system.

Remote real-time imaging As represented in the blue in the right side of the flowchart of **Fig.5.8**, the system is prepared for remote reconstruction and visualization. An example is the case when ANTS2 and TRBReader are running in different machines. In this case, TRBReader, running in the machine that stores the events, must send the processed files (.DAT) to ANTS2 machine. This is done through the communication modules of the two applications (**appendix D.2**).

Instantaneous image reset Not represented in the flowchart is a feature for the "reset" of the *real-time buffer*. This can be useful, for instance, to have an immediate update of the image when scanning for gamma activity in a region of the patient body and moving the detector to other completely different region.

Optional *high-statistics* image The system is prepared for using a second buffer of higher size (*high-statistics buffer*) in order to supply images with higher quality (more events per image pixel). One usage scenario would be when it is desired to see and possibly save an image with more contrast than that possible to obtain with the maximum number of events defined for the *real-time buffer* (FIFO operation). The *high-statistics buffer* saves in real-time the number of events previously selected (e.g. 300 thousand events). When the instruction to show the high-density image is given to the system, this second buffer is copied to the ANTS2 *Events DataHub* for the reconstruction and plotting of all events.

Real-time imaging: *snapshots* of image sequences **Fig.5.9** shows photographs taken during the experimental campaign for the characterization of the gamma camera prototype. The real-time feature of the developed imaging system was successfully tested in the course of the experimental campaign. Moreover, it proved to be really useful to speed up the alignment of the masks (slits) and phantoms (capillary tubes) during the characterization, namely

in the trial and error step for the correct positioning of those masks and phantoms. Each reconstructed image that can be seen in a display in the photographs is a *snapshot* showing an image presented at that moment by the real-time imaging system. The image belongs to a video sequence visualized at the time the *snapshot* was taken. Four cases are presented: 1) two WC alloy rings with different sizes, which serve as a mask, 2) three air bubbles in a capillary tube filled with a ^{99m}Tc solution with an orange dye, 3) three parallel capillary tubes (1 mm diameter inner tube), with a transparent ^{99m}Tc solution and 4) a phantom resembling a simplified brain slice, filled with a ^{99m}Tc solution with orange dye.

5.3.2 Monitoring of the quality of the camera response model

The quality of the camera response model can be monitored in each real-time cycle or at regular intervals. This control is performed after the reconstruction of the events, by comparing the average χ^2 with a threshold value. If the averaged χ^2 is above the threshold, an alarm is triggered. In this case, one knows that the detector model is not adequate to describe the current camera response and so, a new dataset of flood field irradiation should be acquired and new LRFs (the model) should be estimated, for instance, using the automatic LRFs reconstruction script (**section 5.2**).

5.3.3 Performance of the real-time imaging system

The analysis on the timing performance of the developed real-time imaging system (events per second) was divided in two: 1) the events acquisition rate and 2) the processing time of the real-time procedures chain.

Event acquisition rate The maximum acquisition rate can be usually limited by the ADCs sampling rate, depending on the number of channels and the number of samples, or limited by the transfer rate. In this work, the ADCs sampling rate is not the limiting factor (40 MHz). The limiting factor is the TRB3 platform maximum transfer rate, which depends on the communication overheads, the number of channels, the number of samples per channel and the number of bytes per sample. TRB3 gigabit ethernet connection has a nominal maximum transfer rate of 95 MBytes/s. However, from my measurements, it can only effectively transfer data at a rate of around 55 MBytes/s, saturating at this value, as can be seen in **Fig.5.10**, which presents the transfer rate reported by the TRB3 real-time monitoring system for different trigger rates, set by the internal pulse generator. Curves with different colors correspond to the transfer rates measured when different number of samples were acquired per waveform. The number of samples was varied from 10 to 30 and each sample is encoded with 4 bytes (TRB3 ADC add-on cannot be configured to change this number of bytes/sample). The number of channels readout per event is 68 (64 SiPMs and 4 sum signals).

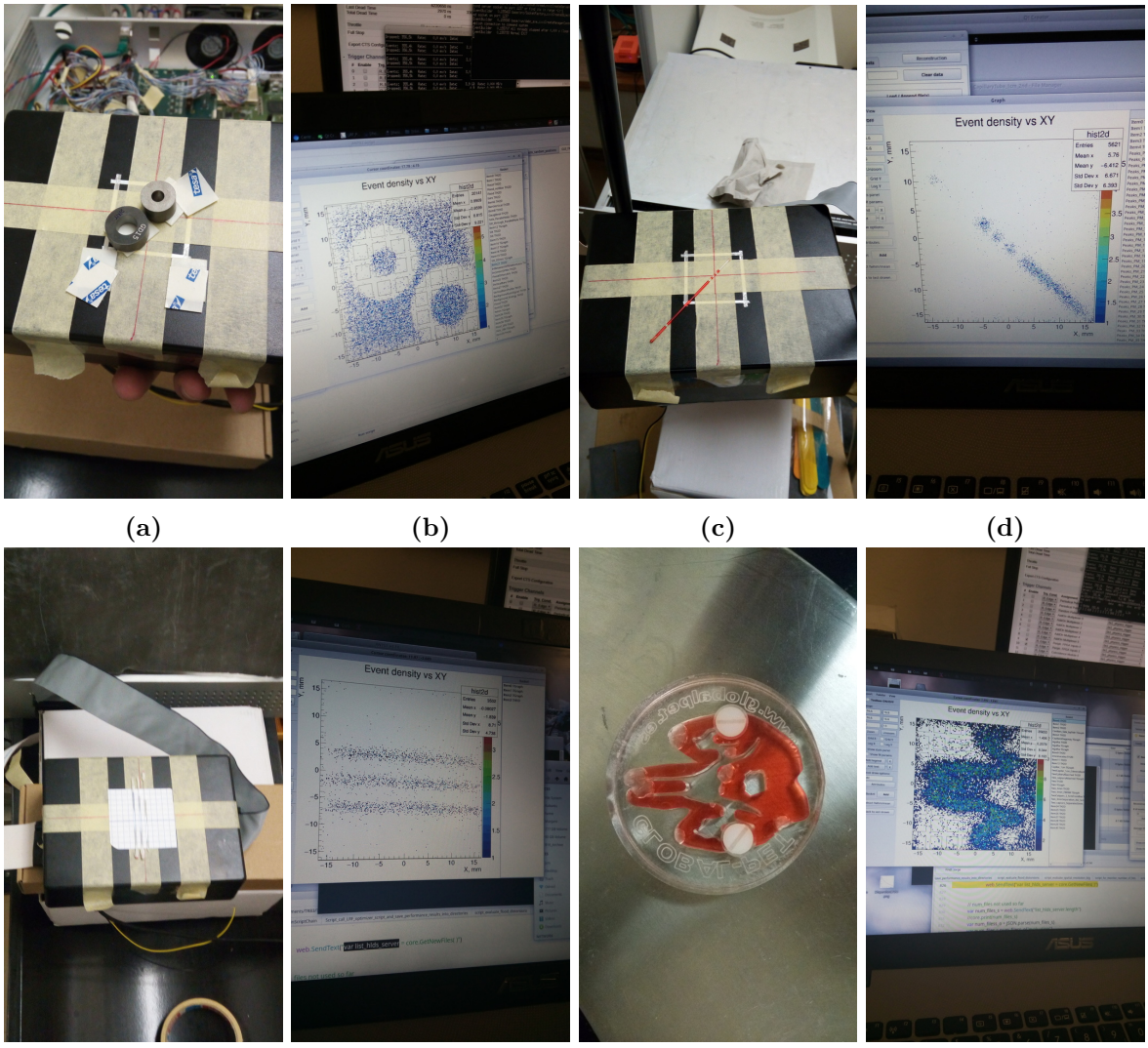

(a) (b) (c) (d)

(e) (f) (g) (h)

Figure 5.9: Photographs with masks, phantoms and *snapshots* of the corresponding real-time reconstructed image sequences. Both the mask and the phantom with the radioactive source containers are shown. **a**: *Two rings* mask made of WC alloy. **b**: Snapshot of the *two rings* (made of WC alloy) reconstructed image. **c**: *Three air bubbles* in a capillary tube. **d**: *Three air bubbles* reconstructed image. **e**: Three parallel capillary tubes. **f**: Three capillary tubes reconstructed image. **g**: Phantom resembling a simplified *brain slice* phantom. **h**: Reconstructed image of the *brain slice* phantom.

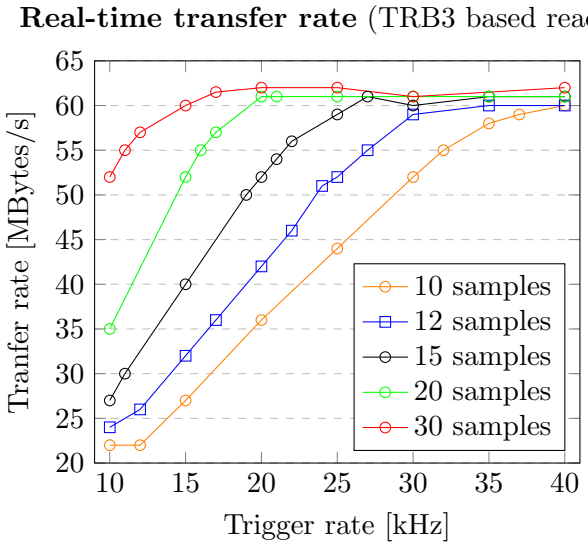

Figure 5.10: TRB3 DAQ real-time data transfer rate as a function of the events trigger rate. Each curve corresponds to the number of samples per waveform used in the measurement.

Fig.5.11 a shows the maximum acquisition rate achieved when using different number of samples per waveform. The more the number of samples, the lower is the maximum acquisition rate, because more data is transferred by event and consequently the saturation limit in the transfer rate is achieved faster than for less number of samples. The plot shows the maximum acquisition rate for two sizes of the .HLD files, in which the acquired data is saved by the event builder application (**section 4.3.2**). The biggest size (200 MB) allows to achieve higher acquisition rates than the smallest (100 MB). The reason for this difference is related with the time that the event builder application takes to create each new .HLD files. **Fig.5.11 b** shows the maximum acquisition rate achieved using different .HLD file sizes, for a fixed number of 12 samples per waveform. It can be seen that there is no significant increase in the acquisition rate when the size of the .HLD file is bigger than 300 MB.

Processing time of the real-time procedures chain For each real-time cycle, the .HLD files must be searched in the acquisition directory and a list with the files name is filled. This procedure takes 150 ms. A fraction of that time is used for the communication and data exchange between the TRBReader application (which peforms the processing) and ANTS2. Then, starts the processing chain of each individual file, starting by the integration of the waveforms samples (process .HLD file) and ending with the visualization of the reconstructed positions of the newly processed events in a density plot with the reconstructed positions of all events present in the *real-time buffer*. The new events loaded in ANTS2 are saved in the *Event DataHub*, previously cleaned to save at this moment only the new events. Then, these new events are copied to the *real-time buffer*, which saves all the events in a FIFO mode. As

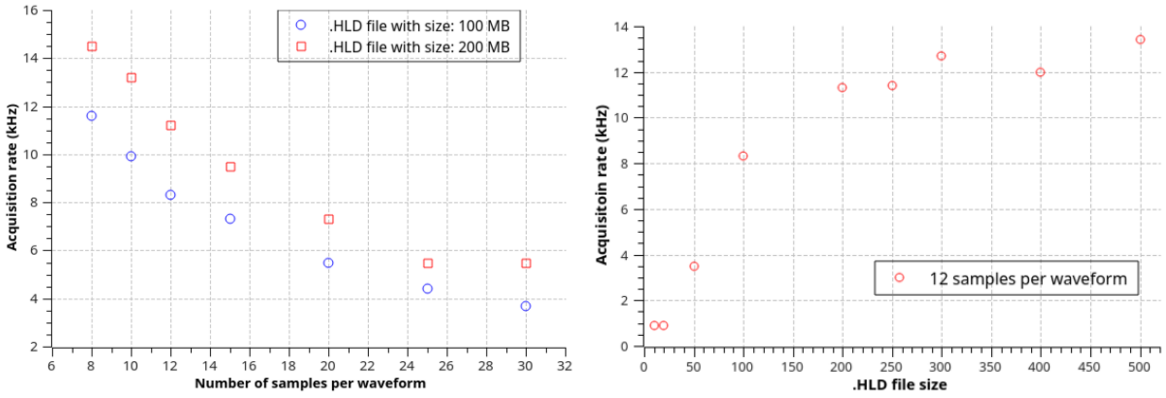

(a) **(b)**

Figure 5.11: Maximum acquisition rate of the TRB3 readout system. **a**: Maximum acquisition rate *vs* number of samples per waveform (for two .HLD file size: 100 MB and 200 MB). **b**: Acquisition rate *vs* .HLD file size (for waveforms of 12 samples).

the reconstruction in ANTS2 takes the events from the *Event DataHub* structure, all events in the *real-time buffer* must be copied back to it in order to be reconstructed.

The **table 5.1** presents the processing time per event (ms) of each procedure of the real-time processing chain. These performance times were recorded using .HLD files with 15 MB, which corresponds to 1344 events per file, with 68 waveforms per event and 30 samples per waveform.

Procedure	Processing time per event (ms)
Process .HLD files	0.186
Load events (.DAT files) in ANTS2	0.161
Copy events from *Event DataHub* to *real-time buffer*	0.00001
Copy events from *real-time buffer* to *Event DataHub*	0.0006
Reconstruction of events (4 threads)	0.0030
Visualization (refresh density plot)	0.0038

Table 5.1: Timing performance of real-time processing. Event processing rate (ms/event) of each step in the real-time processing.

The overall processing of each file takes on average 476.3 ms, so the refresh rate of the density plot with the reconstructed positions is about 2 Hz. Considering that each file has 1344 events, the real-time imaging rate is about 2800 events per second. This rate is not as high as the acquisition rate of 10 kHz that can be achieved by the readout system. The bottleneck in the processing time come from the "Processing .HLD files" and "Load events (.DAT files) in ANTS2" steps (**table 5.1**). The relatively large amount of time required by these two steps are most probably related with the time needed for reading the files from the disk. However, the measured imaging rate is sufficient for the acquisition rates expected in

the clinical applications for which this work was mainly developed (SLN detection and thyroid imaging).

For the FOV of the developed camera (around 32×32 mm^2) and the size of the density plot matrix (number of pixels or bins) 2.8 kHz is an acceptable rate when imaging in real-time. As a rule of thumb three bins should be used per the size of the spatial resolution. The developed system has a resolution of approximately 1.5 mm FWHM when the parallel-hole collimator is used and a resolution no better than 1 mm in the detector plane when the pinhole collimator is used to obtain a strong de-magnification (**section 6.6**). If considering the resolution of 1.5 mm, the matrix should have 1 bin per each 0.5 mm, which means 64 bins (32/0.5) in each direction. If considering the resolution of 1 mm, the matrix should have 1 bin per each 0.33 mm, which means about 97 bins (32/0.33) in each direction. Thus, the density plot matrix should have 64×64 bins or 100×100 bins. It was verified that a refresh rate of 2 Hz in the two matrix sizes gives a fairly good real-time perception in clinical practices. Starting from 10 thousand events (displayed after 3 or 4 seconds at a real-time imaging rate of 2800 events per second), images with enough contrast to start seeing "hot" regions can be produced for the referred matrix sizes. Furthermore, in the system developed in this work, the physician has the possibility of pressing a button to see a *high-statistics* image (e.g. 200 thousand events), whenever the required number of events was already acquired.

Nevertheless, the refresh rate can be increased, for instance, using higher amount of RAM memory and a processor with higher number of cores and fast processing rate. The computer used in the presented timing performance measurements has a HDD disk, 8 GB of RAM and a Intel Core i7 of 4^{th} generation. A dedicated computer would allow a much better timing performance. Other possible strategy, if enough RAM memory is available (say 32 GB), is to save the acquired .HLD files directly to the RAM memory, which increases significantly the reading times.

It should be noted that the event reconstruction rate (time per event) is not linear with the number of events and it decreases with higher number of events. For instance, the reconstruction rate of a bunch of 1344 events is 0.003 ms/event, while the reconstruction of a bunch of 4469 events is 0.0023 ms/event. The reconstruction time (and rate) depends on the number of threads used by the processor because, although the code of the *contracting grids* reconstruction method runs on the GPU, the code to calculate the center-of-gravity (to determine the initial search position) and to calculate the reduced *chi-square* runs on the CPU and was implemented in ANTS2 in a parallel computing mode. **Fig.5.12** shows the time required by the processor to reconstruct 35 thousand events and the reconstruction rates when different number of threads are used, from only one up to four threads. The higher is the number of threads, the higher is the reconstruction rate, as expected.

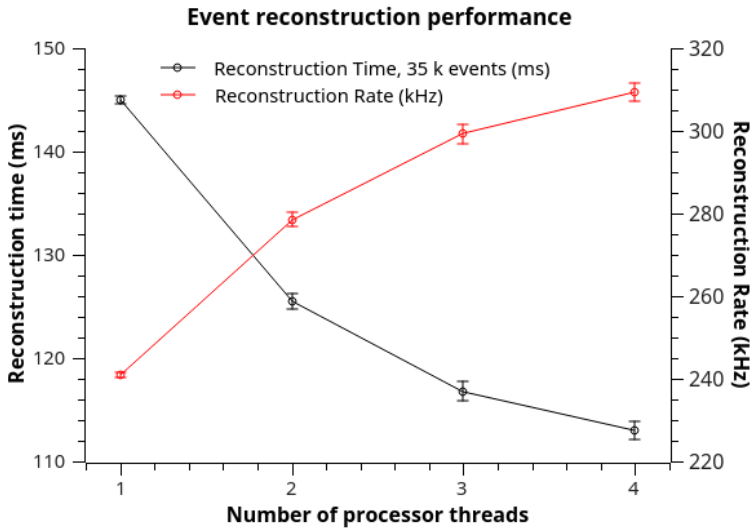

Figure 5.12: Event reconstruction timing performance. Black curve: time (ms) to reconstruct 35 thousand events; Red curve: reconstruction rate (kHz).

6

Camera prototype and imaging system characterization

6.1 SFOV imaging system

6.1.1 Gamma camera prototype

Two versions of a gamma camera prototype were built based on the results of the optimization study from **section 3**. The only difference between them is the scintillator material and its thickness. In a gamma camera, for the same scintillator material, the thicker it is, the higher is the γ-ray interaction efficiency and the worse is the spatial resolution. The variation in the depth-of-iteration of γ-ray is higher for thicker crystals, affecting the reconstruction accuracy. As LYSO has higher mass attenuation coefficient[1] and higher density[2] than GAGG, a thinner scintillator plate was necessary in the case of LYSO than in the case of GAGG for equivalent efficiencies. The selected thickness for the LYSO scintillator was 2 mm, while for the GAGG scintillator it was 3 mm.

Fig.6.1 presents the geometry of the gamma camera prototypes, which include the following components: 1) an array of four SensL Array-C 30035 SiPMs, 2) a 1 mm thick plexiglass lightguide , 3) the scintillator crystal, 3) a 2 mm thick Teflon reflector plate and 4) a black ABS plastic material covering the crystal lateral surfaces. All components are coupled with thin layers of Saint Gobain BC630 optical grease ($n = 1.465$). The first four components have an area of 33.2×33.2 mm^2, so they are packed inside a slightly larger black ABS plastic frame, with an inner area of 33.8×33.8 mm^2. Optical grease fills the space between the lateral sides of the components and the black frame.

The prototype with the 2 mm thick LYSO:Ce scintillator (Prelude 420, from Saint-Gobain) was assembled for the experimental validation of the simulation models, as presented in **sec-**

[1]The mass attenuation coefficient for 140 keV is 1.372 cm^2/g and 0.827 cm^2/g for LYSO and GAGG, respectively.

[2]The LYSO density is 7.1 g/cm^3 and the GAGG density is 6.63 g/cm^3.

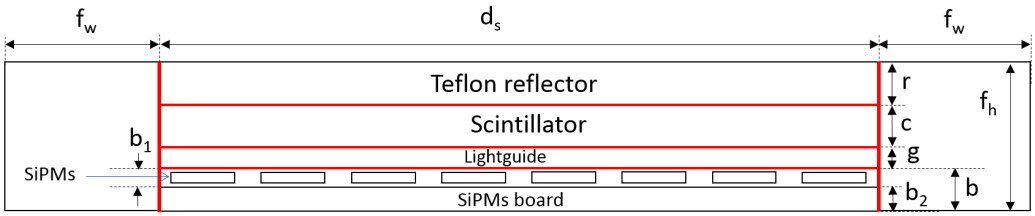

(a)

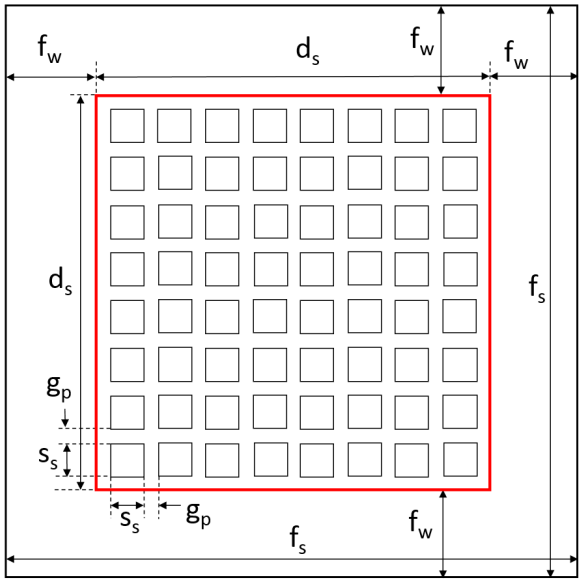

(b)

Figure 6.1: Schematic drawing of the gamma cameras prototype geometry. **a**: Lateral view with components dimension labels. $d_s = 33.2$ mm; $r = 2$ mm; $c = 3$ mm for GAGG and $c = 2$ mm for LYSO; $g = 1$ mm; $b = 2$ mm; $b_1 = 0.7$ mm; $b_2 = 1.3$ mm. Red lines represent thin layers of optical coupling grease. **b**: Top view of the SiPMs array layer. The array of squares represent the sensitive areas of the SiPMs. $d_s = 33.2$ mm; $s_s = 3$ mm; $g_p = 1.2$ mm.

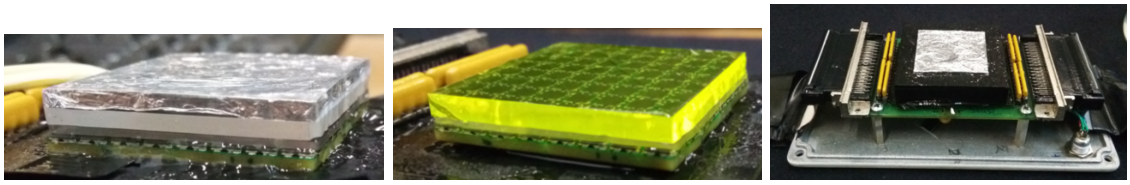

(a) (b) (c)

Figure 6.2: Photographs of the two gamma camera prototype versions. The SiPMs array is at the bottom, with the lighguide and the scintillator mounted on it. **a**: LYSO based prototype with an aluminum foils wrapping the reflector plate, which is on the top. **b**: GAGG based prototype without the reflector plate. The SiPMs array can be seen through the semitransparent yellow crystal. **c**: View of the prototype assembled to a board which is the bottom part of a light tight box. The connectors for the readout cables are visible. The gamma camera is hidden by the black ABS plastic frame around it. The aluminum foil can be seen in the top, covering the reflector plate.

tion 3.2.3. The LYSO camera model used in simulations (**section 3.2.4.1**) reproduced the design of this prototype. The interaction efficiency for 140 keV γ-rays is 85.7% for a 2 mm thick LYSO scintillator. The prototype with the 3 mm thick GAGG scintillator has a gamma interaction efficiency higher than 80.7%.

Fig.6.2 shows photographs of the assembled gamma camera prototype versions. The array of photosensors is at the bottom of the camera, followed by the lightguide, the scintillator crystal and the Teflon plate. Aluminum foil covers the 2 mm Teflon plate, improving the back reflection fraction of the scintillation photons. In **Fig.6.2 c** the black frame (ABS plastic) can be seen, covering the camera components. The aluminum foil that covers the Teflon plate is also visible, as well as the connectors for the flat cables used to read the SiPMs signal (32 SiPMs per flat cable).

6.1.2 Collimators: design and manufacturing

The most used types of collimators were presented in **section 2.2.1**, along with the equations that allow to design collimators with specific spatial resolutions and sensitivities. In **section 3.2.6** those analytical formulas, traditionally applied to large FOV cameras, were validated for small FOV cameras comparing the resolutions and sensitivities with those from simulations.

Parallel-hole collimator The parallel-hole collimator dimensions were selected based on the analysis of the trade-off curves presented in the **section 3.4**. The collimator has an overall area of 64 $\times$ 64 mm^2 with hexagonal holes with 0.5 mm between two opposite hexagone sides (d). The separation between holes (septa t) is 0.3 mm, so the holes pitch p is 0.8 mm (see **Fig.6.3 a**). The area with holes is 60 $\times$ 60 mm^2. There is a 2 mm wide compact frame around the region with holes, to add mechanical strength to the collimator. The height of the holes (collimator thickness) is 8 mm. For these dimensions, the analytically calculated spatial

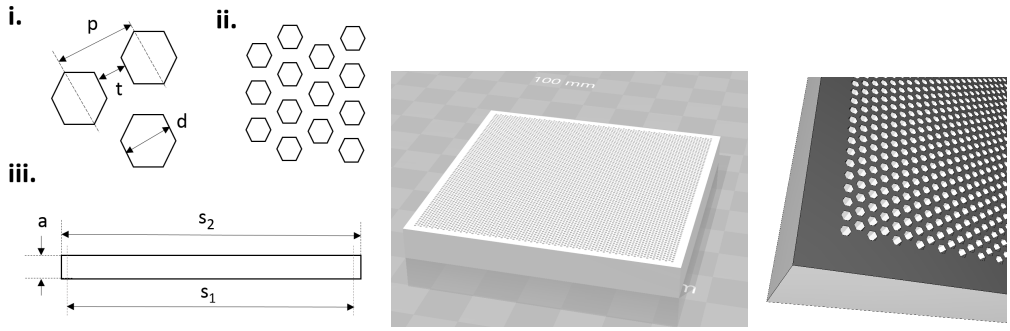

(a) (b) (c)

Figure 6.3: Parallel-hole collimator drawings. **a**: Geometry and dimensions. **(i).** Unitary cell details: $d = 0.5$ mm; $t = 0.3$ mm; $p = 0.8$ mm; **(ii).** Detail of the hexagones arrangement (relative positions). **(iii).** Side view of the parallel-hole collimator: $a = 8$ mm; $s_1 = 60$ mm; $s_2 = 64$ mm. **b**: CAD drawing for production. **c**: Zoom in of the collimator face, where the hexagonal shape of the holes is visible.

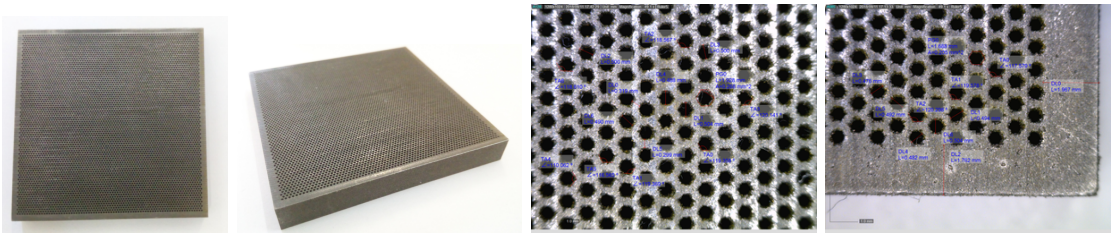

(a) (b) (c) (d)

Figure 6.4: Photograph of the parallel-hole collimator produced by M&I Materials Co. b: Top view. **b**: Overview. **c**: Zoom in photograph of the middle region of the collimator, with the indication of the dimensions. **d**: Zoom in photograph of a collimator corner.

resolution for a point source at 50 mm from the collimator face is 4.1 mm[1] and the sensitivity is around 120 cps/MBq (see **section 3.4.1**).

The production of the parallel-hole collimator was ordered to the company M&I Materials (Manchester, UK). This company was the only one that I found which is able to produce a parallel-hole collimator with dimensions referred above. The collimator CAD drawing was designed in the LIP laboratory and it is shown in **Fig.6.3**. The collimator is made of pure tungsten (W) by means of selective laser melting, a technique referred in **section 2.2.1.3**. **Fig.6.4** shows photographs of the produced parallel-hole collimator.

Pinhole collimator The design of the manufactured pinhole collimator was based on the analysis presented in the **section 3.4.2**. The pinhole diameter is 1 mm and the aperture angle is 90°. The pinhole edge is of "channel-edge" type (**section 2.2.1.2**). The channel length is ≈0.5 mm. With these dimensions, the expected spatial resolution is 2.73 mm and the expected

[1]For the same parallel-hole dimensions, if the point source is at a distance of 10 mm, 20 mm and 100 mm, the spatial resolution is 1.4 mm, 2.1 mm and 7.4 mm, respectively.

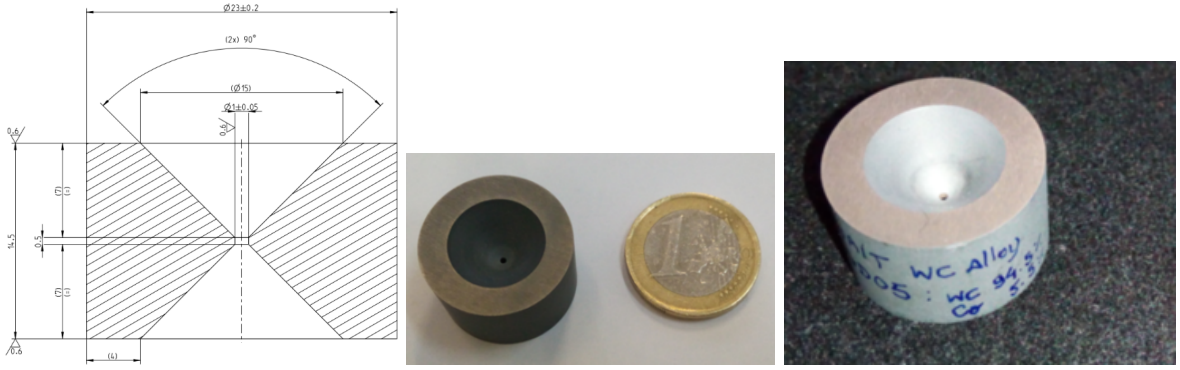

(a) **(b)** **(c)**

Figure 6.5: Pinhole collimator drawing and photographs. **a**: Lateral cut view of the pinhole collimator drawing. The dimensions are given in mm. The areas filled with lines are made of tungsten carbide alloy**b**: Photograph with Euro coin as size reference. **c**: Photograph where the hole "channel" can be seen.

sensitivity is about 219 cps/MBq for a setup with no magnification and the source at 50 mm from the detector face. The exterior of the collimator part is a cylinder with 23 mm diameter and 14.5 mm height.

The production of the pinhole collimator was ordered to DURIT company (Albergaria-a-Velha, Portugal). The production method was the electric discharge machining (EDM), referred in the **section 2.2.1.3**. The material is tungsten carbide (94.5% WC and 5.5% Co). **Fig.6.5 a** shows the drawing made by DURIT based on the ordered dimensions. **Fig.6.5 b** and **c** show photographs of the produced WC pinhole collimator.

The next sections present the measurement setups and the calibration of the readout system used in the characterization of the two versions of the gamma camera prototype, as well as the procedures to populate the detector models (see **section 2.5.2**).

6.2 Measurement setups

The two versions of the gamma camera prototype were connected (one at a time) to the readout system presented in **section 4**. The readout system, which includes the front-end and data acquisition electronics, was controlled by a mini-computer (Odroid-C2) through a command-line interface. **Fig.6.6** depicts schematically the setup for the measurements. A diaphragm was present for the measurements of the intrinsic performance, both when irradiating the entire FOV of the camera (**Fig.6.6 a.**) and when using a mask (**Fig.6.6 b.**). For instance, a rectangular diaphragm was used for measurements which have a slit mask close to the camera. For the measurement of the extrinsic performance, either a parallel-hole collimator or a pinhole collimator were present, as well as the phantom to be imaged (**Fig.6.6 c.**). The range of the distance h was in the order of half a meter for the intrinsic characterization and from 5 mm to

≈60 mm for the extrinsic characterization. The parallel-hole collimator was attached to the camera (u is 0 mm), while the pinhole was placed at a u distance in a range from 23.5 mm to ≈60 mm, to obtain different magnification factors.

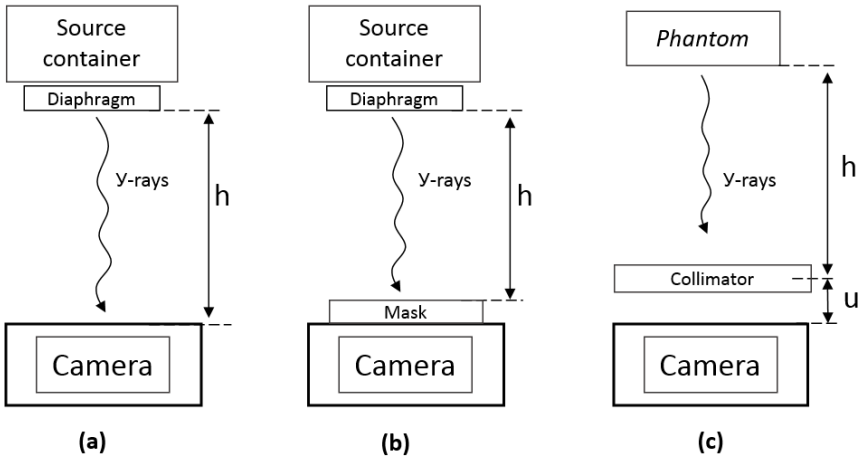

Figure 6.6: Schematic representation of the measurement setup. **a.** Setup for flood field data recording (no mask). **b.** Setup for intrinsic characterization measurements which require a mask (e.g. slit, parallel bars). **c.** Setup for extrinsic characterization measurements. Both a collimator (either parallel-hole or pinhole type) and a phantom are present.

To perform the measurements with a gamma camera prototype, it was mounted inside a light-tight enclosure. The distance between the scintillator crystal inside the camera and the outer face of the camera enclosure in the source direction is 15 mm. Two flat cables connect the SiPM outputs from a board inside the camera to the readout system. The measurements for the validation of simulation models were performed at 122 keV, using a ^{57}Co source (**section 3.2.4.2**). The assessement of the two versions of the gamma camera prototype (GAGG and LYSO) presented in this section was performed for the energy of 140 keV (^{99m}Tc). The temperature inside the camera was 21±0.1°C and it was very stable, as the measurements were performed in a temperature controlled environment.

6.2.1 Masks and phantoms

In order to measure the intrinsic resolution and linearity of the gamma camera prototypes, three masks were produced: **1)** a single 0.2 mm slit and **2)** four parallel 0.2 mm slits, both for intrinsic spatial resolution assessment and **3)** a parallel bars mask, for linearity assessment. The masks material is an alloy of tungsten carbide (WC 92% + Co 8%). The thickness of 2 mm is sufficient to attenuate 99.9% of 140 keV γ-rays. **Fig.6.7** presents the masks geometries.

Slits (0.2 mm): single and multiple Two blocks of tungsten carbide (WC) were used to make a single slit 0.2 mm wide (**Fig.6.7 (i)** and **(ii)**). They are of the same size: 10 mm ×

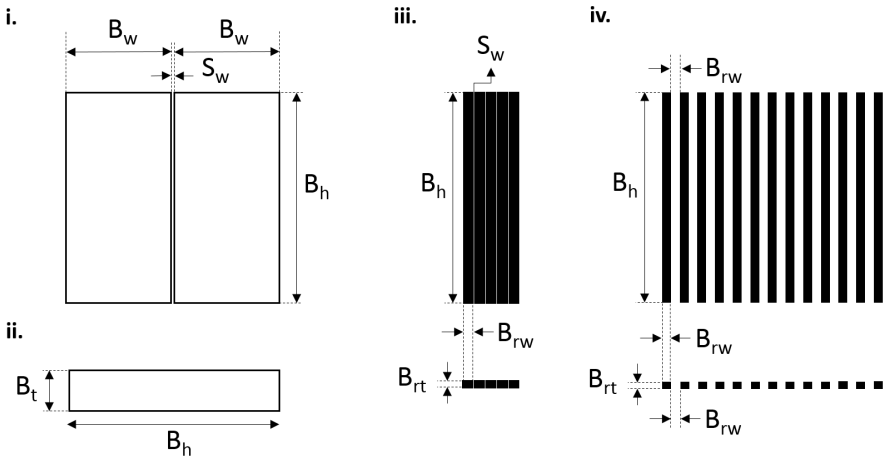

Figure 6.7: Schematic drawings of the masks geometry. (i). Top view of the 0.2 mm slit (*single slit*) made with two WC 10 mm thick blocks. S_w = 0.2 mm; B_w = 25 mm and B_h = 50 mm. **(ii).** Lateral view of the 0.2 mm *single slit*. B_t = 10 mm and B_h = 50 mm. **(iii).** *Multislit* mask (four parallel 0.2 mm slits made with five WC bars). S_w = 0.2 mm; B_h = 50 mm; B_{rw} = 2 mm and B_{rt} = 3 mm. **(iv.)** *Parallel bars mask*. The dimensions of the bars are the same as in iii), B_h = 50 mm, B_{rw} = 2 mm and B_{rt} = 3 mm.

25 mm × 50 mm. The blocks were firmly attached, separated by two 0.1 mm thick cellulose based material layers, to form the slit with S_w = 0.2 mm (*single slit*). **Fig.6.8 a** shows a photograph of the slit formed with the blocks. Five 2 mm × 3 mm × 50 mm bars made of tungsten carbide were tightly attached with two layers of 0.1 mm cellulose based material in between them, to form a multiple slits mask of four parallel slits (*multislit*) with width of S_w = 0.2 mm (**Fig.6.7 (iii)**).

Mask made of 2 mm wide parallel bars An aluminum structure was built in LIP workshop to hold 13 WC bars with dimension of: 2 mm × 3 mm × 50 mm. The WC bars were ordered from DURIT company. They were placed in parallel (2 mm wide), alternating with 2 mm acrylic bars. **Fig.6.7 (iv)** presents the geometry of the mask, representing the 2 mm WC bars in black color. **Fig.6.8 b** shows a photograph of the 2 mm wide WC bars placed in the holder, alternating with the 2 mm acrylic bars. This mask is referred below as *parallel bars mask*.

Phantoms For the extrinsic characterization of gamma cameras (with collimator present), two types of phantoms were used: capillary tubes and a plastic container that resembles a simplified shape of a *brain slice*. The capillary tubes have an external diameter of 1.6 mm and an internal diameter of 1.0 mm. Its length is 75 mm. The *brain slice* phantom container is a 8 mm thick acrylic cylinder with about 40 mm diameter. The capillary tubes and the brain phantom were filled with a solution that contained ^{99m}Tc, to be used as radioactive sources

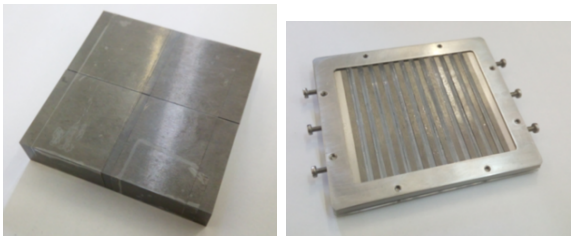

(a) (b)

Figure 6.8: Photograph of two masks used in the prototypes characterization: 0.2 mm slit and 2 mm wide parallel bars with 4 mm pitch. a: *single slit* made of two 10 mm thick blocks of WC. **b**: *Parallel bars mask* made of 2 mm wide WC parallel bars with 4 mm pitch. The WC bars are 3 mm height and have a length of 50 mm. They have 2 mm acrylic bars between them.

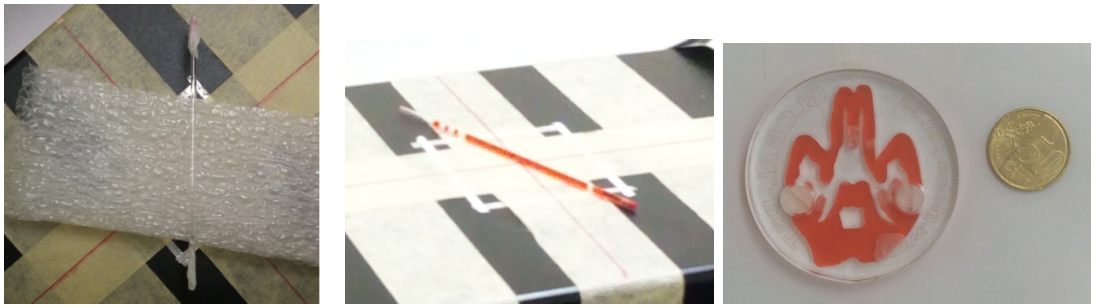

(a) (b) (c)

Figure 6.9: Photographs of the capillary tube and *brain slice* phantoms, filled with a solution containing ^{99m}Tc source a: Capillary tube filled with a transparent solution. **b**: Capillary tube filled with an orange color solution. **a**: *Brain slice* filled with an orange color solution.

imaged by the gamma camera. **Fig.6.9** shows photographs of the capillarity tube and the *brain slice*.

6.2.2 Performance assessment setups

Intrinsic spatial resolution To assess the intrinsic spatial resolution, both the *single slit* and the *multislit* masks presented before were used, one at a time. For the two cases, the mask was attached to the camera enclosure, on the side closer to the reflector, thus, at 15 mm from the scintillator. The resolution was calculated as the FWHM of the transverse profile of the reconstructed slit image. To study the position dependence of the spatial resolution (see **section 2.4.2.1**), the assessment with the mask of the *single slit* was performed twice, placing the slit in two different parallel positions. For the first position, the slit was placed in front of the centers of eight SiPMs (*Slit_center*) and, for the other position, the slit was placed in front of the space between SiPMs (*Slit_between*). The *single slit* was oriented differently in the assessment of the two prototype versions, only due practical reasons at the measurement

time. For the *GAGG prototype*, the *Slit_center* and the *Slit_between* were placed at X = 2.1 and X = 0, respectively. For the *LYSO prototype*, the *Slit_center* and the *Slit_between* were placed at Y = -2.1 and Y = 0, respectively. The source was always placed at 380 mm from the masks.

Uniformity According to the NEMA standards on the performance measurements of gamma cameras[82], the intrinsic uniformity expresses the quality of the response of the system without a collimator to a uniform flux of radiation from a point source. The gamma camera prototype was irradiated with a ^{99m}Tc point source placed at a distance h (see **Fig.6.6 b.**) bigger than 5 FOVs[1], as recommended in NEMA procedures (flood field). However, h depended on the activity of the source available when assessing the uniformity for each prototype version, which was not under my control. The distance was selected to achieve a count rate of about 2000 counts per second (cps) through the photopeak window (140 keV) of 30%. For the *GAGG prototype*, h was 800 mm and for the *LYSO prototype*, h was 380 mm. Both distances respect the 5 FOVs rule.

Due to the selected triggering strategy of the readout system presented in **section 4** the trigger rate was not uniform over the entire FOV of the camera, resulting in an apparent low degree of uniformity of the density plot of the reconstructed event positions. Thus, the uniformity was assessed after applying an uniformity correction map and smooth the resulting image with a 9-pixel filter function, as recommend in the NEMA standard [82]. The correction map was calculated from a separate flood field dataset. This map contains the factors that must be applied to the original uniformity density plot in order to improve its uniformity. The integral and differential uniformity parameters were calculated following **Eq.2.44** and **Eq.2.45**.

Linearity The linearity assessment was performed with the parallel bars mask presented in **section 6.2.1**. The ^{99m}Tc radioactive source was at 800 mm from the mask. Two measurements were made for different orientations of the mask: horizontal direction and diagonal direction (45°). The *parallel bars mask* was attached to the camera enclosure (out of the camera), in the side of the reflector (the distance mask-to-scintillator was 15 mm). The linearity performance was assessed following the NEMA standard (deviation from a straight line). Both the differential (statistics of the deviations) and absolute linearity performance are given.

[1]The diagonal lenght of the camera sensitive area is ∼44.7 mm.

6.3 Readout system calibration

The SiPMs were connected to the readout system, where the acquired waveforms were sampled, digitized and sent to the processing unit. Then, the waveforms were integrated in a 650 ns window. The result for each SiPM is a value proportional to the number of photons detected by that SiPM (given in ADC channel units). The calibration consists in the calculation of the SiPM relative gains. These gains g, for each SiPM, are the number of ADC channels that correspond to one single registered photoelectron in that SiPM ($C_{p.e.}$) (**section 5.1.3**).

Around 50 thousand events were acquired in the absence of any source at a periodic rate of 1 kHz during 45 seconds. The SiPM signals of those events correspond to the electronic pedestals of the SiPMs, and can also include dark counts and natural background radioactivity. Thus, the acquired data were used to calculate the pedestal of each sensor, using the procedure presented in **section 5.1.1**. The factor to convert the SiPM signals into number of photoelectrons was calculated using the data from the irradiation of the entire FOV of the prototype with ^{99m}Tc source. The method was explained in the **section 5.1.3**. The convertion factor is the slope of the line which results from the linear regression over the peak centers (signals given in ADC channels) in the SiPM signal histogram plotted as a function of the number of the relative position of the peaks. The peak number zero is the most left peak (lowest signals). Note that both the pedestal and the relative gain of each SiPM depends on the overvoltage ΔV. For this reason, two calibrations were performed, because two overvoltages were used. For the measurements with the *GAGG prototype*, the SiPMs were biased with 28 V (thus, the overvoltage ΔV is 3.5 V, as the breakdown voltage is 24.5 V). The bias voltage applied to the SiPMs for the measurements with the *LYSO prototype* was 27 V (so ΔV is 2.5 V).

Fig.6.10 presents an example of the histogram of signals for two SiPMs, when ΔV is 2.5 V. The histogram peaks, corresponding to a certain number of detected photons, are clearly resolved. Red dashed lines indicate the peak positions and a label shows the calculated gain g (or $C_{p.e.}$). The relative gain of the respective SiPMs are written in a label.

6.4 Populating the camera response models

For each prototype, data from uniform irradiation of the entire detector FOV with a ^{99m}Tc source was used to estimate the set of light response functions (camera response model). A 30% energy window was defined around the 140 keV photopeak, to select the events that most likely correspond to photoelectric absorption. **Fig.6.11** shows the energy spectrum of the flood field irradiation for the GAGG and LYSO versions of the prototype. For the model reconstruction, it was assumed that the SiPMs response is axially symmetric. Therefore, the LRFs were parameterized as functions of the distance from the sensor center. The adaptive algorithm

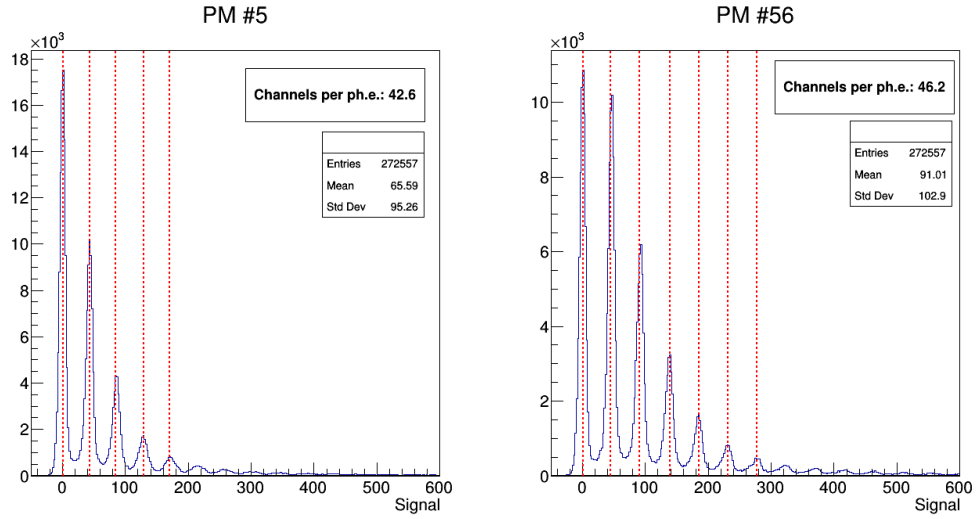

(a) **(b)**

Figure 6.10: Histogram of signals of two SiPMs when ΔV is 2.5 V. The red dashed lines indicate the peaks, which correspond to a discrete number of photoelectrons (p.e.). The gain (channels per p.e.) of the SiPMs is indicated in the labels inside the images. **a**: SiPM #5: g = 42.6 channels per p.e. **b** SiPM #56: g = 46.2 channels p.e.

(**section 2.6.1**) was applied to flood data, starting with an initial guess given by the Center-of-Gravity algorithm. In the **section 5.2**, the sequence of procedures for the application of the adaptive algorithm were presented. Here, the options and parameters used during the experimental characterization are briefly described. Five iterations were sufficient to obtain LRFs that fit the experimental data (reduced *chi-square* = 1.3), as can be seen in **Fig.6.12**. Between iterations, a blurring of the reconstructed positions was made, starting with random shifts of 1 mm in the first iteration and reducing the shift distance by 0.15 mm every iteration. The distance from which the SiPMs are considered passive in the reconstruction [12] started at 8 mm in the first iteration and increased until 12 mm in the last iteration (1 mm step between iterations). Events with energy out of the previously defined energy window of 30% around the photopeak are filtered out, as well as events reconstructed with reduced *chi-square* higher than 2.5. **Fig.6.12** presents examples of three LRF curves estimated with the adaptive algorithm for the GAGG based prototype. For the three cases, the LRF accurately represents the average SiPM signals as a function of the distance from the scintillation position to the SiPM center.

Examples of LRFs for the LYSO based prototype are shown in **Fig.6.13**. The top images present the LRF curves of three SiPMs, which represent very well the color encoded data: the average SiPM signals as a function of the radial distance to the SiPM center. The insets are a closer view of the LRF values up to 10 photo-electrons. The bottom images shows both the LRFs estimated from experimental data (blue curves) and from simulated data (red curves).

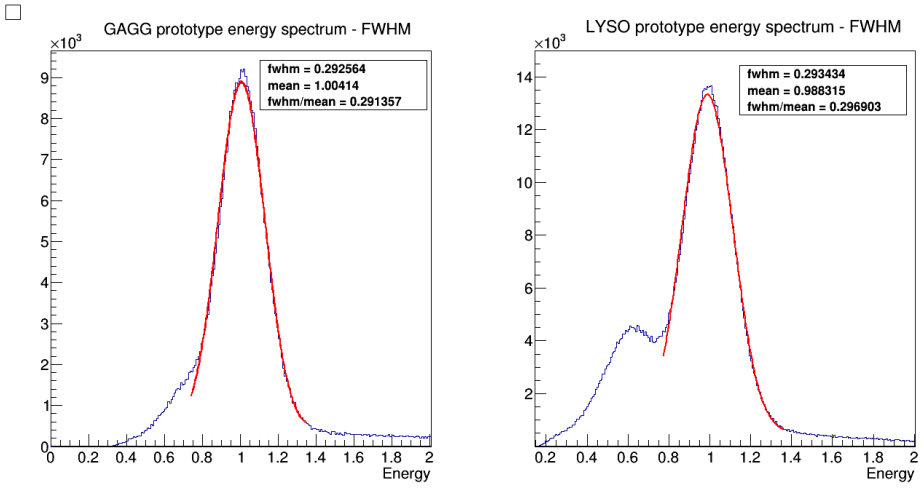

(a) (b)

Figure 6.11: Energy spectra of the gamma camera prototype with (a) GAGG and (b) LYSO scintillators.

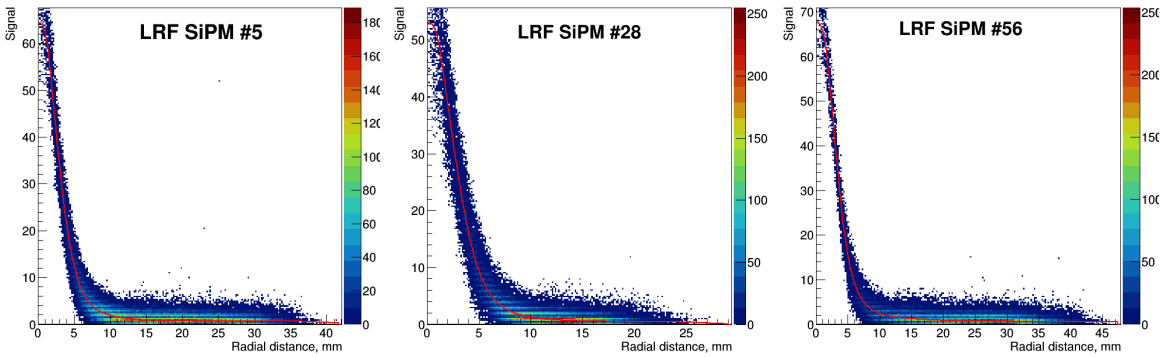

(a) (b) (c)

Figure 6.12: Light response functions of three SiPMs of the GAGG camera prototype. a LRF of SiPM #5. **b** LRF of SiPM #28. **c**: LRF of SiPM #56.

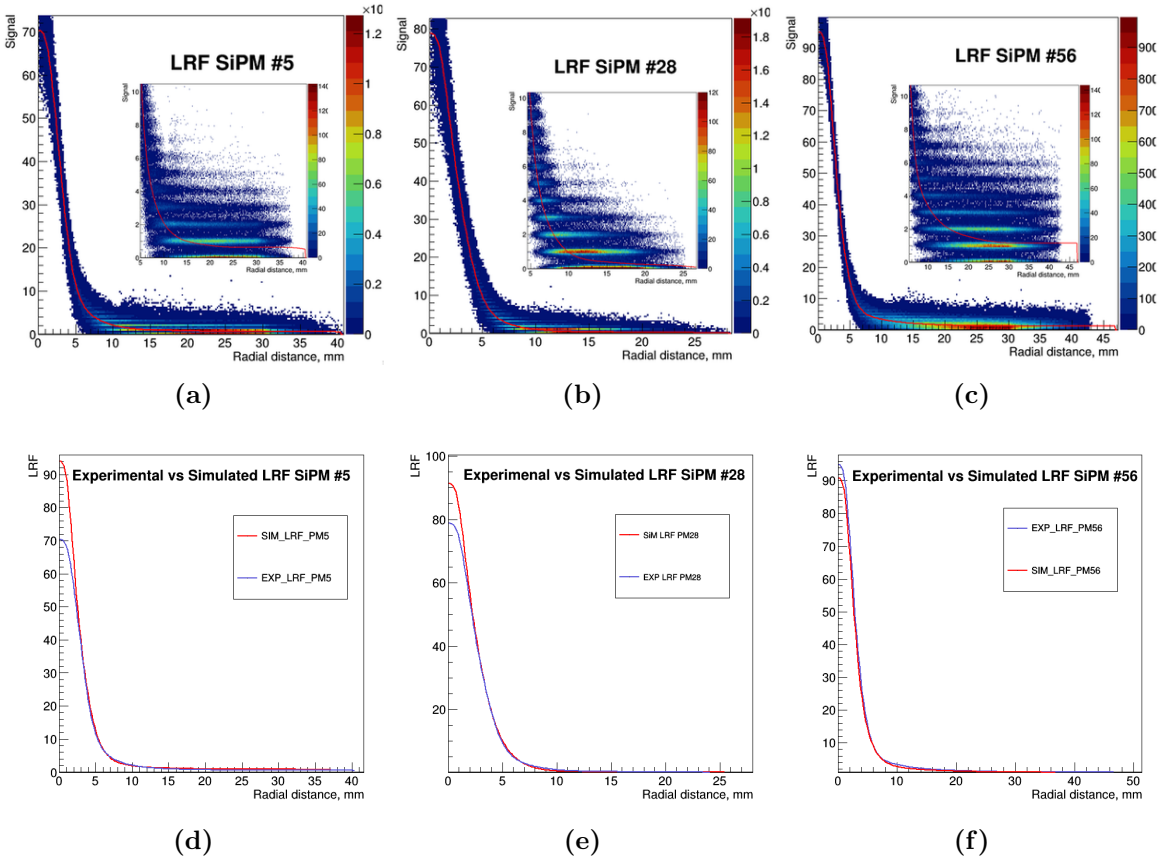

Figure 6.13: Light response function (LRF) curves of three SiPMs (LYSO camera): #5, #28 and #56. Top: LRFs curves well represent the average SiPM signals *vs* the radial distance from the SiPM centers to the scintillation position. The insets are a zoom of the LRF values until 10 photo-electrons. **Bottom:** Experimental and simulated LRF curves superimposed. **a** and **d**: SiPM #5 (periphery of the camera). **b** and **e**: SiPM #28 (center of the camera). **c** and **f**: SiPM #56 (corner of the camera).

The agreement of the LRF shapes is good (including the LRFs tails, which model mainly dark noise events), although there are some differences in the expected number of detected photons for the radial distances near zero (close to SiPM centers).

6.4.1 Reconstructing experimental data with a response model estimated from simulations

In this section the LRFs estimated from simulated flood data are used to reconstruct experimental data. The purpose of this study is to analyze how well the simulation model of the gamma camera represents the camera prototype.

Simulated LRFs to reconstruct experimental data The study was performed for the *LYSO prototype*, presented in the **section 6.1.1**. The simulation model employed was the one presented in (**section 3.2.4.1**). The simulated LRFs were estimated from flood field

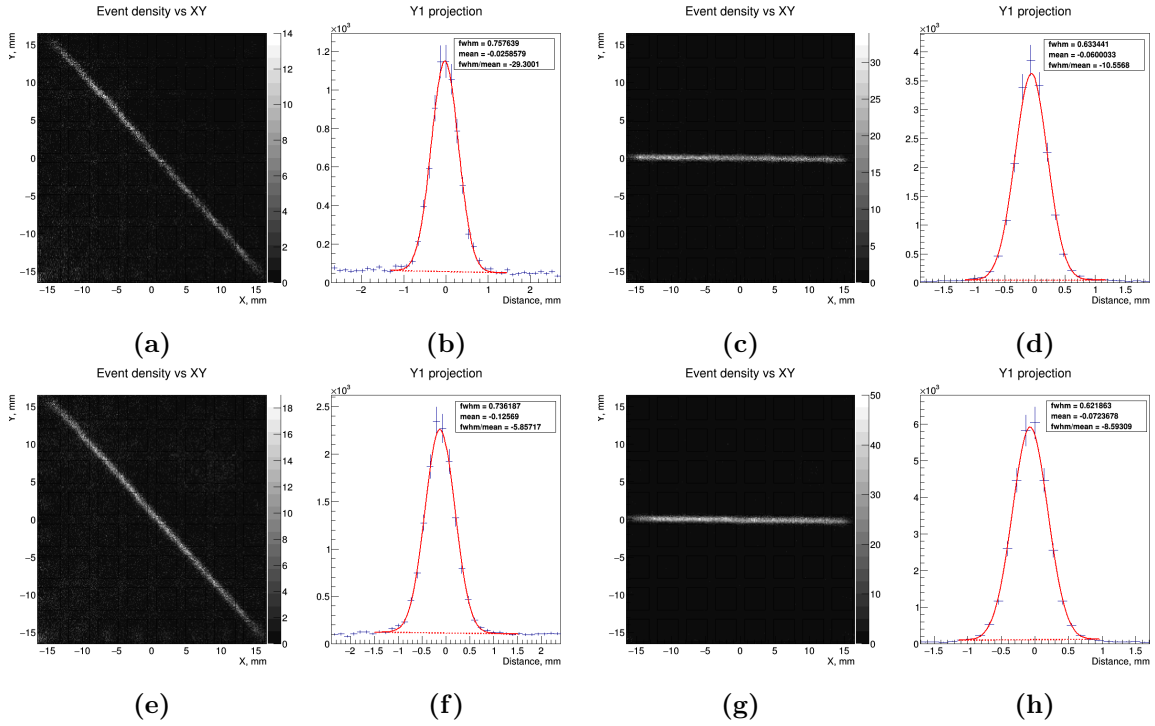

Figure 6.14: Comparison of experimental slit data reconstruction using LRFs estimated from simulations and LRFs estimated from experimental data. **Top**: Reconstruction results with the "simulated LRFs" **Bottom**: Reconstruction of the same data with LRFs estimated directly from experimental data. **a**, **c**, **e** and **g**: XY events density plot of the reconstructed positions from the source projection through the slits. **b**, **d**, **f** and **h**: Profile of the density plot projection along the slit.

irradiation data. These LRFs were used to reconstruct two datasets of experimental data from the detector irradiation through: **1)** a horizontal 0.2 mm slit and **2)** a diagonal 0.2 mm slit.

Fig.6.14 shows that the reconstructed 0.2 mm slit images have essentially the same transverse profile both in the case when LRFs from simulation were used (top images) and when LRFs estimated from the experimental data were used (bottom images). These results were expected due to the good agreement between the LRF shapes for the two cases. **Fig.6.15** presents for a central SiPM (#28) and for a peripheral SiPM (#5) the profiles of the LRFs estimated both from ^{99m}Tc experimental and simulated data.

One can conclude that the "simulated LRFs" can effectively be used to accurately reconstruct experimental data. Even if the "simulated LRFs" are not used directly to reconstruct the experimental data, they can be used as the initial guess on LRFs in order to have adequate LRFs when applying the adaptive procedure for LRFs estimation using experimental data.

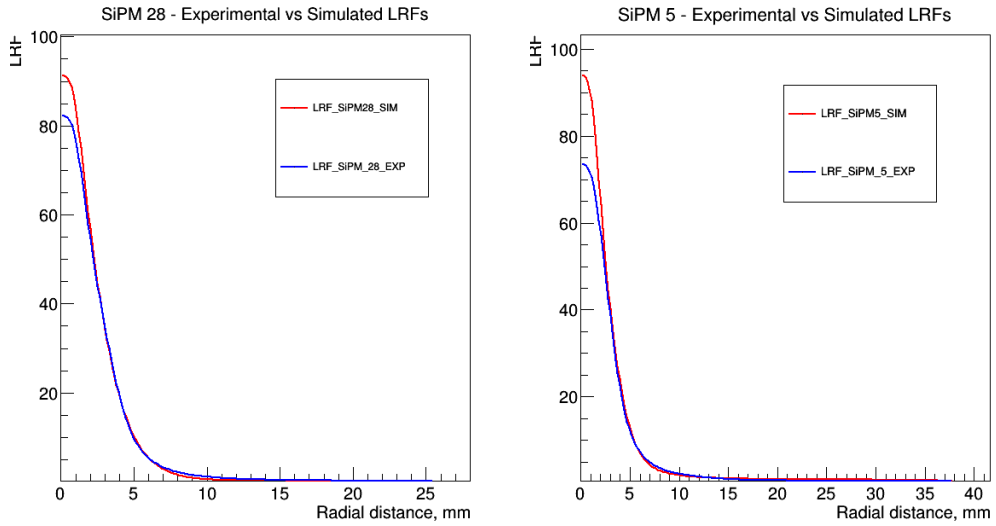

(a) **(b)**

Figure 6.15: LRFs comparison (estimated from experimental and simulated ^{99m}Tc data) for one central SiPM (#28) and on peripheral SiPM (#5). **a**: LRFs comparison for SiPM #28 **b**: LRFs comparison for SiPM #5.

6.5 Characterization of the prototype intrinsic parameters

This section presents the results of the characterization performance of the two versions of the compact gamma camera prototype. The performance parameters were assessed using the setups, materials and methods presented in **section 6.2**.

6.5.1 GAGG based camera prototype characterization

6.5.1.1 Intrinsic spatial resolution assessment

Fig.6.16 shows the XY density plot of the reconstructed positions obtained with the *multislit* mask diagonally oriented and the profile of the projection of that density plot along the slits. The FWHM of the profile curves is written in the image labels. Sub-millimeter spatial resolution was achieved, an objective for this work. The four resolutions are: 0.93 mm, 0.83 mm, 0.84 mm and 0.96 mm (the mean is 0.89 mm).

Fig.6.17 a and **b** present the reconstructed images of the *single slit* placed at two X positions: 1) *Slit_center* at X = 2.1 mm and 2) *Slit_between* at X = 0 mm. The measured spatial resolutions were 0.90 mm FWHM and 0.87 mm FWHM respectively. Such a difference was predictable, as discussed in **section 2.4.2.1**. As an additional example, **Fig.6.17 c** presents the results when the *single slit* was positioned diagonally. The FWHM of the profile of the density plot[1] projection along the slit is 0.87 mm. These results are close to the expected

[1]From now on, if nothing is said on contrary, the expression "density plot" is a short expression to "XY density plot of the reconstructed positions".

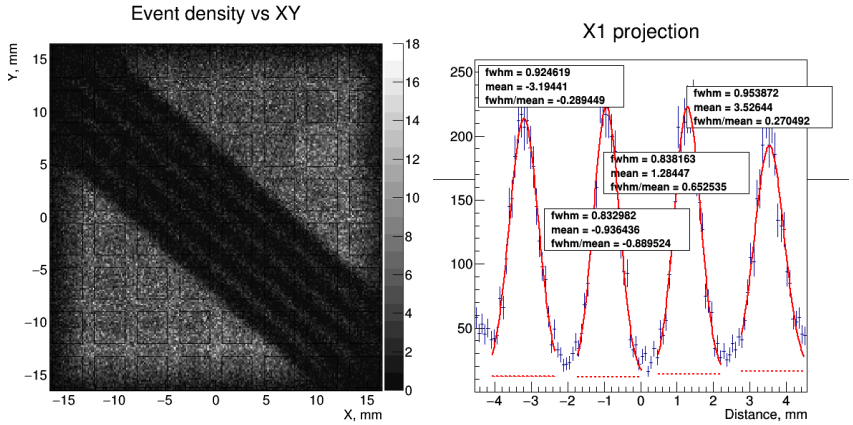

(a) **(b)**

Figure 6.16: Spatial resolution assessment (*GAGG prototype*) - four parallel slits. **a**: XY density plot of the reconstructed events positions - four parallel slits 0.2 mm thick **b**: Profile of the density plot projection along the slits (the average FWHM for the four slits is 0.89 mm).

from simulations. As can be seen in **table 3.5** with results for simulations with the GAGG based gamma camera (standard design), the average and the worst (maximum value) spatial resolutions along the entire FOV of the GAGG camera (with 1 mm thick lightguide, as in the experimental prototype) are 0.76 mm and 0.87 mm respectively.

6.5.1.2 Uniformity assessment

Fig.6.18 a presents the XY density plot of the reconstructed events when the entire FOV of the camera was irradiated with ≈175 thousand ^{99m}Tc γ-rays (uniformity image with 64 × 64 pixels). **Fig.6.18 b** and **Fig.6.18 b** show the uniformity image after applying the correction map and after applying a smooth filter in the corrected image, respectively.

The assessed integral and differential uniformity parameters values are, respectively, 72.6% (integral uniformity) and 78.9% (differential in X direction), 79.9% (differential in Y direction). The degree of uniformity is not, thus, within the requirement of more than 90% specified for this work (**table 3.1**), and far from the minimum recommended value of 95% for commercial systems. This poor observed uniformity can be attributed to statistical fluctuation of the bin count due to insufficient total event number. Although the uniformity level is not good, it should be noted that the main goal in the optimization of the camera was to achieve a spatial resolution below 1 mm (sub-millimeter).

6.5.1.3 Linearity assessment

Fig.6.19 shows the reconstruction results for the measurements with the *parallel bars mask* oriented both horizontally and diagonally (45°). The density plots of the reconstructed event positions and the profiles of the projections along the bars are presented.

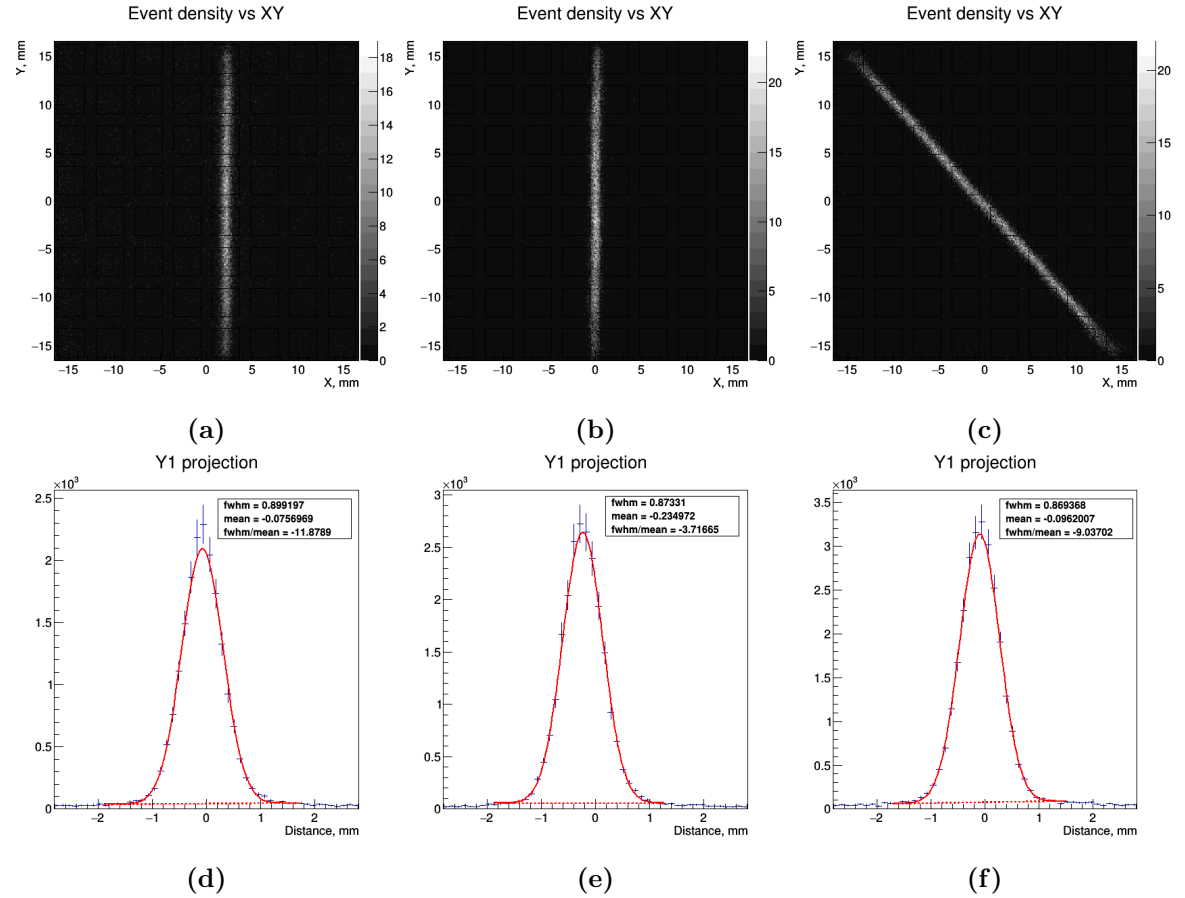

Figure 6.17: Spatial resolution assessment (*GAGG prototype*) - *single slit*. **Top:** XY events density plot of the reconstructed positions. **Bottom:** Profile of the density plot projection along the slits. **a** and **d**: Slit placed in front of the centers of eight SiPMs (*Slit_center*). **b** and **e**: Slit placed in front of the space between SiPMs (*Slit_between*). **c** and **f**: Slit diagonally oriented.

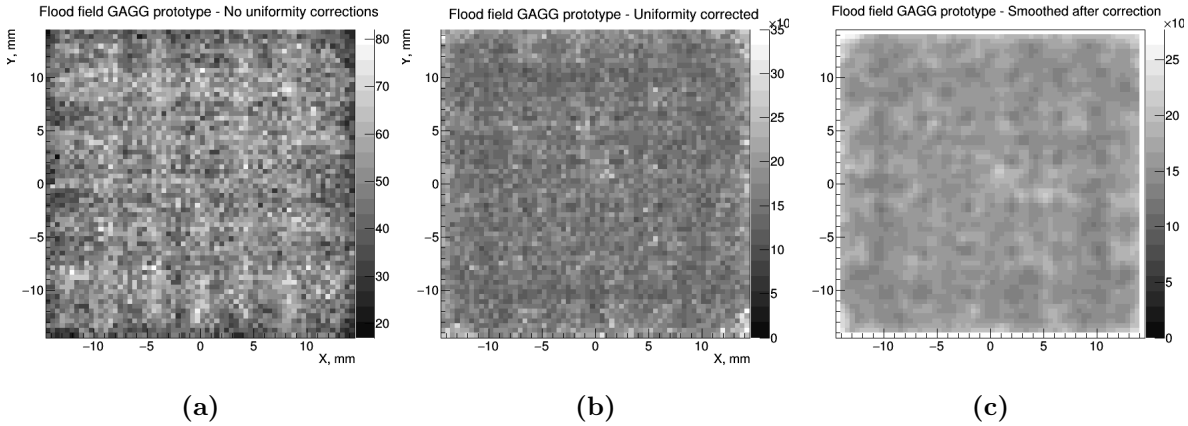

Figure 6.18: Uniformity assessment of *GAGG prototype*. XY events density plot of the flood field dataset reconstructed positions (UFOV: 29×29 mm^2). **a** Before applying the correction map. **b** After applying the correction map. **b** After smooth the image of **b**.

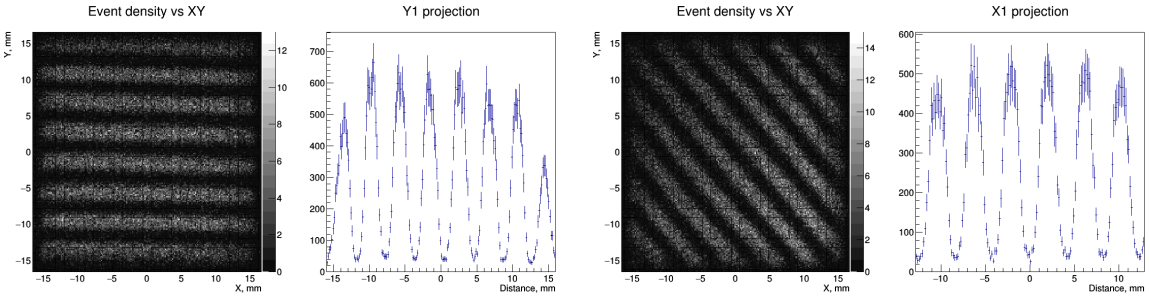

(a) **(b)** **(c)** **(d)**

Figure 6.19: Linearity assessment of *GAGG prototype* using the *parallel bars mask* (2 mm thick and 2 mm spaced). **a** and **c**: XY events density plots of the reconstructed positions of the events obtained with the bars mask oriented in two different positions. **b** and **d**: Profiles of the projection of the XY density plots along the bars. **a** and **b**: Horizontally oriented mask. **c** and **d**: Diagonally oriented mask.

Table 6.1 presents the linearity performance for the *GAGG prototype*. Both the absolute linearity and differential values fulfill the requirements (< 0.35 mm and < 0.2 mm, respectively) presented in **table 3.1**.

Deviation from a straight line (mm)	
Differential	**Absolute**
0.191	0.214

Table 6.1: Linearity of *GAGG prototype* (absolute and differential)

6.5.2 LYSO based camera prototype characterization

6.5.2.1 Intrinsic spatial resolution assessment

Fig.6.20 presents the reconstruction results for the *multislits* mask. The FWHM of the profiles of the density plot projection along the slits are: 0.72 mm, 0.69 mm, 0.73 mm and 0.75 mm (the mean value is 0.72 mm).

Fig.6.21 presents the density plot and the profile of the density plot projection along the slit for two Y positions of the *single slit*: 1) *Slit_center* at Y = -2.1 mm (**Fig.6.21 b**) and 2) *Slit_between* at Y = 0 mm (**Fig.6.21 a**). As expected, the FWHM is better when the slit is placed in front the space between two lines of SiPMs. In this case the spatial resolution is 0.64 mm FWHM, while it is 0.71 mm FWHM when the slit is placed in front of the centers of the SiPMs. As an additional example, **Fig.6.21 c** and **f** shows the density plots of the reconstructed positions and the profile of the density plot projection along the slit obtained for the *single slit* positioned diagonally (45°). The measured FWHM is 0.68 mm, which is

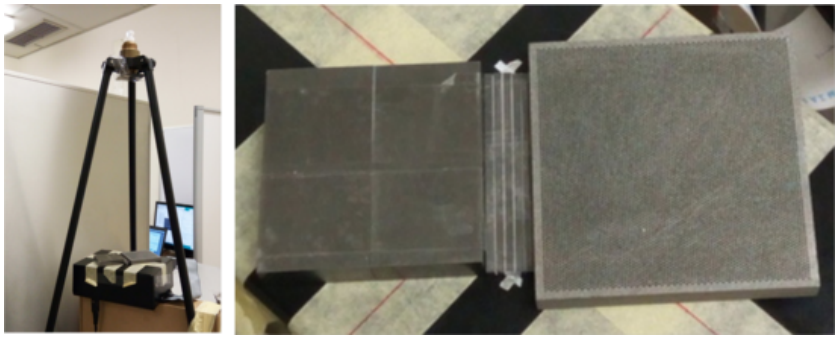

(a)

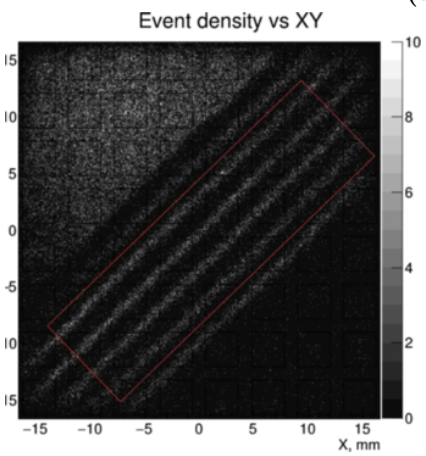

(b)

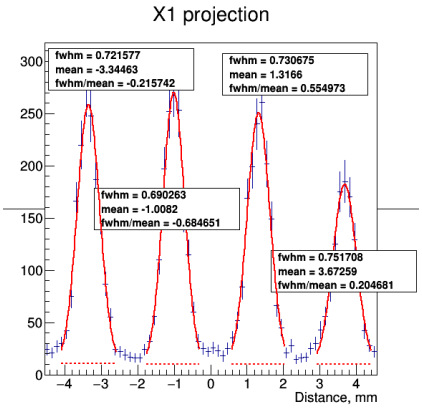

(c)

Figure 6.20: Intrinsic spatial resolution assessment (LYSO prototype) using four 0.2 mm parallel slits. **a**: Photograph of *multislits* mask. **b**: Events density plot of the *multislits* mask reconstructed image. The lines inside the red rectangle correspond to the four slits. **c**: Profile of the density plot projection along the slits (the average FWHM for the four slits is 0.72 mm).

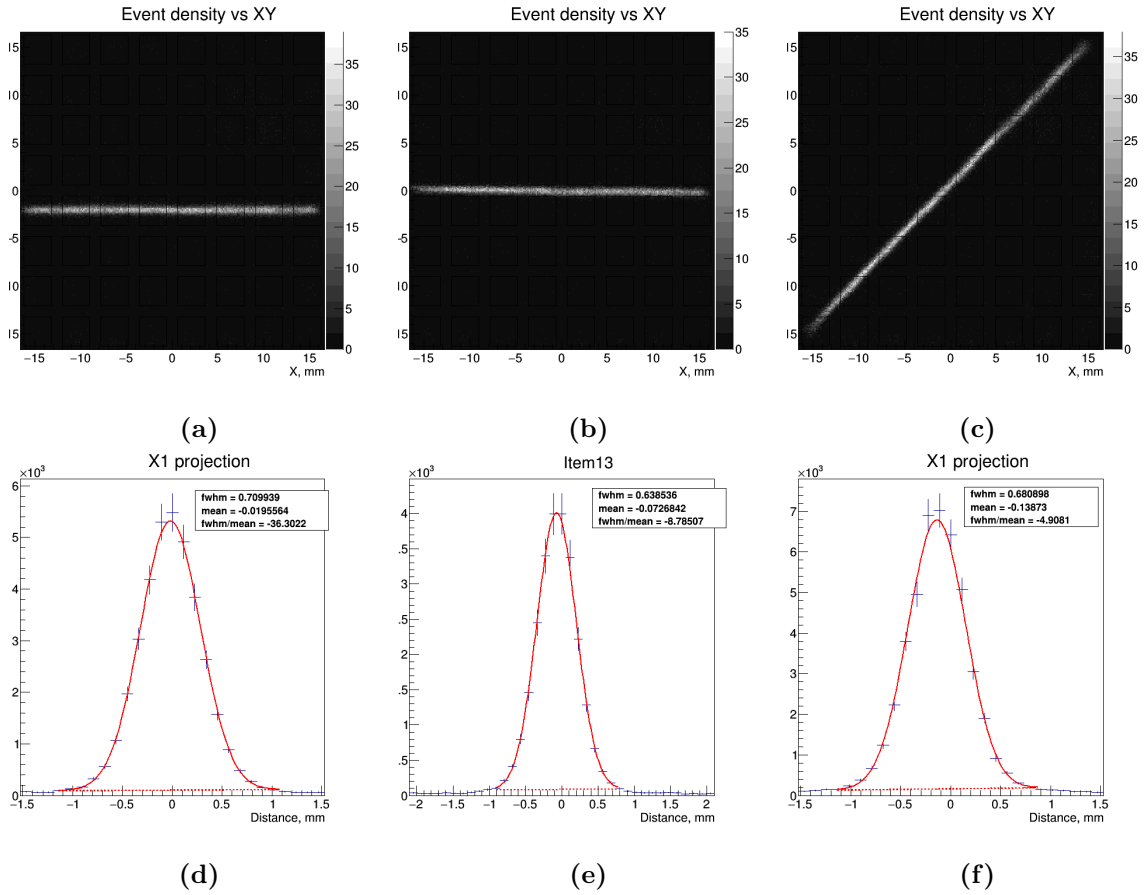

Figure 6.21: Spatial resolution assessment (*LYSO prototype*) - *single slit*. **Top:** XY events density plot of the reconstructed positions. **Bottom:** Profile of the density plot projection along the slits. **a** and **d**: Slit placed in front of the centers of eight SiPMs (*Slit_center*). **b** and **e**: Slit placed in front of the space between SiPMs (*Slit_between*). **c** and **f**: Slit diagonally oriented.

quite close to the spatial resolution predicted by simulations, 0.64 mm FWHM, when the energy deposition is simulated in Geant4 (**section 3.2.5**).

6.5.2.2 Uniformity assessment

Fig.6.22 a shows the event XY density plot of the reconstructed positions from field irradiation over the entire camera FOV before applying the correction map. **Fig.6.22 b** shows that the non-uniformities were corrected applying the uniformity correction map. **Fig.6.22 c** shows the result of applying a smooth filter to **Fig.6.22 b**.

The degree of uniformity of the LYSO based camera prototype is sufficient to make nuclear imaging (as it is shown in the next sections), but it is below the 90% defined as requirement in this work and below the commonly accepted uniformity level of ∼95% for commercial devices. The integral uniformity is 77.7% and the differential uniformity for the X and Y directions are 82.2% and 82.7%, respectively.

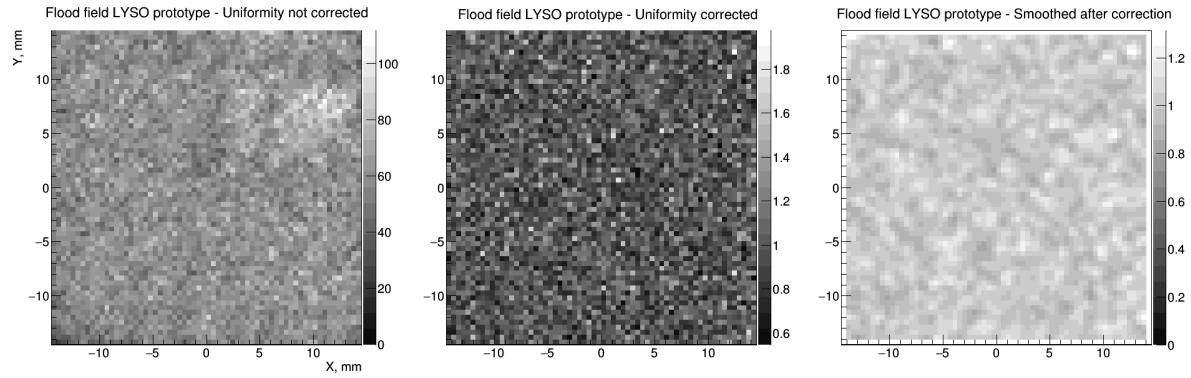

(a) **(b)** **(c)**

Figure 6.22: Uniformity assessment of *LYSO prototype*. XY event density plot of the flood field dataset reconstructed positions (UFOV: 29 × 29 mm^2). **a** Before applying the correction map. **b** After applying the correction map. **c** After smooth the map from image **b**.

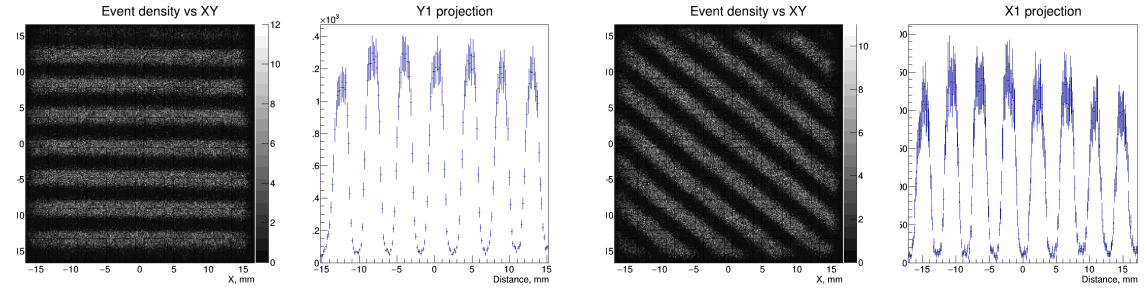

(a) **(b)** **(c)** **(d)**

Figure 6.23: Linearity assessment (LYSO prototype) performed with 2 mm thick bars mask. **a** and **c**: XY event density plots of the reconstructed positions of the events obtained with the bars mask oriented in different positions. **b** and **d**: Profiles of the projection of the XY density plots along the bars. **a** and **b**: Bars mask horizontally oriented. **c** and **d**: Bars mask diagonally oriented.

6.5.2.3 Linearity assessment

Fig.6.23 presents both the XY density plot of the reconstructed events and the profile of the density plot projection along the bars for two cases: horizontally and diagonally (∼45°) oriented *parallel bars mask*.

Table 6.2 presents the linearity performance results of the *LYSO prototype*. Both the differential (statistics of the deviations) and the absolute linearity parameter values are according to the requirements for the developed gamma camera (see **table 3.1**).

6.6 Characterization of the imaging system

In the frame of this work, two collimators were designed and manufactured (**section 6.1.2**): a parallel-hole collimator and a pinhole collimator. The imaging system was equipped with these

Deviation from a straight line (mm)	
Differential	**Absolute**
0.096	0.269

Table 6.2: Linearity of *LYSO prototype* (absolute and differential)

interchangeable collimators and the extrinsic spatial resolution of the system was assessed for both cases and compared with that given by the simulation results.

6.6.1 Imaging system with the parallel-hole collimator

6.6.1.1 System spatial resolution

The 1 mm diameter capillary tube phantom presented in **section 6.2.1** was used as the container of the ^{99m}Tc source solution. It was placed at five distances from the parallel hole in the case of *GAGG prototype* based system: 5.8 mm, 15.8 mm, 30.8 mm, 58.8 mm and 105.8 mm. For the *LYSO prototype* based system the distances were also five: 5.8 mm, 15.8 mm, 20.8 mm, 58.8 mm and 105.8 mm. For both prototype versions, the parallel-hole colimator was attached to the camera inside the camera enclosure. **Fig.6.24** shows two pictures of the parallel-hole collimator attached to the camera and a schematic drawing indicating the distance from the collimator face to the top of the camera enclosure (5 mm). Note that the SiPMs are attached to the electronics board (green color in **Fig.6.24 a** and **c**).

Fig.6.25 presents reconstructed images of the capillary tube phantom for the five source-to-collimator distances using the *GAGG prototype*, with the respective FWHM measured in the profile of the density plot projection along the capillary tube.

The images obtained with the *LYSO prototype* with the parallel-hole collimator were similar to those obtained with the *GAGG prototype*, so **Fig.6.26** shows only one example of the density plot and the profile of its projection along the capillary tube, namely, for the case when the source was placed at 5.8 mm from the collimator. The measured and simulated spatial resolutions are plotted for both prototype versions as a function of the source-to-collimator distance in **Fig.6.27**. While the simulations were performed only for the *GAGG prototype*, the *LYSO prototype* resolutions must be similar.

Experiment *vs* simulation (ANTS2): A comparison between the extrinsic spatial resolution obtained experimentally and in simulations was performed for both the *LYSO prototype* and the *GAGG prototype*. The simulations were performed using the parallel-hole collimator design presented in **section 3.2.6.1**, which dimensions follow those of the collimator prototype (see **section 6.1.2**). **Fig.6.27** depicts the results at six distances of the capillary tube relative

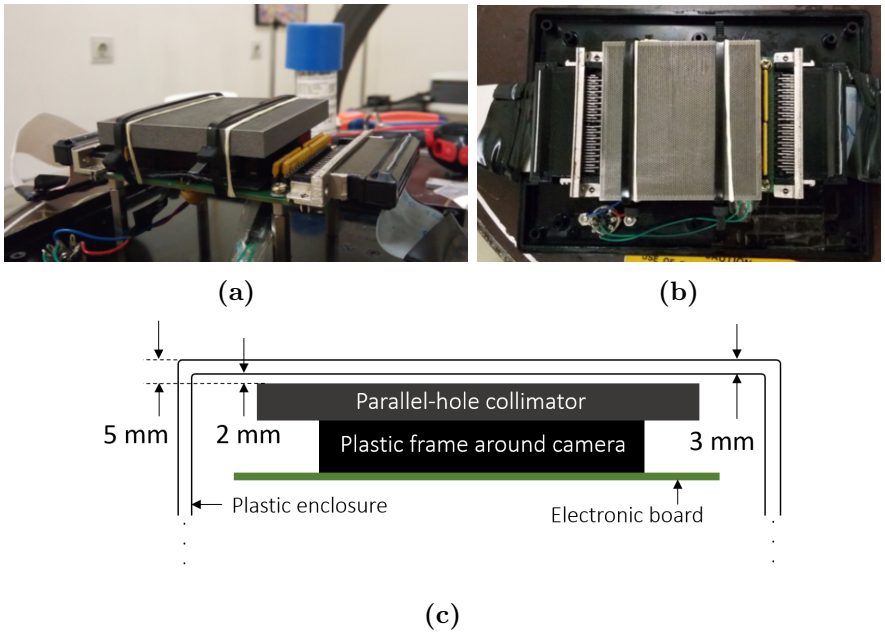

Figure 6.24: Photograph and drawing of the gamma camera with the parallel-hole collimator attached. **a**: Overview photograph. **b** Top view photograph. **c** Schematic drawing of the parallel-hole collimator inside the gamma camera enclosure. The distance from the parallel-hole collimator face to the top of the camera enclosure is 5 mm.

to the parallel-hole collimator face. The FWHM calculated in the profiles of experimental data and simulation (ANTS2) data are presented. The extrinsic resolution is mainly defined by the collimator resolution, so it is not a surprise that although there are differences in the intrinsic spatial resolution of the two prototype versions, the extrinsic resolution is similar. A good agreement can be demonstrated between the system resolutions given by simulations and by experimental measurements. For the experimental measurements, the distance between the source and the face of the parallel-hole collimator was measured with a 1 mm precision ruler.

6.6.1.2 Experimental simulation of *in vivo* imaging with the parallel-hole collimator

The characterization of the spatial resolution of the developed imaging system was performed in the previous section. In this section additional measurements are presented in order to simulate *in vivo* imaging and further analyze the capability of the developed system to resolve radioactive spots located in close proximity from each other or the details of a simplified phantom resembling a mice *brain slice*. In sentinel lymph node scintigraphy, the ganglia under observation are typically less than 10 mm in size and they can be very close from each other. To simulate such a case, 1 mm diameter capillary tubes filled with ^{99m}Tc were placed together in different layouts, in a plane parallel to the collimator face (at ≈6 mm), to form different geometries (phantoms).

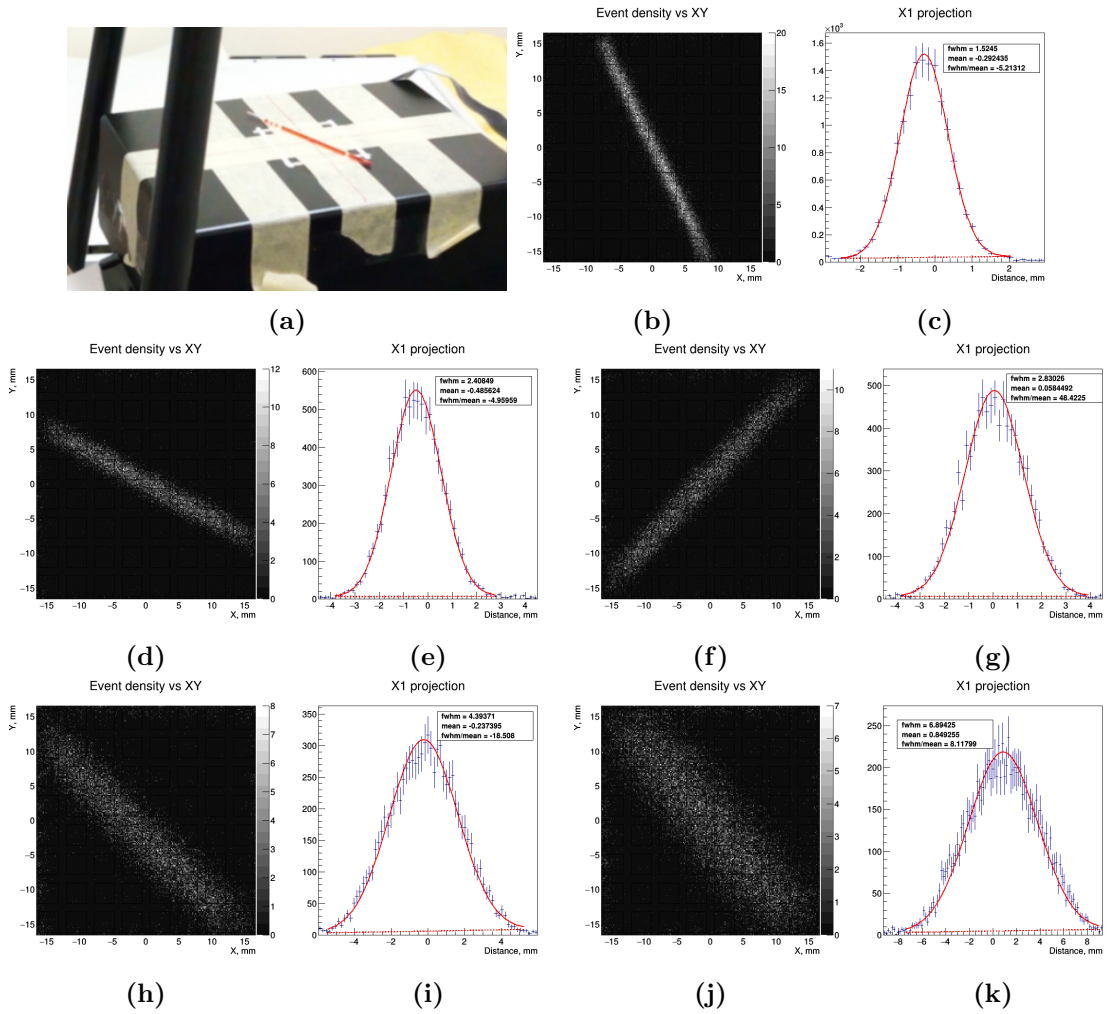

Figure 6.25: Density plots of the reconstructed event positions when the *GAGG prototype* with the parallel-hole collimator attached was irradiated by a capillary tube filled with a ^{99m}Tc solution (orange color). A Gaussian fit was performed to the corresponding profiles of the density plot projections along the tubes. **a**: Photograph of the capillary tube on top of the camera enclosure. **b**, **d**, **f**, **h** and **j**: XY density plots of the reconstructed positions for several capillary-tube to parallel-hole collimator distances. **c**, **e**, **g**, **i** and **k**: Profile of the density plot projection along the capillary tube (Gaussian fit). **b** and **c**: $d = 5.8$ mm, FWHM = 1.53 mm. **d** and **e**: $d = 15.8$ mm, FWHM = 2.40 mm. **f** and **g**: $d = 30.8$ mm), FWHM = 2.83 mm. **h** and **i**: $d = 58.8$ mm, FWHM: 4.39 mm. **j** and **k**: $d = 105.8$ mm, FWHM: 6.89 mm.

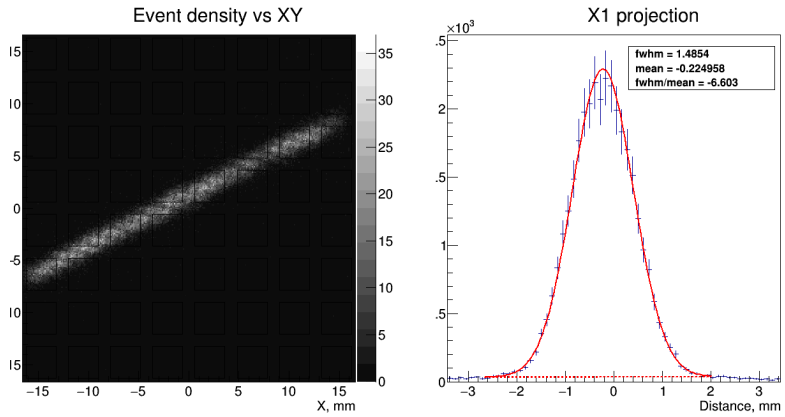

(a) (b)

Figure 6.26: Reconstruction of a capillary tube (1 mm thick) filled with a ^{99m}Tc solution, placed on the top of the LYSO camera enclosure. **b**: XY density plot of the reconstructed positions. **b** Profile of the density plot projection along the tube. The FWHM is 1.49 mm.

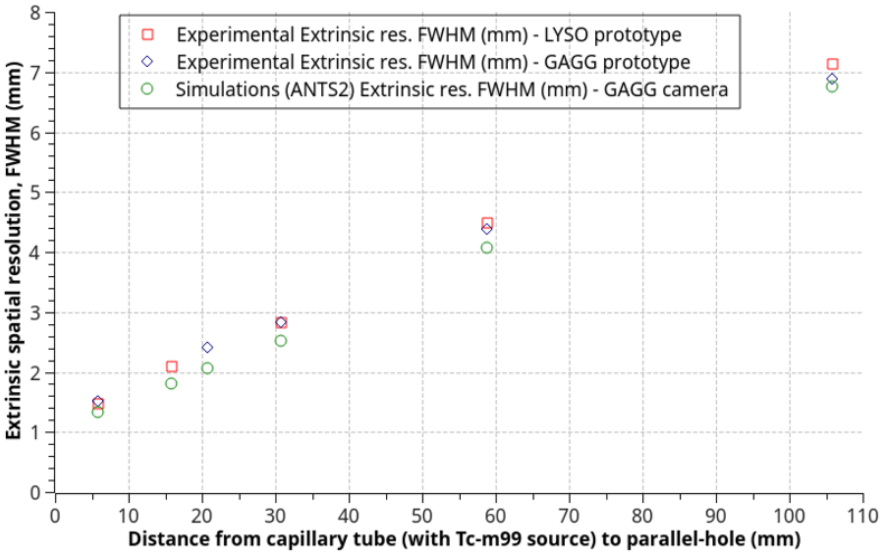

Figure 6.27: Extrinsic spatial resolution of the parallel-hole collimator. Experimental *vs* simulation.

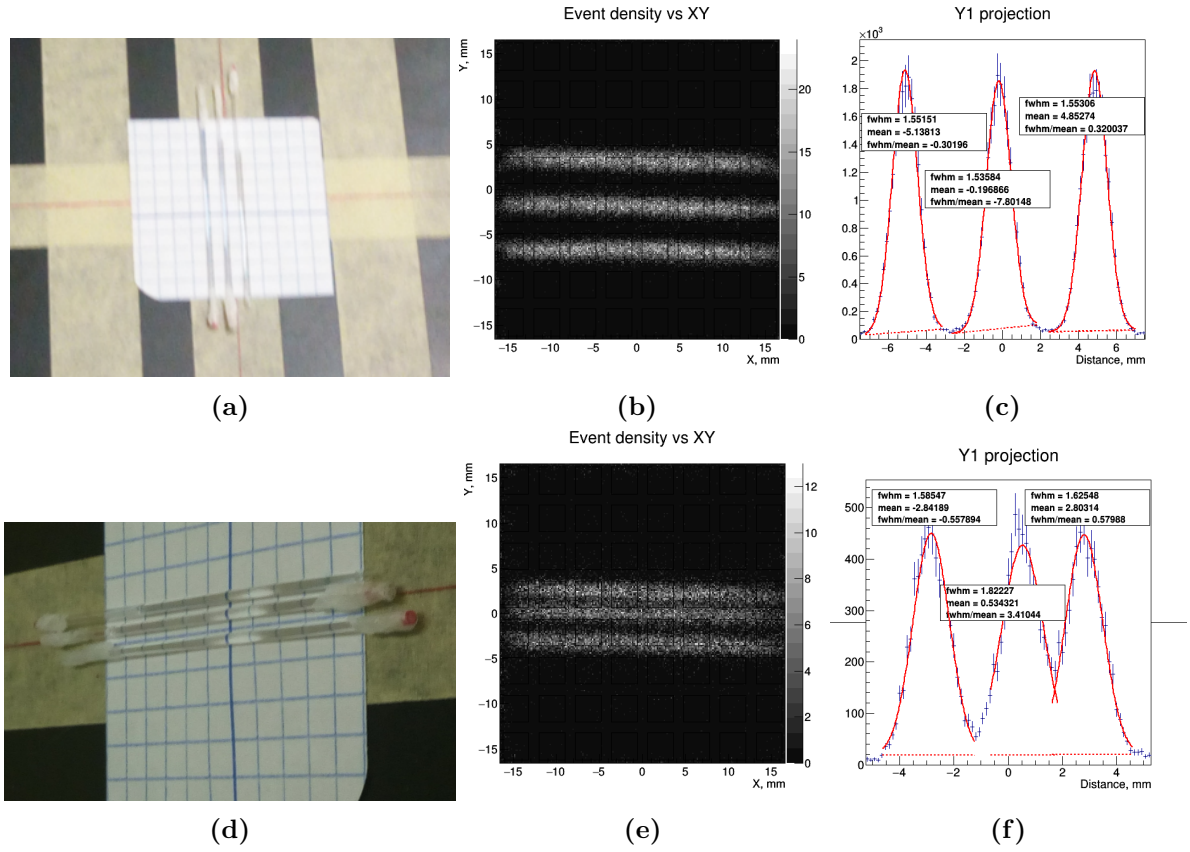

Figure 6.28: Reconstruction results for three parallel capillary tubes (1 mm thick) filled with ^{99m}Tc. **a** and **d**: Photographs of the capillary-tubes on top of LYSO camera enclosure. **b** and **e**: XY density plots of the reconstructed positions. **c** and **f**: Profile of the density plot projections along the tubes.

The results of imaging different source phantoms with the *GAGG prototype* are presented below, namely: **1)** three capillary tubes placed in parallel, **2)** two crossed capillary tubes (20° and 30°), **3)** three regions inside a capillary tube separated by air bubbles and **4)** a *brain slice* phantom.

1. Three parallel capillary tubes Three capillary tubes were placed in parallel, spaced by approximately 5 mm. **Fig.6.28 a** shows a photograph of the tubes and **Fig.6.28 b** shows the resulting image. The three tubes are clearly resolved. **Fig.6.28 d** shows a photograph of the same tubes, but closer to each other and not equally spaced. The separation between two of the tubes is approximately 3 mm, while the separation between one of those tubes from a third tube is approximately 2 mm. All the tubes are well resolved.

2. Crossed capillary tubes Two phantoms made of two cross-placed source tubes were prepared to analyze the resolution capability of the system when the distance between two radioactive regions gradually decreases. The difference between the two phantoms is the

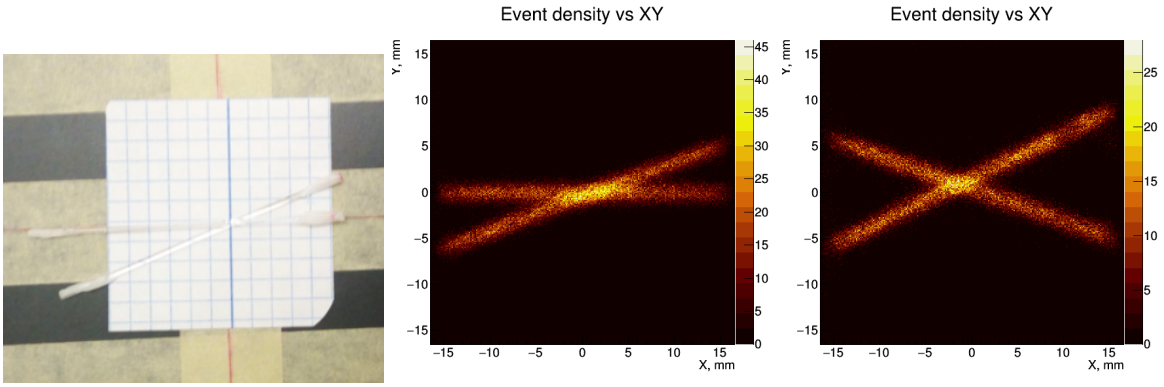

(a) (b) (c)

Figure 6.29: Density plot of the reconstructed event positions of two crossed capillary tubes filled with ^{99m}Tc (20 and 30 degrees). **a** Photograph of the crossed capillary tubes (∼20 degrees). **b** and **c**: Density plot of the reconstructed event positions of the crossed capillary tubes. The color map is the "dark body radiator", as it is commonly used in clinical practice aside with "gray scale" and "rainbow" color maps. **b**: ≈20 degrees between the tube. **c**: ≈30 degrees between the tubes.

angle formed by the cross-placed tubes: 20° and 30°, referred below as CPT-20 and CPT-30. **Fig.6.29 a** presents a photograph of the CPT-20 phantom. **Fig.6.29 b** and **c** show the density plots obtained with CPT-20 and CPT-30 phantoms, respectively. Note that the used color map is the "dark body radiator", as it is a common option in clinical practice aside with "gray scale" and "rainbow" color maps. Looking at the scale of **Fig.6.29 b** it can be seen that the position of the source inside the two tubes can be distinguished until the separation between the tubes is about 1.5 mm, which roughly corresponds to the system resolution for a source-to-collimator distance of 6 mm (see **Fig.6.27**).

3. Three small regions inside a capillary tube An image of three small "spots" (between 1 and 1.5 mm in their longest dimensions) of radioactive source (^{99m}Tc) was also taken with the LYSO based gamma camera. A capillary tube with air bubbles between the three spots of radioactive source (hot spots) was used. **Fig.6.30** shows the picture of the three hot stops and the reconstructed image, in which the three spots are well resolved.

4. A *brain slice* phantom A phantom that resembles a slice of a simplified mice brain was filled with ^{99m}Tc diluted in water with an orange dye. **Fig.6.31** shows a photograph of that phantom and the image obtained from it.

6.6.2 Imaging system with the pinhole collimator

The pinhole collimator spatial resolution was assessed at four distances between the pinhole and the source, keeping always the same focal lenght f (distance between the pinhole to the

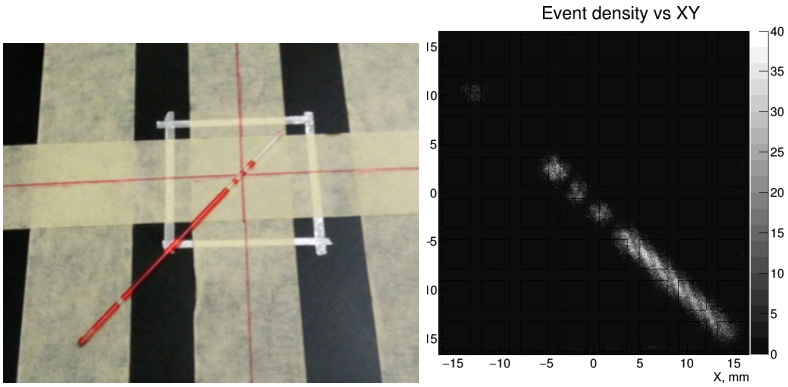

(a) (b)

Figure 6.30: Imaging of three radioactive spots with volume of approximately 1 mm^3. **a** Photograph of the three radioactive spots (^{99m}Tc) inside a capillary tube. **b** Events density plot of the reconstruction of the three radioactive spots.

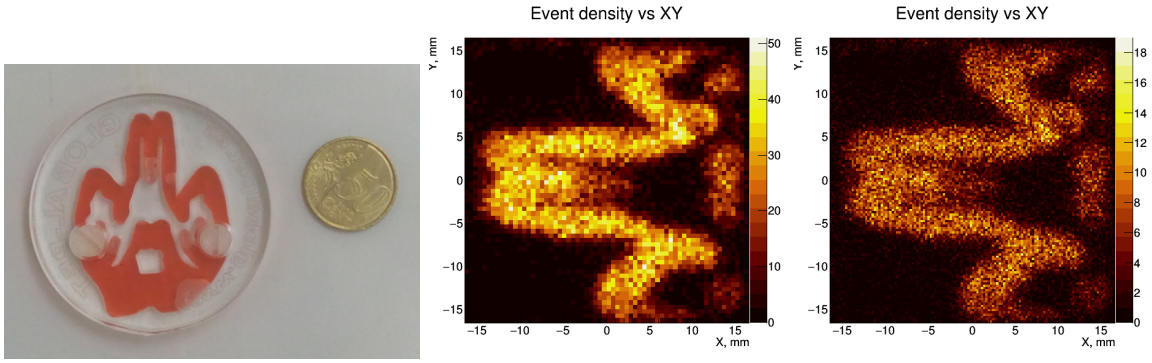

(a) (b) (c)

Figure 6.31: *Brain slice* phantom imaging with parallel-hole collimator. **a** Photograph with a 50 Cent coin. **b** and **c**: XY density plot of the events reconstructed positions. **b** 64×64 matrix. **c** 128×128 matrix.

camera). Each distance corresponds to a magnification factor. The version of the gamma camera prototype in use was the GAGG based one. The results were compared with simulations performed for the same geometries. The *brain slice* phantom imaged with the parallel-hole collimator was also imaged with the pinhole collimator.

6.6.2.1 System spatial resolution

Similar to the case of the parallel-hole collimator, 1 mm diameter capillary tubes filled with ^{99m}Tc solution were used to assess the pinhole extrinsic spatial resolution. The focus length f was 23.5 mm. Depending on the distance between the source and the pinhole z, different magnification factors M can be achieved ($M = f/z$). Four measurements were performed, at four different z distances that result in the following magnification factors: 0.36, 0.5, 1.0 and 2.24. Note that the distances f and z were measured with a 1 mm precision ruler. **Fig.6.32** shows the reconstruction results for these four measurements. For example, a resolution of ≈1 mm in the object plane[1] was achieved for a magnification factor of 2.24 and an overall source-to-detector distance of about 35 mm. In the case of no magnification and an overall source-to-detector distance of about 47 mm the resolution in the object plane was ≈ 1.64 mm.

Simulations were made for the same magnification factors and a source similar to the capillary tube. **Fig.6.33** presents the simulation reconstruction results and resolutions.

Fig.6.34 presents a comparison between the pinhole resolution obtained in simulations and experiments, calculated as the FWHM of the Gaussian fit to the profile of the density plot projection along the capillary tube. For the simulation data, the intrinsic spatial resolution of the *GAGG prototype* is assumed to be 0.9 mm (the worst case). As expected, the pinhole resolution in the source plane (object resolution) is lower for higher magnification factors. The agreement between the experimental results and the corresponding simulations is good (≈0.16 mm of difference, on average, for the four comparative cases).

I wanted to verify that there were no effects disturbing the magnification expected from the pinhole collimator. For instance, even without accurate information on the length of the radioactive liquid inside the capillary tube, a comparison can be done between two reconstructed images for two magnification (M) cases in order to confirm the magnification effect. The length of the reconstructed tube when M = 0.36 is 15 mm. The length for M = 0.5 is 21.6 mm. The ratios 0.36/0.5 and 15/21.6 are respectively 0.72 and 0.69, which are very close, confirming that magnification is being performed by the pinhole collimator.

[1]To obtain the resolution in the object plane (or source plane), the FWHM obtained in the detector plane (e.g. 2.21 mm) must be divided by the magnification factor (e.g. 2.24).

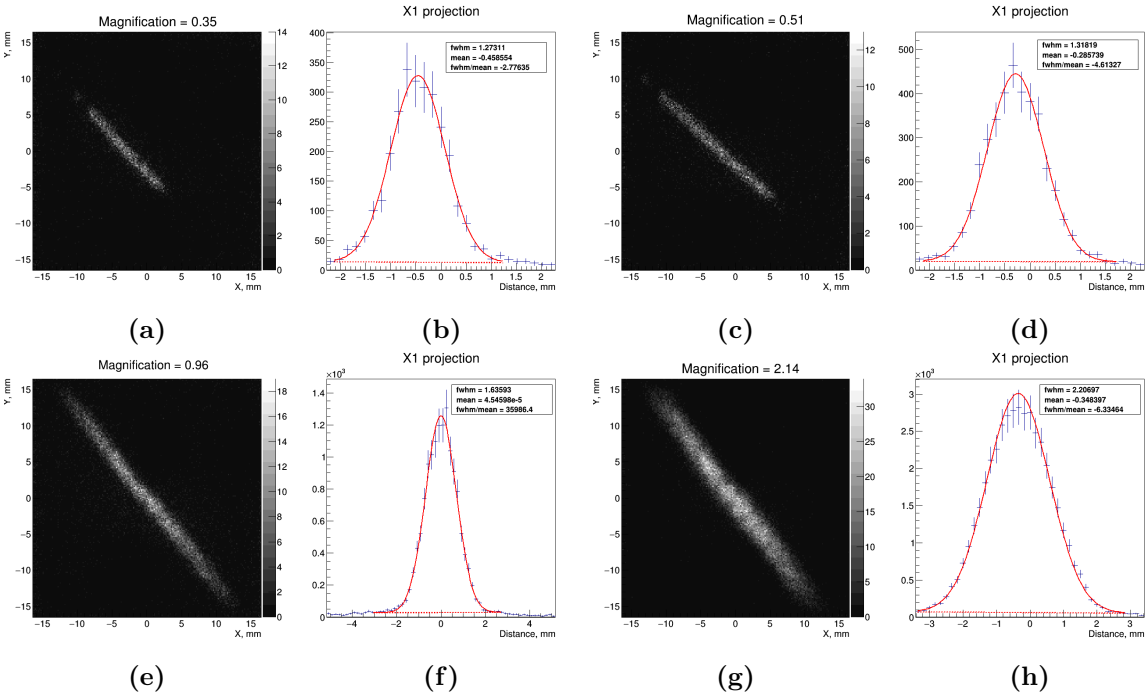

(a) **(b)** **(c)** **(d)**

(e) **(f)** **(g)** **(h)**

Figure 6.32: Experimental pinhole resolution at four distances between the 1 mm capillary tube (filled with a ^{99m}Tc solution) and the pinhole. **a**, **c**, **e** and **g**: XY density plot of the reconstructed positions. **b**, **d**, **f** and **h**: Gaussian fit to the profile of the density plot projection along the tube. **a** and **b**: M = 0.36, FWHM = 1.27 mm. **c** and **d**: M = 0.50, FWHM = 1.31 mm. **e** and **f**: M = 1.0, FWHM = 1.64 mm. **g** and **h**: M = 2.24, FWHM = 2.21 mm.

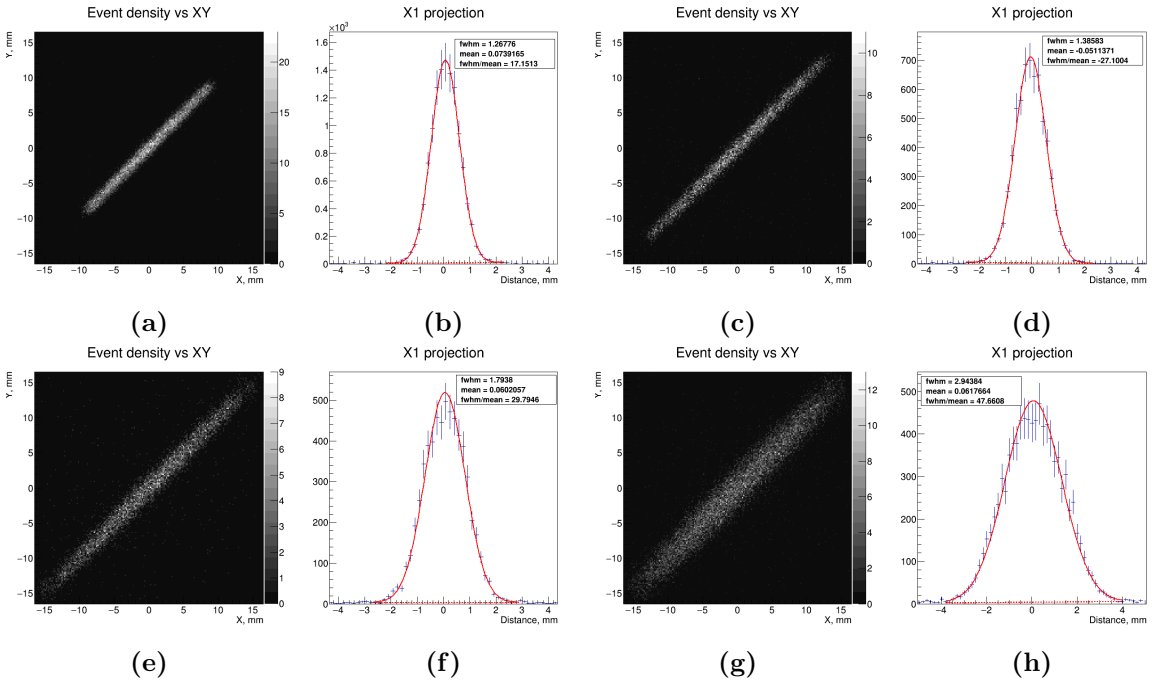

Figure 6.33: Simulated pinhole resolution at four distances between the 1 mm capillary tube filled with a ^{99m}Tc solution and the pinhole. **a**, **c**, **e** and **g**: XY density plots of the reconstructed positions. **b**, **d**, **f** and **h**: Gaussian fit to the profile of the density plot projection along the tube. **a** and **b**: M = 0.36, FWHM = 1.27 mm. **c** and **d**: M = 0.50, FWHM = 1.39 mm. **e** and **f**: M = 1.0, FWHM = 1.79 mm. **g** and **h**: M = 2.24, FWHM = 2.94 mm.

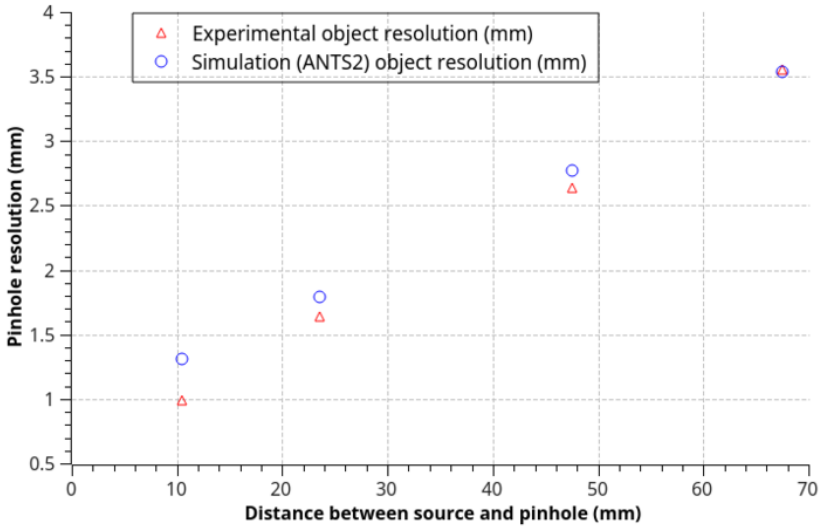

Figure 6.34: Pinhole resolution for four distances between the source and the pinhole collimator. This distance z defines the magnification factor, M: z = 10.5 mm (M = 2.24), z = 23.5 mm (M = 1.0), z = 47.5 mm (M = 0.5) and z = 67.5 mm (M = 0.36). The focal length f is always 23.5 mm. The round blue symbols show the resolutions from simulations, while the triangular red ones show the experimental resolutions.

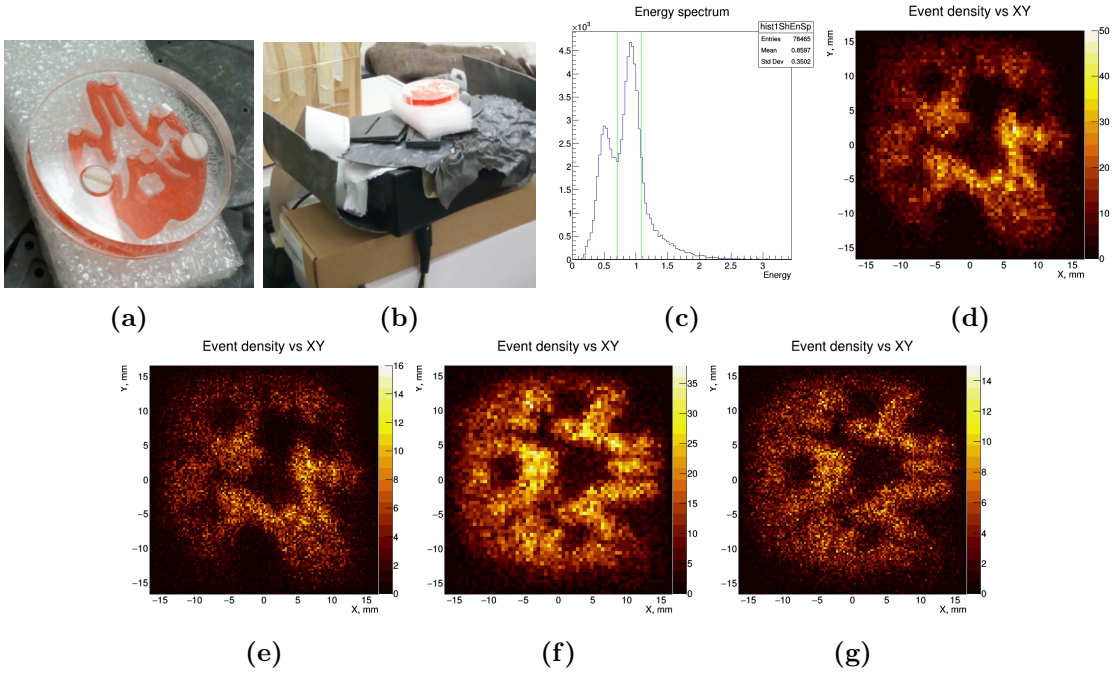

Figure 6.35: *Brain slice* imaging with pinhole collimator. **a** Photography of the *brain slice* phantom. **b** Photograph showing the lead shielding around the gamma camera. **c** Energy spectrum of the reconstructed events. **d**, **e**, **f** and **g**: XY density plot of the events reconstructed positions. **d** and **e**: *Brain slice* phantom rotated by 45°. **f** and **g**: *Brain slice* phantom horizontally oriented. **d** and **f**: 64 × 64 matrix image. **e** and **g**: 128 × 128 matrix image.

6.6.2.2 Experimental simulation of *in vivo* imaging with the pinhole collimator

The *brain slice* phantom was also imaged with the pinhole. **Fig.6.35 a** shows a photograph of the phantom filled with a ^{99m}Tc source diluted in water (orange). Several air bubbles can be seen. **Fig.6.35 b** shows a photograph of the lead shielding around the gamma camera. It covers only partially the camera from the γ-rays scattered in the environment objects. All the available shielding material was used, but unfortunately it was not sufficient to produce the proper shielding, as can be seen from the energy spectrum of the reconstructed events (**Fig.6.35 c**). The scattered γ-rays strongly contribute for the left peak in the energy spectrum, which, under better conditions, looks more like a "shoulder" to the left of the main peak.

Fig.6.35 d to **g** show the images of the *brain slice* phantom obtained with the imaging system equipped with the pinhole collimator, when the magnification factor is 0.8 (reducing the object size in the image plane). Images of two orientations of the phantom are shown (in a 64 × 64 matrix). The shape of the phantom is not totally imaged because the magnification factor is not sufficient to get all its area fitted in the camera FOV. However, the main features of the phantom can be distinguished in the reconstruced images.

6.6.3 Summary on the imaging system performance

Table 6.3 summarizes the performance parameters of the two versions of the imaging system prototype: 1) GAGG crystal based and 2) LYSO crystal based.

Prototype	Uniformity[a] Int, Diff X, Diff Y (%)	Linearity[b] Abs, Diff (mm)	Spatial resolution (mm)	Energy resolution (%)	Extrinsic spatial resolution (mm)		
					@ 6 mm (P.H.)[c]	@ 50 mm (P.H.)	@ 47 mm (Pin.)[d]
GAGG	72.6, 78.9, 79.9	0.214, 0.191	0.90	29	1.53	3.9	1.64
LYSO	77.7, 82.2, 82.7	0.269, 0.096	0.72	29	1.49	3.9	1.64

Table 6.3: Gamma camera prototypes performance parameters. The parameters were assessed for the UFOV of 28×28 mm^2. In the extrinsic spatial resolution assessment, the reported values correspond to distances measured from the source to the collimator face in the case of the parallel-hole collimator and to distances measured from the source to the detector in the case of the pinhole collimator.

[a] Uniformity is reported as the integral (Int) and differential uniformity in X and Y (Diff X, Diff Y).

[b] Linearity is reported as the absolute (Abs) and differential (Diff) linearity, according to NEMA standard [82].

[c] "P.H." is a short for Paralle-hole collimator.

[d] "Pin." is a short for Pinhole collimator. Note that the focal lenght is 23.5 mm, so for a source-to-detector distance of 47 mm, the source-to-pinhole distance is also 23.5 mm, which results in no magnification.

As the result of the characterization, it can be concluded that the developed prototype can be used in sentinel lymph node detection and thyroid imaging, for which the requirement of 5 mm extrinsic spatial resolution at a source-to-collimator distance of 50 mm was specified. The two versions of the gamma camera prototype feature sub-millimeter intrinsic spatial resolution. The extrinsic spatial resolution of the prototype is 3.9 mm for a source at 50 mm from the parallel-hole collimator and 1.64 mm for a source projected from 47 mm to the detector through the pinhole collimator (and no magnification), which are esults clearly below the 5 mm stated as the objective. As a reference, in two of the cameras presented in **table 2.3** which use SiPMs and monolithic scintillators (the compounds selected for the developed camera), the reported system resolutions at 50 mm from the collimator are 10.3 mm and 6.25 mm (see Popovic and Goertz cameras in **table 2.3**). Two prototypes that feature system spatial resolution below 5 mm (at 50 mm) were also presented, but they use different technologies both for the scintillation and for the light collection, which are based on a pixellated crystal and a PS-PMTs array, respectively (see Moji and Olcott in **table 2.3**).

Concerning the intrinsic spatial resolution, the best results that can be found in **table 2.3** are 0.5-0.6 mm (Nakanishi cameras: pixellated scintillator + SiPMs) and 0.63 mm (Bugby cameras: pixellated scintillator + EMCCD). The *LYSO prototype* has the best spatial resolution for the combination of a monolithic crystal with a SiPMs array. LYSO, however has a non negligible self-radiation rate, which results in excessive background radiation for SLN detection, for instance. Thus, an alternative scintillator with no self-radiactivity was used,

GAGG. The Nakanishi camera also used the GAGG crystal but in the pixellated format and one third thinner than the GAGG crystal used in this work. The *GAGG prototype* built in the course of this thesis work has a worse spatial resolution than that of the *LYSO prototype*, but it is still below 1 mm (0.9 mm), which was one of the objectives of this work (high-resolution camera). The reasons for the better performance of LYSO were discussed in **section 3**, namely the larger thickness of GAGG.

The assessment of the sensitivity of both the parallel-hole collimator and the pinhole collimator was not reported in this document because of the difficulties in assessment of the dead time of the readout system at the time of the measurements. However, Monte Carlo simulations were performed for the optimization of the developed collimators (**section 3.4.1**) and they showed that in the optimal designs the sensitivities are within the defined specifications.

The energy resolution of both the GAGG and LYSO prototypes is 29%, which would be considered poor for a full-size gamma camera. However this is not so important for a SFOV camera performance, because, firstly, it is intended for single isotope detection and secondly, the developed system does not use the energy information for the suppression of multiple events, but the reduced *chi-square* of the reconstructed event instead.

7

Conclusions and future outlook

7.1 Summary and conclusions

The goal of this work was to develop a high-resolution self-calibrating compact gamma camera imaging system able to continuously perform acquisition and reconstruction of scintillation events (real-time imaging). The design of a small field-of-view (SFOV) gamma camera was optimized in order to achieve an intrinsic spatial resolution better than 1 mm for the lowest possible level of distortions. Then, two types of collimator were optimized to get the best trade-off between efficiency and resolution for the complete gamma camera imaging system. The optimization of the gamma camera was performed using simulations, through several rounds of validation of the design with experimental results. In order to validate the assumptions and models used in the simulations, the comparison between the simulated and the experimentally measured light collection was performed, demonstrating a good agreement between the two in both the number of optical photons collected per scintillation event and the shape of the estimated light response functions (LRFs). This allowed to rely on simulations for the optimization of the design of a SFOV gamma camera detector. The collimators were optimized through the trade-off curves given by the standard equations for collimator design.

Two versions of a SFOV gamma camera were assembled, based on different scintillators: LYSO and GAGG. A readout system was assembled and the required software was developed in order to acquire the signals of the photosensors for each scintillation event. The two versions of the camera prototype were characterized using a ^{99m}Tc (140 keV) gamma source and their performance was compared.

In the optimization process, the intrinsic spatial resolution was the first parameter taken into account to determine what were the components of the camera design that should be the focus of the optimization. The most important factor that influences the intrinsic spatial resolution is the thickness of both the scintillator and the lightguide, as they affect the distribution

of light through the array of photosensors. The thickness of the GAGG scintillator was set to 3 mm in this optimization study, to provide a γ-rays collection efficiency higher than 80%. Thus, the first optimization was performed by changing the lightguide thickness. The optimal thickness was found to be 1.0 mm. In a second optimization study, two configurations of the camera were compared, with two different optical coupling solutions. The simpler solution has the same standard optical grease, with refractive index of 1.465, in all interfaces of the optical components. A more advanced solution has a different optical grease in each interface. The refractive index of each grease has a mean value between the indexes of the components that it is coupling. The standard grease proved to result in a camera performance very similar to that of the advanced solution. The average intrinsic spatial resolution obtained in simulations for the optimized GAGG-based camera was 0.75 mm FWHM and the average level of distortions was about 0.06 mm. These results refer to a 28 $\times$ 28 mm^2 FOV, for a scintillator dimension of 33.2 $\times$ 33.2 mm^2.

Before using the standard equations, given in the literature for conventional cameras, in the design of two collimators to be used with a SFOV camera, it was verified that these still hold for scaled-down collimator dimensions. This validation was successfully performed by comparing the spatial resolution and the sensitivity obtained analytically and from simulations. Two collimators were designed and manufactured based on the validated formulas: 1) a 8 mm thick parallel-hole collimator with hexagonal holes of 0.5 mm size and 0.3 mm septa and 2) a channel edge pinhole collimator with 1 mm diameter, 0.5 mm channel height and 90° acceptance angle.

Another objective of this work was to select and assemble a multichannel readout and data acquisition system capable of reading output of 64 SiPM with rate sufficient for using a SFOV gamma camera in real-time mode. The TRB3 platform was selected among five alternatives as the DAQ solution. The readout system was assembled and tested using the software developed to streamline the acquisition and data processing processes. The continuous acquisition and reconstruction of scintillation events with the subsequent presentation of the reconstructed positions in a XY density plot was demonstrated, accomplishing the objective of the real-time operation of the system.

For the reconstruction of the scintillation event position and energy, statistical methods (maximum likelihood) were used with a model obtained from flood field irradiation of the entire camera FOV. The model of the camera response (one LRF per photosensor) can be built through the adaptive algorithm which is able to estimate the photosensor LRFs starting with an initial guess on the LRFs, either based on the results of the CoG reconstruction or based on the results from simulations. A script was developed in this work to perform automatically this iterative procedure. It was demonstrated both in simulations and experimentally that the model of the prototype light response can be obtained with that adaptive algorithm using

data from flood irradiation of the detector FOV. This algorithm provides the imaging system with a self-calibration capability.

I have performed the assessment of the intrinsic and extrinsic performance parameters of the two versions of the prototype of the complete imaging system in the nuclear medicine department of the Centro Hospitalar da Universidade de Coimbra. The objective of obtaining a sub-millimeter intrinsic resolution was accomplished: 0.72 mm FWHM and 0.9 mm FWHM were measured for the *LYSO prototype* and the *GAGG prototype*, respectively.

Despite the good resolution of the LYSO based camera, this detector is not adequate for applications where the activity of the radiotracer is low (e.g. sentinel lymph node detection, thyroid imaging), because LYSO has strong intrinsic radioactivity. This results in a significant amount of background detections, and consequently in a decreasing of the contrast in the reconstructed image.

The experimental extrinsic spatial resolutions nearly match those obtained for simulation data and analytical equations. The best spatial resolution of 1 mm FWHM in the object plane was experimentally achieved with the pinhole collimator and a magnification of 2 times (overall source-camera distance of 35 mm). For the parallel-hole collimator, a resolution of 4.4 mm FWHM was measured, with the source at ∼60 mm from the top collimator plane. These results show that the developed camera can be used in clinical diagnostic exams where high-resolution imaging is required, for instance, thyroid studies and sentinel lymph node detection.

The real-time imaging system was successfully tested with high activity sources. The reconstruction of the scintillation events was always performed in this work applying statistical reconstruction algorithms, which gives the possibility to monitor how faithfully the camera response model describes the current response of the camera. The average *chi-square* of the statistical reconstruction can be used as an indicator of adequacy of the currently used camera response model.

The goal to develop a high-resolution self-calibrating compact gamma camera able to perform real-time imaging and to monitor the quality of the camera response model was successfully accomplished.

7.2 Future outlook

In vivo imaging was not performed in this work. However, based on the performance of the developed imaging system, one can envision applications of that system in the *in vivo* imaging of small organs. The developed compact gamma camera can be integrated in a SPECT device to image the tri-dimensional distribution of the radiotracer inside the body. The gamma camera can also be a part of an equipment with augmented reality visualization, for instance

to be used in sentinel lymph node detection through radioguided surgery. The augmented reality visualization would be achieved by superposition of the image given by the gamma camera with an optical image showing the region of the body being imaged.

An alternative methods to the adaptive algorithm presented in this thesis for the automatic estimation of the detector response can be investigated. I have performed preliminary tests with the self-organizing map (SOM) algorithm using flood field irradiation data to build the camera model. SOM is an unsupervised iterative learning algorithm that has a training phase. For a gamma camera response model, a bi-dimensional map (grid of cells) is built saving in each cell a vector with the average sensor signals which correspond to a source position at the camera FOV. In the reconstruction phase, the event position is obtained as the cell position for which the vector of expected signals has the smallest Euclidean distance to the vector of measured signals. The results have shown that although the precision of reconstruction in the camera central FOV of 28×28 mm^2 is not as good as that given by the maximum-likelihood statistical reconstruction (SR), the reconstruction in the periphery of the camera obtained with SOM is significantly better when compared with that given by the SR. A mixed reconstruction method could result in the increasing of the camera useful FOV: using the results given by the SR reconstruction in the central region of the camera, and using the results obtained with the self-organized map in the camera periphery.

The collaboration started between the LIP-Coimbra and the department of nuclear medicine of CHUC can be continued at least in the following two ways: 1) to build and to test a prototype of a gamma camera with a larger FOV, as for large organs (e.g. heart, kidney, lung) the FOV of the developed camera is insufficient and 2) to start the endeavor to built a hand-held SPECT system. It should be noted that besides medical imaging, the new gamma camera can be used for other applications, for instance as a device to image the distribution of a gamma source contamination when monitoring radioactive waste disposal. Moreover, the self-calibration technique and the procedures for real-time imaging and monitoring of the model quality can be used with several position sensitive scintillation detectors, for example, neutron Anger cameras.

Appendices

Appendix A

Distribution of the number of detected photons

Poisson distribution can be derived from the binomial probability density function. If the number of photons that impinge the sensitive area of the photosensor window when N photons are isotropically emitted from the scintillation position is the variable to be statistically described, there are two possible outcomes for each independent "trial" (one photon emitted to a random position in 4π): the photon impinge the sensor window or not. This can be described by the binomial density function:

$$P_{Binomial}(n_i) = \frac{N!}{n_i!(N-n_i)!} p^{n_i}(1-p)^{N-n_i} \tag{A.1}$$

where N is the total number of emitted photons (trials), p is the probability of success (the photon impinge the sensor window) and n_i is the number of successes. The mean μ and standard deviation σ of the binomial probability density function are:

$$\mu = pN \tag{A.2}$$

and

$$\sigma = \sqrt{pN(1-p)} \tag{A.3}$$

It can be shown that for high value of N and when p is small and constant, the binomial distribution can be reduced to the form:

$$P_{Binomial}(n_i) = \frac{pN^{n_i}}{n_i!} e^{-pN} \tag{A.4}$$

and that $\sigma \approx \sqrt{pN} = \sqrt{\mu}$.

From **Eq.A.2** and **Eq.A.4** appear the familiar Poisson distribution:

$$P_i(n_i) = \frac{\mu_i^{n_i} e^{-\mu_i}}{n_i!} \tag{A.5}$$

Appendix B

Scintillation based SFOV gamma cameras

In this appendix, several small field-of-view gamma cameras based on scintillator crystals are presented. They are divided by the type of readout: 1) SiPMs, 2) digital SiPMs and 3) multianode PMTs.

B.1 SFOV cameras with SiPMs readout

Nakanishi et al. [141] have compared the performance of pixelated LYSO scintillator with that of pixelated GAGG in a gamma camera with SiPMs from Hamamatsu (S11064-050P). The crystal columns dimensions were $0.2 \times 0.2 \times 2.0$ mm^3 for LYSO and $0.2 \times 0.2 \times 1.0$ mm^3 for GAGG, forming scintillators with a main area of 20×20 mm^2. The LYSO plate is thicker than the GAGG plate because it was originally intended to be used in a detector for high energy γ-rays. In both cases there were 0.1 mm wide slits between pixels. The 3×3 mm^2 active area SiPMs were arranged in a 8×8 array and they were optically coupled with the pixelated scintillators through a 1.5 mm thick lightguides using silicon rubber. The energy resolutions were 30% and 23% FWHM for LYSO and GAGG based cameras, respectively, for 122 keV γ-rays. The intrinsic resolution (122 keV) of the GAGG camera was 0.5 mm FWHM, better than that of the LYSO camera, which was 0.6 mm FWHM. The background counts and the system sensitivity were measureed using a 122 keV point source (30 kBq activity) with a 1 mm diameter pinhole collimator attached to the cameras (focal lenght of 40 mm and source at 10 mm from the apperture). The sensitivity of the LYSO based camera was 2.5 times higher than that of GAGG based camera. The background counts and background fraction (ratio of background counts to signal counts) were 28 times an 11 times larger for the LYSO based camera and the GAGG based camera, respectively. This is mainly due to the ^{176}Lu intrinsic radioactivity in LYSO. With a 1 mm thick LYSO crystal the background counts can

be reduced by half. Based on the performance parameters given before, the authors concluded that GAGG scintillator is more appropriated for gamma cameras with SiPM readout.

Fujita et al. [142] have developed a prove of concept of a γ-rays detector consisting of a finely pixellated scintillator prepared from a 10 $\times$ 10 $\times$ 1 mm^3 GAGG plate. Micro-grooves 50 μm wide and with a depth of 900 μm were carved in the plate using a dicing saw. For comparison, two arrays were fabricated. One array has a 0.25 mm pixel pitch and the other a 0.6 mm pixel pitch. The grooves were filled with a reflective material ($BaSO_4$). A 14 $\times$ 14 $\times$ 1 mm^3 borosilicate lightguide (larger than the scintillator array) was placed between the scintillator and a 4 $\times$ 4 SiPM array (Hamamatsu S11830-3344MB sensors with 3 $\times$ 3 mm^2 active area). The spatial and energy resolutions of the 0.6 mm pitch array were 13% (122 keV) and 0.77 mm FWHM respectively, and 14% (122 keV) and 0.48 mm FWHM for the 0.25 pitch array. The spatial resolutions in the two cases are quite good.

Lipovec et al. [221] have studied the influence of the glass lightguide thickness on the CoG event reconstruction precision. The scintillator was made of a 48 $\times$ 48 array of 0.4 $\times$ 0.4 $\times$ 20 mm^3 GAGG:Ce crystal pixels (500 μm pitch). The light collection was performed with a 26 $\times$ 26 mm^2 array of 64 SiPMs (Hamamatsu S12642-0808PA-50), each one with a 3 $\times$ 3 mm^2 active area. Using glasses with five thicknesses (0.8 mm, 1.0 mm, 1.35 mm, 1.85 mm, 2.5 mm) both in an experimental prototype and in simulations, the authors have demonstrated that the distribution of light widens for thicker glasses, allowing more precise event reconstruction. However, when the glass thickness reaches a certain upper limit (1.85 mm in this study configuration) the light collected by the sensors becomes scarcer, resulting in worse reconstructions. The crystal pixels can be distinguished in the flood diagram for all simulated glass thicknesses, which indicates that a 0.5 mm FWHM spatial resolution is possible to be achieved. Glass thickness between 1.35 mm and 1.85 mm are recommended to obtain the best resolution.

Popovic et al. [139] described a hand-held gamma camera for intraoperative guided surgery also based on the same SiPMs used by Nakanishi et al. (Hamamatsu S11064-050P). The camera is constituted by a 5% cerium doped lanthanum bromide (LaBr3:Ce) monolithic scintillator with round shape (60 mm diameter) and 6 mm thick. The scintillator is coupled through a 1 mm glass lightguide to an array of 80 SiPMs arranged in a quasi circular shape. $LaBr_3$ has a good spectral match with the PDE of the used SiPMs. The camera featured an intrinsic resolution of 4.2 mm FWHM and an energy resolution of 21.1% FWHM at 140 keV. This energy resolution is relatively large for $LaBr_3$, which has a 7-8 % intrinsic energy resolution. Using a 5.5 mm thick parallel-hole collimator with 0.6 mm diameter holes (1 mm pitch) made of tungsten polymer (attenuation coefficient is 18.7 cm^{-1}) the achieved system resolution was 10.3 mm FWHM at 50 mm from the collimator surface (for a sensitivity of 481 cps/MBq).

The authors have also attached a second collimator similar to the first one and aligned with it, making a 11 mm thicker collimator. With the source also at 50 mm to the collimator face, the system resolution improves to 6.4 mm FWHM, while the sensitivity highly degrades to 73 cps/MBq.

Goertzen et al. [143] have also developed a hand-held camera for radioguided sentinel lymph node biopsy surgical procedures, based on SiPMs readout (SensL SPMArray4SL). The camera with 13.2 × 13.2 mm^2 FOV has 4 × 4 CsI(Tl) scintillator elements with size of 3.3 × 3.3 × 5 mm^3 coupled to an array of 4 × 4 SiPMs (active area of 2.85 ×2.85 mm^2 and 0.2 mm inter-SiPM gap). The energy resolution was 40.2% FWHM at 122 keV. A low-energy high resolution collimator (LEHR) was attached to the camera and a 1 mm cylindrical source (122 keV) was placed 50 mm apart to characterize the extrinsic parameters. The system spatial resolution was measured as 6.25 mm FWHM and the sensitivity as 149.7 cps/MBq.

More examples of gamma cameras prototypes with SiPMs readout can be found, for instance, in [222, 223, 224, 225, 226, 227, 228].

B.2 SFOV cameras with digital SiPMs readout

From 2009 a new type of SiPMs has been developed for the direct readout of the binary information from the SiPMs microcells (fired or not fired by a photon) [229, 230]. They are called digital SiPM (dSiPM) or digital photon counter (DPC). These type of sensors do not need front-end electronics in order to shape and digitize the signals of the collected charges. The acquisition process is controlled using logical networks on the microcells level. For instance, microcells with a high dark count rate can be disabled. A presentation on the dSiPM principal of operation and intrinsic performance can be found in [229]. Bouckaert *et* al. [93] have evaluated a high-resolution SPECT detector consisting of a 2 mm monolithic LYSO crystal and a digital photon counter. They have investigated the influence of the dark rate (temperature dependent) on the camera performance. At 3°C the energy resolution (140 keV) was 28.8% FWHM and the spatial resolution 0.48 mm FWHM. At 18°C the energy resolution (140 keV) was 29.2% FWHM and the spatial resolution 0.52 mm FWHM [93]. Brown [231] has performed a Monte Carlo comparative study of the performance of four 32 × 32 mm^2 monolithic scintillators (NaI(Tl), GAGG:Ce, CsI(Tl) and LYSO:Ce) coupled to the Philips DPC3200 dSiPM. Five thicknesses were simulated for each scintillator (1 to 5 mm). The author has concluded that for SPECT/CT applications using pinhole collimator, a 3 mm thick GAGG:Ce was an optimal scintillator. This thickness improves the spatial resolution reducing the DoI effect impact with a minimal cost in the detection efficiency and reduction in the energy resolution. The spatial and energy resolutions of that 3 mm thick GAGG based

gamma camera with dSiPM readout and CoG reconstruction are 0.5 mm FWHM and 18% FWHM, respectively.

B.3 SFOV cameras with multianode PMTs readout

There are many SFOV gamma cameras based on the combination of a scintillator crystal with position-sensitive multianode PMTs (PSPMT) (see, for example [150] and [232]). Initially, PSPMTs based scintillation cameras pose problems due to their nonlinear and non-uniform responses, which were caused by gain non-uniformity. However, several methods were developed to mitigate that problem [233, 234, 235, 236, 237].

Hyun Kim et al. [238] have optimized through Monte Carlo simulation both the design of a gamma camera based on a monolithic crystal with PSPMT readout and a micro parallel-hole collimator. The gamma camera consists of a 50 × 50 mm^2 LGSO scintillator and a flat panel of 16 × 16 PSPMTs (Hamamatsu H9500) with a 1.5 mm thick lightguide in between. A thin layer (0.1 mm) of optical grease couple the three components. The collimator with an area of 52 × 52 mm^2 has 128 × 128 square holes, arranged in a square matrix. The holes area is 0.34 × 0.34 mm^2 with a 0.04 mm thin septa. Two isotopes were used: ^{125}I (35.5 keV) and ^{99m}Tc (140 keV). Only a 3 mm thick crystal yields a γ-rays collection efficiency suitable for both ^{125}I and ^{99m}Tc. For 140 keV rays, the efficiency was around 70%. The optimization of the crystal intrinsic performance was focused on the crystal lateral sides finishing. The standard deviation of an angle between the normal of the mean surface and a micro facet (sigma alpha) was set in simulation as 0.1° for polished and as 6.0° for the not polished (rough) surfaces. The energy resolution was 18% for 140 keV and has no significant dependence on the crystal lateral sides finishing. However, it got worse when the source was moved to the edge of the crystal. At the crystal periphery, the energy resolution was 20% and 28% lower than in the center of the crystal for rough and polished finishing, respectively. Rough surfaces have higher reflectivity (more 14%) than polished surfaces. The intrinsic spatial resolution was 0.57 mm in the central FOV (30 × 30 mm^2) and got worse until 1.04 mm at the crystal periphery. Practically the same resolutions were measured for the two crystal finishings.

Deprez et al. [46] compared the performance of two monolithic scintillators: a 2 mm thick LYSO crystal and 5 mm thick NaI(Tl). The crystals were coupled to a Hamamatsu H8500 PSPMT through a 2mm thick quartz lightguide. The lateral sides of the LYSO crystal were covered with black material, while those of the NaI(Tl) were covered with a reflective material. To optimize the spatial resolution and the useful detector area, the authors used a k-nearest neighbor event reconstruction method. The intrinsic spatial resolution with the LYSO and the NaI(Tl) crystals was 0.93 mm FWHM and 1.37 mm FWHM, respectively. The energy

resolutions at 140 keV were 9.3% for LYSO and 21.3% for NaI(Tl). The intrinsic radioactivity of LYSO (for a 42% photopeak window) was measured as 125.6 counts per second (cps).

Moji et al. [149] developed the HiReSPECT, a SPECT system with two gamma cameras, each one consisting of an array of 46 × 89 CsI(Tl) columnar crystals (1 mm × 1 mm × 5 mm, 1.2 mm pitch), and two arrays of 8 × 8 PSPMT (Hamamatsu H8500) with 49 × 49 mm^2 active area each one and a LEHR parallel-hole collimator (34 mm thick, 1.2 mm hexagonal holes and 0.2 septal thickness). The energy resolution at 140 keV is ∼19% FWHM. The system resolution is ∼1.6 mm FWHM and ∼2.3 mm FWHM for the short- and long-axis, respectively at the collimator surface. The corresponding resolutions at 50 mm from the collimator are ∼3 mm FWHM and ∼4 mm FWHM. The integral system uniformity after uniformity correction is 1.7% in the useful field of view (UFOV).

Olcott et al. [135] developed a intraoperative hand-held gamma camera (IHGC) dedicated to breast imaging and localization of sentinel nodes in head-and-neck (melanoma). The camera consists of a 50 × 50 mm^2 pixelated NaI(Tl) crystal (1.5 × 1.5 × 6.0 mm^3 pixels and 1.7 mm pitch) attached to a flat panel PSPMT (Hamamatsu H8500). The energy resolution was 12% FWHM at 140 keV. The intrinsic resolution was 1.8 mm FWHM. A 15 mm thick parallel-collimator was selected, with 1.3 mm hexagonal holes and 0.2 mm septa. The system spatial resolution is 1.81 mm FWHM for a source-to-collimator distance of 6 mm.

Kim et al. [150] developed a monolithic scintillator based camera mainly intended for scintimammography (molecular breast imaging). The 60 × 60 × 6 mm^3 crystal is coupled with a PSPMT (Hamamatsu R3941), which has a 16 × 18 crossed wire anode with a pitch of 3.7 mm. The intrinsic energy and spatial resolutions are 12.9% FWHM (140 keV) and 3.1 mm FWHM, respectively.

Appendix C

Neutron Anger camera

The performance of the readout system presented in the **section 4** was first tested with a neutron Anger camera, developed by the Neutron Detector Group from LIP. I have participated in the detector characterization measurements at the Institut Laue-Langevin (ILL) in Grenoble. It is a thermal neutron detector, very similar with the gamma camera developed in this work. The main difference is the material of the scintillator, which is a silicate glass scintillator crystal. The SiPMs array is the same used in the gamma camera prototype, working at a slightly lower bias voltage. The suitability of the event reconstruction algorithm (including the adaptive algorithm for LRFs reconstruction) for the neutron detector was verified by this group. In this appendix, the neutron detector working principle and its design are briefly outlined.

C.1 Detector working principle

There are three main types of thermal neutron detectors: proportional gas counters, semiconductor detectors and scintillation detectors. For all cases, in the neutron capture nuclear reactions occur, producing ionizing particles that deposit their energy in the detector. Our group have published recently a work presenting experimental results on a scintillation neutrons detector [220] and part of that results are also presented further, in **section C.3**. Position sensitive detectors based on scintillators are also being used for thermal neutrons detection. Thermal neutrons can only be detected indirectly. The working principle of the assembled neutrons detector is similar to that of gamma cameras. The presented detector featured a 1 mm thick lithium-6 loaded cerium activated silicate glass scintillator crystal (GS20). The capture of a neutron by the lithium-6 nucleus results in a nuclear reaction:

$$^{6}Li + n \rightarrow ^{3} H(2.75MeV) + ^{4} He(2.05MeV) \tag{C.1}$$

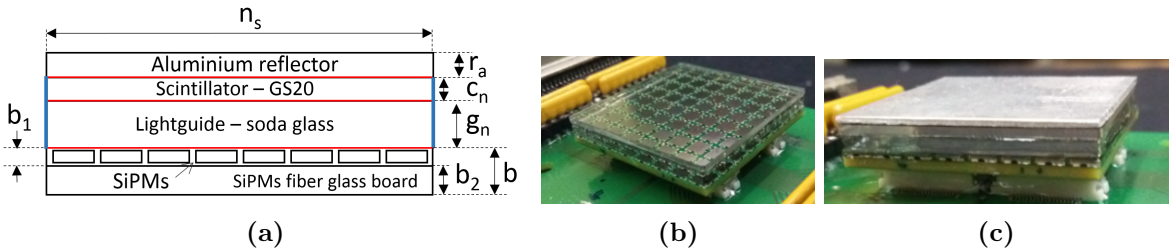

Figure C.1: Neutrons detector prototype photograph. **a**: Drawing of the neutrons detector geometry with component dimensions labels. $r_a = 1$ mm; $c_n = 1$ mm; $g_n = 2$ mm; $b = 2$mm; $b_1 = 0.7$ mm; $b_2 = 1.3$ mm. Red lines represent thin layers of optical grease, while the blue lines represent few layers of Teflon tape. **b**: Reflector is removed. The SiPMs array is visible **c**: View with the aluminum reflector.

The reaction products deposit their energies, which results in the emission of about 6200 photons (395 nm emission peak). The position of the energy deposition is close to the neutron capture position (<150 μm), so it can be obtained reconstructing the scintillation event position.

C.2 Prototype and experimental setup

The geometry of the assembled detector is the same as for gamma cameras, but with different scintillator and lightguide thicknesses and a different encapsulation of the crystal lateral sides. The scintillator in this camera is a lithium-6 loaded cerium activated glass scintillator (GS20 from Scintacor), with an area of 33.3 × 33.3 mm^2 and 1 mm thick. According to the manufacturer, this thickness results in 73% interaction probability for 2.5 Å neutrons. The scintillator was wrapped with several layers of Teflon tape, to reflect back the photons escaping from the scintillator lateral sides. As plexiglass would scatter a significant amount of neutrons, the selected lightguide material was soda lime glass (2 mm thick). The array of SiPMs of the neutron detector is the same as for the gamma cameras presented in **section 6.1.1**. The reflector is a 1 mm thick aluminium plate. **Fig.C.1** shows photographs of the assembled neutrons detector prototype.

Setup The neutrons detector prototype was mounted inside a light-tight enclosure with a 1 mm thick aluminium entrance window. The detector was installed at the CT1 beam line of ILL (2.5 Å neutron wavelength). The entrance window was positioned perpendicularly to the beam, for normal incidence. The SiPMs were operated at 1.8 V above the breakdown voltage. SensL provides photon detection efficiency of ∼41% at for the 425 nm detection peak. Weighed by the GS20 emission spectrum, the effective PDE is about 25%.

For the detector characterization, two cadmium masks were prepared. Both were 1 mm thick. One mask has an array of 0.4 mm diameter holes with a pitch of 2 mm in both X and Y

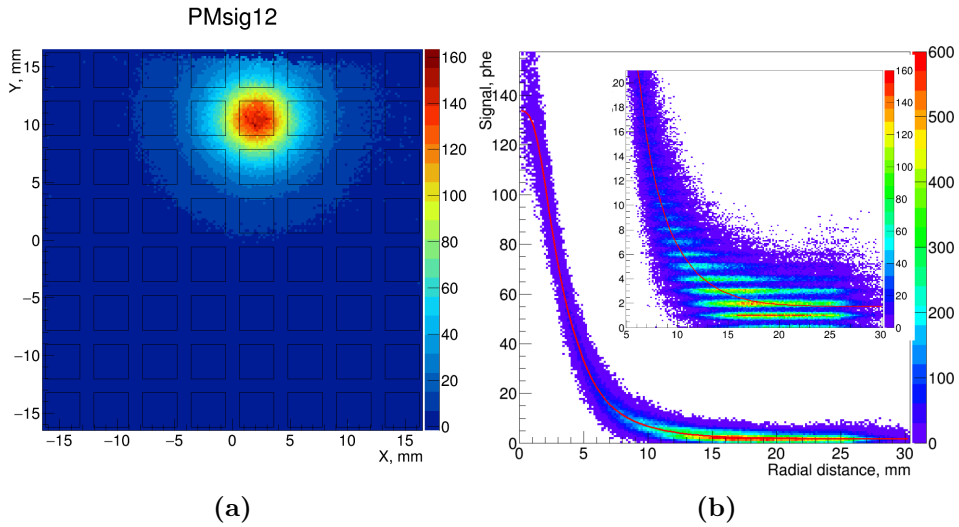

Figure C.2: LRFs of one SiPM (#12) of the neutrons detector. **a** SiPM signal as a function of the reconstructed positions. **b**: LRF curve fitted to the reconstructed data. The inset shows the signal values up to 20 photoelectrons.

directions. It was used to assess reconstruction fidelity. The second mask has a 0.4 mm wide and 40 mm long slit and was used to measure the spatial resolution. For all the measurements using cadmium masks, they were installed inside the camera enclosure in direct contact with the light reflector. The whole sensitive area of the detector was irradiated with neutrons to record a flood field dataset.

C.3 Prototype characterization

C.3.1 Estimation of the camera model

As for the gamma cameras, the LRFs were obtained from flood field irradiation data, using the iterative procedure, with no need of any scanning calibration. It was verified an axially-symmetric response of all LRFs except those at the border of the camera. **Fig.C.2 a** presents an example of the average signal in one SiPM (#12) as a function of the reconstructed positions. In **Fig.C.2 b** can be verified that the estimated LRF curve fitted very well the experimental data. In the inset one can see that for radial distances far than 15 mm the LRF signal is still 2 photoelectrons, a value larger than the average background contibution of ∼0.25 photoelectrons due to dark counts.

Fig.C.3 presents the XY density plot of the event positions of a flood irradiation dataset reconstructed using the center-of-gravity (CoG) method and the maximum-likelihood (ML) statistical algorithm (**section 2.5.4.1**). A reduced intensity in the density plot in the top-right corner of the camera is attributed to significant degree of non-uniformity of the CT1 neutrons beam at ILL. This fact was confirmed by ILL facility personnel.

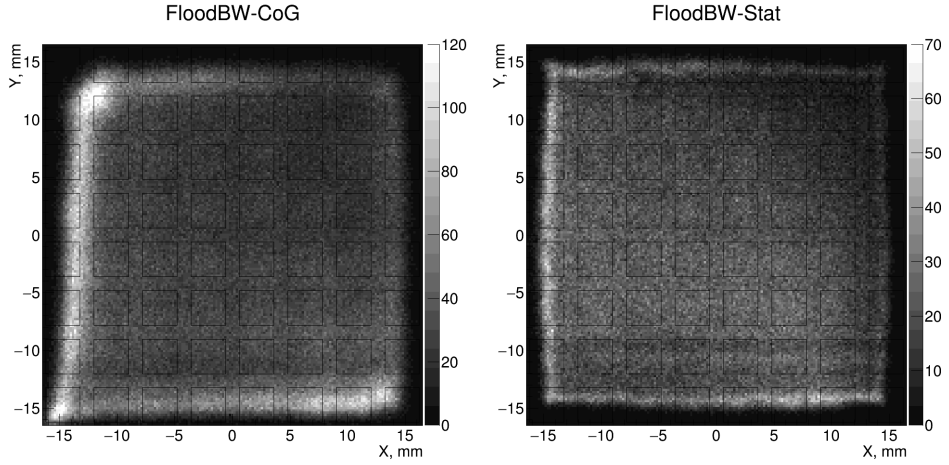

(a) (b)

Figure C.3: XY events density plot of the reconstructed positions of the neutrons registered in the camera. **a** CoG reconstruction. **b**: Maximum-likelihood reconstruction.

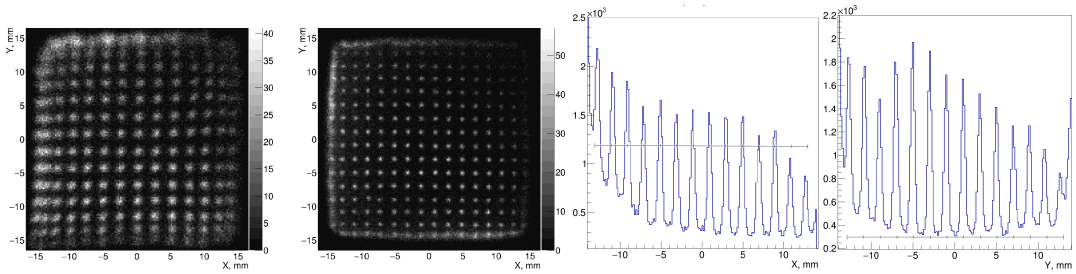

(a) (b)

Figure C.4: Event reconstruction of a dataset recorded in the neutron Anger camera with a cadmium plate with a grid of 0.4 mm holes (pitch 2 mm). The contours of the SiPM sensitive areas are shown by thin black lines. **a** XY events density plot of CoG (left) and ML (right) reconstructed positions. **b**: Profiles along X and Y for ML reconstructed image.

C.3.2 Intrinsic spatial distortions assessment

The spatial distortions were assessed with the cadmium plate with a grid of 0.4 mm diameter holes (2 mm pitch in both X and Y directions). **Fig.C.4 a** presents the results of the positions reconstruction using CoG and ML for a dataset acquired with that mask. The projections along X and Y axes corresponding to ML reconstruction are shown in **Fig.C.4 b**.

The ML reconstruction is quite precise in the central region of 28×28 mm^2. In the periphery of the camera there is a region of 2 mm where the events either fail the χ^2 discrimination [85] or are reconstructed in wrong positions, which results in a higher density of events in that region. In a previous study of our group on a compact gamma camera, a similar reconstruction pattern was observed [85].

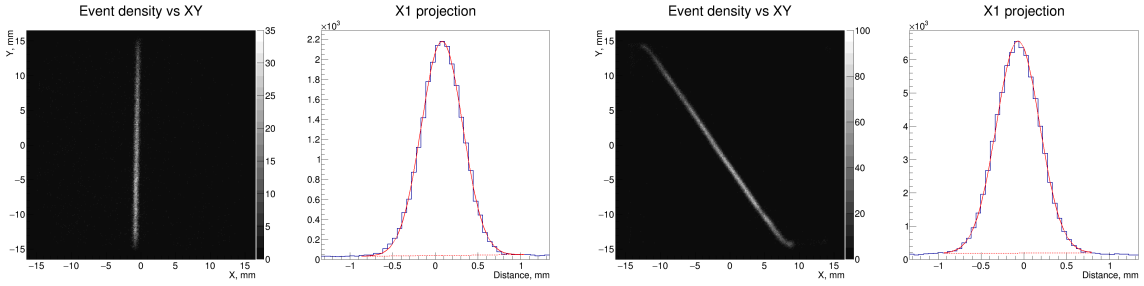

Figure C.5: Reconstruction of a 0.4 mm wide slit by the neutron Anger camera. **a** and **c**: XY event density plot of the reconstructed positions. **b** and **d**: Profiles of the projection of the reconstructed images along the direction perpendicular to the slits and the respective Gaussian fits. **a** and **b**: Slit vertically oriented (along Y). **c** and **d**: Slit diagonally oriented.

C.3.3 Intrinsic spatial resolution assessment

Fig.C.5 shows the ML reconstructed images of the data recorded with a cadmium mask with a slit (0.4 mm wide and 40 mm long). The slit was oriented along two directions: the X axis (**Fig.C.5 a**) and diagonally in respect to Cartesian axis (**Fig.C.5 c**). The projections of the density plots of the reconstructed positions in the prependicular direction to those slits are also presented (**Fig.C.5 b** and **d**). The spatial resolution was assessed calculating the FWHM of the Gaussian fit to the profiles, which is for both slits orientations less than 0.60 mm.

The results presented in this appendix were published in the Journal of Instrumentation at March 2019 [220][1].

[1]The paper published in Jinst journal is available at https://doi.org/10.1088/1748-0221/14/03/P03016

Appendix D

Software packages and libraries

This appendix presents the software packages and libraries used for the acquisition procedures and data processing.

D.1 DABC Library and TRBReader package

DABC[1] is a C++ library which contains functions to handle TRB3 acquired data. It is used either to store the data sent from TRB3 (as .HLD binary files) and to extract the stored data (e.g. information on the waveform encoded in the .HLD files). The information on the .HLD file structure (e.g. *RawEvent* and *RawsubEvent* structures[2]) to be able of extract the data can be found in the **TRB3 Manual**[3]. It has two useful pictures (Figures 21 and 22 of the manual) with the schematic structure of the .HLD file and of the "event header" and "sub-event" inside the .HLD file. The data sent by the readout system is organized by "events" in the storage unit by the "event builder software". For the TRB3 configurations used in this work, one event stores the samples of 64 waveforms that correspond to the SiPMs signals and the samples of 4 waveforms that correspond to the "sum signals" (**section 4.3.2**). The samples of the different SiPMs waveforms are labeled with the ID of the FPGA that controls the ADC *add-on* that digitized that waveform (**section 4.3.2**).

For the automation of the signals extraction (e.g. waveform integration), a custom made signal extraction C++ application called *TRBReader* was used. In TRBReader application the "signal" extraction can be performed through two main options: by taking the maximum amplitude or the waveform integral. Signals with both positive and negative polarities can be handled.

[1] DABC library is available in the GSI webpage: https://web-docs.gsi.de/~dabc/doc/dabc2/hadaq_trb3_package.html#trb3_install.

[2] The definition of the *RawEvent* and *RawsubEvent* structures belong to the file *defines.h* in the include directory of the library **DABC**.

[3] The TRB3 manual can be found in the section "TRB3 Documents" of the TRB3 GSI website: http://trb.gsi.de

If local pedestal calculation is desired (**section 5.1.1**) the software allows the subtraction of the individual pedestal calculated for each waveform (averaging the first samples). Local pedestal calculation might be useful to account for the changes in time of the SiPM baseline (electronic zero level). Besides allowing performing the signal extraction and local pedestal subtraction, TRBReader also permits the visual inspection of the waveforms (including the sum signals used for event triggering). TRBReader processes each .HLD binary file to produce a file (.DAT) with the signal of all photosensors (PMs) for all triggered scintillation events. This file (.DAT) can be loaded in ANTS2 for event reconstruction, filtering and visualization.

D.2 ANTS2 modules for data processing

ANTS2 is used to the reconstruction of scintillation events. This section summarizes the procedures required to make a reconstruction that are available on ANTS2. The data files (.DAT) should be first loaded and pre-processed (pedestals subtraction, conversion into number of photons using SiPM gain). If calibration data is not already available, ANTS2 has the tools for both pedestals calculation (**section 5.1.1**) and gain calculation (**section 5.1.3**). For statistical reconstruction, a set of LRFs must be loaded or estimated. ANTS2 has a dedicated module for the calculation of the LRFs, where the user can run the procedures of the adaptive algorithm (**section 2.6.1**), such as calculate the LRFs, reconstruct events and randomly shift the reconstructed positions. ANTS2 has implemented several reconstruction algorithms: center-of-gravity, statistical reconstruct (SR) methods, kNN, ANN. From ANTS2 reconstruction methods, only "contracting grids" optimization algorithm (SR) - **section 2.5.4.2** - is implemented in the GPU. Filters can be applied to the reconstructed events (e.g. filter by reconstructed energy, by the reduced *chi-square* χ^2, by the sum of all SiPMs signals, or by reconstructed positions). The reconstructed events can be shown as XY density plots: positions, energy, chi-square, SiPM signal.

High level scripting engines in ANTS2 and TRBreader Both TRBReader and ANTS2 packages include a scripting mode module (which runs a JavaScript interpreter). For this, a Qt based interface between the interpreter of the Javascript scripting language and C++ object files was implemented.

In both ANTS2 and TRBReader scripting modules the user have access to *wrappers* to already implemented C++ functions, which are organized in *units*. *Unit* is the name given to a group of functions that are related with the same software modules of either ANTS2 or TRBReader (e.g: configuration, geometry, events, simulation, reconstruction, LRFs, photon, PMs, hld,...). A special unit (called *gui*) was prepared to give users access to Qt widgets (e.g

buttons, text field, labels, etc). Using the *gui* unit, an acquisition GUI was programmed in scripting language in the script environment of ANTS2.

The *units* gather C++ implemented functions related with the same ANTS2 module (hopefully expressed in the *unit* name). I have implemented a new unit called *custom*. This unit contain some C++ functions to be called in scripting mode. They are mainly related with the real-time processing and the optional reduced *chi-square* χ^2 monitoring.

Communication with TRBReader scripting engine ANTS2 has a communication module to allow communication between ANTS2 and TRBReader (either text and binary files transfer) and it is encapsulated in the units *web* and *server*. ANTS2 communicates with TRBReader using a client to server protocol. Both software packages have implemented the required functions for socket communication through the network. As the communication runs over the TCP/IP protocol (sockets communication), TRBReader and ANTS2 can be running in different machines.

Appendix E

Acquisition software

The required software for the communication between the modules presented in **section 4.3.2** (**Fig.4.7**) was developed. Three tasks were required: 1) to communicate with the Control and Monitoring unit, 2) to send configuration and control commands to the TRB3 board and 3) to configure and launch the application that organizes the incoming signals in the EventBuilder and Storage unit (event builder software).

The communication with TRB3 board was performed through the TRB3 drivers. A startup function was implemented to call the driver commands that configure the central FPGA, the FPGAs that control the ADCs add-ons and the GbE communication. Other function starts the data acquisition into a specified storage unit, during the specified time window. When commands need to be sent to remote machines, the *ssh* protocol was used. Several TRB3 configurations can be set through a web browser interface developed by TRB3 team, as well as to start and to stop an acquisition. Below the details on the referred software and routines are presented.

The "acquisition software" is organized in three layers, represented in **Fig.E.1**. The **drivers layer** is the lower software level and offers the set of functions to control and configure the TRB3 board (device). The device drivers are provided by the GSI TRB3 team. The **bash scripting layer** is the intermediate software level that uses the bash script interpreter to execute system operations (e.g. *ssh* commands for remote communication and data transfer between machines) and to call the hardware functions. The **application layer** is the highest level in software hierarchy. It corresponds to the user developed software (e.g. ANTS2[1], TRBReader[2]) in any high level programming language to interface with the bash scripting layer.

[1] ANTS2 application has both graphical user interfaces and a high level scripting engine, which will be presented in **section 5**.

[2] TRBReader is a custom made software developed in LIP Coimbra to process data sent by the ADC *add-ons* in the TRB3 board. It is briefly presented in **appendix D.1**.

Software level	Software Layer	Platform
High Level	Application Layer	ANTS2, TRBReader
Intermediate Level	Bash scripting Layer	Bash interpreter
Low level	Drivers Layers (e.g. TRB3 drivers)	Hardware

Figure E.1: Acquisition software layers.

The bash scripts call device drivers to perform various tasks associated with data acquisition: setup the board and addons, configure, start and stop acquisition, configure trigger, etc. In this section are only presented, briefly, the bash scripts (**intermediate software level**) necessary to make the readout system works, the required configuration file and a web browser interface to monitor the acquisition rate, to select the trigger thresholds and to start and stop the acquisitions. The scripts and configuration file are available on a web repository[1]. A further description of the operations made by the scripts is given in the **section 5.2**. The purpose here is to only give a quick start guide for acquisition with the TRB3 based readout system.

1. **TRB3 startup**

   One instance of the Trbnet software should be first launched to allow communication with the board. Once verified that the connection with the board is established, the configurations are sent for the central controller FPGA and for the ADCs FPGAs. The configuration of the central FPGA is mainly the identification of the peripherical FPGAs with active addons (e.g. with ADCs) and the setting of the GbE communication parameters (e.g. the IP address and port of the controller unit and that of the data storage machine). The configuration of the ADCs addon requires to set the values of several parameter: trigger channels, trigger thresholds, disabled channels, number of samples per waveform, number of samples after trigger and the number of samples to average the baseline in the trigger channels. After the FPGAs configurations, the Central Trigger System (presented below) can be started.

   The TRB3 commands to perform the configurations referred above are called by a bash script[2]. This script must be executed in the TRB3 controller unit.

2. **Acquisition configuration file**

   The directory where the acquired data should be stored and the size of the data files must

[1]GitHub repository: https://github.com/jsmarcos/TRB3-GSI-based-DAQ. From now on, whenever "repository" is mentioned, it refers to this same repository, unless the contrary is explicitly said.

[2]The code of the script *startup_TRB49.sh* can be found in the repository, inside the directory */userscripts_trb49_on_control_unit_OdroidC2*.

be specified in a .xml configuration file[1]. The .xml file must be also in the Acquisition and Storage unit.

3. **Application that manage the storage of data**

   The TRB3 team developed an application to be executed in the storage machine that is responsible for the encapsulation of the acquired data. The application is called DABC.exe[2] and should be launched with the configuration file (.xml) as the argument. This can be done, for instance, inside a bash script[3].

4. **Central Trigger System**

   The "Central Trigger System" CTS is a module on the central FPGA that manages the events triggering and the reading of signals from the ADCs add-ons. The CTS includes a web browser interface with web 2.0 interactivity. This webpage is accessible in the controler unit[4] using a port specified in the configuration file. There is also a configuration webpage[5] in which one can set some parameters on the ADCs add-ons, for example the number of samples and the trigger thresholds of the acquisition channels.

   CTS web interface allows to monitor the trigger rate, to change the trigger thresholds and to start and stop the acquisitions. The data transferred to the storage unit, will only be stored if the "EventBuilder" is already running in that machine.

   The initial settings on the CTS (e.g. number of samples, the number of samples after trigger, the number of the trigger channels, etc) are set through a script called cts-dump.sh[6], which is called by the startup script referred in 1).

Although no additional software is needed to make acquisitions than that previously described, the operation of the TRB-based DAQ via CTS web interface can be a challenging task for users not familiar with TRB operation. I made a graphical user interface (GUI) to give simple access to functionalities as the control, configurations and acquisition. That GUI should be available in the acquisition and storage unit. The idea was to add an additional layer of abstraction - application layer of **Fig.E.1** - for the end user of the readout system. Both the GUI and the software behind it are presented in the **appendix F**.

[1] An example of the .xml configuration file, EventBuilder_TRB49.xml, can be downloaded from the repository.

[2] The DABC Library, that contain the application DABC.exe, can be download and installed following the instructions on the website https://subversion.gsi.de/dabc/trb3/Readme.txt.

[3] A copy of the bash script that calls DABC.exe is the file startDABCnoSleep.sh that is available in the repository.

[4] For example, if the Odroid-C2 IP address is 10.0.0.1, the *url* of the CST would be: 10.0.0.1:1234/cts/cts.htm.

[5] For the exemplary IP address of the previous footnote, other webpage is available for configurations: 10.0.0.1:1234/addons/adc.pl?BufferConfig

[6] A copy of the cts-dump.sh is available in the repository, inside the directory */userscripts_trb49_on_control_unit_OdroidC2*

Appendix F

"TRB3 Acquisition ANTS2 GUI"

A GUI application was developed to make the acquisitions and the pre-processing tasks more user friendly (**Fig. F.1**). In the **appendix E** the minimal software to start an acquisition is presented. With this minimal software, there is a need to manually set the acquisition directory and file size and to launch two scripts: a startup script in the mini-computer and the one that calls DABC.exe in the computer. The directory of the files, if does not exist already, must be created by the user. If one wants to change the trigger thresholds, he must do it manually in CTS, at least with 4 clicks. The pre-processing of the acquired files must be done separately using TRBReader.

The **GUI** makes simpler the choice of the acquisition settings (files directory, files size, trigger thresholds) and gives the user a set of functionalities at "one click distance". The Acquisition GUI has **four main blocks**:

1. Simple acquisition
2. Pedestals acquisition and calculation
3. Real-time acquisition
4. LRFs calculation

These blocks are only operational after the connection with the TRB3 board is established. This is done pressing the button "Connect TRB3 DAQ", which also triggers the TRB3 startup script mentioned in the **appendix E**.

Below the **software layers of the acquisition GUI interface** are briefly presented. That interface was built in the scripting module of ANTS2 (see **appendix D.2**), using a special *unit* called *gui* for adding widgets (graphical control elements). These scripting widgets are Qt C++ widgets in their root.

This programming option (develop the GUI in scripting mode) made faster the development, mainly because ANTS2 scripting mode has several *units* to call C++ implemented

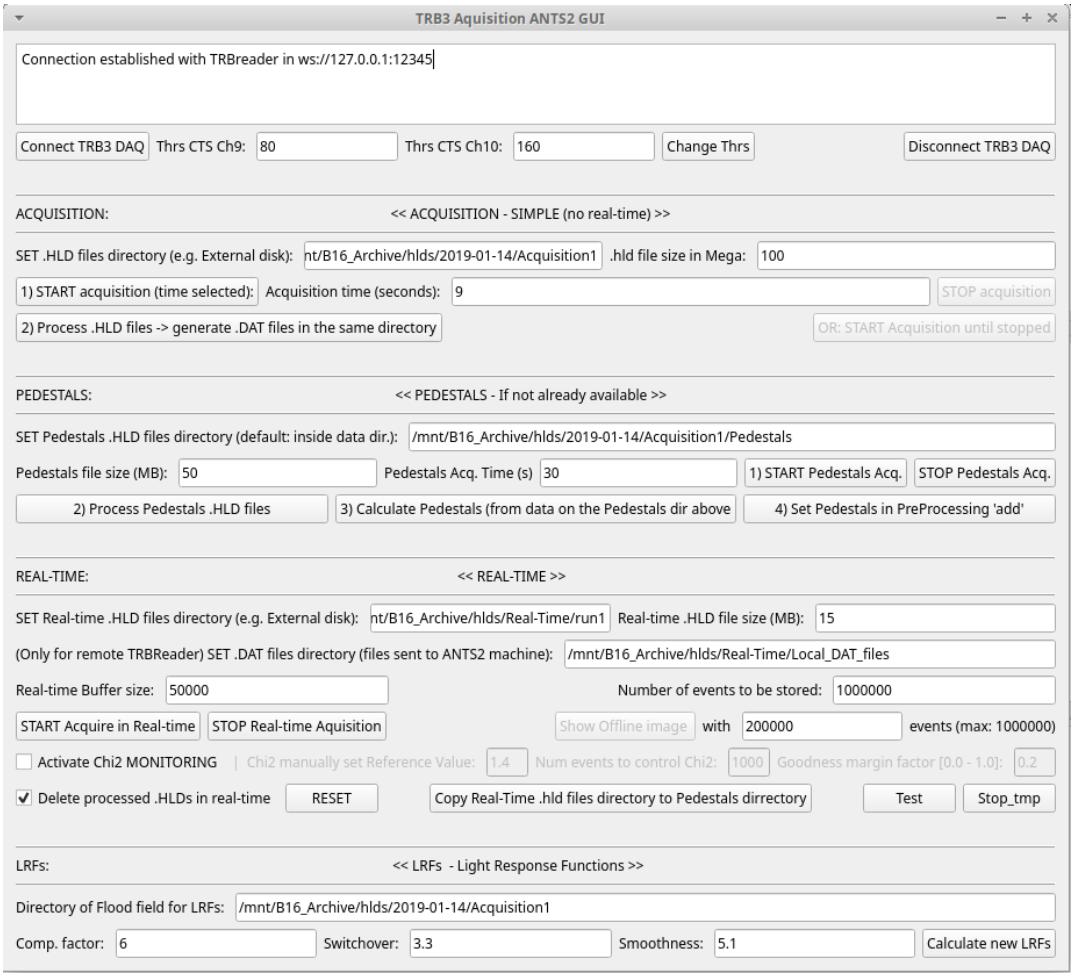

Figure F.1: TRB3 Acquisition ANTS2 GUI. After the connection with TRB3 board in established, four units are available: Simple acquisition, Pedestals acquisition and calculation, Real-time acquisition and LRFs calculation.

function of the ANTS2 modules (configuration, simulation, event reconstruction, LRFs estimation, etc). The functions and scripts behind the GUI buttons can be found in the repository[1], where documentation is also available.

The **Fig.F.2** is a snapshot of the scripting environment in ANTS2. A red rectangle points out the panel with the scripting *units* names. These *units* gather C++ implemented functions related with the same ANTS2 module (hopefully expressed in the *unit* name). The communication between the scripting interpreter and the compiled C++ functions (object files) is performed by a dedicated interface of ANTS2. Note that a blue filled rectangle highlights a unit called *custom*. This *unit* contain the functions I have implemented in C++ to be called in scripting mode. They are mainly related with the real-time processing and the optional reduced *chi-square* χ^2 monitoring.

It should be stressed that the GUI for acquisition could be implemented only in pure C++ using, for instance, Qt widgets and the required functions (either newly implemented functions or functions taken from ANTS2 source code, when they exist). Part of the nearly future work aims to do this. I have already C++ shell applications for pedestals calculation, .HLD files unpacking, waveform integration, etc.

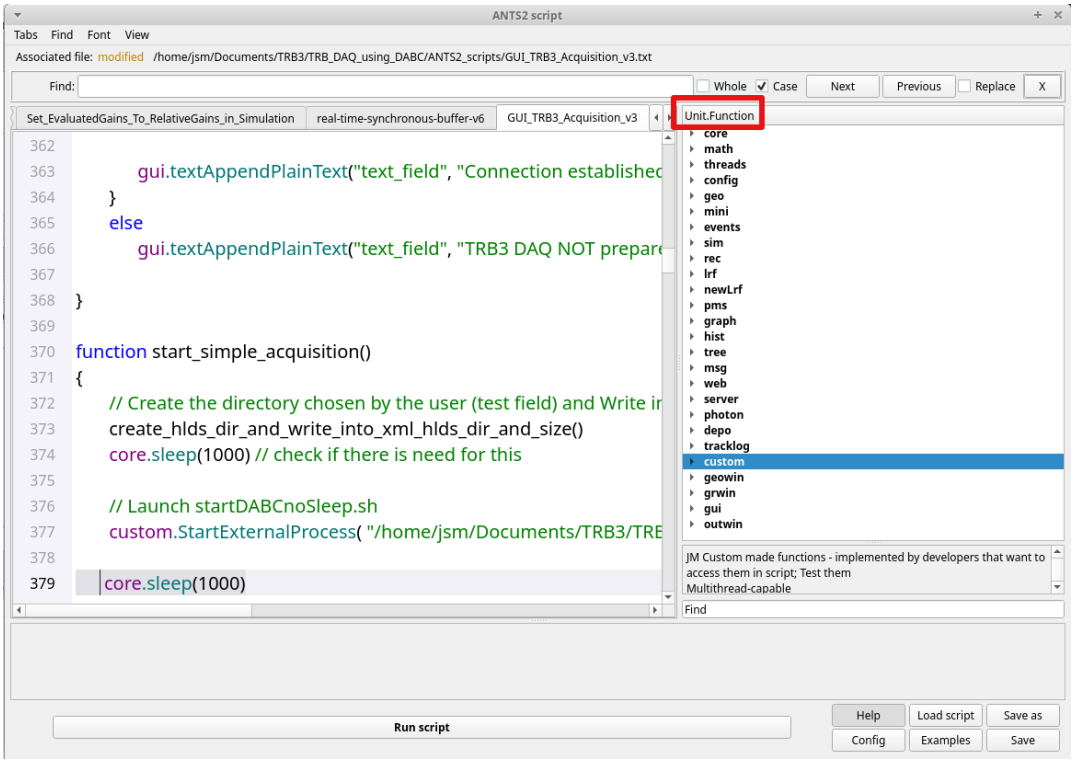

Figure F.2: Snapshot of the ANTS2 scripting environment. A red rectangle is pointing out the panel with the scripting *units*. These *units* gather C++ implemented functions related with the *unit* name. The communication between the scripting interpreter and the compiled C++ functions is performed by a dedicated interface of ANTS2.

[1]GitHub repository: https://github.com/jsmarcos/TRB3-GSI-based-DAQ.

GUI Software layers The **Fig.F.3** gives an overview of the software layers behind the GUI.

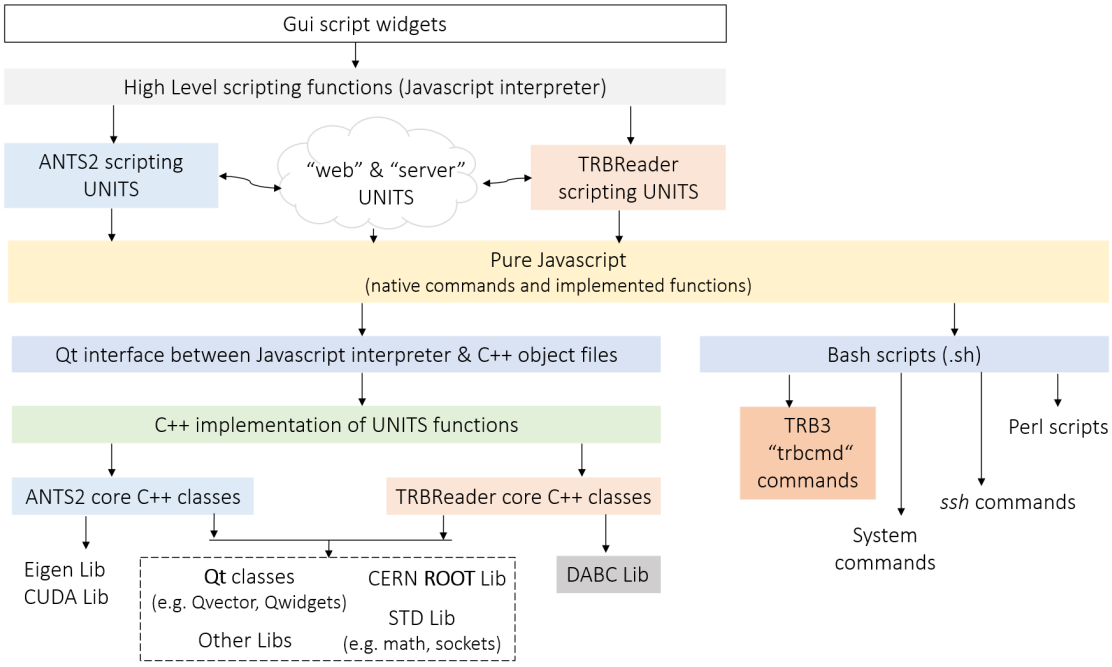

Figure F.3: Software Layers of the Acquisition GUI. The scripting ***units*** (both in ANTS2 and TRBReader) are *wrappers* for C++ implemented functions. There are several *units* common to ANTS2 and TRBReader. This diagram highlights two particular *units*, ***web*** and ***server***, responsible for the communication between ANTS2 and TRBReader. The name of other *units* can be seen in the **Fig. F.2**.

1. **High level scripts functions**

   Both TRBReader and ANTS2 packages include a scripting mode module (JavaScript). The acquisition GUI itself (**Fig.F.1**) was programmed in scripting language in the script environment of ANTS2. When some widget is activated (e.g. a button is pressed) a script function is called. Inside that functions there are native Javascript commands, call of other scripting functions and call of scripting *units*.

2. **Scripting *units***

   Units are available in ANTS2 and TRBReader scripting modules. *Unit* is the name given to a group of functions that are related with the same core modules of either ANTS2 or TRBReader (e.g: config, geo, events, sim, rec, lrf, photon, pms...). The functions in the *units* can be called in the Javascript interpreter and are *wrappers* for the C++ implementations. **Fig.F.4** shows the functions of the *unit* **sim**, which contains funtions related with the ANTS2 simulation module.

3. **Qt Javascript/C++ interface**

   Both ANTS2 and TRBReader packages have a Qt based interface between the interpreter of Javascript scripting language and C++ object files. This feature is very useful, allowing to *wraps* C++ implemented functions in *units* available in the embedded Javascript interpreter of ANTS2 and TRBReader.

4. **DABC (GSI) C++ Library**

   DABC is a C++ library developed by the TRB3 project in GSI Lab. Is has a set of functions to unpack the .HLD binary files that contain the waveforms for each SiPM, for each event. DABC functions are used by TRBReader to process the .HLD files. For instance, according to the TRBReader user configurations, each waveform is integrated and the result is saved in a .DAT file. This file contains one line per event with the result of integration for each PM separated with white spaces.

5. **Bash scripts for automation**

   Many high level scripts or functions (e.g. ANTS2 script) call bash scripts to make operations like: create directories, move and delete files, send **ssh commands** (and also bash scripts) to the TRB3 controller, send **TRB3 commands (trbcmd)** directly to TRB3 board or run **Perl scripts** to interact with the controller databases (e.g where IP addresses are specified).

6. **TRB3 commands: configuration and acquisition**

   TRB3 commands (trbcmd) are sent to the TRB3 board for configuring the hardware (FPGAs) and to start the web based control unit (configure number of samples, samples after trigger, trigger thresholds, etc., and where the acquisition can be started and stopped). Other TRB3 commands start and stop the acquisition.

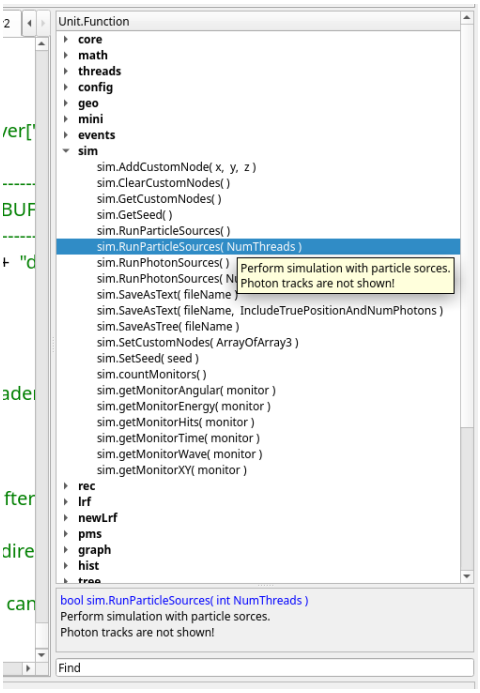

Figure F.4: Detail on the scripting *unit* called sim. The set of functions of this *unit* can be seen. An explanation of the function *RunParticleSources(NumThreads)* is written in a panel in the bottom of the window. Additionally, a tool-tip appears above the function where the cursor is placed.

References

[1] Chris Guy. *An introduction to the principles of medical imaging.* Imperial College Press, 2005. 1

[2] A. Reed R.L. Libby B. Cassen, L. Curtis. *Instrumentation for I-131 use in medical studies.* Nucleonics, 1951. 1

[3] Hal O. Anger. Scintillation camera. *Rev. of Sci. Instruments*, 1958. 1, 11

[4] Eric D. Whitman and Douglas Reintgen. *Radioguided Surgery.* Landes Bioscience, 1999. 2

[5] A. E. Giuliano edited by G. Mariani and H. W. Strauss. *Radioguided Surgery - A Comprehensive Team Approach.* Stringer, 2008. 2

[6] Gopal B. Saha. *Physics and Radiobiology of Nuclear Medicine.* Springer, 3rd edition, 2006. 2, 23, 26, 50

[7] H. H. Barrett, W. C. J. Hunter, B. W. Miller, S. K. Moore, Y. Chen and L. R. Furenlid. Maximum-likelihood methods for processing signals from gamma-ray detectors. *IEEE Trans. Nucl. Sci.*, 56: 725–735, 2009. 2, 57, 66

[8] Lars R. Furenlid Todd Peterson. SPECT detectors: the Anger Camera and beyond. *Physics in Medicine and Biology*, 56(17):145–182, 2011. doi: 10.1088/0031-9155/56/17/R01. 2, 32, 33, 65, 66, 72, 73

[9] Miyaoka R. S. *et al.* Calibration procedure for a continuous miniature crystal element (cMiCE) detector. *IEEE Nuclear Science Symp. and Medical Imaging Conf. (NSS/MIC)*, 2010. doi: 10.1109/NSSMIC.2007.4437070. 3

[10] Vladimir. N. Solovov *et al.* Position reconstruction in a dual phase xenon scintillation detector. *IEEE Transactions on nuclear sciences*, 59(6), 2012. doi: 10.1109/NSSMIC.2011.6154607. 3, 61, 62, 63, 66

[11] Andrey Morozov *et al.* Adaptive algorithms of position and energy reconstruction in anger-camera type detectors: experimental data processing in ants. *Journal of Instrumentation*, (8), 2013. doi: https://doi.org/10.1088/1748-0221/8/05/P05002. 3, 58, 62, 66

[12] Andrey Morozov *et al.* Iterative reconstruction of detector response of an anger gamma camera. *Physics in Medicine & Biology*, (60):4169–4184, 2015. doi: https://doi.org/10.1088/1748-0221/8/05/P05002. 3, 4, 58, 62, 64, 181

[13] Suzanne Amador Kane. *Introduction to Physics in Modern Medicine.* CRC Press, 2009. 11

[14] Sarah Louise Bugby. *Development of a hybrid portable medical gamma camera.* PhD thesis, University of Leicester, 2015. 13, 78

[15] Ellery Storm and Harvey I. Israel. *Photon cross sections from 1 KeV to 100 MeV for elements Z = 1 to Z = 100.* Los Alamos Scientific Laboratory, 1970. 13

[16] NIST. XCOM mass attenuation coeffients datbase. URL `https://physics.nist.gov/PhysRefData/Xcom/html/xcom1-t.html`. Accessed: 01.11.2015. 13, 91

[17] Edwin M. Leidholdt Jr. John M. Boone Jerrold T. Bushberg, J. Anthony Seibert. *The Essential Physics of Medical Imaging.* North American, 3rd edition, 2011. ISBN 978-0781780575. 14

[18] Hamamatsu Photonics K. K. *Photomultiplier tubes - Basics and Applications*, chapter 0. Hamamatsu, 2007. 15

[19] William. R. Leo. *Techniques for Nuclear and Particle Physics Experiments.* Springer, 1994. 16, 30, 46, 48

[20] Saint-Gobain. Prelude® 420 datasheet from Saint-Gobain, . URL `https://bit.ly/30DOj6W`. Accessed: 01.06.2016. 16, 17

[21] University of Florida — Department of Physics. Gamma Ray Spectroscopy - Experiment GRS. URL `http://www.phys.ufl.edu/courses/phy4803L/group_I/gamma_spec/gamspec.pdf`. Accessed: 01.12.2015. 16

[22] R.Cardarelli R. Santonico. Development of resistive plate counters. *Nuclear Instruments and Methods in Physics Research*, 187(Issues 2-3):377–380, 1981. doi: 10.1016/0029-554X(81)90363-3. 17

[23] Crespo P., Blanco A., Couceiro M. *et al.* Resistive plate chambers in positron emission tomography. *The European Physical Journal Plus*, 2013. doi: 10.1140/epjp/i2013-13073-5. 17

[24] Alexander I. Lvovsky. Fresnel equations. *Encyclopedia of Optical Engineering*, 2013. doi: http://dx.doi.org/10.1081/E-EOE-120047133. 19, 20, 21

[25] Sophocles J. Orfanidis. *Electromagnetic Waves and Antennas.* ECE Department Rutgers University, 2008. 20

[26] Alma E. F. Taylor. *Illumination fundamentals.* Lighting Research Center, Rensselaer Polytechnic Institute, 2000. 22

[27] Illuminating Engineering Society of North America. *IESNA Lighting Handbook.* Illuminating Engineering; 9 edition, 2000. ISBN 978-0879951504. 22

[28] Edited by Béla Kári. Structure of gamma cameras. URL `http://oftankonyv.reak.bme.hu/tiki-index.php?page=Structure+of+Gamma+Cameras`. Accessed: 01.06.2016. 24

[29] James A. Sorenson Simon R. Cherry and Michael E. Phelps. *Physics in Nuclear Medicine.* Elsevier Inc, 4th Edition, 2012. ISBN 978-1-4160-5198-5. 24, 25, 26, 50

[30] Hal O. Anger. Scintillation camera with multichannel collimator. *Journal of nuclear medicine*, 5 (7):515–531, 1964. 24, 26, 27

[31] Mark S. Gerber and Don W. Miller. Parallel-hole, collimator design. *The Journal of Nuclear Medicine*, 15(8):724–725, 1974. 25

[32] E. Russell Ritenour William R. Hendee. *Medical imaging physics.* Wiley-Liss, 4th edition, 2002. 26

[33] Cecchin D., Poggiali D., Riccardi L., Turco P., Bui F. and De Marchi S. Analytical and experimental FWHM of a gamma camera: theoretical and practical issues. *PeerJ 3:e722*, 2015. doi: https://doi.org/10.7717/peerj.722. 26

[34] Michael E. Phelps James A. Sorenso. *Physics inNuclear Medicine*. Grune and Stratton, New York, 1987. 27

[35] Donald L. Gunter. *Emission Tomography -The Fundamentals of PET and SPECT*, chapter 8 - Collimator Design for Nuclear Medicine. Elsevier Inc., 2004. 27

[36] Amanda L. Weinmann, Carrie B. Hruska and Michael K. O'Connor. Design of optimal collimation for dedicated molecular breast imaging systems. *Medical Physics*, 36(3):845–856, 2009. doi: https://doi.org/10.1118/1.3077119. 27

[37] Van Audenhaege, Van Holen R., Vandenberghe S., Vanhove C., Metzler S.D. and Moore S.C. Review of SPECT collimator selection, optimization, and fabrication for clinical and preclinical imaging. *Medical Physics*, 42(8):4796–813, 2015. doi: 10.1118/1.4927061. 28, 29, 30

[38] David Paix. Pinhole imaging of gamma rays. *Physics in medicine and biology*, 1967. doi: DOI:10.1088/0031-9155/12/4/004. 28, 29

[39] Metzler S.D., Bowsher J.E., Smith M.F. and Jaszczak R.J. Analytic determination of pinhole collimator sensitivity with penetration. *IEEE Trans. Med. Imaging*, 20(8):730–41, 2001. 28

[40] Van Der Have F., Vastenhouw B., Ramakers R. M., Branderhorst W., Krah J.O., Ji C., Staelens S.G. and Beekman F.J. U-SPECT-II: An ultra-high-resolution device for molecular small-animal imaging. *The Journal of Nuclear Medicine*, 50:599–605, 2009. 29

[41] Miller B.W., Furenlid L.R., Moore S.K., Barber H.B., Nagarkar V.V. and Barrett H. System integration of FastSPECT III, a dedicated SPECT rodent-brain imager based on BazookaSPECT detector technology. *IEEE Nuclear Science Symposium Conference Record*, page 4004–4008, 2009. 29

[42] Lin K., Hsiao I.T., Wietholt C. *et al.* Performance evaluation of an animal SPECT using modified NEMA standards. *The Journal of Nuclear Medicine*, 49, 2008. 29

[43] Schramm N., Ebel G., Engeland U., Schurrat T., Behe M. and Behr T. High-resolution SPECT using multipinhole collimation. *IEEE Trans. Nucl. Sci.*, 50:315–320, 2003. doi: 10.1109/TNS.2003.812437. 29

[44] J. Bae *et al.* Experimental evaluation of a multi-pinhole collimator for a small organ by using a small-field-of-view gamma camera. *Journal of the Korean Physical Society*, 70(4):416–423, 2017. doi: 10.3938/jkps.70.416. 29

[45] Saint-Gobain. Prelude® 420 datasheet from Saint-Gobain (engineered version), . URL `https://www.crystals.saint-gobain.com/sites/imdf.crystals.com/files/documents/lyso-material-data-sheet.pdf`. Accessed: 01.06.2019. 31

[46] K. Deprez, R. Van Holen and S. Vandenberghe. A high resolution SPECT detector based on thin continuous LYSO. *Phys. Med. Biol.*, 59, 2014. 31, 78, 216

[47] Alva-Sánchez H., Zepeda-Barrios A., Díaz-Martínez V.D., Murrieta-Rodríguez T., Martínez-Dávalos A. and Rodríguez-Villafuerte M. Understanding the intrinsic radioactivity energy spectrum from 176Lu in LYSO/LSO scintillation crystals. *Nature - Scientific report*, 8, 2018. doi: doi:10.1038/s41598-018-35684-x. 32, 83

[48] Qingyang Wei *et al.* Measure PET detector performance with the intrinsic radioactivity of scintillator. *IEEE Nuclear Science Symposium and Medical Imaging Conference Record (NSS/MIC)*, Date of Conference: 27 Oct.-3 Nov. 2012, . doi: ElectronicISBN:978-1-4673-2030-6. 32

[49] Andrew George Stewart et al. Energy resolution of Ce:GAGG and Pr:LuAG scintillators coupled to 3mm x 3mm silicon photomultipliers. *IEEE Transactions on Nuclear Science*, 63(Issue 5): 2496–2501, 2016. doi: 10.1109/TNS.2016.2574773. 32

[50] Marco T. Lucchini *et al.* Effect of Mg2+ ions co-doping on timing performance and radiation tolerance of Cerium doped $Gd_3Al_2Ga_3O_{12}$ crystals. *Nuclear Instruments and Methods in Physics Research A*, 816:176–183, 2016. doi: 10.1016/j.nima.2016.02.004. 32, 95

[51] Pawel Sibczynski *et al.* Characterization of some modern scintillators recommended for use on large fusion facilities in gamma-ray spectroscopy and tomographic measurements of gamma-emission profiles. *NUKLEONIKA*, 62(3):223–228, 2017. doi: 0.1515/nuka-2017-0032. 32, 93

[52] Jung Yeol Yeom *et al.* First Performance Results of Ce:GAGG Scintillation Crystals With Silicon Photomultipliers. *IEEE Transactions on Nuclear Science*, 60(2), 2013. doi: 10.1109/TNS.2012.223349. 32

[53] Stuart R. Miller *et al.* Recent advances in columnar CsI(TI) scintillator screens. *Proceedings of SPIE - The International Society for Optical Engineering*, 2005. doi: 10.1117/12.625927. 32

[54] Dalin Yao *et al.* Fabrication and Performance of CsI(Tl) Scintillation Films With Pixel-Like Columnar-Matrix Structure. *IEEE Transactions on Nuclear Science*, 2005. doi: 10.1109/TNS.2015.2391197. 32

[55] Dalin Yao *et al.* Recent Advances in SPECT Imaging. *Journal of Nuclear Medicine*, 48:661–673, 2007. doi: 10.2967/jnumed.106.032680. 32, 65

[56] Habib Zaidi and Rameshwar Prasad. Advances in multimodality molecular imaging. *J Med Phys.*, 34(3):122–128, 2009. doi: 10.4103/0971-6203.54844. 32

[57] Steven R Meikle. Small animal SPECT and its place in the matrix of molecular imaging technologies. *Physics in Medicine and Biology*, 50(22), 2005. doi: 10.1088/0031-9155/50/22/R01. 32, 65, 69

[58] G. Konstantinou. Subsurface laser engraving techniques for scintillator crystals: Methods, applications, and advantages. *IEEE TRANSACTIONS ON RADIATION AND PLASMA MEDICAL SCIENCES*, 1(5), 2017. doi: 10.1109/TRPMS.2017.2714265. 32, 33

[59] G. Konstantinou. Light spread manipulation in scintillators using laser induced optical barriers. *IEEE Trans Nucl Sci.*, 65(8):2208–2215, 2018. doi: 10.1109/TNS.2018.2809570. 33

[60] Sabet H., Bläckberg L., Uzun Oszahin D. and El Fakhri G. Novel laser-processed CsI:Tl detector for SPECT. *Medical physics*, 43(5):2630–2638, 2016. doi: g/10.1118/1.4947294. 33

[61] Carel W. E. van Eijk. Inorganic scintillators in medical imaging detectors. *Phys. Med. Biol.*, 47, 2012. 33

[62] Jennifer Prekeges. *Nuclear Medicine Instrumentation.* Jones and Bartlett Publishers, 2nd edition, 2013. 33, 50

[63] Hamamatsu. Photomultiplier tubes - basics and applications, . URL `https://www.hamamatsu.com/resources/pdf/etd/PMT_handbook_v3aE.pdf`. Accessed: 05.09.2019. 33, 36, 37

[64] Hamamatsu. A technical guide to silicon photomultipliers (MPPC) - Section 1, . URL https://hub.hamamatsu.com/us/en/technical-note/sipm-mppc-technical-note/section1.html. Accessed: 05.09.2019. 33

[65] SensL. An introduction to the silicon photomultiplier - technical note, . URL https://bit.ly/3amNPa1. Accessed: 01.06.2016. 33, 37, 38, 39, 40, 41, 97

[66] SensL. How to evaluate and compare silicon photomultiplier sensors - white paper, . URL http://sensl.com/downloads/ds/WP-Evaluate_and_Compare_SiPM.pdf. Accessed: 20.07.2019. 33

[67] K. Lung *et al.* Characterization of the Hamamatsu R11410-10 3-Inch Photomultiplier Tube for Liquid Xenon Dark Matter Direct Detection Experiments. *Nucl.Instrum.Meth.*, pages 32–39, 2012. doi: 10.1016/j.nima.2012.08.052. 36

[68] AdvanSiD Advanced Silicon Detectors. Application note - Introduction to SiPMs, 2014. URL http://advansid.com/attachment/get/up_89_1411030571.pdf. Accessed: 01.08.2019. 37, 38

[69] Shi Feng *et al.* Comparative studies of silicon photomultipliers and traditional vacuum photomultiplier tubes. *Chinese Physics C*, 35(1), 2011. 39

[70] Chistoph Hoeschen Marie Claire Cantone. *Radiation physics for nuclear medicine.* Springer, 2011. 41

[71] Elektroarsenal.net - biomedical enginneering. URL http://elektroarsenal.net/category/biomedical-engineering/page/27. Accessed: 01.06.2016. 43

[72] Planet Analog. Understand and apply the transimpedance amplifier. URL https://www.planetanalog.com/understand-and-apply-the-transimpedance-amplifier-part-1-of-2/. Accessed: 01.06.2016. 44

[73] A. J. Boston (University of Liverpool). Pulse timing system - nuclear instrumentation: Lecture 5. URL http://ns.ph.liv.ac.uk/~ajb/ukgs_nis/pre-course-material/lec5-03.pdf. Accessed: 01.06.2016. 45

[74] ORTEC company. Fast-timing discriminator introduction. URL www.ortec-online.com/download/fast-timing-discriminator-introduction.pdf. Accessed: 01.06.2016. 45

[75] PhysWiki. Spatial resolution. URL http://physwiki.apps01.yorku.ca. Accessed: 01.06.2016. 50

[76] GE Healthcare. CZT Technology: Fundamentals and Applications - White paper. URL https://bit.ly/3axuy5V. Accessed: 05.09.2019. 50

[77] AAPM. Computer-aided scintillation camera acceptance testing, AAPM report n^{o} 9. URL https://www.aapm.org/pubs/reports/rpt_09.pdf. Accessed: 01.06.2016. 52, 54

[78] Edited by Habib Zaidi. *Molecular Imaging of Small Animals: Instrumentation and Applications.* Stringer, 2014. 54

[79] Medimaging. URL http://www.medimaging.gr. Accessed: 01.06.2016. 54

[80] Medphysics. URL http://www.medphysics.wisc.edu. Accessed: 01.06.2016. 54

[81] M. A. Alkhorayef *et al.* Toward standardising gamma camera quality control procedures. *Radiation Physics and Chemistry*, 116:95–99, 2015. doi: 10.1016/j.radphyschem.2015.05.016. 54

[82] National Electrical Manufacturers Association. NEMA Standards Publication NU 1-2007, 2007. URL https://www.nema.org/Standards/Pages/Performance-Measurements-of-Gamma-Cameras.aspx. Accessed: 01.08.2019. 55, 179, 203

[83] V. Solovov, A. Morozov, V. Chepel, V. Domingos and R. Martins. B-spline parameterization of spatial response in a monolithic scintillation camera. *J. Instrum.*, 11, 2016. 57, 58, 64

[84] Albert Macovski Robert M. Gray. Maximum a posteriori estimation of position in scintillation cameras. *IEEE Transactions on Nuclear Science*, 23(1):849–852, 1976. doi: 10.1109/TNS.1976.4328354. 58, 60

[85] Andrey Morozov *et al.* Iterative reconstruction of SiPM light response functions in a square-shaped compact gamma camera. *Physics in Medicine & Biology*, (62):3619–3638, 2017. doi: https://doi.org/10.1088/1361-6560/aa6029. 58, 64, 67, 158, 222

[86] Jason Philip Brodsky. *xy Position Reconstruction in DarkSide-50.* PhD thesis, Princeton University, 2015. 61

[87] B. Borchers R. Aster and C. Thurber. *Parameter Estimation and Inverse Problems.* Elsevier Inc., 2nd edition, 2013. 61

[88] J.A. Nelder and R. Mead. A simplex method for function minimization. *The Computer Journal*, 7(4):308–313, 1965. doi: 10.1093/comjnl/7.4.308. 61

[89] George B. Dantzig. *A history of scientific computing*, chapter Origins of the Simplex Method. ACM New York, 1987. 61

[90] Britannica. Simplex method. URL https://www.britannica.com/science/optimization/The-simplex-method. Accessed: 01.09.2019. 61

[91] ROOT math library team. Minuit package. URL http://project-mathlibs.web.cern.ch/project-mathlibs/sw/5_10/Minuit2/html/index.html. Accessed: 01.09.2019. 61

[92] F. James and M. Roos (CERN). Minuit: A system for function minimization and analysis of the parameter errors and correlations. *Comput.Phys.Commun.*, 10(4):343–367, 1975. doi: 10.1016/0010-4655(75)90039-9. 61

[93] Bouckaert C., Vandenberghe S. and Van Holen R. Evaluation of a compact, high-resolution SPECT detector based on digital silicon photomultipliers. *Phys Med Biol.*, 59(23):7521–39, 1975. doi: 10.1088/0031-9155/59/23/7521. 62, 215

[94] Andrey Morozov *et al.* ANTS2 package: simulation and experimental data processing for Anger camera type detectors. *Journal of Instrumentation*, 11, 2016. 64, 87, 88, 89

[95] Humm J.L., Rosenfeld A. and Del Guerra A. From PET detectors to PET scanners. *Eur J Nucl Med Mol Imaging*, 30(11):1574–97, 2003. doi: 10.1007/s00259-003-1266-2. 64

[96] Peremans K., Cornelissen B., Van Den Bossche B., Audenaert K. and Van de Wiele C. A review of small animal imaging planar and pinhole spect gamma camera imaging. *Vet. Radiol. Ultrasound*, 46(2):162–70, 2005. doi: 0.1111/j.1740-8261.2005.00031.x. 64

[97] Omgo E. Nieweg Edited by: Ken Herrmann and Stephen P. Povoski. *Radioguided Surgery - Current Applications and Innovative Directions in Clinical Practice.* Stringer, 2016. ISBN 3319260499. 65, 73, 75

[98] Nathan C. Hall *et al.* Intraoperative scintigraphy using a large field-of-view portable gamma camera for primary hyperparathyroidism: Initial experience. *BioMed Research International*, 2015. doi: 10.1155/2015/930575. 65

[99] Benjamin L. Franc *et al.* Small-Animal SPECT and SPECT/CT: Important Tools for Preclinical Investigation. *J Nucl Med*, 49(10):1651–1663, 2008. doi: 10.2967/jnumed.108.055442. 65

[100] Eric J. Meester *et al.* Perspectives on small animal radionuclide imaging; considerations and advances in atherosclerosis. *Front Med (Lausanne)*, 6(39), 2019. doi: 10.3389/fmed.2019.00039. 65

[101] Ling Han *et al.* System Calibration for FastSPECT III: An Ultra-High Resolution CCD-Based Pinhole SPECT System. *2017 IEEE Nuclear Science Symposium and Medical Imaging Conference (NSS/MIC)*, 2017. doi: 10.1109/NSSMIC.2017.8533027. 65

[102] J. Mejia *et al.* Performance assessment of the single photon emission microscope: high spatial resolution SPECT imaging of small animal organs. *Braz J Med Biol Res.*, 46(11):936–942, 2013. doi: 10.1590/1414-431X20132764. 65

[103] Umeda I.O., Tani K., Tsuda K. *et al.* High resolution SPECT imaging for visualization of intratumoral heterogeneity using a SPECT/CT scanner dedicated for small animal imaging. *Ann. Nucl. Med.*, 26(67), 2012. doi: 10.1007/s12149-011-0542-7. 65

[104] Eric P. Visser *et al.* Image quality phantom and parameters for high spatial resolution small-animal SPECT. *Nuclear Instruments and Methods in Physics Research A*, 654(1):539–545, 2011. doi: 10.1016/j.nima.2011.06.036. 65

[105] Benjamin L. Franc *et al.* Small-Animal SPECT and SPECT/CT: Important Tools for Preclinical Investigation. *J. Nucl. Med.*, 49(10):1651–1663, 2018. doi: 10.2967/jnumed.108.055442. 65

[106] Funk T., Després P., Barber W.C., Shah K.S. and Hasegawa B.H. A multipinhole small animal SPECT system with submillimeter spatial resolution. *Med Phys.*, 33(5):1259–1268, 2006. doi: 10.1118/1.2190332. 65

[107] Wenze Xi *et al.* Maximum likelihood positioning of scintillation events: Preliminary experiments. *IEEE Nuclear Science Symposium Conference Record*, 2004. doi: 10.1109/NSSMIC.2007.4436950. 66

[108] D.W. Wilson, H.H. Barrett and E.W. Clarkson. Maximum likelihood positioning of scintillation events: Preliminary experiments. *IEEE Trans Med Imaging.*, 19(5), 2000. doi: 10.1109/42.870252. 66

[109] Lerche C.W., Salomon A., Goldschmidt B., Lodomez S., Weissler B. and Solf T. Maximum likelihood positioning and energy correction for scintillation detectors. *Phys Med Biol.*, 61(4):1650–1676, 2000. doi: 10.1088/0031-9155/61/4/1650. 66

[110] M. Morrocchi *et al.* Evaluation of event position reconstruction in monolithic crystals that are optically coupled. *Phys Med Biol.*, 61(23):8298–8320, 2016. doi: 10.1088/0031-9155/61/23/8298. 66

[111] P. Garcia de Acilu. Study and optimization of positioning algorithms for monolithic PET detectors blocks. *JINST - The 9^{th} international conference on position sensitive detectors*, 2011. 67

[112] Marnix C. Maas *et al.* Monolithic scintillator PET detectors with intrinsic depth-of-interaction correction. *Physics in Medicine and Biology*, 54(7), 2011. 67

[113] P. Bruyndonckx, S. Leonard, S. Tavernier *et al.* Neural network-based position estimators for pet detectors using monolithic lso blocks. *IEEE Transactions on Nuclear Science*, 51(5):2520–2525, 2004. doi: 10.1109/TNS.2004.835782. 67

[114] Samuel España *et al.* Fast calibration of SPECT monolithic scintillation detectors using uncollimated sources. *Phys. Med. Biol.*, 58:4807–4825, 2013. doi: 10.1088/0031-9155/58/14/4807. 67, 68

[115] Giacomo Borghi *et al.* A 32 mm × 32 mm × 22 mm monolithic LYSO:Ce detector with dual-sided digital photon counter readout for ultrahigh-performance TOF-PET and TOF-PET/MRIs. *Phys. Med. Biol.*, 61:4929–4949, 2016. doi: 10.1088/0031-9155/61/13/4929. 67

[116] Alexei Ulyanov *et al.* Localisation of gamma-ray interaction points in thick monolithic $CeBr_3$ and $LaBr_3$:Ce scintillators. *Nuclear Instruments and Methods in Physics Research Section A Accelerators Spectrometers Detectors and Associated Equipment*, 844, 2018. doi: 10.1016/j.nima.2016.11.025. 67

[117] J.E. Lees, D.J. Bassford, O.E. Blake, P.E. Blackshaw and A.C. Perkins. Optimization of large-angle pinhole collimator for environmental monitoring system. *IEEE Transactions on Nuclear Science*, 57(3), 2010. 69, 70

[118] Yujin Qi. Optimized collimator designs for small animal SPECT imaging with a compact gamma camera. In *Proceedings of the 2005 IEEE Engineering in Medicine and Biology 27th Annual Conference*, pages 1780–1782. IEEE, 2005. 69, 70, 132

[119] Hyun-Woo Jeong *et al.* A numerical study of different types of collimators for a high-hesolution preclinical CdTe pixelated semiconductor SPECT system. *Journal of the Optical Society of Korea*, 20(6):663–668, 2016. doi: 10.3807/JOSK.2016.20.6.663. 71, 72

[120] Jaekeon Bae *et al.* Experimental evaluation of a multi-pinhole collimator for a small organ by using a small-field-of-view gamma camera. *Journal of the Korean Physical Society*, 70(4):416–423, 2017. 71, 86

[121] M.C.M. Rentmeester *et al.* Optimizing multi-pinhole SPECT geometries using an analytical model. *Physics in Medicine and Biology*, 52(9):2567–2581, 2007. doi: 10.1088/0031-9155/52/9/016. 71

[122] J.P. Islamian *et al.* Advances in pinhole and multi-pinhole collimators for single photon emission computed tomography imaging. *World J Nucl Med.*, 14(1):3–9, 2015. doi: 10.4103/1450-1147.150505. 71

[123] Zixiong Cao *et al.* Optimal number of pinholes in multi-pinhole SPECT for mouse brain imaging - A simulation study. *Physics in Medicine and Biology*, 50(19):4609–4624, 2015. doi: 10.1088/0031-9155/50/19/013. 71

[124] Marlies C. Goorden *et al.* VECTor: A Preclinical Imaging System for Simultaneous Submillimeter SPECT and PET. *J Nucl Med*, 54(2):306–312, 2015. doi: 10.2967/jnumed.112.109538. 71

[125] Ricardo M. Capote *et al.* Optimization of convergent collimators for pixelated SPECT systems. *Nuclear Medicine Physics*, 40(6), 2013. doi: 10.1118/1.4804053. 71

[126] Koichi Ogawa and Masaaki Muraishi. Feasibility Study on an Ultra-High-Resolution SPECT With CdTe Detectors. *IEEE Transactions on Nuclear Science*, 57(1):17–24, 2013. doi: 10.1109/TNS.2009.2034460. 71

[127] Francesco Giammarile *et al.* The EANM and SNMMI practice guideline for lymphoscintigraphy and sentinel node localization in breast cancer. *Eur J Nucl Med Mol Imaging*, 40(12):1932–1947, 2013. doi: 10.1007/s00259-013-2544-2. 72

[128] Makoto Tsuchimochi and Kazuhide Hayama. Intraoperative gamma cameras for radioguided surgery: Technical characteristics, performance parameters, and clinical applications - review paper. *Physica Medica*, 29(2):126–138, 2013. doi: 10.1016/j.ejmp.2012.05.002. 72

[129] T. Oda, K. Hayama and M. Tsuchimochi. Evaluation of small semiconductor gamma camera–simulation of sentinel lymph node biopsy by using a trial product of clinical type gamma camera. *Physica Medica*, 46(1):1–12, 2009. 72

[130] Edited by Alan Perkins and John E. Lees. *Gamma Cameras for Interventional and Intraoperative Imaging*. Series in Medical Physics and Biomedical Engineering. CRC Press, 2017. 72

[131] R. Pani *et al.* Recent advances and future perspectives of gamma imagers for scintimammography. *Nuclear Instruments and Methods in Physics Research, Section A: Accelerators, Spectrometers, Detectors and Associated Equipment*, 569(2):296–300, 2016. doi: 10.1016/j.nima.2006.08.024. 72

[132] Bricou A., Duval M.A., Charon Y. and Barranger E. Mobile gamma cameras in breast cancer care - a review. *European journal of surgical oncology*, 39(5):409–416, 2013. 73

[133] More M.J., Goodale P.J., Majewski S. and Williams M.B. Evaluation of gamma cameras for use in dedicated breast imaging. *IEEE Transactions on Nuclear Science*, 53(5-1):2675–2679, 2016. doi: 10.1109/TNS.2006.876003. 73

[134] Soluri A., Scafè R., Falcini F. *et al.* New localization technique for breast cancer biopsy: mammotome guidance with imaging probe. *Tumori*, 88(3):37–39, 2002. 73

[135] Peter D. Olcott *et al.* Clinical evaluation of a novel intraoperative handheld gamma camera for sentinel lymph node biopsy. *Physica Medica*, 30(3):340–345, 2014. doi: 10.1016/j.ejmp.2013.10.005. 74, 86, 217

[136] Elgin Ozkan and Aydan Erogl. The utility of intraoperative handheld gamma camera for detection of sentinel lymph nodes in melanomay. *Nucl Med Mol Imaging.*, 49(4):318–320, 2015. doi: 10.1007/s13139-015-0341-5. 74

[137] Zanzonico P. Heller S. Nuclear probes and intraoperative gamma cameras. *Semin Nucl Med*, 41:166–181, 2011. doi: 10.1053/j.semnuclmed.2010.12.004. 74

[138] Joaquin Ortega *et al.* Potential role of a new hand-held miniature gamma camera in performing minimally invasive parathyroidectomy. *Eur J Nucl Med Mol Imaging*, 34:165–169, 2007. doi: 10.1007/s00259-006-0239-7. 74

[139] Kosta Popovic *et al.* Development and characterization of a round hand-held silicon photomultiplier based gamma camera for intraoperative imaging. *IEEE Trans Nucl Sci.*, 61(3):1084–1091, 2014. doi: 10.1109/TNS.2014.2308284. 74, 78, 86, 214

[140] Mohammed Saeed M. Alqahtani. *Assessment of a novel small field of view medical hybrid gamma camera*. PhD thesis, University of Leicester, 2017. 75

[141] Kouhei Nakanishi *et al.* Performance comparison of finely pixelated LYSO- and GAGG-based Si-PM gamma cameras for high resolution SPECT. *Nuclear Instruments and Methods in Physics Research Section A: Accelerators, Spectrometers, Detectors and Associated Equipment*, 872:107–111, 2017. doi: 10.1016/j.nima.2017.08.013. 78, 213

[142] T. Fujita *et al.* Two-dimensional diced scintillator array for innovative, fine-resolution gamma camera. *Nuclear Instruments and Methods in Physics Research Section A: Accelerators, Spectrometers, Detectors and Associated Equipment*, 765:262–268, 2014. doi: 10.1016/j.nima.2014.04.060. 78, 214

[143] Andrew L. Goertzen *et al.* Characterization of a handheld gamma camera for intraoperative use for sentinel lymph node biopsy. *IEEE Nuclear Science Symposium conference record. Nuclear Science Symposium*, 2013. doi: 10.1109/NSSMIC.2013.6829332. 78, 86, 215

[144] Lucia Riccardi *et al.* Assessing good operating conditions for intraoperative imaging of melanoma sentinel nodes by a portable gamma camera. *Physica Medica*, 31(1):92–97, 2015. doi: 10.1016/j.ejmp.2014.10.079. 78

[145] Mathelin C. *et al.* A new intraoperative gamma camera for the sentinel lymph node procedure in breast cancer. *Anticancer*, 28(5B):2859–2864, 2008. 78

[146] Peter D. Olcott. Performance characterization of a miniature, high sensitivity gamma ray camera. *IEEE Transactions on Nuclear Science*, 54(5), 2007. 78

[147] Digirad. 2020tc imager: flexible single-head gamma camera. URL `https://www.digirad.com/download/2020tc_s.pdf`. Accessed: 01.10.2019. 78

[148] A. Ferretti *et al.* Phantom study of a new hand-held gamma-imaging probe for radio-guided surgery. *Nucl Med Commun*, 34(1):86–90, 2013. 78

[149] Moji V. *et al.* Performance evaluation of a newly developed high-resolution, dual-head animal SPECT system based on the NEMA NU1-2007 standard. *Appl Clin Med Phys.*, 15(6), 2014. doi: 10.1120/jacmp.v15i6.4936. 78, 217

[150] Kim J.H. *et al.* Development of a miniature scintillation camera using an NaI(Tl) scintillator and PSPMT for scintimammography. *Phys Med Biol.*, 45(11):3481–3488, 2000. 78, 216, 217

[151] A. Abe *et al.* Performance evaluation of a hand-held, semiconductor (CdZnTe)-based gamma camera. *Eur J Nucl Med Mol Imaging*, 30(6):805–811, 2003. 78

[152] Makoto Tsuchimochi *et al.* A prototype small CdTe gamma camera for radioguided surgery and other imaging applications. *Eur J Nucl Med Mol Imaginga*, 30(12):1605–1614, 2003. doi: 10.1007/s00259-003-1301-3. 78

[153] Crystal Photonics. Handheld USB-Gamma Camera CrystalCam. URL `https://crystal-photonics.com/enu/products/cam-crystalcam--enu.htmf`. Accessed: 01.09.2019. 78

[154] Euro Medical Instruments. Technical data - MiniCam II. URL `https://www.gammadata.se/assets/Uploads/minicam2.2.pdf`. Accessed: 01.09.2019. 78

[155] Mitsuru Koizumi *et al.* Sentinel node detection using 99mTc-rhenium sulphide colloid in breast cancer patients: Evaluation of 1 day and 2 day protocols, and a dose-finding study. *Nuclear Medicine Communications*, 24(6):663–670, 2003. doi: 10.1097/01.mnm.0000075195.18521.53. 81

[156] Dodia N., El-Sharief D. and Kirwan CC. The use of isotope injections in sentinel node biopsy for breast cancer: are the 1- and 2-day protocols equally effective? *SpringerPlus*, 15(4):495, 2015. doi: 10.1186/s40064-015-1314-y. 81

[157] L. Swiderski *et al.* Non-proportionality of electron response and energy resolution of compton electrons in scintillators. *IEEE Transactions on Nuclear Science*, 59(1):222–229, 2012. doi: 10.1109/TNS.2011.2175407. 83, 93

[158] Junhua Luo and Xiangzhong Kong. Half-life of ^{176}Lu. *Applied Radiation and Isotopes*, 64: 588–590, 2006. doi: 10.1016/j.apradiso.2005.11.013. 83

[159] SensL. C-series low noise, blue-sensitive silicon photomultipliers - datasheet, . URL `http://www.sensl.com/downloads/ds/DS-MicroCseries.pdf`. Accessed: 01.06.2016. 84, 97, 98

[160] Hamamatsu. MPPC array - S13361-3050 series, . URL `https://www.hamamatsu.com/resources/pdf/ssd/s13361-3050_series_kapd1054e.pdf`. Accessed: 05.09.2019. 84

[161] AdvanSiD. Hybrid TD Arrays NUV-SiPMs. URL `http://advansid.com/attachment/get/up_57_1432820427.pdf`. Accessed: 05.09.2019. 84

[162] S. L. Bugby *et al.* Characterisation of a high resolution small field of view portable gamma camera. *Physica Medica*, 30(3):331–339, 2014. doi: 10.1016/j.ejmp.2013.10.004. 86

[163] Maria DaCosta *et al.* Comparison of 4 different gamma cameras in pinhole collimator imaging of a thyroid phantom with I-131 and Tc-99m. *J. Nucl. Med.*, 53(1):2535, 2012. 86

[164] M.B. Williams *et al.* Investigation of efficiency and spatial resolution using pinholes with small pinhole angle. *IEEE Transactions on Nuclear Science*, 50(5):1562–1568, 2003. doi: 10.1109/TNS.2003.817317. 86

[165] Tomas M.B., Pugliese P.V., Tronco G.G. *et al.* Pinhole versus parallel-hole collimators for parathyroid imaging: an intraindividual comparisone. *J. Nucl. Med. Technol.*, 36(4):189–194, 2008. doi: 10.2967/jnmt.108.055640. 86

[166] Ghanem M.A., Elgazzar A.H., Elsaid M.M. and Shehab F. Comparison of pinhole and high-resolution parallel-hole imaging for nodular thyroid disease. *Clin. Nucl. Med.*, 36(9):770–771, 2011. doi: 10.1097/RLU.0b013e318219ac29. 86

[167] D. Potgieter. Comparison of thyroid image quality for pinhole and parallel hole collimators: A phantom study. *Physica Medica*, 32(2):150–151, 2016. doi: 10.1016/j.ejmp.2016.07.039. 86

[168] F. Sanchez *et al.* Design and tests of a portable mini gamma camera. *Medical Physics*, 31(6): 1384–1397, 2011. doi: 10.1118/1.1755570. 86

[169] Mark F. Smith *et al.* Optimizing pinhole and parallel hole collimation for scintimammography with compact pixellated detectors. *IEEE Transactions on Nuclear Science*, 50(3):321–326, 2003. doi: 10.1109/TNS.2003.812436. 86

[170] CERN. GDML user's guide. URL `http://lcgapp.cern.ch/project/simu/framework/GDML/doc/GDMLmanual.pdf`. Accessed: 01.06.2016. 87

[171] S. Agostinelli *et al.* (GEANT4 Collaboration). Geant4 — a simulation toolkit. *Nucl.Instrum.Meth.*, 506:250–303, 2003. doi: 10.1016/S0168-9002(03)01368-8. 88

[172] J. Allison *et al.* (GEANT4 Collaboration). Geant4 developments and applications. *IEEE Transactions on Nuclear Science*, 53(1):270–278, 2006. doi: 10.1109/TNS.2006.869826. 88

[173] J. Allison *et al.* (GEANT4 Collaboration). Recent developments in GEANT4. *Nucl.Instrum.Meth.*, 835:186–225, 2016. doi: 10.1016/j.nima.2016.06.125. 88

[174] Geant4 collaboration. Geant4 - a simulation toolkit — Overview, . URL `https://geant4.web.cern.ch/`. Accessed: 01.06.2016. 88

[175] Geant4 collaboration. Geant4 physics manual, . URL `http://geant4-userdoc.web.cern.ch/geant4-userdoc/UsersGuides/PhysicsReferenceManual/fo/PhysicsReferenceManual.pdf`. Accessed: 01.09.2019. 88

[176] Geant4 collaboration. Geant4 physics list guide, . URL `http://geant4-userdoc.web.cern.ch/geant4-userdoc/UsersGuides/PhysicsListGuide/html/physicslistguide.html`. Accessed: 01.09.2019. 88

[177] Geant4 collaboration. Geant4 deexcitation, . URL `https://twiki.cern.ch/twiki/bin/view/Geant4/LoweAtomicDeexcitation`. Accessed: 01.09.2019. 88

[178] Raimundo Miguel O. Martins. Optimization of a compact medical gamma camera. Master's thesis, Universidade de Coimbra, www.uc.pt, July 2016. 89, 117

[179] Luís Pereira *et al.* Emulation workbench for position sensitive gaseous scintillation detectors. *Journal of Instrumentation*, 10, 2015. 89

[180] LNHB-KRI / C.Morillon, M.M. Bé, V. Chechev and A. Egorov. LNE – LNHB/CEA Table de Radionucleides: Nucleide ^{99m}Tc. URL `http://www.nucleide.org/DDEP_WG/Nuclides/Tc-99m_tables.pdf`. Accessed: 01.08.2019. 90

[181] Nucleonica. Reduced decay schemes: Nucleide 99mTc, . URL `https://www.nucleonica.com/Application/ReducedDecaySchemes/Tc99_TXT.htm`. Accessed: 01.08.2019. 90

[182] Nucleonica. Reduced decay schemes: Nucleide ^{57}Co, . URL `https://www.nucleonica.com/Application/ReducedDecaySchemes/Co57TXT.htm`. Accessed: 01.08.2019. 91

[183] KRI / V.P. Chechev and N.K. Kuzmenko. LNE – LNHB/CEA Table de Radionucleides: Nucleide ^{57}Co. URL `http://www.nucleide.org/DDEP_WG/Nuclides/Co-57_tables.pdf`. Accessed: 01.08.2019. 91

[184] L. Pidol et al. High efficiency of lutetium silicate scintillators, Ce-doped LPS and LYSO crystals. *Conference: Nuclear Science Symposium Conference Record*, 2(8), 2003. doi: 10.1109/NSSMIC.2003.1351838. 93

[185] Kaewkhao J., Limkitjaroenporn P., Chaiphaksa W. and Kim H.J. Non-proportionality study of $CaMoO_4$ and GAGG:Ce scintillation crystals using Compton coincidence technique. *Appl Radiat Isot.*, 115:221–226, 2016. doi: 10.1016/j.apradiso.2016.06.030. 93

[186] Samuel Bradley Donnald. *A Study of Energy Resolution and Non-proportionality of YAlO3:Ce and $Gd_3Ga_3Al_2O_{12}$:Ce*. PhD thesis, The University of Tennessee, Knoxville, 2014. 93

[187] Martin Janecek. Reflectivity spectra for commonly used reflectors. *IEEE Transactions on Nuclear Science*, 59(3):490–497, 2012. doi: 10.1109/TNS.2012.2183385. 96

[188] Martin Janecek and William W. Moses. Optical reflectance measurements for commonly used reflectors. *IEEE Transactions on Nuclear Science*, 55(4):2432–2437, 2008. doi: 10.1109/TNS.2008.2001408. 96

[189] Masato Yamawaki, Norihide Takeyama and Yousuke Katsumura. Study of reflection and connection materials used for transmitting and condensing scintillation light by means of optical fiber. *Japanese Journal of Applied Physics*, 47(2R), 2008. 96

[190] Francisco Neves *et al.* Measurement of the absolute reflectance of polytetrafluoroethylene (PTFE) immersed in liquid xenon. *Journal of Instrumentation*, 12(1), 2016. doi: 10.1088/1748-0221/12/01/P01017. 96

[191] SensL. ArrayC PCB srrays of SiPM - User manual, . URL `https://www.sensl.com/downloads/ds/UM-ArraySMT.pdf`. Accessed: 01.06.2016. 97

[192] Kamil Barczak *et al.* New optical glasses with high refractive indices for applications in optical current sensors. *Acta Physica Polonica*, 2009. doi: 10.12693/APhysPolA.116.247. 114

[193] Serviço de Medicina Nuclear do Centro Hospitalar da Universidade de Coimbra. Personal communication. 126, 128

[194] M. Ohiduzzaman *et al.* Thyroid Uptake of 99m-Tc and Its Agreement with I-131 for Evaluation of Hyperthyroid Function. *Universal Journal of Public Health*, 7(5):201–206, 2019. doi: 0.13189/ujph.2019.070502. 128

[195] Campennì A., Siracusa M., Ruggeri R.M. *et al.* Differentiating malignant from benign thyroid nodules with indeterminate cytology by 99mTc-MIBI scan: a new quantitative method for improving diagnostic accuracy. *Scientific Reports*, 7(6147), 2017. doi: 10.1038/s41598-017-06603-3. 128

[196] Helena R. Balon *et al.* Society of nuclear medicine procedure guideline for thyroid uptake measurement - version 3.0, . URL `https://bit.ly/2NK3dDE`. Accessed: 01.08.2019. 128

[197] Celso Darío Ramos *et al.* Thyroid uptake and scintigraphy using 99m-Tc pertechnetate: standardization in normal individuals. *Sao Paulo Med. J*, 120(2), 2002. doi: 10.1590/S1516-31802002000200004. 128

[198] M. F. Smith and R. J. Jaszczak. The effect of gamma ray penetration on angle-dependent sensitivity for pinhole collimation in nuclear medicine. *Medical Physics*, 24:1701–1709, 1997. doi: 10.1118/1.597957. 131

[199] Su-Ying Li *et al.* Off-axis imaging in keel-edge pinhole single photon emission computed tomography system based on monte carlo simulation. *chinese Physic letters*, 33(4), 2016. doi: 10.1088/0256-307X/33/4/048701. 132

[200] Tae Yong Song *et al.* Optimization of pinhole collimator for small animal SPECT using Monte Carlo simulation. *IEEE Nuclear Science Symposium Conference Record*, 2002. doi: 10.1109/NSSMIC.2002.1239449. 132

[201] Blin S., Barrillon P. and de La Taille C. MAROC, a generic photomultiplier readout chip. *Conf. Record of IEEE NSS/MIC*, 2010. doi: 10.1109/NSSMIC.2010.5874062. 136

[202] João Pedro Rodrigues. Desenvolvimento do sistema de leitura e aquisição para uma câmara de anger utilizando fotomultiplicadores de silício. Master's thesis, Universidade de Coimbra, www.uc.pt, July 2014. 136

[203] PETsys Electronics. TOFPET2: a high-performance ASIC for time andamplitude measurements of SiPM signals in time-of-flight applications, . URL `https://www.petsyselectronics.com/web/website/docs/products/product1/TOFPET2_Overview.pdf`. Accessed: 05.09.2019. 137, 138

[204] R. Bugalho et al. Experimental characterization of the TOFPET2 ASIC. URL https://www.petsyselectronics.com/web/website/docs/products/product1/TOFPET2_Overview.pdf. Accessed: 05.09.2019. 137, 138

[205] PETsys Electronics. Products, . URL https://www.petsyselectronics.com/web/public/products-list. Accessed: 05.09.2019. 138

[206] PETsys Electronics. PETsys SiPM Readout System, . URL https://www.petsyselectronics.com/web/public/products/6. Accessed: 05.09.2019. 139

[207] Salleh Ahmad *et al.* Triroc: A Multi-Channel SiPM Read-Out ASIC for PET/PET-ToF Application. *IEEE Transactions on Nuclear Science*, 62(3):664–668, 2015. doi: 10.1109/TNS.2015.2397973. 139, 140

[208] Salleh Ahmad *et al.* Triroc, a versatile 64-channel SiPM readout ASIC for time-of-flight PET. *IEEE Nuclear Science Symposium, Medical Imaging Conference and Room-Temperature Semiconductor Detector Workshop (NSS/MIC/RTSD)*, 2016. doi: 10.1109/NSSMIC.2016.8069882. 139

[209] Weeroc High end microelectronics design. Triroc 1A: All-in-one SiPM read-out for multimodal PET inserts. URL https://www.weeroc.com/products/sipm-read-out/triroc-1a. Accessed: 30.11.2019. 139

[210] Dirk Meier *et al.* An ASIC for SiPM/MPPC Readout. *IEEE Nuclear Science Symposuim & Medical Imaging Conference*, 2010. doi: 10.1109/NSSMIC.2010.5874056. 141, 142

[211] Ideas Integrated detector electronics AS. VATA64HDR16.2: 64 Channel Silicon Photomultiplier (SiPM) Readout. URL https://ideas.no/products/vata64hdr16-2/. Accessed: 01.08.2019. 141

[212] M.G. Bagliesi *et al.* A custom front-end ASIC for the readout and timing of 64 SiPM. *Nuclear Physics B (Proc. Suppl.)*, 215(1):344–348, 2011. doi: 10.1016/j.nuclphysbps.2011.04.049. 141

[213] Manuel Penschuck. Development and implementation of a central trigger system for trbnet-based systems. Master's thesis, Goethe Universitat, December 2012. 142, 146

[214] Grzegorz Korcyl et al. (GSI. A Users Guide to the TRB3 and FPGA-TDC Based Platforms. URL http://trb.gsi.de/. Accessed: 01.08.2019. 142, 146

[215] Daniel Belver, Alberto Blanco *et al.* The HADES RPC inner TOF wall. *Nuclear Instruments and Methods in Physics Research Section A Accelerators Spectrometers Detectors and Associated Equipment*, 602(3):687–690, 2009. doi: 10.1016/j.nima.2008.12.090. 143

[216] F.M.C. Clemencio, C.F.M. Loureiro, P. Fonte, and J. Landeck. An all-digital coincidence-selection and coincidence-trigger generation for a small animal RPC-PET camera. *IEEE Trans. Nucl. Sci.*, 60(4):2912–2917, 2009. doi: 10.1109/TNS.2013.2273416. 143

[217] Paulo Martins, Paulo Crespo, Rui Ferreira Marques *et al.* Experimental sub-millimeter resolution with a small-animal RPC-PET prototype. *IEEE Nuclear Science Symposium and Medical Imaging Conference Record (NSS/MIC)*, 2012. doi: 10.1109/NSSMIC.2012.6551863. 143

[218] Jan Michel *et al.* (HADES colaboration). The HADES DAQ System: Trigger and Readout Board Network. *IEEE Transactions on Nuclear Science*, 58(4), 2011. doi: 10.1109/TNS.2011.214115. 145

[219] Jan Michel *et al.* (HADES colaboration). The upgraded HADES trigger and data acquisition system. *JINST, Topical workshop on electronics for particle physics 2011*, 2011. doi: doi:10.1088/1748-0221/6/12/C12056. 145, 146

[220] A. Morozov, J. Marcos, L. Margato *et al.* SiPM-based neutron Anger camera with auto-calibration capabilities. *Journal of Instrumentation*, 14(1), 2019. 149, 219, 223

[221] A. Lipovec, K. Shimazoe and H. Takahashi. Development of high-resolution gamma detector using sub-mm GAGG crystals coupled to TSV-MPPC array. In Journal of Instrumentation, editor, *17th International Workshop on Radiation Imaging Detectors*, volume 11. IOP Publishing Ltd and Sissa Medialab srl, March 2016. 214

[222] Yiping Shao, Xishan Sun, Chad Bircher, Allan Lan and Vikram Jayaram. Gamma camera development with CsI and silicon photomultipler arrays. *J Nucl Med*, 51(2), 2010. doi: 10.1109/NSSMIC.2013.6829332. 215

[223] N.Dinua *et al.* SiPM arrays and miniaturized readout electronics for compact gamma camera. *Nuclear Instruments and Methods in Physics Research Section A: Accelerators, Spectrometers, Detectors and Associated Equipment*, 787:367–372, 2010. doi: 10.1016/j.nima.2015.01.083. 215

[224] Philippov *et al.* SiPM-MAROC gamma-camera prototype with monolithic NaI(Tl) scintillator. *EJNMMI Physics*, 2(1), 2015. doi: 10.1186/2197-7364-2-S1-A49. 215

[225] Giulia Cozzi *et al.* Development of a SiPM-based detection module for prompt gamma imaging in proton therapy. In *IEEE Nuclear Science Symposium - Medical Imaging Conference and Room-Temperature Semiconductor Detector Workshop (NSS/MIC/RTSD)*. IEEE, November 2016. doi: 10.1109/NSSMIC.2016.8069393. 215

[226] Paolo Trigilio *et al.* A SiPM-Readout ASIC for SPECT Applications. *IEEE Transactions on Radiation and Plasma Medical Sciences*, 2(5), 2018. doi: 10.1109/TRPMS.2018.2856201. 215

[227] Junhyeok Kim *et al.* Efficient design of a 2 inch diameter × 2 inch NaI(Tl) scintillation detector coupled with a SiPM in an aquatic environment. *Nuclear Engineering and Technology*, 51(4): 1091–1097, 2019. doi: 10.1016/j.net.2019.01.017. 215

[228] Young Jun Jung *et al.* Development of a sub-miniature gamma camera for multimodal imaging system. *Nuclear Instruments and Methods in Physics Research, Section A: Accelerators, Spectrometers, Detectors and Associated Equipment*, 2019. doi: 10.1016/j.nima.2018.12.020. 215

[229] Thomas Frach *et al.* The digital silicon photomultiplier - principle of operation and intrinsic detector performance. In *IEEE Nuclear Science Symposium conference record. Nuclear Science Symposium*. IEEE, December 2009. doi: 10.1109/NSSMIC.2009.5402143. 215

[230] York Haemischa *et al.* Fully digital arrays of silicon photomultipliers (dSiPM) – a scalable slternative to vacuum photomultiplier tubes (PMT). *Physics Procedia*, 37:1546–1560, 2012. doi: 10.1016/j.phpro.2012.03.749. 215

[231] Jeremy M. C. Brown. In-silico optimisation of tileable sipm based monolithic scintillator detectors for spect applications, 2019. 215

[232] Williams M.B. *et al.* Performance of a PSPMT based detector for scintimammography. *Phys Med Biol.*, 45(3):781–800, 2000. doi: 10.1088/0031-9155/45/3/315. 216

[233] Daniel Steinbach *et al.* Development of a small field of view scintimammography camera based on a YAP crystal array and a position sensitive PMT. *IEEE Nuclear Science Symposium. Conference Record*, 1996. doi: 10.1109/NSSMIC.1996.591638. 216

[234] R. Wojcik *et al.* High spatial resolution gamma imaging detector based on a 5 inches diameter R3292 Hamamatsu PSPMT. *IEEE Transactions on Nuclear Science*, 45(3):487–491, 1996. doi: 10.1109/23.682432. 216

[235] R. Wojcik *et al.* Optimized readout of small gamma cameras for high resolution single gamma and positron emission imaging. *IEEE Nuclear Science Symposium Conference Record (Cat. No.01CH37310)*, 2001. doi: 10.1109/NSSMIC.2001.1008696. 216

[236] Jeong M.H. *et al.* Performance improvement of small gamma camera using NaI(Tl) plate and position sensitive photo-multiplier tubes. *Phys Med Biol.*, 49(21):4961–4970, 2004. doi: 10.1088/0031-9155/49/21/008. 216

[237] Hector Alva *et al.* Characterisation of a Position-Sensitive Photomultiplier Tube for MicroPET Detection Modules. *Medical Physics: Ninth Mexican Symposium on Medical Physics*, 2006. doi: 10.1063/1.2356396. 216

[238] Kim J.H., Ito M., Kim S.M. *et al.* Design optimization of a small-animal SPECT system using LGSO continuous crystals and micro parallel-hole collimators. *Journal of the Korean Physical Society*, 67(224), 2006. doi: 10.3938/jkps.67.224. 216